Polyether- and serum albumin-based hydrogels and bioplastics for bio-interfacing applications leveraging additive manufacturing

Siyami Cem Millik

A dissertation

submitted in partial fulfillment of the

requirements for the degree of

Doctor of Philosophy

University of Washington

2024

Reading Committee:

Alshakim Nelson, Chair

Matthew R. Golder

Jesse G. Zalatan

Program Authorized to Offer Degree:

Department of Chemistry

University of Washington

Abstract

Polyether- and serum albumin-based hydrogels and bioplastics for bio-interfacing applications leveraging additive manufacturing

Siyami Cem Millik

Chair of the Supervisory Committee:

Alshakim Nelson

Department of Chemistry

Additive manufacturing, commonly referred to as 3D printing, affords numerous advantages as an automated means of fabricating 3D objects with excellent design freedom and minimal waste. Despite remarkable progress over the past couple of decades toward making 3D printing technologies more capable and more accessible, there is still a need for more diverse functional materials for 3D printing. For example, in biomedical science and engineering, 3D printing has been used to fabricate anatomical models, medical devices, and tissue- and organ-like constructs comprising living cells. For many of these applications, there is a need for materials that better mimic or interface with the living systems in question. In tissue engineering and therapeutic delivery, hydrogels have shown great promise, as hydrated three-dimensional networks in which

cells can be cultured or therapeutics can be encapsulated. Additionally, when naturally derived hydrogels are dehydrated, more functional or sustainable alternatives to petroleum-derived plastics can be obtained. These materials, which can be referred to as “bioplastics,” can be used to fabricate functional objects via 3D printing. This dissertation focuses on the design, synthesis, and application of functional hydrogels and bioplastics for additive manufacturing in the biomedical space. Chapter 1 contains a brief overview of 3D printing, hydrogels, and water-processable bioplastics, with an emphasis on their biomedical applications. Chapter 2 features a methodology that leverages additive manufacturing to fabricate coaxial nozzles for extrusion of hydrogel tubes toward modeling vascular endothelium. Chapter 3 highlights a highly tunable protein-based bioplastic platform for light-based (vat photopolymerization) 3D printing of functional objects. Chapter 4 describes dynamic hydrogels utilizing a protein-ligand interaction toward potential applications in therapeutic delivery or 3D bioprinting.

Acknowledgements

First, I would like to thank my doctoral advisor, Prof. Alshakim Nelson, who has been an outstanding mentor since I first started working in his lab as an undergraduate. I consider myself very lucky to have been a member of the Nelson Lab for all these years, and I could not have asked for a better advisor and mentor. I would also like to thank all the other faculty and staff who have helped me along the way, both in my research and in my coursework. Finally, I would like to thank all my coauthors, colleagues, and everyone else who has mentored me, lent a hand with experiments, and/or made the time for productive discussions over the years.

Table of Contents

List of Figures

after 24 h in culture. Cells stained with calcein AM (green) for visualization show aggregation and rounded morphology, indicating lack of adhesion. Percent coverage was determined to be 20% ± 9% (SD; n = 3). This image is representative of three replicates. (b) HUVECs seeded on cross-linked, collagen I-treated F127-BUM hydrogel disc with collagen I additive after 24 h in culture. Cells stained with calcein AM for visualization show spreading, indicating adhesion. Percent coverage was determined to be 52% ± 8% (SD; n = 3). This image is representative of three replicates. (c) Viability assay (calcein AM, green/ethidium homodimer-1, red) of HUVECs seeded on cross-linked, collagen-I-treated F127-BUM hydrogel disc with collagen I additive after 72 h in culture. Green indicates live cells, red indicates dead cells; cell viability is high. This image is representative of three replicates. (d,e) Confocal micrographs of HUVECs seeded on the luminal surfaces of tubes composed of cross-linked, collagen-I-treated F127-BUM hydrogel with collagen I additive. Cells stained with DAPI (blue: nuclei) and labeled via indirect immunofluorescence (green: CD31, inter-endothelial junction marker) exhibit characteristic cobblestone morphology. These images are representative of six replicates. (f) Identical treatment to samples in Figure 2.10d,e. Entire width of tube section is visualized, showing good cell coverage. This image is representative of six replicates. (g–i) Identical treatment to samples in Figure 2.10d–f. Luminal surface of tube is visualized via confocal microscopy showing good cell coverage. These images are representative of six replicates.

Figure 3.1. Incorporation of glycerol or HPGs as plasticizing additives into BSA-PEGDA-based aqueous resins for light-based 3D printing affords bioplastics with mechanical properties which vary from rigid and strong (obtained natively) to soft and ductile (obtained with plasticizers).

Figure 3.2. (a) BSA cartoon from crystal structure (PDB ID: 3V03).[92–94] (b) Scheme for derivatization of BSA with PEGDA via *aza*-Michael addition. (c) Hypothetical depiction of the aqueous resin state with soluble BSA (red) derivatized with PEGDA (blue), excess soluble PEGDA (blue), and a generic soluble additive (yellow). (d) Depiction of the hydrogel state with copolymerized BSA and PEG-DA following photo-curing of the resin. (e) Depiction of the bioplastic state following dehydration of the hydrogel. (f) Dynamic light scattering traces showing that Michael addition over 24 h incubation of the resin produces BSA-PEGDA conjugate species of increased size. (g) Photo-rheometry showing prompt curing of resins with and without additives at 405 nm (5 mW cm^{-2}) following 24 h incubation.

Figure 3.3. (a) Additives explored include large-, medium-, and small-sized HPGs (HPG-L, HPG-M, and HPG-S, respectively), and glycerol. (b) Scheme of HPG synthesis via ring-opening multibranching polymerization. (c) ^{1}H NMR spectra of HPG-S, HPG-M, and HPG-L in methanol-d_4. (d) Hydrodynamic diameters of HPG-S, HPG-M, and HPG-L, determined by dynamic light scattering. (e) Apparent steady-shear viscosities of aqueous resins with different additives included at 15 wt%.

Figure 3.4. 3D printed objects, demonstrating 3D printability and functionality of BSA- and PEG-DA-based bioplastics with additives. (a) Block "W" printed using the resin with 15 wt% HPG-M. (b) Gecko model[89] printed using the resin with 15 wt% glycerol. (c) Dialysis clip, with integral catch and hinge, printed using a resin with 10 wt% glycerol. (d) Dialysis clip clipped onto a folded poly(ethylene) bag. (e) 3D printed "W" as printed with the 15 wt% glycerol resin and dehydrated. (f) "W" after heating at 50 °C, flattening between glass slides, and cooling to 21 °C. (g) "W" after recovery at 100 °C in < 2 min.

Figure 4.2. (a) Hypothetical depiction of HPG-C16 self-association in formation of dynamic networks. (b) 15 wt% HPG-C16 hydrogel vial inversion, showing the reversible transition between a nearly transparent gel state and an opaque gel state. (c) Steady-shear viscosity and stress curves for the 15 wt% HPG-C16 hydrogel. (d) Frequency sweep data for the 15 wt% HPG-C16 hydrogel. (e) Stress amplitude sweep data for the 15 wt% HPG-C16 hydrogel. (f) Multi-step high- and low-amplitude oscillatory tests showing self-healing and thixotropy of 15 wt% HPG-C16 hydrogel. (g) Temperature ramp data for the 15 wt% HPG-C16 hydrogel.

Figure 4.3. (a) Photograph of the 15 wt% 1:1 BSA and HPG-C16 mixture after vial inversion, showing viscous liquid character (left); and photographs showing the appearance of unsaturated and saturated 15 wt% 1:1 BSA and HPG-C16 mixtures (right). "Unsaturated" (unsat.) refers to mixtures comprising fatty-acid-free BSA. "Saturated" (sat.) refers to mixtures comprising BSA pre-saturated with free palmitate. (b) Steady-shear viscosity and stress curves for the 15 wt% 1:1 BSA and HPG-C16 mixtures (unsaturated and saturated). (c) Steady-shear viscosity and stress curves for the 30 wt% 1:1 BSA and HPG-C16 mixtures (unsaturated and saturated). (d) Frequency sweep data for the 15 wt% 1:1 BSA and HPG-C16 mixtures (unsaturated and saturated). (e) Frequency sweep data for the 30 wt% 1:1 BSA and HPG-C16 mixtures (unsaturated and saturated). (f) Stress amplitude sweep data for the 15 wt% and 30 wt% saturated 1:1 BSA and HPG-C16 mixtures. Unsaturated mixtures did not show yield stresses. (g) Comparison of apparent viscosity at shear rate, $\dot{\gamma} = 1.0\ s^{-1}$ and power law index, n, for all 1:1 BSA and HPG-C16 mixtures. (h) Comparison of G' and tan δ at angular frequency, $\omega = 10$ rad s^{-1} for all 1:1 BSA and HPG-C16 mixtures. (i) Comparison of apparent yield stress for 15 wt% and 30 wt% saturated 1:1 BSA and HPG-C16 mixtures.

Figure 4.4. (a) Abbreviated synthetic scheme for SAN-30, SAN-45, and SAN-60. (b) Dynamic light scattering traces for SANs and native BSA. (c) Comparison of Z-average hydrodynamic diameters, d_H and dispersities by DLS for SANs and native BSA. (d) Circular dichroism (CD) spectra for SANs and native BSA showing that SANs retained the characteristic α-helical secondary structure of serum albumin.

Figure 4.5. (a) Hypothetical depiction of SAN + HPG-C16 dynamic network formation. (b) The 15 wt% (3:2) SAN-45 and HPG-C16 hydrogel (termed "intermediate") inverted, inside of a syringe. (c) Steady-shear viscosity and stress curves for the intermediate gel (unsaturated and saturated). "Unsaturated" (unsat.) refers to mixtures comprising fatty-acid-free SAN. "Saturated" (sat.) refers to mixtures comprising SAN pre-saturated with free palmitate. (d) Frequency sweep data for the intermediate gel (unsaturated and saturated). (e) Stress amplitude sweep data for the intermediate gel (unsaturated and saturated). (f) Comparison of apparent viscosity at shear rate, $\dot{\gamma} = 1.0\ s^{-1}$ and power law index, n, for the intermediate gel (unsaturated and saturated). (g) Comparison of G' at angular frequency, $\omega = 10$ rad s^{-1}, and tan δ at two angular frequencies, for the intermediate gel (unsaturated and saturated). (h) Comparison of apparent yield stress for the intermediate gel (unsaturated and saturated).

Figure 4.6. (a) Photographs of hydrogels with 3:2 mass fraction of SAN-45 and HPG-C16, with variable total concentration. (b) Photographs of hydrogels with 15 wt% SAN-45 and HPG-C16, with variable mass fraction of the components. (c) Photograph of hydrogels with 15 wt% (3:2) SAN and HPG-C16, with variable SAN size. (d–f) Steady-shear viscosity and stress curves for the three variable sets. (g–i) Frequency sweep data for the three variable sets. (j–l) Stress amplitude sweep data for the three variable sets.

Figure 4.7. (a–c) Comparisons of apparent viscosity at shear rate, $\dot{\gamma} = 1.0\ s^{-1}$ and power law index, n, for the three variable sets (varied total concentration, varied ratio of components, and varied SAN size). (d–f) Comparisons of G' and tan δ at angular frequency, $\omega = 10$ rad s^{-1} for the three variable sets. (g–i) Comparison of apparent yield stress for the three variable sets.

Figure 4.8. (a) The 15 wt% (1:1) SAN-60 and HPG-C16 hydrogel (termed "combined") inverted, inside of a syringe (right), compared to the intermediate gel (left). (b) Steady-shear viscosity and stress curves for the intermediate and combined gels. (c) Frequency sweep data for the intermediate and combined gels. (d) Stress amplitude sweep data for the intermediate and combined gels. (e) Comparison of apparent viscosity at shear rate, $\dot{\gamma} = 1.0\ s^{-1}$ and power law index, n, for the intermediate and combined gels. (f) Comparison of G' and tan δ at angular frequency, $\omega = 10$ rad s^{-1} for the intermediate and combined gels. (g). Comparison of apparent yield stress for the intermediate and combined gels. (h) Multi-step high- and low-amplitude oscillatory tests showing self-healing and thixotropy of intermediate and combined gels. (i) Temperature ramp data for the intermediate and combined gels. (j) Comparison of G' and tan δ at 21 °C and 37 °C for the intermediate and combined gels.

Figure 4.9. (a) Steady-shear viscosity and stress curves for the 15 wt% (1:1) SAN-60 and HPG-C16 hydrogel (termed "combined")—saturated and unsaturated. (b) Frequency sweep data for the combined gel (saturated and unsaturated). (c) Stress amplitude sweep data for the combined gel (saturated and unsaturated). (d) Comparison of apparent viscosity at shear rate, $\dot{\gamma} = 1.0\ s^{-1}$ and power law index, n, for the combined gel (saturated and unsaturated). (e) Comparison of G' at angular frequency, $\omega = 10$ rad s^{-1}, and tan δ at two angular frequencies, for the combined gel (saturated and unsaturated). (f) Comparison of apparent yield stress for the combined gel (saturated and unsaturated).

Figure 4.10. (a) Schematic representation of injection force measurement using a load frame. (b) Injection force curves obtained using 1 mL syringes with 0.5 in needles (23 G and 27 G), using a 1.2 mL min^{-1} injection rate. (c) Comparison of plateau force using 23 G needle. (d) Comparison of plateau force using 27 G needle. Data for 30 wt% F-127 gel included for comparison.

Figure 4.11. (a) SAN + HPG-C16 gel before and after immersing in water. The increased opacity suggests phase separation is occurring in the presence of excess aqueous medium. (b) Materials after 31.5 d in dissolution medium (1X PBS or DMEM with 10% FBS) at 37 °C, static conditions. (c) Cumulative mass loss of materials in 1X PBS at 37 °C, static conditions. (d) Cumulative mass loss of materials in DMEM with 10% FBS at 37 °C, static conditions.

Figure 4.12. (a) Schematic representation of in vitro release experiments. (b) Comparison of cumulative release of Cy5-labeled IgG or Cy-5 labeled IgG-C16 from materials after 15.5 d in DMEM with 10% FBS at 37 °C, static conditions. (c–f) Cumulative release of Cy5-labeled IgG or Cy5-labeled IgG-C16 from materials over 15.5 d.

Figure 4.13. (a) Schematic representation of direct ink writing. (b) Single-layer print with intermediate gel (dyed blue). (c) Multi-layered print with combined gel (dyed maroon).

Figure A1. ^{1}H NMR spectrum of F127-BUM (500 MHz, 293 K, $CDCl_3$).

Figure A2. ^{1}H NMR spectrum of F127 (500 MHz, 293 K, $CDCl_3$).

Figure A3. (a) GPC trace of F127; $Đ = 1.28$. (b) GPC trace of F127-BUM; $Đ = 1.28$.

Figure B1. ^{1}H NMR spectrum of HPG-S (500 MHz, CD_3OD). Asterisk denotes signal from vacuum grease. “TMP” refers to TMP core of HPG.

Figure B2. ^{1}H NMR spectrum of HPG-M (500 MHz, CD_3OD). Asterisk denotes signal from vacuum grease.

Figure B3. ^{1}H NMR spectrum of HPG-L (500 MHz, CD_3OD). Asterisk denotes signal from vacuum grease.

Figure B4. DLS trace for HPG-S in deionized water.

Figure B5. DLS trace for HPG-M in deionized water.

Figure B6. DLS trace for HPG-L in deionized water.

Figure B7. ^{1}H NMR spectrum of LAP (500 MHz, D_2O).

Figure B8. ATR-FTIR spectra for bioplastics (amide I region).

Figure C1. (a) Steady-shear viscosity and stress curves for 30 wt% F-127 hydrogel. (b) Frequency sweep data for 30 wt% F-127 hydrogel. (c) Stress amplitude sweep data for 30 wt% F-127 hydrogel. (d) Multi-step high- and low-amplitude oscillatory tests showing self-healing and thixotropy of 30 wt% F-127 hydrogel.

Figure C2. Hypothetical depiction of saturated SAN + HPG-C16 dynamic network formation.

Figure C3. Custom syringe holder used for injection force measurements. It was 3D printed using fused filament fabrication, with poly(lactide) filament.

List of Tables

Chapter 1

Introduction

1.1. Additive Manufacturing (3D printing) in Bio-Interfacing Applications

The utility of 3D printing in bio-interfacing applications extends from the fundamental features of 3D printing technology that make it useful in numerous other areas, including in aerospace, automotive, and electronics industries.[1–3] These fundamental features include computerized motion control, integration with computer-aided design (CAD), and the additive nature of the fabrication process.[3,4] Computer control of the additive process affords precision, reproducibility, and simplified fabrication workflows.[2–4] Centimeter-scale objects with feature resolution down to hundreds of micrometers can be reliably obtained using common 3D printers and 3D printing materials; more specialized hardware and materials can extend feature resolution down to the nano scale.[5,6] Particularly in the context of bio-fabrication, 3D printing technologies can also afford impressive fabrication efficiency in terms of the ratio of feature resolution to fabrication time.[7] Finally, the additive nature of the process is intrinsically well suited to patterning of cells and other sensitive biologics under physiological conditions. For example, using 3D printing, one could fabricate replicate sets of nearly dimensionally identical hydrogel constructs containing viable cultured cells, at scale, in a relatively short time.[8,9] Such capability has been exploited for fabrication of engineered tissues and organ-like constructs for use in sophisticated in vitro models as well as toward clinical translation.[10–14]

Integration of 3D printing technologies with CAD, as well as the additive nature of the methodology, allow fabrication of complex form factors which can be difficult or impossible to achieve using formative or subtractive techniques.[2–4] Using 3D printing, complex objects with irregular features, voids, or nested or hierarchical features can often be fabricated with ease. Additionally, CAD designs can be computationally optimized in terms of physical or mechanical properties, or to minimize material waste.[15,16] Structures can also be obtained from 3D scans or medical imaging data toward fabrication of personalized medical devices.[17–19] For example, in the hearing-aid industry, 3D scans of patients' ear canals have been used to 3D print hearing aid shells with near-perfect fit.[20] Similarly, 3D printing technology has greatly impacted the field of digital dentistry, where diagnostic models, surgical guides, implants, and restorative devices can be fabricated—again, through integration with 3D scanning and medical imaging technology.[21]

In biomedical science, as well as in any other industry, 3D printing technologies can be indispensable in research and development operations. The lack of a need for specialized tooling, as well as the minimally wasteful nature of the additive process enable rapid iteration of designs.[1] This cost- and material-efficiency makes 3D printing particularly well suited to prototyping, research, and small- to moderate-volume manufacturing applications.[22] For example, once a researcher identifies a need, a solution can be quickly visualized in CAD and a prototype can be 3D printed and evaluated in application nearly immediately. Losses in time and material are minimal if designs fail and need to be reworked.

Over the last fifteen years, 3D printing technologies have become substantially more accessible. Inexpensive, easily transportable, and highly capable 3D printers are now widely commercially available.[23,24] CAD software[25,26] and 3D models[27,28] are also freely available online. The current accessibility of 3D printing hardware, software, and materials represents a

lower barrier to adoption of the technology than ever before, allowing users from many different technical backgrounds to leverage the advantages of 3D printing in a wide scope of use cases. Notably, 3D printing proved useful for production of medical supplies and personal protective equipment (PPE) during the COVID-19 pandemic. Much of this fabrication, particularly of PPE, took place outside of research or healthcare settings (e.g., in private residences), illustrating the value of broad accessibility to 3D printing as well as the utility of 3D printing in decentralized manufacturing.[29–31]

Although 3D printing hardware, software, and materials are becoming more capable and more accessible every day, there is still a need for more diverse and functional materials for 3D printing. For extrusion-based 3D printing, the large majority of materials currently used are rigid thermoplastics.[32,33] Medical devices or anatomical models 3D printed from these materials are non-hydrated, unphysiologically stiff structures which cannot meaningfully recapitulate the properties of many biological systems nor effectively integrate with them. The physical, chemical, and mechanical mismatch between such materials and biological systems preclude their use in many bio-interfacing applications, such as those in tissue engineering, therapeutic delivery, and biosensing.[34–36] For vat photopolymerization, the large majority of materials currently used are rigid and brittle thermosets,[37–39] which again lack physical, chemical, and mechanical similarity to many biological systems. More recently, elastomeric resins for vat photopolymerization have become available.[40,41] Elastomers can exhibit softness and elasticity reminiscent of soft tissues and can thus serve as mechanical models of soft tissues, e.g., for preoperative planning.[42] However, 3D printable elastomers are still relatively few. Additionally, the large majority of commercially available materials for vat photopolymerization are derived from petroleum feedstocks, which are not sustainable sources.[43–46] Printing with these materials

also typically requires the use of non-trivial quantities of organic wash solvents. 3D printable hydrogels, water-processable materials, and materials with biological functionality are virtually absent from the commercial market. Thus, from a materials perspective, despite the remarkable advances of the last few decades, there are still many innovations to be made toward realizing the potential of additive manufacturing.

1.2. Introduction to Hydrogels and Water-Processable Plastics

Hydrogels are typically defined as macromolecular materials comprising a substantial volume (e.g., 70–99%) of water.[35,47,48] The macromolecular units within a hydrogel associate to form a network, spanning a bulk volume and imparting solid-like character to the material.[47–49] Hydrogel networks are the products of covalent polymerization or cross-linking processes, or non-covalent or physical interactions, including mechanical or topological interactions such as particle jamming or chain entanglement.[47,48,50–52] Water molecules associate with hydrogel networks to varying degrees. Additional free water diffuses through molecular-scale or larger pores within these networks.[47] This free water can act as a solvent for small molecules or dissolved macromolecules which diffuse through the pores of the hydrogel. A hydrogel can thus be conceptualized as a liquid solution phase permeated by a solid skeleton. Consequently, hydrogels can be given stable form factors via suitable fabrication techniques (e.g., formative or additive manufacturing), which can enable construction of functional devices from hydrogels.[53]

The useful attributes of hydrogels stem principally from their high volume fractions of free water, their solid-like character, and their general biocompatibility. Hydrogels are often used as bulk materials in biomedical applications. Proven applications include 3D cell culture and

therapeutic delivery.[34,35] In 3D cell culture applications, hydrogels afford solid-like, three-dimensional structure to the cultured cells, while providing a hydrated environment and allowing transport of nutrients.[34] Hydrogels can be engineered to exhibit viscoelasticity reminiscent of soft tissues, more closely mimicking the native environments of cultured cells than unphysiologically stiff and two-dimensional traditional culture substrates.[34,54] Hydrogels can also be engineered to present insoluble biochemical cues to cultured cells via biomolecular functionalization of the network, which can help direct cell growth and behavior.[55,56]

For therapeutic delivery, hydrogels can be loaded with therapeutic small molecules, macromolecules, or therapeutic cells.[35,57] Therapeutics localized within hydrogels can be released in a predictable and/or inducible manner over specific timescales via tuning of network porosity, degradation behavior, or interactions between the therapeutic cargo and the network. Controlled delivery of therapeutics via hydrogel depots can obviate the need for high or repeated dosing and can thus more safely and efficiently elicit therapeutic effects.[35]

Removal of the water from hydrogels can yield dense, fluid-free macromolecular networks.[58–60] Here, fluid-free macromolecular networks will be referred to simply as plastics, or bioplastics in cases where macromolecular components are bio-sourced. For production of water-processable plastics, the reagents necessary for network formation can be dissolved in water to afford an aqueous resin (also known as a prepolymer solution). Water-dispersible additives (e.g., therapeutics, nanomaterials, living microorganisms) can be included in these resins. The aqueous resins can then be cured via a polymerization or cross-linking process to afford a parent hydrogel. Water can then be evaporated from the parent hydrogel to obtain the plastic, which is typically stronger, stiffer, and often more ductile than the parent hydrogel.[58,59] Water-processable plastics prepared in this way can retain some advantages of their parent hydrogels (e.g.,

biocompatibility and biodegradability), combining these advantages with potentially superior mechanical properties typical of plastics. However, if rehydration back to the hydrogel state is not desired, additional treatment of these plastics (e.g., hydrophobization) will likely be necessary.[61,62]

Hydrogels and water-processable plastics can be fabricated from a range of synthetic or naturally derived macromolecules. These macromolecules must simply be soluble or dispersible in water. Commonly used synthetic polymers include poly(ethylene glycol),[63,64] poly(vinyl alcohol),[65,66] polyacrylates,[67,68] and polyacrylamides.[69,70] Commonly used natural macromolecules include gelatin,[71–73] collagen,[74,75] fibrin,[76,77] hyaluronic acid,[78,79] and alginate.[80,81] Hybrid systems comprising natural and synthetic components are often employed. Hybrid systems can be advantageous because their natural components can afford biocompatibility or specific biological functionality while their synthetic components can provide improved control over network synthesis and properties or improved scalability.[82,83]

1.3. Dynamic Hydrogels for Injection and Extrusion-Based Processes

Hydrogels based on non-covalent/physical or dynamic-covalent networks show dynamic mechanical and rheological behaviors.[50,51] These behaviors can include reversible flowability under stress, which enables injection/extrusion, spreading, or sculpting/molding. In such cases, applied stress causes the material to flow via a transition from a gel state (solid) to a sol state (liquid). This transition is the result of mechanical disruption of the network.[50,51]

In systems which are particularly well-suited to fabrication by extrusion, once stress is removed, immediate cessation of flow (i.e., reversal of the gel-sol transition) can effectively

preserve the fabricated form factor. This sort of dynamic behavior is valuable for injectable therapeutic delivery as well as for fabrication of objects from gels via 3D printing.[57,84–88]

In the case of injectable therapeutic delivery, dynamic gels can be loaded with a therapeutic cargo simply by mixing the cargo into the gel. The loaded gel can be delivered minimally invasively through a needle or catheter. Following delivery, solid-like character facilitates local retention of the gel. The therapeutic cargo can then be released from the gel in a controlled manner.[57,84,85]

For 3D printing via material deposition (i.e., direct ink writing (DIW)), a dynamic gel can be dispensed from a nozzle or needle onto a surface.[89] Multiple layers of material can be deposited to afford a three-dimensional construct. Following deposition, prompt recovery of solid-like character prevents buckling or sagging of the structure or loss of fine features due to excessive coalescence of material.[84,86,88] Once again, additives can be mixed into the gel prior to dispensing. When living cells are included in the gel toward printing of engineered tissues, the living-cell composite gel is referred to as a bioink, and the additive manufacturing technique is referred to as 3D bioprinting.[86,90] The utility of 3D bioprinting via DIW of dynamic hydrogels extends in large part from its intrinsic suitability for multi-material fabrication, which is important for fabrication of complex tissue or organ constructs.[86,89] Additionally, the solid-like properties of dynamic gels used in DIW can prevent cell sedimentation prior to printing, which is a potential problem when cells are loaded into liquid resins for vat photopolymerization.[88]

Dynamic hydrogel networks are often formed by non-covalent interactions such as hydrogen bonds, ionic bonds, metal-ligand coordination, and hydrophobic interactions.[50,51] Dynamic covalent chemistries have also been used.[91] Topological entanglement of polymer chains or nonspecific associations between macromolecular or supramolecular units (e.g.,

micelles) can also contribute to stabilization of a network structure.[51,88,92] Granular dynamic hydrogels based on jamming of covalently cross-linked hydrogel particles have also been reported.[52] An interesting class of dynamic networks is that based on host-guest complexation.[51] These interactions are notable for their specificity and directionality. Examples include networks utilizing cyclodextrins or cucurbit[*n*]urils as "host" moieties. In both cases network formation occurs by inclusion of a hydrophobic "guest" moiety within the hydrophobic cavity of the macrocyclic host.[51,93,94] Similarly, ligand binding (i.e., specific biomolecular recognition) by proteins or polypeptides has been utilized for network formation, albeit examples in the literature are relatively few.[95] One such example is leucine-zipper hydrogels, where amphiphilic leucine-rich helices assemble via charged and hydrophobic interactions.[96,97] Another example is hydrogels based on the specific association of "WW" and proline-rich peptide domains.[98,99] A potential drawback of dynamic hydrogels report to date that utilize biomolecular recognition for network formation is that these systems comprise engineered peptides or recombinant proteins, which may limit their accessibility or scalability.[50,84]

1.4. Static Hydrogels and Their Dehydrated Counterparts

Hydrogels comprising static covalent networks can provide physical and mechanical advantages over dynamic hydrogels.[47,51,95] Static networks exhibit largely time-independent dominant elastic character.[49] After the network has been formed via a polymerization or cross-linking process, the material will not appreciably flow, nor can it be permanently reshaped without irreversible rupture of the network. However, this static character, which is derived from irreversible bonding within the network, also typically affords higher mechanical strength and

rigidity relative to dynamic networks.[47–49] This strength and rigidity can allow fabrication of mechanically functional objects from these hydrogels. Static networks are also insoluble, which often affords long-term physical stability in aqueous media. When networks are formed from hydrolytically stable bonds, static hydrogels may be maintained indefinitely in aqueous media, including in complex biological media.[100,101]

Since typical static hydrogels cannot be permanently reshaped without undesirable degradation of the network, formation of the static network must occur during fabrication of the desired "final" form factor. As such, additive or formative manufacturing techniques are employed, where polymerization or cross-linking reactions take place during the fabrication process.[53,102,103] In the case of 3D printing, the specific technique to be used depends on the physical state of the precursor material. When precursors to the static hydrogel are relatively low-viscosity liquids (i.e., aqueous resins), fabrication via selective curing of the resin by precise projection of light (e.g., vat photopolymerization) can be conveniently employed.[38,53] The use of vat photopolymerization techniques requires that static network formation occur via a photo-initiated polymerization or cross-linking reaction. In this case, the rate of the reaction must be matched to the desired rate of fabrication.[38] Alternatively, when the precursor to the static hydrogel is a dynamic hydrogel, DIW can be used to produce the desired form factor, which can be further stabilized by secondary covalent polymerization or cross-linking.[86,89] In some cases, the advantages afforded by 3D printing do not warrant the potential complications it can introduce—for example, challenges in synthesis of defect-free networks.[104] In such cases, casting of precursor materials, using a mold, followed by a time-dependent or photo-initiated curing process can be a convenient alternative.

Static hydrogels can be conceptualized as water-filled thermosets. Accordingly, water can be removed from these networks via evaporation to afford thermoset plastics.[58,61,105] This approach can be a viable strategy for fabrication of mechanically robust plastics from hydrophilic polymers.[61] Perhaps the greatest advantages of fabricating thermosets via dehydration of static hydrogels are safety and sustainability.[43] Many naturally sourced and biodegradable macromolecules are hydrophilic and are thus well suited to aqueous processing to afford "bioplastics." Since the solvent used is water, hazard controls necessary are often less stringent than would be if organic solvents were used, and hazardous waste products are minimal. A potential disadvantage of this approach is that removal of water from a parent hydrogel post-fabrication to afford a plastic is accompanied by substantial shrinkage of the construct. This shrinkage is often apparently isotropic and can be accounted for when molding or modeling. However, in cases where water occupies a large fraction of the initial volume, warping of parts can occur during evaporation. To reduce the extent of shrinkage and the likelihood of warping, it is often advantageous to formulate precursor resins or gels with high macromolecular loading. Control of airflow and pressure during drying can additionally help reduce or eliminate warping. Another potential disadvantage of water-processable plastics is that they can often rehydrate upon water exposure, precluding use in water-contacting applications where stable plastic-like properties are required. However, the potential for water reuptake following dehydration can be greatly reduced by thermal treatment, additional cross-linking, coating, or hydrophobization approaches.[61,62]

Suitable chemistries for fabrication of static hydrogels and water-processable thermosets include radical polymerizations, radical addition (i.e., thiol-ene), Michael additions, and other click-type reactions.[47,48] Photo-induced reactions are generally the most practical chemistries for

these purposes, in large part due to the spatial control over curing that they afford and thus their adaptability to 3D printing.

References

(1) Rayna, T.; Striukova, L. From Rapid Prototyping to Home Fabrication: How 3D Printing Is Changing Business Model Innovation. *Technol. Forecast. Soc.* **2016**, *102*, 214–224. https://doi.org/10.1016/j.techfore.2015.07.023.

(2) Attaran, M. The Rise of 3-D Printing: The Advantages of Additive Manufacturing over Traditional Manufacturing. *Bus. Horizons* **2017**, *60* (5), 677–688. https://doi.org/10.1016/j.bushor.2017.05.011.

(3) Ngo, T. D.; Kashani, A.; Imbalzano, G.; Nguyen, K. T. Q.; Hui, D. Additive Manufacturing (3D Printing): A Review of Materials, Methods, Applications and Challenges. *Compos. Part B: Eng.* **2018**, *143*, 172–196. https://doi.org/10.1016/j.compositesb.2018.02.012.

(4) Gross, B. C.; Erkal, J. L.; Lockwood, S. Y.; Chen, C.; Spence, D. M. Evaluation of 3D Printing and Its Potential Impact on Biotechnology and the Chemical Sciences. *Anal. Chem.* **2014**, *86* (7), 3240–3253. https://doi.org/10.1021/ac403397r.

(5) Xing, J.-F.; Zheng, M.-L.; Duan, X.-M. Two-Photon Polymerization Microfabrication of Hydrogels: An Advanced 3D Printing Technology for Tissue Engineering and Drug Delivery. *Chem. Soc. Rev.* **2015**, *44* (15), 5031–5039. https://doi.org/10.1039/C5CS00278H.

(6) Vyatskikh, A.; Delalande, S.; Kudo, A.; Zhang, X.; Portela, C. M.; Greer, J. R. Additive Manufacturing of 3D Nano-Architected Metals. *Nat. Commun.* **2018**, *9* (1), 593. https://doi.org/10.1038/s41467-018-03071-9.

(7) Moroni, L.; Boland, T.; Burdick, J. A.; De Maria, C.; Derby, B.; Forgacs, G.; Groll, J.; Li, Q.; Malda, J.; Mironov, V. A.; Mota, C.; Nakamura, M.; Shu, W.; Takeuchi, S.; Woodfield, T. B. F.; Xu, T.; Yoo, J. J.; Vozzi, G. Biofabrication: A Guide to Technology and Terminology. *Trends Biotechnol.* **2018**, *36* (4), 384–402. https://doi.org/10.1016/j.tibtech.2017.10.015.

(8) Lerman, M. J.; Lembong, J.; Gillen, G.; Fisher, J. P. 3D Printing in Cell Culture Systems and Medical Applications. *Appl. Phys. Rev.* **2018**, *5* (4), 041109. https://doi.org/10.1063/1.5046087.

(9) Ma, Z.; Wang, J.; Qin, L.; Chortos, A. 3D Printing in Biofabrication: From Surface Textures to Biological Engineering. *Chem. Eng. J.* **2024**, *500*, 156477. https://doi.org/10.1016/j.cej.2024.156477.

(10) Murphy, S. V.; Atala, A. 3D Bioprinting of Tissues and Organs. *Nat. Biotechnol.* **2014**, *32* (8), 773–785. https://doi.org/10.1038/nbt.2958.

(11) Ma, X.; Liu, J.; Zhu, W.; Tang, M.; Lawrence, N.; Yu, C.; Gou, M.; Chen, S. 3D Bioprinting of Functional Tissue Models for Personalized Drug Screening and in Vitro Disease Modeling. *Adv. Drug Deliver. Rev.* **2018**, *132*, 235–251. https://doi.org/10.1016/j.addr.2018.06.011.

(12) Mazzocchi, A.; Soker, S.; Skardal, A. 3D Bioprinting for High-Throughput Screening: Drug Screening, Disease Modeling, and Precision Medicine Applications. *Appl. Phys. Rev.* **2019**, *6* (1), 011302. https://doi.org/10.1063/1.5056188.

(13) Murphy, S. V.; De Coppi, P.; Atala, A. Opportunities and Challenges of Translational 3D Bioprinting. *Nat. Biomed. Eng.* **2020**, *4* (4), 370–380. https://doi.org/10.1038/s41551-019-0471-7.

(14) Kang, H.-W.; Lee, S. J.; Ko, I. K.; Kengla, C.; Yoo, J. J.; Atala, A. A 3D Bioprinting System to Produce Human-Scale Tissue Constructs with Structural Integrity. *Nat. Biotechnol.* **2016**, *34* (3), 312–319. https://doi.org/10.1038/nbt.3413.

(15) Feng, J.; Fu, J.; Lin, Z.; Shang, C.; Li, B. A Review of the Design Methods of Complex Topology Structures for 3D Printing. *Vis. Comput. Ind. Biomed. Art* **2018**, *1* (1), 5. https://doi.org/10.1186/s42492-018-0004-3.

(16) Ford, S.; Despeisse, M. Additive Manufacturing and Sustainability: An Exploratory Study of the Advantages and Challenges. *J. Clean. Prod.* **2016**, *137*, 1573–1587. https://doi.org/10.1016/j.jclepro.2016.04.150.

(17) Marro, A.; Bandukwala, T.; Mak, W. Three-Dimensional Printing and Medical Imaging: A Review of the Methods and Applications. *Curr. Prob. Diagn. Radiol.* **2016**, *45* (1), 2–9. https://doi.org/10.1067/j.cpradiol.2015.07.009.

(18) Goyanes, A.; Det-Amornrat, U.; Wang, J.; Basit, A. W.; Gaisford, S. 3D Scanning and 3D Printing as Innovative Technologies for Fabricating Personalized Topical Drug Delivery Systems. *J. Control. Release* **2016**, *234*, 41–48. https://doi.org/10.1016/j.jconrel.2016.05.034.

(19) Vaz, V. M.; Kumar, L. 3D Printing as a Promising Tool in Personalized Medicine. *AAPS PharmSciTech* **2021**, *22* (1), 49. https://doi.org/10.1208/s12249-020-01905-8.

(20) Sandström, C. G. The Non-Disruptive Emergence of an Ecosystem for 3D Printing — Insights from the Hearing Aid Industry's Transition 1989–2008. *Technol. Forecast. Soc.* **2016**, *102*, 160–168. https://doi.org/10.1016/j.techfore.2015.09.006.

(21) Tian, Y.; Chen, C.; Xu, X.; Wang, J.; Hou, X.; Li, K.; Lu, X.; Shi, H.; Lee, E.-S.; Jiang, H. B. A Review of 3D Printing in Dentistry: Technologies, Affecting Factors, and Applications. *Scanning* **2021**, *2021* (1), 9950131. https://doi.org/10.1155/2021/9950131.

(22) Berman, B. 3-D Printing: The New Industrial Revolution. *Bus. Horizons* **2012**, *55* (2), 155–162. https://doi.org/10.1016/j.bushor.2011.11.003.

(23) *Creality*. https://www.creality.com/ (accessed 2024-11-24).

(24) *Anycubic*. https://www.anycubic.com/ (accessed 2024-11-24).

(25) *Tinkercad*. https://www.tinkercad.com/ (accessed 2024-11-24).

(26) *Autodesk Fusion*. https://www.autodesk.com/products/fusion-360/ (accessed 2024-11-24).

(27) *GrabCAD*. https://grabcad.com/ (accessed 2024-11-24).

(28) *Thingiverse*. https://www.thingiverse.com/ (accessed 2024-11-24).

(29) Mueller, T.; Elkaseer, A.; Charles, A.; Fauth, J.; Rabsch, D.; Scholz, A.; Marquardt, C.; Nau, K.; Scholz, S. G. Eight Weeks Later—The Unprecedented Rise of 3D Printing during the COVID-19 Pandemic—A Case Study, Lessons Learned, and Implications on the Future of Global Decentralized Manufacturing. *Appl. Sci.* **2020**, *10* (12), 4135. https://doi.org/10.3390/app10124135.

(30) Longhitano, G. A.; Nunes, G. B.; Candido, G.; da Silva, J. V. L. The Role of 3D Printing during COVID-19 Pandemic: A Review. *Prog. Addit. Manuf.* **2021**, *6* (1), 19–37. https://doi.org/10.1007/s40964-020-00159-x.

(31) Oladapo, B. I.; Ismail, S. O.; Afolalu, T. D.; Olawade, D. B.; Zahedi, M. Review on 3D Printing: Fight against COVID-19. *Mater. Chem. Phys.* **2021**, *258*, 123943. https://doi.org/10.1016/j.matchemphys.2020.123943.

(32) Daminabo, S. C.; Goel, S.; Grammatikos, S. A.; Nezhad, H. Y.; Thakur, V. K. Fused Deposition Modeling-Based Additive Manufacturing (3D Printing): Techniques for Polymer Material Systems. *Mater. Today Chem.* **2020**, *16*, 100248. https://doi.org/10.1016/j.mtchem.2020.100248.

(33) Rajan, K.; Samykano, M.; Kadirgama, K.; Harun, W. S. W.; Rahman, Md. M. Fused Deposition Modeling: Process, Materials, Parameters, Properties, and Applications. *Int J Adv. Manuf. Technol.* **2022**, *120* (3), 1531–1570. https://doi.org/10.1007/s00170-022-08860-7.

(34) Caliari, S. R.; Burdick, J. A. A Practical Guide to Hydrogels for Cell Culture. *Nat. Methods* **2016**, *13* (5), 405–414. https://doi.org/10.1038/nmeth.3839.

(35) Li, J.; Mooney, D. J. Designing Hydrogels for Controlled Drug Delivery. *Nat. Rev. Mater.* **2016**, *1* (12), 1–17. https://doi.org/10.1038/natrevmats.2016.71.

(36) Herrmann, A.; Haag, R.; Schedler, U. Hydrogels and Their Role in Biosensing Applications. *Adv. Healthc. Mater.* **2021**, *10* (11), 2100062. https://doi.org/10.1002/adhm.202100062.

(37) Appuhamillage, G. A.; Chartrain, N.; Meenakshisundaram, V.; Feller, K. D.; Williams, C. B.; Long, T. E. 110th Anniversary: Vat Photopolymerization-Based Additive Manufacturing: Current Trends and Future Directions in Materials Design. *Ind. Eng. Chem. Res.* **2019**, *58* (33), 15109–15118. https://doi.org/10.1021/acs.iecr.9b02679.

(38) Pagac, M.; Hajnys, J.; Ma, Q.-P.; Jancar, L.; Jansa, J.; Stefek, P.; Mesicek, J. A Review of Vat Photopolymerization Technology: Materials, Applications, Challenges, and Future Trends of 3D Printing. *Polymers* **2021**, *13* (4), 598. https://doi.org/10.3390/polym13040598.

(39) Al Rashid, A.; Ahmed, W.; Khalid, M. Y.; Koç, M. Vat Photopolymerization of Polymers and Polymer Composites: Processes and Applications. *Addit. Manuf.* **2021**, *47*, 102279. https://doi.org/10.1016/j.addma.2021.102279.

(40) Kasprzak, C.; Brown, J. R.; Feller, K.; Scott, P. J.; Meenakshisundaram, V.; Williams, C.; Long, T. Vat Photopolymerization of Reinforced Styrene–Butadiene Elastomers: A Degradable Scaffold Approach. *ACS Appl. Mater. Inter.* **2022**, *14* (16), 18965–18973. https://doi.org/10.1021/acsami.2c03410.

(41) Cao, S.; Zhang, S.; Liu, M.; Heydaroglu, M.; Wen, C.; Sun, J.; Wang, Y.; Yu, M.; Han, X. Mechanically Robust and Highly Stretchable Acrylated Glycerol Polyether Elastomers for Vat Photopolymerization 3D Printing. *ACS Appl. Polym. Mater.* **2024**, *6* (21), 13268–13280. https://doi.org/10.1021/acsapm.4c02560.

(42) Lu, Y.; Chen, X.; Han, F.; Zhao, Q.; Xie, T.; Wu, J.; Zhang, Y. 3D Printing of Self-Healing Personalized Liver Models for Surgical Training and Preoperative Planning. *Nat. Commun.* **2023**, *14* (1), 8447. https://doi.org/10.1038/s41467-023-44324-6.

(43) Sanchez-Rexach, E.; Johnston, T. G.; Jehanno, C.; Sardon, H.; Nelson, A. Sustainable Materials and Chemical Processes for Additive Manufacturing. *Chem. Mater.* **2020**, *32* (17), 7105–7119. https://doi.org/10.1021/acs.chemmater.0c02008.

(44) Voet, V. S. D.; Guit, J.; Loos, K. Sustainable Photopolymers in 3D Printing: A Review on Biobased, Biodegradable, and Recyclable Alternatives. *Macromol. Rapid Comm.* **2021**, *42* (3), 2000475. https://doi.org/10.1002/marc.202000475.

(45) Maines, E. M.; Porwal, M. K.; Ellison, C. J.; Reineke, T. M. Sustainable Advances in SLA/DLP 3D Printing Materials and Processes. *Green Chem.* **2021**, *23* (18), 6863–6897. https://doi.org/10.1039/D1GC01489G.

(46) Sardon, H.; Long, T.; Le Ferrand, H. Sustainable Additive Manufacturing of Plastics. *ACS Sustain. Chem. Eng.* **2022**, *10* (6), 1983–1985. https://doi.org/10.1021/acssuschemeng.2c00475.

(47) Hoffman, A. S. Hydrogels for Biomedical Applications. *Adv. Drug Deliver. Rev.* **2012**, *64*, 18–23. https://doi.org/10.1016/j.addr.2012.09.010.

(48) Zhang, Y. S.; Khademhosseini, A. Advances in Engineering Hydrogels. *Science* **2017**, *356* (6337), eaaf3627. https://doi.org/10.1126/science.aaf3627.

(49) Oyen, M. L. Mechanical Characterisation of Hydrogel Materials. *Int. Mater. Rev.* **2014**, *59* (1), 44–59. https://doi.org/10.1179/1743280413Y.0000000022.

(50) Guvendiren, M.; Lu, H. D.; Burdick, J. A. Shear-Thinning Hydrogels for Biomedical Applications. *Soft Matter* **2011**, *8* (2), 260–272. https://doi.org/10.1039/C1SM06513K.

(51) Appel, E. A.; Barrio, J. del; Loh, X. J.; Scherman, O. A. Supramolecular Polymeric Hydrogels. *Chem. Soc. Rev.* **2012**, *41* (18), 6195–6214. https://doi.org/10.1039/C2CS35264H.

(52) Riley, L.; Schirmer, L.; Segura, T. Granular Hydrogels: Emergent Properties of Jammed Hydrogel Microparticles and Their Applications in Tissue Repair and Regeneration. *Curr. Opin. Biotech.* **2019**, *60*, 1–8. https://doi.org/10.1016/j.copbio.2018.11.001.

(53) Li, J.; Wu, C.; Chu, P. K.; Gelinsky, M. 3D Printing of Hydrogels: Rational Design Strategies and Emerging Biomedical Applications. *Mat. Sci. Eng. R.* **2020**, *140*, 100543. https://doi.org/10.1016/j.mser.2020.100543.

(54) Baker, B. M.; Chen, C. S. Deconstructing the Third Dimension – How 3D Culture Microenvironments Alter Cellular Cues. *J. Cell Sci.* **2012**, *125* (13), 3015–3024. https://doi.org/10.1242/jcs.079509.

(55) Hern, D. L.; Hubbell, J. A. Incorporation of Adhesion Peptides into Nonadhesive Hydrogels Useful for Tissue Resurfacing. *J. Biomed. Mater. Res.* **1998**, *39* (2), 266–276. https://doi.org/10.1002/(SICI)1097-4636(199802)39:2<266::AID-JBM14>3.0.CO;2-B.

(56) Burdick, J. A.; Anseth, K. S. Photoencapsulation of Osteoblasts in Injectable RGD-Modified PEG Hydrogels for Bone Tissue Engineering. *Biomaterials* **2002**, *23* (22), 4315–4323. https://doi.org/10.1016/S0142-9612(02)00176-X.

(57) Marquardt, L. M.; Heilshorn, S. C. Design of Injectable Materials to Improve Stem Cell Transplantation. *Curr. Stem Cell Rep.* **2016**, *2* (3), 207–220. https://doi.org/10.1007/s40778-016-0058-0.

(58) Smith, P. T.; Narupai, B.; Tsui, J. H.; Millik, S. C.; Shafranek, R. T.; Kim, D.-H.; Nelson, A. Additive Manufacturing of Bovine Serum Albumin-Based Hydrogels and Bioplastics. *Biomacromolecules* **2020**, *21* (2), 484–492. https://doi.org/10.1021/acs.biomac.9b01236.

(59) Nonoyama, T.; Lee, Y. W.; Ota, K.; Fujioka, K.; Hong, W.; Gong, J. P. Instant Thermal Switching from Soft Hydrogel to Rigid Plastics Inspired by Thermophile Proteins. *Adv. Mater.* **2020**, *32* (4), 1905878. https://doi.org/10.1002/adma.201905878.

(60) Shu, L.; Zhang, X.-F.; Wang, Z.; Yao, J. Structure Reorganization of Cellulose Hydrogel by Green Solvent Exchange for Potential Plastic Replacement. *Carbohyd. Polym.* **2022**, *275*, 118695. https://doi.org/10.1016/j.carbpol.2021.118695.

(61) Smith, P. T.; Altin, G.; Millik, S. C.; Narupai, B.; Sietz, C.; Park, J. O.; Nelson, A. Methacrylated Bovine Serum Albumin and Tannic Acid Composite Materials for Three-Dimensional Printing Tough and Mechanically Functional Parts. *ACS Appl. Mater. Inter.* **2022**, *14* (18), 21418–21425. https://doi.org/10.1021/acsami.2c01446.

(62) Qazanfarzadeh, Z.; Kumaravel, V. Hydrophobisation Approaches of Protein-Based Bioplastics. *Trends Food Sci. Tech.* **2023**, *138*, 27–43. https://doi.org/10.1016/j.tifs.2023.06.002.

(63) Peppas, N. A.; Keys, K. B.; Torres-Lugo, M.; Lowman, A. M. Poly(Ethylene Glycol)-Containing Hydrogels in Drug Delivery. *J. Control. Release* **1999**, *62* (1–2), 81–87. https://doi.org/10.1016/S0168-3659(99)00027-9.

(64) Lin, C.-C.; Anseth, K. S. PEG Hydrogels for the Controlled Release of Biomolecules in Regenerative Medicine. *Pharm. Res.* **2009**, *26* (3), 631–643. https://doi.org/10.1007/s11095-008-9801-2.

(65) Hassan, C. M.; Peppas, N. A. Structure and Applications of Poly(Vinyl Alcohol) Hydrogels Produced by Conventional Crosslinking or by Freezing/Thawing Methods. In *Biopolymers · PVA Hydrogels, Anionic Polymerisation Nanocomposites*; Springer: Berlin, Heidelberg, 2000; pp 37–65. https://doi.org/10.1007/3-540-46414-X_2.

(66) Wang, M.; Bai, J.; Shao, K.; Tang, W.; Zhao, X.; Lin, D.; Huang, S.; Chen, C.; Ding, Z.; Ye, J. Poly(Vinyl Alcohol) Hydrogels: The Old and New Functional Materials. *Int. J. Polym. Sci.* **2021**, *2021* (1), 2225426. https://doi.org/10.1155/2021/2225426.

(67) Monleón Pradas, M. Porous Poly(2-Hydroxyethyl Acrylate) Hydrogels. *Polymer* **2001**, *42* (10), 4667–4674. https://doi.org/10.1016/S0032-3861(00)00742-4.

(68) Elliott, J. E.; Macdonald, M.; Nie, J.; Bowman, C. N. Structure and Swelling of Poly(Acrylic Acid) Hydrogels: Effect of pH, Ionic Strength, and Dilution on the Crosslinked Polymer Structure. *Polymer* **2004**, *45* (5), 1503–1510. https://doi.org/10.1016/j.polymer.2003.12.040.

(69) Kandow, C. E.; Georges, P. C.; Janmey, P. A.; Beningo, K. A. Polyacrylamide Hydrogels for Cell Mechanics: Steps Toward Optimization and Alternative Uses. *Methods in Cell Biology*; Elsevier, 2007; Vol. 83, pp 29–46. https://doi.org/10.1016/S0091-679X(07)83002-0.

(70) Abdurrahmanoglu, S.; Can, V.; Okay, O. Design of High-Toughness Polyacrylamide Hydrogels by Hydrophobic Modification. *Polymer* **2009**, *50* (23), 5449–5455. https://doi.org/10.1016/j.polymer.2009.09.042.

(71) Van Den Bulcke, A. I.; Bogdanov, B.; De Rooze, N.; Schacht, E. H.; Cornelissen, M.; Berghmans, H. Structural and Rheological Properties of Methacrylamide Modified Gelatin Hydrogels. *Biomacromolecules* **2000**, *1* (1), 31–38. https://doi.org/10.1021/bm990017d.

(72) Yue, K.; Trujillo-de Santiago, G.; Alvarez, M. M.; Tamayol, A.; Annabi, N.; Khademhosseini, A. Synthesis, Properties, and Biomedical Applications of Gelatin Methacryloyl (GelMA) Hydrogels. *Biomaterials* **2015**, *73*, 254–271. https://doi.org/10.1016/j.biomaterials.2015.08.045.

(73) Jaipan, P.; Nguyen, A.; Narayan, R. J. Gelatin-Based Hydrogels for Biomedical Applications. *MRS Commun.* **2017**, *7* (3), 416–426. https://doi.org/10.1557/mrc.2017.92.

(74) Wallace, D. Collagen Gel Systems for Sustained Delivery and Tissue Engineering. *Adv. Drug Deliver. Rev.* **2003**, *55* (12), 1631–1649. https://doi.org/10.1016/j.addr.2003.08.004.

(75) Antoine, E. E.; Vlachos, P. P.; Rylander, M. N. Review of Collagen I Hydrogels for Bioengineered Tissue Microenvironments: Characterization of Mechanics, Structure, and Transport. *Tissue Eng. Part B–Re.* **2014**, *20* (6), 683–696. https://doi.org/10.1089/ten.teb.2014.0086.

(76) Janmey, P. A.; Winer, J. P.; Weisel, J. W. Fibrin Gels and Their Clinical and Bioengineering Applications. *J. Roy. Soc. Interface* **2008**, *6* (30), 1–10. https://doi.org/10.1098/rsif.2008.0327.

(77) Liu, J.; Tan, Y.; Zhang, H.; Zhang, Y.; Xu, P.; Chen, J.; Poh, Y.-C.; Tang, K.; Wang, N.; Huang, B. Soft Fibrin Gels Promote Selection and Growth of Tumorigenic Cells. *Nat. Mater.* **2012**, *11* (8), 734–741. https://doi.org/10.1038/nmat3361.

(78) Burdick, J. A.; Prestwich, G. D. Hyaluronic Acid Hydrogels for Biomedical Applications. *Adv. Mater.* **2011**, *23* (12), H41–H56. https://doi.org/10.1002/adma.201003963.

(79) Highley, C. B.; Prestwich, G. D.; Burdick, J. A. Recent Advances in Hyaluronic Acid Hydrogels for Biomedical Applications. *Curr. Opin. Biotech.* **2016**, *40*, 35–40. https://doi.org/10.1016/j.copbio.2016.02.008.

(80) Rowley, J. A.; Madlambayan, G.; Mooney, D. J. Alginate Hydrogels as Synthetic Extracellular Matrix Materials. *Biomaterials* **1999**, *20* (1), 45–53. https://doi.org/10.1016/S0142-9612(98)00107-0.

(81) Augst, A. D.; Kong, H. J.; Mooney, D. J. Alginate Hydrogels as Biomaterials. *Macromol. Biosci.* **2006**, *6* (8), 623–633. https://doi.org/10.1002/mabi.200600069.

(82) Millik, S. C.; Dostie, A. M.; Karis, D. G.; Smith, P. T.; McKenna, M.; Chan, N.; Curtis, C. D.; Nance, E.; Theberge, A. B.; Nelson, A. 3D Printed Coaxial Nozzles for the Extrusion of

Hydrogel Tubes toward Modeling Vascular Endothelium. *Biofabrication* **2019**, *11* (4), 045009. https://doi.org/10.1088/1758-5090/ab2b4d.

(83) Trujillo, S.; Gonzalez-Garcia, C.; Rico, P.; Reid, A.; Windmill, J.; Dalby, M. J.; Salmeron-Sanchez, M. Engineered 3D Hydrogels with Full-Length Fibronectin That Sequester and Present Growth Factors. *Biomaterials* **2020**, *252*, 120104. https://doi.org/10.1016/j.biomaterials.2020.120104.

(84) Loebel, C.; Rodell, C. B.; Chen, M. H.; Burdick, J. A. Shear-Thinning and Self-Healing Hydrogels as Injectable Therapeutics and for 3D-Printing. *Nat. Protoc.* **2017**, *12* (8), 1521–1541. https://doi.org/10.1038/nprot.2017.053.

(85) Uman, S.; Dhand, A.; Burdick, J. A. Recent Advances in Shear-Thinning and Self-Healing Hydrogels for Biomedical Applications. *J. Appl. Polym. Sci.* **2020**, *137* (25), 48668. https://doi.org/10.1002/app.48668.

(86) Schwab, A.; Levato, R.; D'Este, M.; Piluso, S.; Eglin, D.; Malda, J. Printability and Shape Fidelity of Bioinks in 3D Bioprinting. *Chem. Rev.* **2020**, *120* (19), 11028–11055. https://doi.org/10.1021/acs.chemrev.0c00084.

(87) Lopez Hernandez, H.; Souza, J. W.; Appel, E. A. A Quantitative Description for Designing the Extrudability of Shear-Thinning Physical Hydrogels. *Macromol. Biosci.* **2021**, *21* (2), 2000295. https://doi.org/10.1002/mabi.202000295.

(88) Hull, S. M.; Brunel, L. G.; Heilshorn, S. C. 3D Bioprinting of Cell-Laden Hydrogels for Improved Biological Functionality. *Adv. Mater.* **2022**, *34* (2), e2103691. https://doi.org/10.1002/adma.202103691.

(89) Saadi, M. a. S. R.; Maguire, A.; Pottackal, N. T.; Thakur, M. S. H.; Ikram, M. Md.; Hart, A. J.; Ajayan, P. M.; Rahman, M. M. Direct Ink Writing: A 3D Printing Technology for Diverse Materials. *Adv. Mater.* **2022**, *34* (28), 2108855. https://doi.org/10.1002/adma.202108855.

(90) Hospodiuk, M.; Dey, M.; Sosnoski, D.; Ozbolat, I. T. The Bioink: A Comprehensive Review on Bioprintable Materials. *Biotechnol. Adv.* **2017**, *35* (2), 217–239. https://doi.org/10.1016/j.biotechadv.2016.12.006.

(91) Tang, S.; Richardson, B. M.; Anseth, K. S. Dynamic Covalent Hydrogels as Biomaterials to Mimic the Viscoelasticity of Soft Tissues. *Prog. Mater. Sci.* **2021**, *120*, 100738. https://doi.org/10.1016/j.pmatsci.2020.100738.

(92) Can, V.; Kochovski, Z.; Reiter, V.; Severin, N.; Siebenbürger, M.; Kent, B.; Just, J.; Rabe, J. P.; Ballauff, M.; Okay, O. Nanostructural Evolution and Self-Healing Mechanism of Micellar Hydrogels. *Macromolecules* **2016**, *49* (6), 2281–2287. https://doi.org/10.1021/acs.macromol.6b00156.

(93) Rodell, C. B.; Kaminski, A. L.; Burdick, J. A. Rational Design of Network Properties in Guest-Host Assembled and Shear-Thinning Hyaluronic Acid Hydrogels. *Biomacromolecules* **2013**, *14* (11), 4125–4134. https://doi.org/10.1021/bm401280z.

(94) Liu, J.; Scherman, O. A. Cucurbit[n]Uril Supramolecular Hydrogel Networks as Tough and Healable Adhesives. *Adv. Funct. Mater.* **2018**, *28* (21), 1800848. https://doi.org/10.1002/adfm.201800848.

(95) Wang, H.; Heilshorn, S. C. Adaptable Hydrogel Networks with Reversible Linkages for Tissue Engineering. *Adv. Mater.* **2015**, *27* (25), 3717–3736. https://doi.org/10.1002/adma.201501558.

(96) Shen, W.; Lammertink, R. G. H.; Sakata, J. K.; Kornfield, J. A.; Tirrell, D. A. Assembly of an Artificial Protein Hydrogel through Leucine Zipper Aggregation and Disulfide Bond Formation. *Macromolecules* **2005**, *38* (9), 3909–3916. https://doi.org/10.1021/ma048348s.

(97) Shen, W.; A. Kornfield, J.; A. Tirrell, D. Structure and Mechanical Properties of Artificial Protein Hydrogels Assembled through Aggregation of Leucine Zipper Peptide Domains. *Soft Matter* **2007**, *3* (1), 99–107. https://doi.org/10.1039/B610986A.

(98) Wong Po Foo, C. T. S.; Lee, J. S.; Mulyasasmita, W.; Parisi-Amon, A.; Heilshorn, S. C. Two-Component Protein-Engineered Physical Hydrogels for Cell Encapsulation. *P. Natl. Acad. Sci.* **2009**, *106* (52), 22067–22072. https://doi.org/10.1073/pnas.0904851106.

(99) Cai, L.; Dewi, R. E.; Heilshorn, S. C. Injectable Hydrogels with In Situ Double Network Formation Enhance Retention of Transplanted Stem Cells. *Adv. Funct. Mater.* **2015**, *25* (9), 1344–1351. https://doi.org/10.1002/adfm.201403631.

(100) Browning, M. B.; Cosgriff-Hernandez, E. Development of a Biostable Replacement for PEGDA Hydrogels. *Biomacromolecules* **2012**, *13* (3), 779–786. https://doi.org/10.1021/bm201707z.

(101) Browning, M. B.; Cereceres, S. N.; Luong, P. T.; Cosgriff-Hernandez, E. M. Determination of the in Vivo Degradation Mechanism of PEGDA Hydrogels. *J. Biomed. Mater. Res. A.* **2014**, *102* (12), 4244–4251. https://doi.org/10.1002/jbm.a.35096.

(102) Mironov, V.; Kasyanov, V.; Zheng Shu, X.; Eisenberg, C.; Eisenberg, L.; Gonda, S.; Trusk, T.; Markwald, R. R.; Prestwich, G. D. Fabrication of Tubular Tissue Constructs by Centrifugal Casting of Cells Suspended in an in Situ Crosslinkable Hyaluronan-Gelatin Hydrogel. *Biomaterials* **2005**, *26* (36), 7628–7635. https://doi.org/10.1016/j.biomaterials.2005.05.061.

(103) Hua, M.; Wu, S.; Ma, Y.; Zhao, Y.; Chen, Z.; Frenkel, I.; Strzalka, J.; Zhou, H.; Zhu, X.; He, X. Strong Tough Hydrogels via the Synergy of Freeze-Casting and Salting Out. *Nature* **2021**, *590* (7847), 594–599. https://doi.org/10.1038/s41586-021-03212-z.

(104) Caplins, B. W.; Higgins, C. I.; Kolibaba, T. J.; Arp, U.; Miller, C. C.; Poster, D. L.; Zarobila, C. J.; Zong, Y.; Killgore, J. P. Characterizing Light Engine Uniformity and Its Influence on Liquid Crystal Display Based Vat Photopolymerization Printing. *Addit. Manuf.* **2023**, *62*, 103381. https://doi.org/10.1016/j.addma.2022.103381.

(105) Sanchez-Rexach, E.; Smith, P. T.; Gomez-Lopez, A.; Fernandez, M.; Cortajarena, A. L.; Sardon, H.; Nelson, A. 3D-Printed Bioplastics with Shape-Memory Behavior Based on Native Bovine Serum Albumin. *ACS Appl. Mater. Inter.* **2021**, *13* (16), 19193–19199. https://doi.org/10.1021/acsami.0c22377.

Chapter 2

3D-Printed Coaxial Nozzles for the Extrusion of Hydrogel Tubes Toward Modeling Vascular Endothelium

This chapter was adapted with permission from the following publication:

> Millik, S. C.; Dostie, A. M.; Karis, D. G.; Smith, P. T.; McKenna, M.; Chan, N.; Curtis, C. D.; Nance, E.; Theberge, A. B.; Nelson, A. 3D Printed Coaxial Nozzles for the Extrusion of Hydrogel Tubes toward Modeling Vascular Endothelium. *Biofabrication* **2019**, *11* (4), 045009. https://doi.org/10.1088/1758-5090/ab2b4d.

2.1. Abstract

Engineered tubular constructs made from soft biomaterials are employed in a myriad of applications in biomedical science. Potential uses of these constructs range from vascular grafts to conduits for enabling perfusion of engineered tissues and organs. The fabrication of standalone tubes or complex perfusable constructs from bio-functional materials, including hydrogels, via rapid and readily accessible routes is desirable. Here we report a methodology in which customized coaxial nozzles are 3D printed using commercially available stereolithography (SLA) 3D printers. These nozzles can be used for the fabrication of hydrogel tubes via coextrusion of two shear-thinning hydrogels: an unmodified Pluronic F-127 (F127) hydrogel and an F127-bisurethane methacrylate (F127-BUM) hydrogel. We demonstrate that different nozzle geometries can be modeled via computer-aided design and 3D printed in order to generate tubes or coaxial filaments with different cross-sectional geometries. We were able to fabricate tubes with luminal diameters or wall thicknesses as small as ~150 μm. Finally, we show that these

tubes can be functionalized with collagen I to enable cell adhesion, and human umbilical vein endothelial cells can be cultured on the luminal surfaces of these tubes to yield tubular endothelial monolayers. Our approach could enable the rapid fabrication of bio-functional hydrogel conduits which can ultimately be utilized for engineering in vitro models of tubular biological structures.

2.2. Introduction

Tubular structures are abundant in nature where they function broadly as conduits for the bulk transport of fluids. Examples include the airways and blood vessels of vertebrates, and the xylems and phloems of vascular plants.[1,2] Fabrication of perfusable structures using bio-functional materials and compatible manufacturing processes is of great interest in the areas of bioengineering (e.g. for in vitro assays) and regenerative medicine.[3–13] While tubes are geometrically simple, their fabrication from soft materials is an existing challenge in the field. Common strategies involve casting or rolling a synthetic or natural polymeric material around a mandrel, wherein the diameter of the mandrel determines the tube's luminal diameter. These mandrel-based approaches have yielded tubes with properties comparable to those of human blood vessels; however, the utility of these approaches is limited when it comes to the fabrication of tubes with small luminal diameters (< 0.5 mm) and arbitrary lengths (> 15 cm).[14–20]

An alternative approach for fabricating tubular structures involves material extrusion through dies with annular orifices. Extrusion-based processes are good candidates for this task because they have the ability to produce constructs with complex cross-sectional profiles and

hollow internal geometries, which are difficult to create using most other types of manufacturing processes.[8–10,12,13,21–23]

Standalone tubular structures have been investigated as vascular grafts,[19,20,24] nerve guidance conduits,[18,25,26] and grafts for urethroplasty.[27–29] More complex, perfusable, cell-laden constructs which utilize tubes as a basic structural motif have also been designed to recapitulate tissue or organ function.[30–32]

Hydrogels are attractive materials for many biomedical applications due to their significant water content and mechanics reminiscent of soft tissues.[33,34] However, it remains challenging to reconcile biocompatibility, bioactivity, and mechanics in hydrogels, with processability in the context of extrusion.[35] Previous reports have succeeded in outlining sets of biochemical and biophysical material properties which are essential for the recapitulation of many physiological functions,[36–38] yet the incorporation of these properties into materials used in extrusion-based fabrication processes remains a challenge.

Hydrogels that have thus far been processed into tubular structures for potential biomedical applications include those based on gelatin,[8,9] hyaluronic acid,[10] alginate,[12,13] collagen,[14,16] poly(vinyl alcohol),[17,20] silk fibroin,[18] fibrin,[19] and decellularized extracellular matrix.[21] Recently, Pi et al have demonstrated coaxial extrusion-based fabrication of circumferentially layered tissue-engineered tubular constructs using materials based on methacrylamide-modified gelatin, alginate, and acrylate-terminated multi-arm poly(ethylene glycol).[8] The authors produced these constructs using urothelial cells, vascular endothelial cells, and smooth muscle cells. These tissue-engineered constructs represent an important step toward creating engineered replacements for tubular biological structures; however, this platform involves handmade nozzles, which may restrict the platform's accessibility and customizability.

Here, we report a practical and versatile 3D-printing-enabled platform for the extrusion-based fabrication of tubular hydrogel constructs and multi-material coaxial filaments (Figure 2.1). Additionally, we demonstrate the fabrication of bioactive collagen-functionalized hydrogel tubes for the culture of human umbilical vein endothelial cells (HUVECS). Our platform utilizes 3D-printed and fully customizable coaxial nozzles in combination with extrudable hydrogels based on a derivative of Pluronic F-127. The employment of 3D printing in our work demonstrates the utility of additive manufacturing in the rapid design, fabrication, and iteration of extrusion hardware possessing relatively complex geometries. The platform outlined here, including the materials and process-design principles highlighted, can broadly serve as an example of effective implementation of design for additive manufacturing in the context of biofabrication. Finally, a notable advantage of this platform stems from its accessibility. The computer-aided design (CAD) files of the coaxial nozzles (available in the supplementary material online at stacks.iop.org/BF/11/045009/ mmedia)[39] can be modified to meet a variety of needs, and the nozzles can be printed on commercially available desktop SLA 3D printers.

2.3. Materials and Methods

2.3.1. Materials

Pluronic F-127 (P2443-1KG; referred to as F127), phenol red solution (P0290-100ML; 0.5%), sodium hydroxide solution (S2770-100ML; 1.0 M), 2-hydroxy-4′-(2-hydroxyethoxy)-2-methylpropiophenone (410896-10G; 98%; referred to as Irgacure 2959), and 2-acrylamido-2-methyl-1-propanesulfonic acid sodium salt solution (655821- 250ML; 50 wt%; referred to as

AMPS) were all purchased from Sigma Aldrich. Dibutyltin dilaurate (D0303; > 95.0%) was purchased from TCI America. 2-Isocyanatoethyl methacrylate (ACT34296) was purchased from Arctom Chemicals. CDCl3 (DLM-7-PK; 99.8%) was purchased from Cambridge Isotope Laboratories. Common solvents (Certified ACS) and phosphate-buffered saline (PBS) tablets (BP2944100) were purchased from Fisher Scientific. Collagen I from rat tail tendon (354249; 8.3 mg mL^{-1} in 0.02 M acetic acid) was purchased from Corning. Ammonium hydroxide (AX1303; 28.0–30.0 wt%) was purchased from EMD Millipore. Autodesk Standard Clear Prototyping Resin (also known as PR48) was purchased from Colorado Photopolymer Solutions. Formlabs Clear photopolymer resin (FLGPCL04) was purchased from Formlabs. All reagents were used as received unless otherwise specified.

Human umbilical vein endothelial cells (C2517A; single donor; in EGM-2; referred to as HUVECs) and endothelial cell growth medium (CC-3162; referred to as EGM-2) were purchased from Lonza. Penicillin-streptomycin cocktail (15140122; 10000 U mL^{-1}), ethidium homodimer-1 (E1169), calcein AM (C3100MP), and 4′,6-diamidino-2- phenylindole (D1306; referred to as DAPI) were all purchased from Thermo Fisher Scientific. Subculture Reagent Kit (090K; containing HBSS, Trypsin/EDTA & Trypsin Neutralizing Solution) was purchased from Cell Applications. Paraformaldehyde solution (50-980-487; 16%), bovine serum albumin (BP9706100; referred to as BSA), polysorbate 80 (AC278632500; referred to as P80), and Alexa Fluor 488-goat anti-mouse IgG (NC0675427; IgG polyclonal; H+L) were all purchased from Fisher Scientific. Triton X-100 (X100-100ML) was purchased from Sigma Aldrich. Mouse anti-human CD31 (MCA1738; IgG1 monoclonal; clone WM59) was purchased from Bio-Rad Laboratories. All reagents were used as received unless otherwise specified.

2.3.2. Instrumentation

^{1}H NMR spectra were obtained using a Bruker AVANCE series instrument with 500 MHz frequency. Bruker TopSpin software was used to analyze the ^{1}H NMR spectrum. Gel permeation chromatography (GPC) was performed using a Waters Breeze 2 chromatograph equipped with two 10 μm Malvern columns (300 mm × 7.8 mm) connected in series with increasing pore size (1000 Å, 10000 Å), using chloroform as the eluent, and calibrated with poly(ethylene glycol) standards (102 g mol^{-1} to 40000 g mol^{-1}). Rheometric experiments were performed using a TA Instruments Discovery Hybrid Rheometer-2 (DHR-2) equipped with an Advanced Peltier Plate system for temperature control, and a 365 nm LED UV-curing accessory with disposable acrylic plates for photo-rheology experiments. All rheometric experiments were performed using a stainless steel 20 mm upper plate. Viscous collagen solutions and gels were volumetrically measured and dispensed using a positive displacement pipette (Gilson MICROMAN E). Coaxial nozzles were 3D printed using an Autodesk Ember DLP 3D Printer with DLP 0.45" WXGA DMD projector (5 W; 405 nm) or a Formlabs Form 2 SLA 3D Printer with EN 60825-1:2007 certified Class 1 laser (250 mW; 405 nm). The photopolymer resin used for 3D printing coaxial nozzles was the Autodesk Standard Clear Prototyping Resin or the Formlabs Clear resin (specified above). Solid modeling of nozzles was performed using the CAD program Autodesk Fusion 360. The slicing program used was Autodesk Print Studio or Formlabs PreForm.

Fluorescence microscopy was performed on a Zeiss Axiovert 200 with Axiocam 503 mono camera. Confocal microscopy was performed on a custom-built simultaneous 4-channel Nikon AR1 with cMOS camera with xyz-motorization. Images obtained using confocal microscopy were processed using FIJI (ImageJ). Z-stacks were created from LIF files using the

built-in stack processing commands, specifically the '3D Project' command. Images were uniformly thresholded to improve contrast and increase brightness of fluorescence.

2.3.3. Synthesis of F127-BUM

Glassware was oven-dried at 125 °C for at least 16 h. F127 (60 g, 4.8 mmol) was dried under vacuum (~ 2 Pa) for at least 16 h at room temperature in a round-bottom flask. Anhydrous CH_2Cl_2 (550 mL) was charged to the flask under N_2 atmosphere. The mixture was stirred at 30 °C, and following complete dissolution of the F127, dibutyltin dilaurate (12 drops) was added using a glass Pasteur pipette. 2-isocyanatoethyl methacrylate (3.5 mL, 24.8 mmol) was diluted in anhydrous CH_2Cl_2 (50 mL) and was added to the reaction mixture at a rate of approximately 1 drop s^{-1}. The reaction was allowed to proceed while stirring under dry N_2 at 30 °C. After 2 d, the reaction was quenched by the addition of MeOH (60 mL), and the mixture was concentrated at 30 °C using a rotary evaporator. The F127-BUM was precipitated in Et2O (2000 mL). During the precipitation, Et_2O was stirred in a large conical flask, and the concentrate was poured in slowly. The precipitate mixture was stirred for an additional 15 min before separation via centrifugation. The F127-BUM precipitate was then washed with excess Et_2O and re-separated via centrifugation. Excess ether was allowed to evaporate while agitating the F127-BUM with a spatula under an N2 atmosphere. The resultant F127-BUM powder was dried fully overnight at room temperature under vacuum (~ 2 Pa) and stored in the dark at 4 °C until further use. ^{1}H NMR (500 MHz, CDCl3): δ 6.10 (s, 1H), 5.58 (s, 1H), 5.13 (s, 1H), 4.21 (t, 2H), 3.38–3.77 (m, 4H, + 2H, + 2H, + 1H, PEG backbone, PPO backbone), 1.92 (s, 3H), 1.12 (d, 3H, PPO methyl).

2.3.4. Preparation of F127-Based Hydrogels

2.3.4.1. Preparation of Sacrificial F127 Core Hydrogel

An approximately 29 wt% F127 hydrogel, for use as the inner (core) hydrogel during fabrication of hydrogel tubes, was prepared by the addition of F127 (1.5 g) to ice-chilled, sterile deionized H_2O (3.5 mL) in a scintillation vial. Immediately after addition of the F127, the mixture was briefly vortex-mixed, and phenol red solution (150 µL; 0.5 wt%) was added in order to dye the gel and afford visibility during coextrusion. NaOH (10 µL; 1.0 M) was also added to bring the gel to approximately pH 7.4. The gel was vortex-mixed again briefly and placed on ice for approximately 3 h until dissolution of the F127 was observed. The gel was stored in the dark at 4 °C until further use. Prior to use, bubbles (if remaining) were eliminated by brief centrifugation at 600 g.

2.3.4.2. Preparation F127-BUM Hydrogel Without Additive

A 30 wt% F127-BUM hydrogel with approximately 0.1 wt% Irgacure 2959 was prepared by the addition of F127- BUM (1.5 g) to ice-chilled, sterile deionized H_2O (3.4 mL) in a scintillation vial. Immediately after addition of the F127- BUM, the mixture was briefly vortex-mixed and placed on ice for approximately 3 h until dissolution of the F127- BUM was observed. A 5 wt% solution of Irgacure 2959 was prepared by adding sterile deionized H_2O to Irgacure 2959 and incubating for 30 min at 70 °C before briefly vortex-mixing. After dissolution of the F127-BUM, the Irgacure 2959 solution (100 µL; 5 wt%) was added to the gel, and the gel

was vortex-mixed again briefly. The gel was stored in the dark at 4 °C until further use. Prior to use, bubbles (if remaining) were eliminated by brief centrifugation at approximately 600 g.

2.3.4.3. Preparation of F127-BUM Hydrogel with AMPS Additive

A 30 wt% F127-BUM hydrogel with 10 wt% 2-acrylamido-2-methyl-1-propanesulfonic acid sodium salt (AMPS) and approximately 0.1 wt% Irgacure 2959 was prepared by the addition of AMPS solution (1.0 g; 50 wt%) to ice-chilled, sterile deionized H_2O (2.4 mL) in a scintillation vial. The mixture was swirled briefly before the addition of F127-BUM (1.5 g). Immediately after addition of the F127-BUM, the mixture was briefly vortex-mixed and placed on ice for approximately 3 h until dissolution of the F127-BUM was observed. Irgacure 2959 solution (100 µL; 5 wt%) was then added to the gel, and the gel was vortex-mixed again briefly. The 5 wt% solution of Irgacure 2959 was prepared as described above. The gel was stored in the dark at 4 °C until further use. Prior to use, bubbles (if remaining) were eliminated by brief centrifugation at approximately 600 g.

2.3.4.4. Preparation of F127-BUM Hydrogel with Collagen I Additive

A 30 wt% F127-BUM hydrogel with 0.2 wt% collagen I and approximately 0.1 wt% Irgacure 2959 was prepared by the addition of collagen I (1.2 mL; 8.3 mg mL^{-1} in 0.02 M acetic acid) to ice-chilled, sterile deionized H_2O (2.21 mL) in a scintillation vial. The mixture was swirled thoroughly before the addition of F127-BUM (1.5 g). Immediately after addition of the F127-BUM, the mixture was briefly vortex-mixed and placed on ice for approximately 3 h until

dissolution of the F127-BUM was observed. Irgacure 2959 solution (100 µL; 5 wt%) was then added to the gel, and the gel was vortex-mixed again briefly. The 5 wt% solution of Irgacure 2959 was prepared as described above. The gel was kept on ice overnight and vortex-mixed the following day on the maximum setting, followed by centrifugation at approximately 600 *g* for 1 min. This process was repeated two or three times until a homogeneous, slightly turbid gel was observed. The gel was kept on ice whenever possible during this time. The gel was stored in the dark at 4 °C and used within 3 d. Prior to use, bubbles (if remaining) were eliminated by brief centrifugation at approximately 600 g.

2.3.5. Rheometry of Hydrogels

Rheometry was performed on a TA Instruments DHR-2 equipped with an Advanced Peltier Plate system and 365 nm LED UV-curing accessory. All rheometric experiments were performed using a stainless steel 20 mm upper plate. All hydrogel samples were kept on ice for at least 30 min before they were loaded onto the lower plate. Prior to sample loading, environmental temperature was set to 5 °C for experiments involving the Peltier plate. The gap between upper and lower plates was set to 1 mm for all experiments. For experiments involving the Peltier plate, a pre-shear was applied at 5 °C for 10 s before equilibration at 25 °C for 8 min. Steady-shear experiments were performed at 25 °C over a shear rate range of 0.01 s^{-1} to 100 s^{-1}. Strain amplitude sweeps were performed at 25 °C from 0.01% to 100% strain amplitude at constant angular frequency of 1 Hz. Frequency sweeps were performed at 25 °C, over an angular frequency range of 0.1 rad s^{-1} to 100.0 rad s^{-1} at constant strain amplitude of 1%. Cyclic shear strain experiments were performed at 25 °C using 6 alternating low- and high-strain intervals.

Low-strain intervals comprised 1% strain amplitude for oscillation at 1 Hz for 5 min; high-strain intervals comprised 100% strain amplitude for oscillation at 1 Hz for 3 min. Temperature ramp experiments were performed over a temperature range of 5 °C to 50 °C, with temperature increasing at a rate of 2 °C min^{-1} (1 Hz, 1% strain). For the photo-rheology experiments, a 365 nm LED UV-curing accessory with disposable acrylic plates was used in place of the Advanced Peltier Plate system. After sample conditioning for 1 min, a 600 s irradiation interval with 365 nm (5 mW cm^{-2}) light was applied; data were collected over a total of 1020 s at angular frequency of 1 Hz and 1% strain amplitude.

2.3.6. Coaxial Nozzle Design and Fabrication

2.3.6.1. Design and Modeling

The CAD program Autodesk Fusion 360 was used for modeling of coaxial nozzles (Figure S6). A sketch was created in the xy-plane and a profile of the nozzle to be revolved around the y-axis was sketched. Fillets were employed in the profile sketch so that the interior geometry of the nozzle would be free of 90° corners and thus facilitate smooth flow of gel. After revolution of the profile, a tangent plane was created on the resultant cylindrical body of the nozzle and a sketch was created on the plane. A profile of the lateral inlet to be extruded normal to the tangent plane was sketched and the inner diameter of the profile was negatively extruded to cut the inlet hole through the cylindrical body of the nozzle. The inner wall of the lateral inlet was placed virtually flush with the superior inner surface (i.e., ceiling) of the nozzle. The keyhole-shaped profile of the lateral inlet was then extruded in both directions to yield the body

of the lateral inlet and join it gap-free to the cylindrical body of the nozzle. A sketch was created on one of the two lateral rectangular faces of the cuboid portion of the body of the lateral inlet. A right triangular profile was sketched and negatively extruded the full thickness of the cuboid portion to yield a triangular support structure. This support structure was added to reduce the risk of the lateral inlet breaking off from the body of the nozzle during use and handling of the loaded coaxial extrusion assembly. The chamfer tool was then used to countersink the lateral and superior inlet holes to increase contact with the conical glued joints of blunt-tip needles (14 gauge × 0.5 in), which would be affixed to the coaxial nozzle after 3D printing. Finally, the fillet tool was used to round both the inner and outer edges of the inner conduit wall at the nozzle tip as well as the outer edge of the outer conduit wall (outermost wall). Both edges of the inner conduit wall were rounded to facilitate interfacing of the inner and outer (core and shell) gels immediately upon exiting the nozzle. For the nozzle with the 5-point star geometry, a sketch was created on the plane of the nozzle tip (parallel to plane of superior surface) before the fillet to the outer conduit was applied. A star profile was then sketched on this plane and the area of the entire nozzle tip, excluding the area of the star, was extruded away from the nozzle end to yield the star-shaped, die-like structure. Finally, the fillet tool was used to round the outer edge of the outer conduit wall (outermost wall).

2.3.6.2. 3D Printing and Assembly

The nozzles were printed using an Autodesk Ember DLP 3D Printer with the Autodesk Standard Clear Prototyping Resin, also known as PR48 (Colorado Photopolymer Solutions) or a Formlabs Form 2 SLA 3D Printer with Formlabs Clear photopolymer resin (Formlabs). Autodesk

Print Studio or Formlabs PreForm was used to process the STL files of the coaxial nozzle models for printing with the Ember or the Form 2, respectively. In the Print Studio interface, Standard Clear was selected as the material, and 50 μm was selected as the layer height. In the PreForm interface, Clear was selected as the material, V4 (FLGPCL04) was selected as the version, and 0.05 mm was selected as the layer height. In Print Studio only, under the advanced settings dropdown menu and support tab, the standoff from the build surface was set to 0.0 mm; and under the model layer tab, separation slide velocity and approach slide velocity were both set to 4.0 rpm. All other settings were kept at their default values for the standard 50 μm layer height print settings profile. In both Print Studio and PreForm, the coaxial nozzle model was positioned such that its superior surface made contact with the build surface. Support structures were not employed. With Print Studio, the processed nozzle file was exported with the .tar.gz extension for printing. With PreForm, the processed nozzle file was directly uploaded to the Form 2 for printing. Following completion of prints, nozzles were carefully removed from the build surface and rinsed with isopropanol according to the manufacturer's instructions. The nozzle was then purged and dried with pressurized air and finally post-cured according to the manufacturer's instructions. On the Ember, often six nozzles were printed at once. The print duration was 56 min regardless of the number of nozzles printed. The Ember was also found to have generally higher resolution and so the small nozzles (Figure S6c) were only printed using the Ember; these nozzles required the use of the Ember's higher-resolution Pattern Mode, but they were otherwise fabricated as described above. Following 3D printing and completion of the post-printing steps described, 14 gauge × 0.5 in straight and bent (45°) blunt-tip needles (OK International) were affixed to the superior and lateral inlets of the coaxial nozzle, respectively. The straight needle was ground short and deburred such that the remaining length of the canula was roughly 5 mm.

This measure was taken to reduce the overall height of the fully assembled coaxial nozzle. Loctite 495 cyanoacrylate adhesive was used according to the manufacturer's instructions to affix the needles. Following full assembly, the nozzle was washed with 70% isopropanol and stored at room temperature in deionized H_2O until further use. Prior to use, nozzles were rinsed briefly with 70% EtOH.

2.3.7. Fabrication of Hydrogel Tubes

A 30 wt% F127-BUM hydrogel with 0.2 wt% collagen I and 0.1 wt% Irgacure 2959 was used as the outer (shell) gel in the fabrication of hydrogel tubes for cell seeding experiments. A 30 wt% F127-BUM hydrogel with 2.5 wt% AMPS and 0.1 wt% Irgacure 2959 was used as the outer (shell) gel in the fabrication of hydrogel tubes for swelling experiments. A 30 wt% F127-BUM hydrogel with 0.1 wt% Irgacure 2959 was used as the outer (shell) gel in the fabrication of hydrogel tubes for all other purposes. An approximately 29 wt% F127 hydrogel dyed with phenol red was used as the sacrificial (core) gel for the fabrication of all tubes.

Unless otherwise specified, tubes were fabricated using the large-size (2 mm outer conduit diameter) nozzle. Gels chilled on ice or in a refrigerator were poured into 10 mL syringe barrels (Figure 2.2a–d) with capped tips, and syringe barrel pistons were inserted (syringe barrels, pistons, and caps were purchased from Nordson EFD). The pistons were pushed down with a spatula to remove the trapped air between the piston and gel. The loaded and capped syringe barrels were briefly centrifuged (600 *g*) with the tip oriented upward, and for no more than 5 s to eliminate any bubbles generated during pouring of the gel. Once the gels reached room temperature, the extrusion setup was assembled. The syringe containing the sacrificial

(core) gel was affixed to the superior inlet and the syringe containing the outer (shell) gel was affixed to the lateral inlet of the coaxial nozzle. Syringe barrel adapters (Nordson EFD) were then attached to each syringe. The resultant coaxial extrusion assembly (Figure 2.2e) was mounted on a ring stand using two three-finger clamps (one gripping each syringe). Pressure to drive the syringe barrel pistons was supplied by an in-house N_2 line. The pressure was controlled independently for each syringe around 55–100 kPa, nominally, by 0–210 kPa pressure regulators and gauges. A laboratory scissor jack was secured to the base of the ring stand with a pair of C-clamps to serve as the platform onto which a tube would be extruded. To adjust pressures prior to extrusion, the tubing of each syringe barrel adapter was clamped using a pinch-clamp and the regulators were set to the desired pressures. To begin extrusion, the tubing of each adapter was unclamped, and after waiting a moment for the coaxial extrusion rate to stabilize, a 4 in × 6 in glass sheet was manually translated across the scissor jack surface to catch the coaxial gel filament. The shell of the coaxial filament (outer gel) was then photo cross-linked for 20 min under a UV lamp (365 nm, 3.3 mW cm^{-2}). The sacrificial core of the coaxial filament (inner gel) was removed via dissolution in aqueous medium to yield the hydrogel tube. 1X PBS was used as the dissolution medium for hydrogel tubes used in cell seeding experiments; deionized H_2O was used for dissolution of the cores for hydrogel tubes for all other purposes.

For the examination of variation in cross-sectional dimensions along the lengths of tubes, two tubes were fabricated as described above, using the medium-size (1.25 mm outer conduit diameter) nozzle. One tube with a relatively small (~ 0.2 mm) luminal diameter was extruded with a nominal core extrusion pressure of approximately 55 kPa and a nominal shell extrusion pressure of approximately 100 kPa. A second tube with a relatively large (~ 0.4 mm) luminal diameter was extruded with a nominal core extrusion pressure of approximately 70 kPa and a

nominal shell extrusion pressure of approximately 95 kPa. Five cross-sections, each taken approximately 10 mm apart, were cut from each tube. Tube sections were stained with a solution of Allura Red AC and Brilliant Blue FCF (food coloring) and photographed under magnification and measured using ImageJ (Figure 2.3a,b). Luminal diameters were taken as the lengths of the major axes of lumens and overall diameters were taken as the lengths of the axes perpendicular to the major axes of tubes.

2.3.8. Cell Seeding and Culture Experiments

2.3.8.1. Preparation of Hydrogel Tubes for Cell Seeding

A 30 wt% F127-BUM hydrogel with 0.2 wt% collagen I and approximately 0.1 wt% Irgacure 2959 was used to fabricate hydrogel tubes for cell seeding experiments. Nominal extrusion pressures were typically around 65 kPa and 100 kPa for core extrusion and shell extrusion, respectively. Following extrusion of the coaxial filament and photo-cross-linking of the shell as described above, the coaxial filament was placed in a glass dish containing sterile 1X PBS (200 mL) pre-heated to 37 °C and incubated at 37 °C for 1 h. The 1X PBS was changed once. Over this 1 h period, the sacrificial core of the coaxial filament (inner gel) was observed to dissolve, yielding the hydrogel tube. The tube was then transferred to a poly(styrene) tissue culture dish and several transverse sections (each approximately 20 mm long) were cut. Tube sections were then transferred to a 1000 mL glass media bottle and sequentially washed with deionized H_2O (3000 mL) for 2 d, 70% EtOH (200 mL) for 1 h, followed by a quick sterile

deionized H_2O rinse, and finally, sterile 1X PBS (200 mL) for 2 h. All washes were done at room temperature on an orbital shaker (125 rpm).

Following the final wash with sterile 1X PBS, the lumens of the tube sections were cleared of PBS using a pipette and dehydrated (Figure 2.4a) via incubation for 2.5 h at 37 °C in a small incubator without humidity control. Following dehydration, tube sections were transferred to a single well of a 6-well poly(styrene) culture plate containing a solution of collagen I (6.0 mg mL^{-1} in 0.014 M acetic acid). Tube sections were submerged in collagen solution, and a pipette was used to make sure the lumens were full of the collagen solution. During this operation, tube sections and collagen solution were kept on ice whenever possible. Tube sections were allowed to rehydrate (Figure 2.4b) at 4 °C for 16 h. Following rehydration, tube sections were removed from collagen solution and the lumens were cleared of the collagen solution using a pipette. Excess collagen solution on the exterior of tube sections was briefly dabbed off by momentarily placing the tube sections in an empty neighboring well in the culture plate, before transferring the tube sections to a poly(styrene) tissue culture dish. Lumens were visually confirmed to be clear of collagen solution and a folded Kimwipe saturated with ammonium hydroxide (28–30 wt%) was placed in the dish with the tube sections, and the dish was covered so that the tube sections would be exposed to ammonia vapors. After 3 min, the Kimwipe was removed, and the tube sections were once again placed in the incubator to dehydrate as before. The ammonia vapor exposure step was adapted from the collagen I manufacturer's instructions, and it serves to facilitate pH- and temperature-dependent cross-linking of the collagen. Following dehydration, the same rehydration procedure was repeated once more. Following another dehydration, a similar rehydration procedure was carried out with endothelial cell growth medium (EGM-2 with 100 units mL^{-1} penicillin and 100 μg mL^{-1} streptomycin) instead of collagen solution; there was

no ammonia vapor exposure. Following a final dehydration, tube sections were rehydrated with the growth medium and stored in medium and covered at 4 °C until cell seeding.

2.3.8.2. Fabrication of Hydrogel Discs and Preparation for Cell Seeding Experiments

A 30 wt% F127-BUM hydrogel with 0.2 wt% collagen I and 0.1 wt% Irgacure 2959 was used to fabricate hydrogel discs for cell seeding experiments. A 30 wt% F127-BUM hydrogel with 0.1 wt% Irgacure 2959, but no collagen I, was used to fabricate hydrogel discs as a negative control. A poly(styrene) form for casting hydrogels was created by milling a rectangular hole (55 mm × 30 mm) in a poly(styrene) sheet (60 mm × 85 mm × 1.2 mm). After attaching a large microscope slide to the poly(styrene) form using small binder clips, a hydrogel chilled on ice was pipetted into the resultant mold using a positive displacement pipette. Another microscope slide was affixed on top, and the gel was allowed to warm up to room temperature. The gel was then photo-cross-linked for 20 min under a UV lamp (365 nm, 3.3 mW cm^{-2}). The resultant cured hydrogel sheet was placed in a glass dish containing sterilized 1X PBS (200 mL) pre-heated to 37 °C and incubated at 37 °C for 1 h. The gel sheet was then transferred to a poly(styrene) tissue culture dish, and a 5 mm disposable biopsy punch (Miltex) was used to make several gel discs. The gel discs were transferred to a 1000 mL glass media bottle and sequentially washed with deionized H_2O (3000 mL) for 2 d, 70% EtOH (200 mL) for 1 h, followed by a quick sterile deionized H_2O rinse, and finally, sterile 1X PBS (200 mL) for 2 h. All washes were done at room temperature on an orbital shaker (125 rpm).

Following the final wash with sterile 1X PBS, the discs with 0.2 wt% collagen I were dehydrated via incubation for 2.5 h at 37 °C in a small incubator without humidity control. The

discs without collagen (negative control) were transferred to endothelial cell growth medium (EGM-2 with 100 units mL^{-1} penicillin and 100 μg mL^{-1} streptomycin) and stored in medium and covered at 4 °C until cell seeding. Following dehydration, the discs with 0.2 wt% collagen I were transferred to a single well of a 6-well poly(styrene) culture plate containing a solution of collagen I (6.0 mg mL^{-1} in 0.014 M acetic acid). Discs were submerged in collagen solution, and during this operation, discs and collagen solution were kept on ice. Discs were allowed to rehydrate at 4 °C for 16 h. Discs were removed from the solution, and care was taken to avoid contacting the top surfaces of the discs. Excess collagen solution was briefly dabbed off by momentarily placing the discs in an empty neighboring well in the culture plate. Discs were transferred to a poly(styrene) tissue culture dish and a Kimwipe saturated with ammonium hydroxide (28.0–30.0 wt%) was placed in the dish with the discs, and the dish was covered. After 3 min, the Kimwipe was removed, and the discs were once again placed in the incubator to dehydrate as before. Following dehydration, the same rehydration procedure was repeated once more. Following another dehydration, a similar rehydration procedure was carried out with endothelial cell growth medium (EGM-2 with 100 units mL^{-1} penicillin and 100 μg mL^{-1} streptomycin) instead of collagen solution; there was no ammonia vapor exposure. Following a final dehydration, discs were rehydrated with the growth medium and stored in medium and covered at 4 °C until cell seeding.

2.3.8.3. Cell Seeding and Culture

HUVECs were maintained in endothelial cell growth medium (EGM-2 supplemented with 100 units mL^{-1} penicillin and 100 μg mL^{-1} streptomycin). Cells were maintained in a 37 °C incubator with 5% CO_2. Cells of passage 4– 8 were used for all cell seeding experiments.

For cell seeding in tube sections, HUVECs were trypsinized and resuspended at a concentration of approximately 1.0×10^6 cells mL^{-1} in EGM-2 with penicillin-streptomycin. Sterilized blunt-tip needles (14 gauge × 0.5 in) were attached to 1 mL syringes, and tube sections were gently slipped onto the needles. Tube sections were briefly rinsed by drawing growth medium into, and through, the lumens. Approximately 100 μL of the cell suspension was then drawn through the tube sections so that lumens were filled with cell suspension. Tube sections with syringes attached were transferred to a poly(styrene) BioAssay dish (245 mm × 245 mm) lined with Kimwipes soaked in 1X PBS. The tube sections and syringes were kept horizontally in the BioAssay dish during a 1 h incubation at 37 °C and 5% CO_2. Throughout the incubation, tube sections and attached syringes were rotated 90° every 15 min to ensure uniform access of cells to luminal walls. While in the dish, syringes were kept from rolling using 3D printed poly(lactic acid) syringe stands (Figure 2.4c). Following the 1 h incubation, tube sections were removed from syringes and transferred to growth medium in a 6-well poly(styrene) culture plate (2 mL of medium per tube section; two tube sections per well) and additionally incubated for up to 72 h at 37 °C and 5% CO_2. Medium was replaced after 48 h. Prior to visualization of cell morphology in tube sections via DAPI staining and indirect immunofluorescence, tube sections were removed from the medium, transferred to a new culture plate, and briefly rinsed with 1X PBS. Cells were fixed at room temperature in 4% paraformaldehyde for 20 min. For rinses and fixation, a 1 mL syringe with blunt-tip needle was briefly used to draw solution into the lumens of tube sections;

tube sections were then immediately slipped off the syringe needle, and into wells of a 6-well poly(styrene) culture plate containing enough solution to submerge the tube sections.

For cell seeding on discs, discs were first transferred to a 96-well poly(styrene) culture plate (one disc per well). Care was taken not to contact the top surfaces of discs during handling. HUVECs were trypsinized and resuspended at a concentration of approximately 1.0×10^6 cells mL^{-1} in EGM-2 with penicillin-streptomycin. The cell suspension was pipetted directly onto each disc (100 µL per disc), then additional growth medium was added around each disc (50 µL per disc). Cells were incubated at 37 °C and 5% CO_2. Medium was replaced every 24 h throughout the duration of the experiment. Cell morphology was evaluated at 24 h and viability was evaluated at 24, 48, and 72 h using fluorescence microscopy.

2.3.8.4. Determination of Cell Viability and Immunocytochemistry

At the appropriate timepoints (24, 48, and 72 h), discs contained in wells of a 96-well poly(styrene) culture plate were removed from the incubator and growth medium was aspirated from each well. Discs were briefly rinsed with 1X PBS. Following the rinse, a solution of calcein AM (0.01 mM) and ethidium homodimer-1 (2 nM) in 1X PBS was added to each well. Discs were incubated for 20 min at 37 °C and 5% CO_2 and then imaged using fluorescence microscopy (Zeiss Axiovert 200 with Axiocam 503 mono camera). Following imaging, the 96-well poly(styrene) culture plate containing the discs was returned to the incubator to await the next timepoint (if applicable). Images of cells stained with Calcein AM were thresholded between 18 and 255 to remove artifacts, and the thresholded area was measured to determine the coverage of cells (ImageJ).

Following fixation (described above in the cell culture section), tube sections were briefly rinsed three times with 1X PBS and allowed to sit for 20 min at room temperature in permeabilization buffer (1X PBS with 0.2% Triton X-100). After removal of permeabilization buffer, blocking buffer (1X PBS with 3% BSA) was added and sections were allowed to sit for 1 h at room temperature. Following removal of blocking buffer, primary antibody solution (10 ng mL^{-1} mouse anti-human CD31 in 1X PBS with 3% BSA; 0.1% Tween-80) was added; sections were allowed to sit overnight at 4 °C. After removal of the primary antibody solution, sections were washed (1X PBS with 0.1% Triton X100) three times (5 min per wash), and secondary antibody solution (15 ng mL^{-1} Alexa Fluor 488-goat anti-mouse IgG in 1X PBS with 3% BSA, 0.1% Tween-80) was added. Sections were allowed to sit for 1 h at room temperature, shielded from light. After removal of the secondary antibody solution, sections were washed (1X PBS with 0.1% Triton X100) three times (5 min per wash), and DAPI (10 ng mL^{-1} in 1X PBS) was added. Following incubation with DAPI for 5 min, sections were washed three more times as before. Finally, 100 μL of 1X PBS was added to each well. Prior to imaging via confocal microscopy (Nikon AR1 with cMOS camera), sections were stored in 1X PBS and in the dark at 4 °C.

For rinses and staining of discs, solution was pipetted into wells of a 96-well poly(styrene) culture plate containing discs, such that each disc was fully submerged. For rinses and immunocytochemical treatment of tube sections, a 1 mL syringe with blunt tip needle was briefly used to draw solution into the lumens of tube sections; tube sections were then immediately slipped off the syringe needles and into wells of a 6-well poly(styrene) culture plate containing enough solution to submerge the tube sections.

2.4. Results and Discussion

2.4.1. Coaxial Nozzle Fabrication

We employed commercially available SLA 3D printers to fabricate coaxial nozzles with intricate, sub-millimeter cross-sectional features and hollow internal geometries. Our basic coaxial nozzle design consisted of a tubular inner conduit supplied by a superior inlet and an annular outer conduit supplied by a lateral inlet (Figure 2.1b; Figure 2.5).

The close tolerances of Luer connectors, as well as the relative brittleness of many cured photopolymer resins, precluded the reliable 3D printing of functional integrated Luer connectors on the nozzles, using our 3D printers. Therefore, once the nozzles were printed, blunt-tip 14-gauge needles were affixed to the nozzle inlets to provide a means of attachment of syringes via a Luer connection (Figure 2.1f,g).

In order to provide a large contact area between the printer's build surface and the nozzles, and thus reduce the risk of nozzle detachment during printing, we included a large superior surface on the nozzles. The nozzles were also designed to be 3D printed without the need for substantial pre-print or post-print processing and without requiring support structures. Additionally, strength and rigidity of the nozzles were prioritized in order to resist elastic-deformation-induced loss of coaxiality during extrusion and also to resist breakage during use and handling of the nozzles. This consideration entailed, in part, inclusion of thick, tapered walls and placement of the lateral inlet virtually flush with the superior inner surface (i.e. ceiling) of the nozzle (Figure 2.5). Finally, to ensure widespread practicability of this platform, we implemented a modular design; rapid iteration and customization of nozzle models is afforded

simply by editing the dimensional constraints of the provided template CAD files (available in the supplementary material online at stacks.iop.org/BF/11/045009/ mmedia).[39] The fully assembled nozzles were used in combination with commercially available pneumatic syringes and adapters for extrusion of shear-thinning hydrogels.

2.4.2. Fabrication of Hydrogel Tubes

Shear-thinning hydrogels are ideal for extrusion-based processes (such as 3D printing via direct ink writing (DIW))[40–43] because they flow readily through nozzles during dispensation but then rapidly regain their gel character upon exiting; this enables retention of the extruded form factor. A material's reversible response to shear load and the time dependence of the response are critical when evaluating a material's suitability for extrusion.[44,45]

In order to ensure fidelity of tubes' cross-sectional profiles to those of the nozzles, we employed two types of hydrogels during the coaxial extrusion process: non-cross-linkable and cross-linkable. A non-cross-linkable hydrogel was formulated from a commercially available amphiphilic triblock copolymer, F127 and was used as a sacrificial core material. A cross-linkable hydrogel was formulated from a derivative of F127, namely, F127-BUM and was employed for the tube walls (Figure 2.1b,c). Irgacure 2959 was added to cross-linkable F127-BUM-based hydrogels as a photo-radical generator.

The F127-BUM was synthesized via reaction of F127 with 2-isocyanatoethyl methacrylate. While there are numerous reports featuring F127 functionalized with (meth)acrylate groups, we found that this particular reaction afforded excellent conversion and facile removal of byproducts. The F127-BUM-based hydrogels retained the rheological

characteristics typical of hydrogels of F127.[46,47] Namely, the hydrogels exhibited strong shear-thinning behavior, as evidenced by their decreasing apparent viscosities with increasing shear rates, as well as rapid yielding and recovery of their solid-like character during cyclic high/low shear strain experiments (Figure 2.6–2.8).

In addition to their reversible shear-yielding and shear-thinning behavior, hydrogels based on F127 or F127-BUM also exhibited a temperature-dependent reversible sol-gel transition, which is driven by a lower-critical-solution-temperature response of the polymer. We have previously reported the utility of the thermo-responsive behavior of these types of hydrogels for the production of shear thinning nanocomposites.[48]

Gelation temperature, T_{gel}, for F127- BUM-based hydrogels was defined as the crossover point between the loss and storage moduli in temperature ramp experiments. For the F127-BUM hydrogel without additive, $T_{gel} \approx 13.7$ °C (Figure 2.6a). For the hydrogel with collagen I additive, $T_{gel} \approx 13.6$ °C (Figure 2.7a). For the hydrogel with AMPS additive, T_{gel} was depressed below 5 °C (Figure 2.8a); however, cooling this gel in an ice bath was sufficient to induce the gel-to-sol transition.

The thermo-responsive behavior of the F127- and F127-BUM-based hydrogels facilitated formulation and processing of these materials. After the gel-to-sol transition was induced for each hydrogel composition, it was possible to transfer these materials into pneumatic syringes without difficulty. The materials were then allowed to return to room temperature, at which point they regained their gel states and were ready for extrusion (Figure 2.2c,d).

Coaxial filaments comprising a sacrificial core (29 wt% F127 hydrogel) and a cross-linkable shell (30 wt% F127-BUM hydrogel with or without additive and with photo-radical generator) were extruded using the 3D printed coaxial nozzles. The extruded coaxial filaments

were irradiated with UV light (365 nm) to initiate polymerization of the methacrylate groups and cross-link the outer hydrogel. The coaxial filaments were then rinsed with excess water or PBS to dissolve the non-cross-linked sacrificial core hydrogel, yielding a tube.

For purposes of fabricating standalone tubes from F127-BUM-based hydrogels, it was not always necessary to extrude a sacrificial core hydrogel. However, if less-stable gel compositions are employed for the shell, it may be necessary to use an F127-based core hydrogel to prevent distortion or collapse of the tube before curing. Regardless, the core hydrogel can be dyed with phenol red to aid in visualization and adjustment of the lumen size during extrusion; this is particularly convenient if extrusion pressures are not predetermined and are to be manually adjusted.

In order to demonstrate the versatility of this approach for fabricating tubes of a range of sizes, we employed three different coaxial nozzle sizes. The largest nozzle in this work consisted of an overall orifice diameter (corresponding to the extruded tube outer diameter) of approximately 2 mm (Figure 2.5a); it was used to produce the tubes pictured in Figure 2.9a,b. The smallest-size nozzle consisted of an overall orifice diameter of approximately 0.5 mm (Figure 2.5c) and was used to produce the smaller tubes pictured in Figure 2.9c,d and Figure 2.9e–g. Following fabrication, these small-diameter tubes were submerged in deionized water and perfused with a dye solution to demonstrate patency (Figure 2.9c,d).

When cured, 30 wt% hydrogels based on F127- BUM were relatively tough and elastic. In fact, we were able to tie knots with these tubes (Figure 2.9b), and also distend them considerably with water pressure (Figure 2.2f,g).

During tube fabrication, luminal diameters and wall thicknesses were determined by the dimensions of the nozzle, as well as the core and shell extrusion pressures. We found that in

cases where inner and outer extrusion pressures were well-matched, higher fidelity to nozzle dimensions was observed, and overall extrusion rate was adjusted by increasing or decreasing the extrusion pressures in tandem. In cases where the shell extrusion pressure was higher than the core extrusion pressure, the overall extrusion rate (i.e. length of coaxial filament generated per unit time) was limited by the core extrusion rate due to adhesion between the two hydrogels. In these situations, the shell hydrogel exhibited a volumetric flow rate mismatched with the overall extrusion rate, which yielded a tube with a relatively small luminal diameter and a thick wall (Figure 2.9e). In cases where the core extrusion pressure was higher than the shell extrusion pressure, the reverse situation occurred—i.e., a tube with a relatively large luminal diameter and a thin wall was produced (Figure 2.9g). In these cases of extrusion-pressure mismatch, overall extrusion rate could still be varied while keeping the coaxial filament geometry approximately constant by adjusting the mismatched pressures in tandem.

The luminal diameters and outer diameters of extruded tubes were found to be generally consistent along the lengths of the tubes. The variations in these dimensions of two different F127-BUM tubes produced using the same (medium-sized, 1.25 mm outer conduit diameter) nozzle with different sets of extrusion pressures were evaluated at five different points, approximately 10 mm apart, along the length of each tube. For the tube with the smaller lumen, the luminal diameter averaged 0.20 ± 0.01 mm (SD), and the outer diameter averaged 0.74 ± 0.01 mm (SD) (Figure 2.3a). For the larger-lumen tube, luminal diameter averaged 0.43 ± 0.01 mm (SD), and the outer diameter averaged 0.70 ± 0.01 mm (SD) (Figure 2.3b).

Extruded tubes or coaxial filaments with more complex cross-sectional profiles may also be fabricated, as seen in Figure 2.9h–j. A tube with a 5-point star cross-sectional geometry was generated analogously to other tubes using a coaxial nozzle with a star geometry at its end. This

demonstrated that more complex orifice geometries could be modeled at the ends of these nozzles; changing the overall nozzle structure or internal geometry was not necessary.

F127-BUM-based hydrogels can be derivatized with other chemical functionalities via co-polymerization with aqueous-soluble (meth)acrylate monomers. This approach for introducing different chemical functionalities into a hydrogel network has been demonstrated for a range of monomers.[45] Here, we examined the incorporation of 2-acrylamido-2-methyl-1-propanesulfonic acid sodium salt (AMPS) to alter the swelling behavior of the extruded hydrogel tube. A hydrogel formulation with 30 wt% F127-BUM and 10 wt% AMPS was prepared, and its rheological properties were evaluated (Figure 2.8). Following fabrication, tubes with and without the AMPS additive were allowed to swell to equilibrium in deionized water. The average water mass fraction of the tubes with AMPS (n = 4) was 92.3% ± 0.3% (SD) (Figure 2.3c). The average water mass fraction of the tube without AMPS (n = 4) was 82.9% ± 1.3% (SD) (Figure 2.3d).

2.4.3. Cell Seeding and Culture Experiments

Endothelial cells, which line the luminal surfaces of blood vessels, are one of the principal cellular components of the vascular system, wherein, in addition to fulfilling a variety of other roles, they make up the vascular barrier (endothelium) and control the extravasation of blood proteins and cells. Typical two-dimensional cultures of vascular endothelial cells on glass or poly(styrene) cultureware do not recapitulate physiology related to 3D geometry. Consequently, there is considerable interest in accessible platforms that enable more representative cultures of vascular endothelial cells.[49–51]

Prior to seeding HUVECs on the luminal surfaces of our hydrogel tubes, we first screened our materials for biocompatibility and cell adhesion by producing small (~ 5 mm in diameter) cross-linked hydrogel discs with identical hydrogel compositions and analogous preparation to our tubes. In preliminary experiments in which we seeded HUVECs on the surfaces of discs made from cross-linked F127-BUM hydrogel without additive, we stained the cells with calcein AM after 24 h in culture in order to visualize cell morphology and infer cell adhesion to the hydrogel surface. These initial results suggested that this material does not promote adhesion of HUVECs—i.e., when cells were seeded directly onto the surfaces of the hydrogel discs, cells retained a rounded morphology as a consequence of a lack of adhesion (Figure 2.10a). These results were consistent with previous reports.[52] The high poly(ethylene oxide) (PEO) content of F127 (72–75%) affords a cross-linked material that resists protein adsorption and cell adhesion.[53–57] It is also worth noting that hydrogels based on F127 or its derivatives are generally not cytocompatible prior to cross-linking, and so these materials are of limited use when cells are to be encapsulated within the material.[58]

Thus, collagen I was used to promote cell adhesion to the F127-BUM surface. The thermo-responsive gelation behavior of F127-BUM facilitated the homogenous incorporation of soluble collagen into the hydrogel at low temperatures. Concentrations of collagen I in excess of 0.2 wt% in the F127-BUM (30 wt%) hydrogels led to substantial aggregation of collagen, causing visible inhomogeneity in the gel, which was detrimental to extrusion quality. The inclusion of collagen I as an additive at no more than 0.2 wt%, however, was not substantially detrimental to the desirable rheological characteristics of the hydrogel (Figure 2.7) and afforded high-quality tubes.

The adhesion of HUVECs to the hydrogel surface improved substantially with the incorporation of collagen into the hydrogel formulation; however, we observed that the functionalization of F127-BUM hydrogel with collagen I was more effective in promoting HUVEC adhesion when collagen was not only incorporated into the hydrogel formulation prior to fabrication of discs or tubes but also coated onto the cross-linked hydrogel surfaces post-fabrication. The latter was achieved via multiple rounds of rehydration of dehydrated hydrogel constructs (i.e. tubes and discs) in solutions of collagen I. After this process was established, HUVEC morphology and viability were again evaluated by fabricating hydrogel discs functionalized in this way and seeding cells onto their surfaces. At 24 h in culture, we observed that cells had adhered to the disc surfaces, as evidenced by the spread morphology (Figure 2.10b). Viability of cells cultured on collagen-treated discs made from the F127-BUM hydrogel with collagen I additive was found to be satisfactory after 72 h in culture (Figure 2.10c).

Finally, to demonstrate the application of this platform toward fabrication of models of vascular endothelium, we prepared tubes for the luminal-seeding and culture of HUVECs. Tubes were prepared with the F127-BUM hydrogel with collagen I additive and were treated with collagen I in a manner analogous to the discs discussed above. To characterize morphology of the HUVECs on the luminal surfaces of tubes, we visualized the inter-endothelial junction marker CD31 (also referred to as platelet endothelial cell adhesion molecule, PECAM1) via indirect immunofluorescence after 72 h of culture. The expression and localization of CD31 indicates appropriate general endothelial phenotype.[59] Figure 2.10d–i shows the presence of inter-endothelial junctions between HUVECs seeded on the luminal surfaces of collagen-functionalized tubes. Cells were found to exhibit characteristic endothelial cobblestone morphology. Figure 2.10d–f provides top-down views of lumens in the XY plane, showing the

coverage of the lumens with HUVECs expressing CD31. Figure 2.10g–i shows re-constructed z-stacks of a tube lumen that has been seeded with HUVECs. Taken together, these results demonstrate that our coaxial extrusion platform comprising the coaxial nozzle and F127-BUM-based hydrogels is effective in fabricating collagen-functionalized tubes, and these tubes are suitable for the culture of tubular monolayers of contiguous endothelial cells.

2.5. Conclusion

In summary, we report a platform for the extrusion-based fabrication of tubular hydrogel constructs using customized, 3D-printed coaxial nozzles. These nozzles can be fabricated using commercially available desktop SLA 3D printers and are amenable to use with existing DIW setups. We demonstrate that hydrogels based on a methacrylate-terminated Pluronic F-127 derivative can be extruded through these nozzles to yield multi-material coaxial filaments and tubes with geometries which are tunable either via alteration of nozzle orifice geometry or extrusion pressures. For example, we were able to fabricate tubes with luminal diameters or wall thicknesses as small as ∼150 μm, as well as tubes with star-shaped cross-sectional geometries. Additionally, we demonstrate that tubes produced using our method can be used for 3D culture of HUVECs; this is enabled by functionalization of the F127 derivative hydrogel using collagen I. Our approach ultimately enables the facile fabrication of bio-functional hydrogel conduits which may be useful for engineering in vitro models of tubular biological structures.

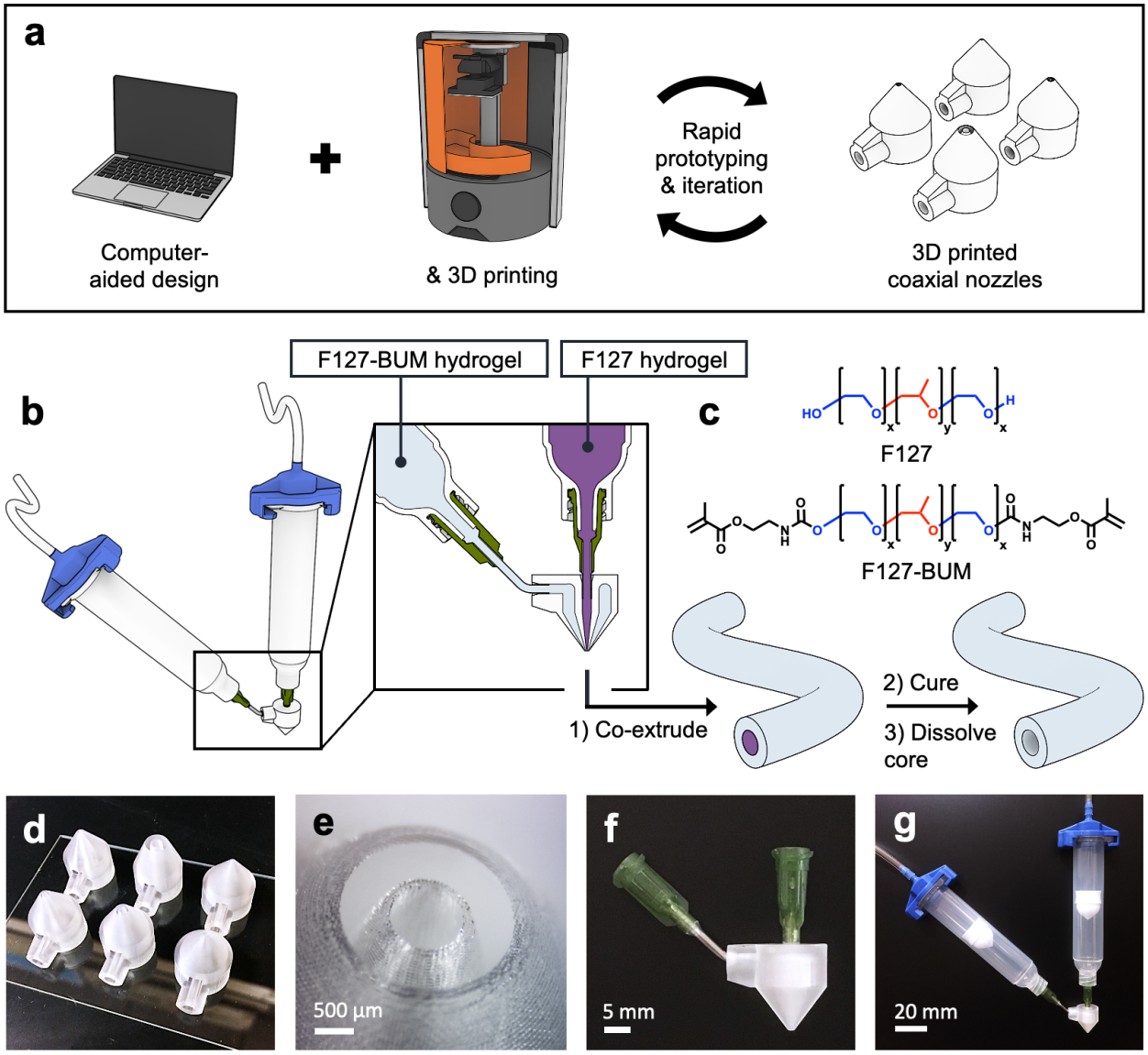

Figure 2.1. Schematic of coaxial nozzle and hydrogel tube production. (a) Computer-aided design (CAD) in conjunction with SLA 3D printing enables the fabrication of fully customizable coaxial nozzles. (b) Tube fabrication workflow. (c) Chemical structures of F127 and F127-BUM. (d) Coaxial nozzles of different diameters after printing. (e) Tip of coaxial nozzle under magnification. (f) Coaxial nozzle after blunt-tip needles have been affixed to inlets. (g) Coaxial extrusion assembly.

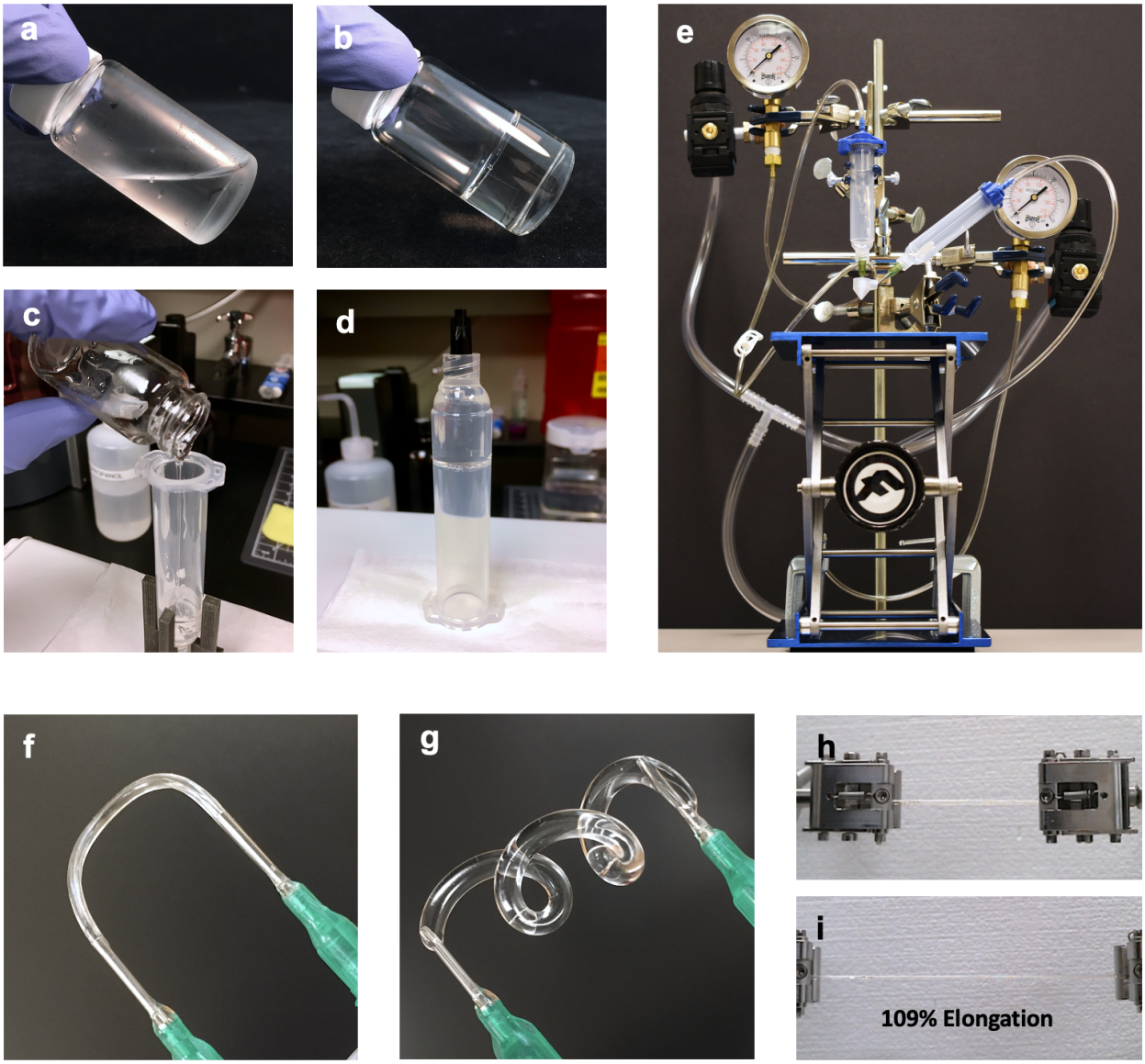

Figure 2.2. F127-BUM hydrogel, hydrogel tube fabrication, and extrusion setup. (a) F127-BUM hydrogel at 4 °C. (b) F127-BUM hydrogel at 20 °C. (c) Pouring F127-BUM hydrogel into syringe at 4 °C. (d) F127- BUM hydrogel inside inverted syringe at 20 °C. (e) Coaxial extrusion setup. (f) F127-BUM hydrogel tube attached to 18-gauge needles, pre-distention. (g) Distention of F127-BUM hydrogel tube with water. (h,i) F127-BUM hydrogel tube tensile experiment.

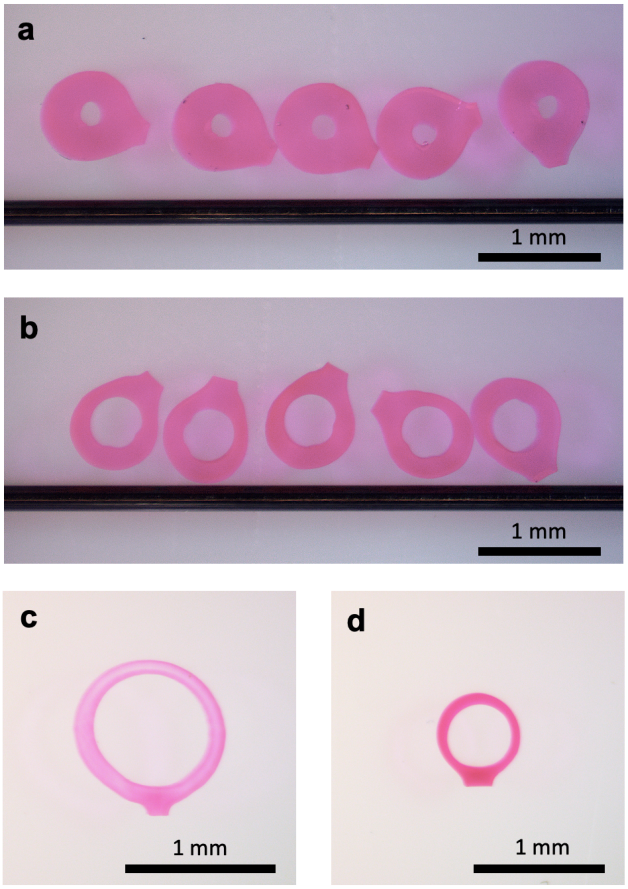

Figure 2.3. Hydrogel tube extrusion-pressure-dependent dimensional control and swelling experiment. (a) Smaller-lumen (~ 0.20 mm) F127-BUM hydrogel tube cross sections. (b) Larger-lumen (~ 0.40 mm) F127-BUM hydrogel tube cross sections. (c) Cross section of tube fabricated from F127-BUM hydrogel with AMPS additive (post-swelling in water). (d) Cross section of tube fabricated from F127-BUM hydrogel without additive (post-swelling in water).

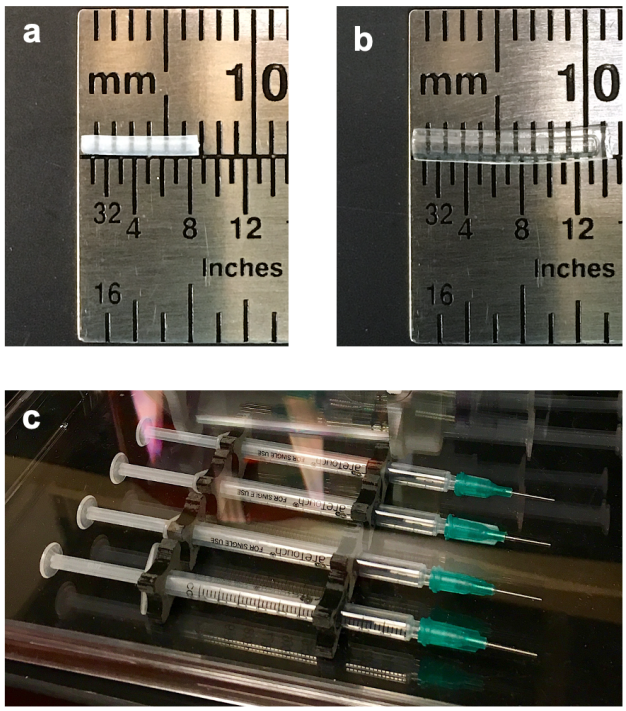

Figure 2.4. Rehydration of a tube section and syringe stands. (a) Short tube section fabricated from F127-BUM hydrogel with collagen I additive in dehydrated state. (b) Same tube section following rehydration with collagen I solution. (c) Syringes for cell seeding immobilized in BioAssay dish using 3D printed syringe stands.

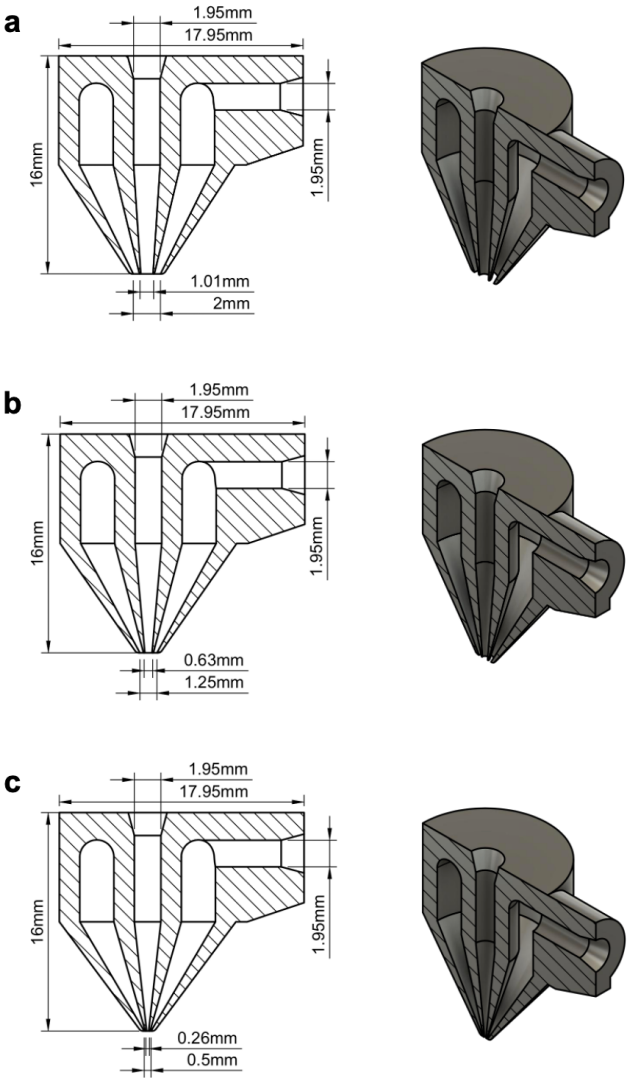

Figure 2.5. Nozzle sizes. (a) Large-sized nozzle. (b) Medium-sized nozzle. (c) Small-sized nozzle.

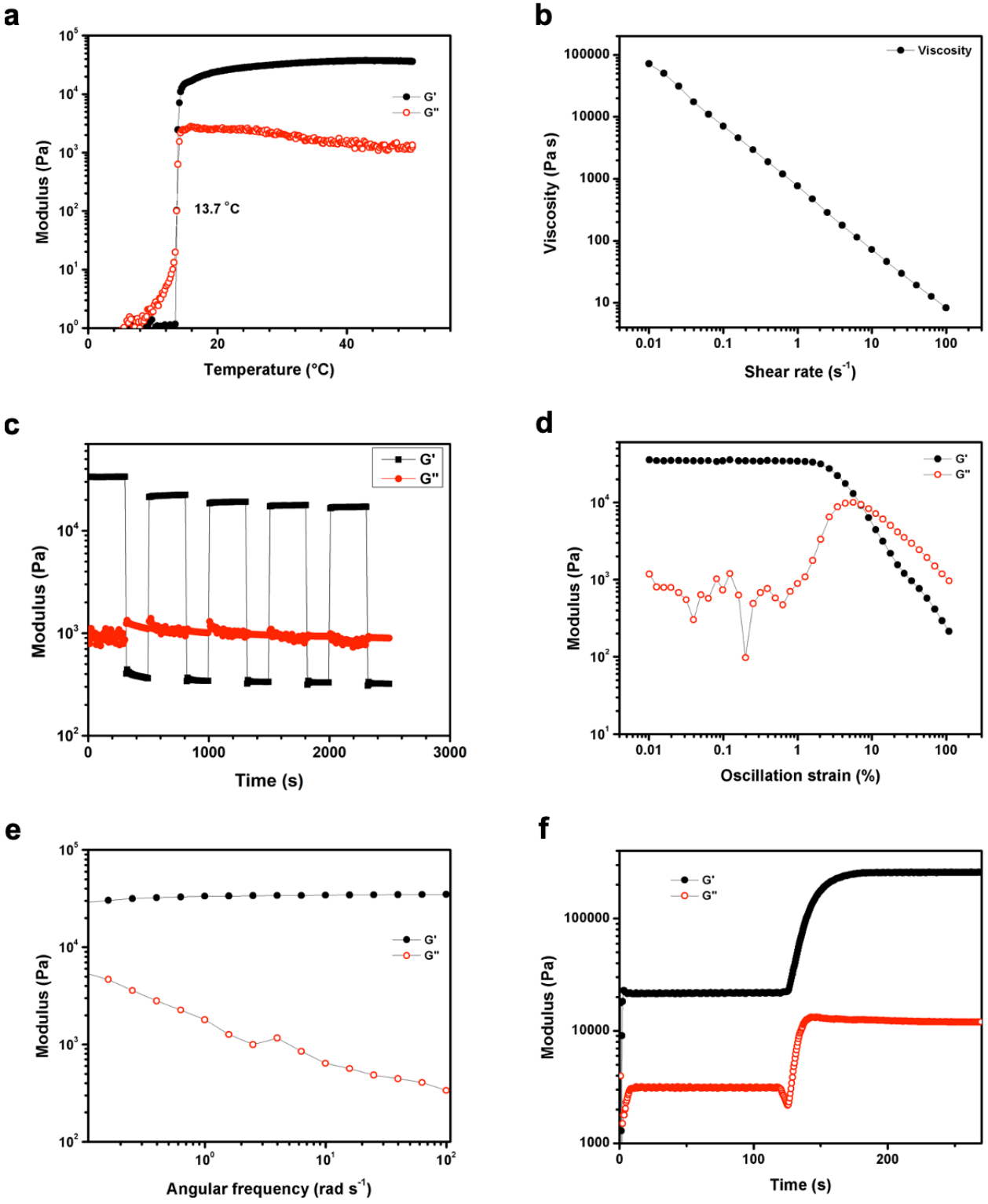

Figure 2.6. Rheology of F127-BUM hydrogel without additive. (a) Temperature ramp. (b) Shear rate sweep. (c) Cyclic shear strain. (d) Strain sweep. (e) Frequency sweep. (f) Photo-rheology.

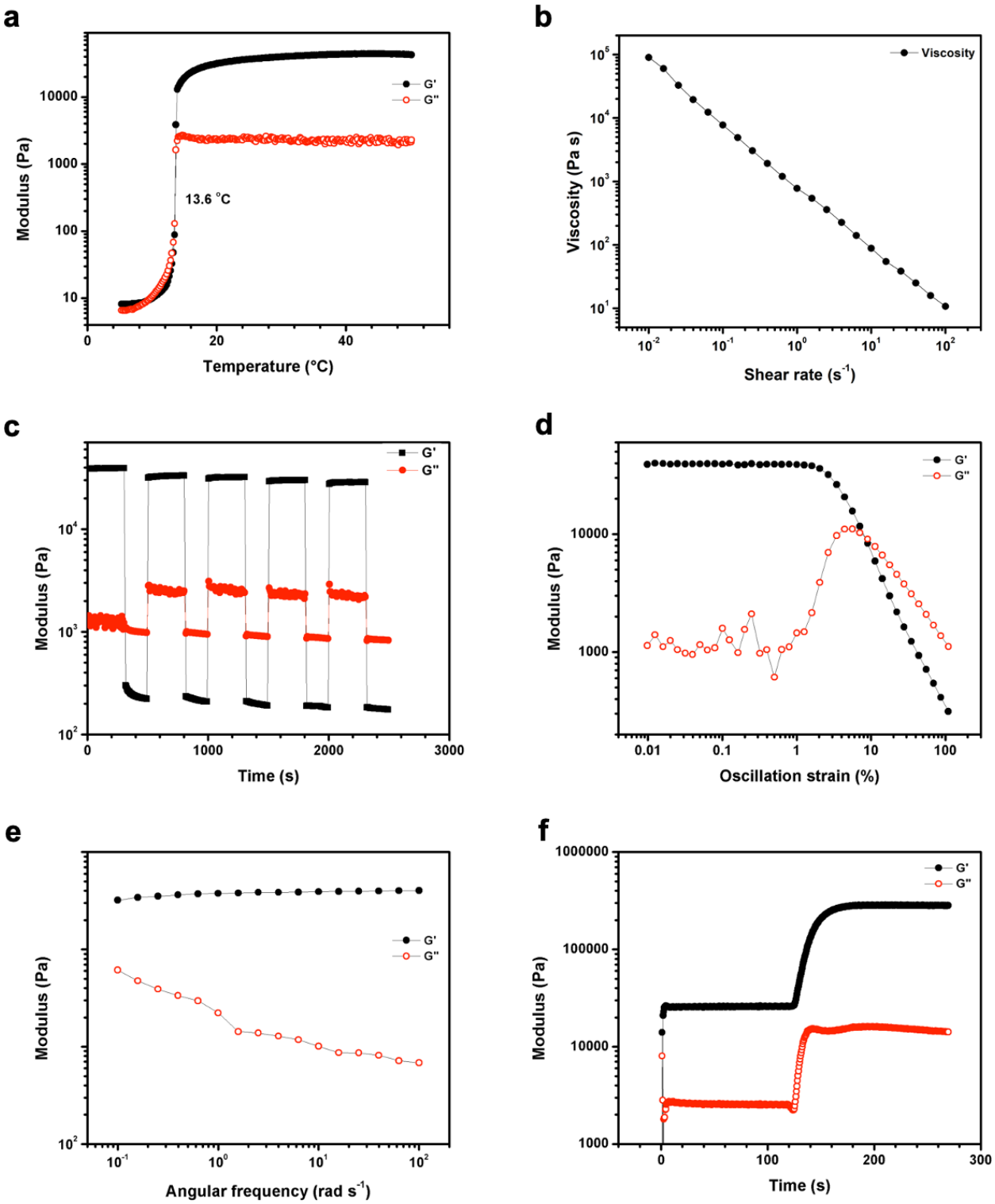

Figure 2.7. Rheology of F127-BUM hydrogel with collagen I additive. (a) Temperature ramp. (b) Shear rate sweep. (c) Cyclic shear strain. (d) Strain sweep. (e) Frequency sweep. (f) Photo-rheology.

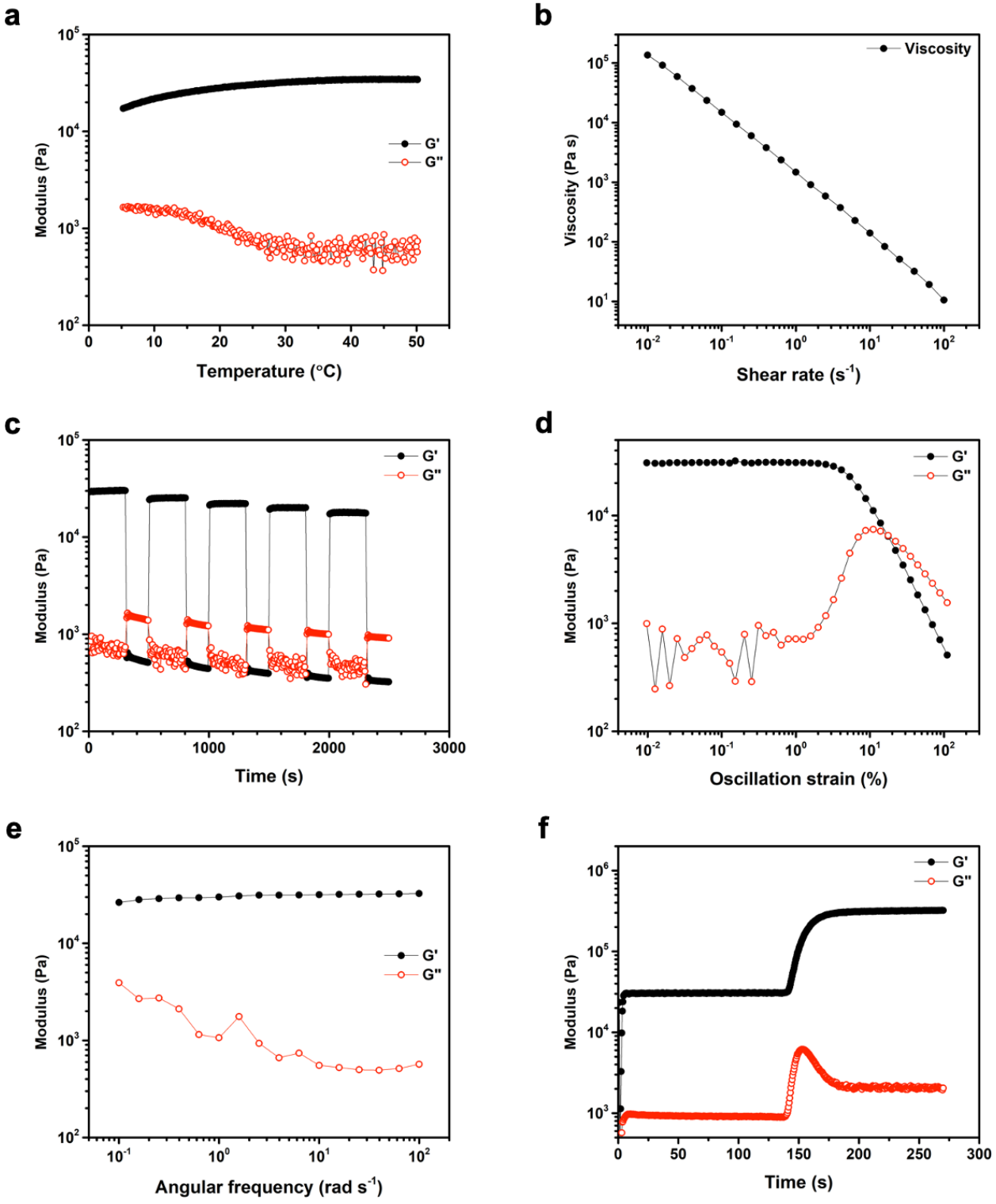

Figure 2.8. Rheology of F127-BUM hydrogel with AMPS additive. (a) Temperature ramp. (b) Shear rate sweep. (c) Cyclic shear strain. (d) Strain sweep. (e) Frequency sweep. (f) Photo-rheology.

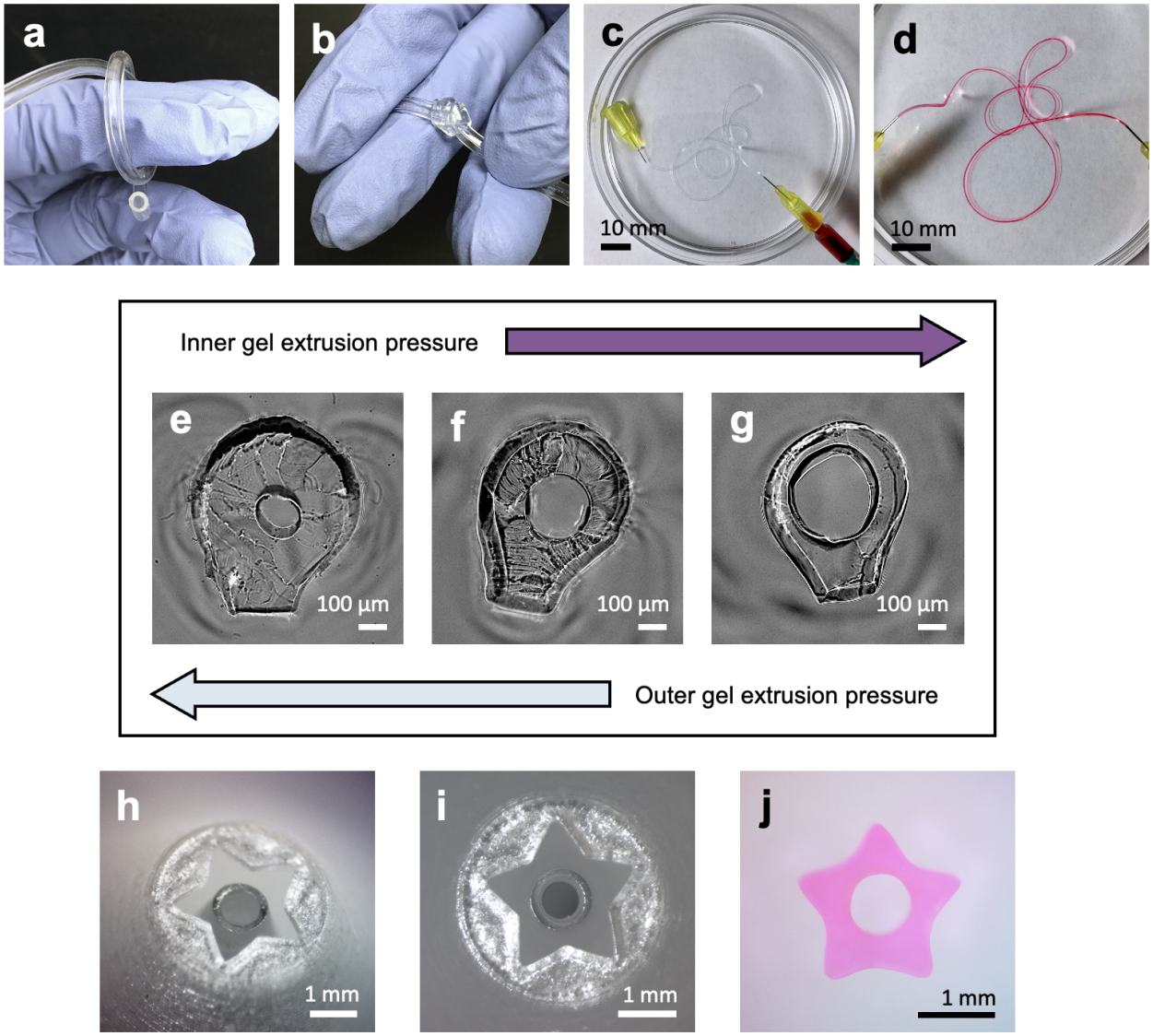

Figure 2.9. Tube geometry can be tuned by altering nozzle size and shape as well as extrusion conditions. (a,b) Tubes produced using large-sized (2 mm outer conduit diameter) coaxial nozzle. Tubes have good elasticity and toughness. (c,d) Tubes fabricated using small-sized (0.5 mm outer conduit diameter) nozzle. Dye perfusion shows lumen patency. Tube walls were stained as dye began to diffuse through walls. (e–g) Summary of extrusion-pressure effects on cross-sectional geometry of small tubes. Luminal diameters or wall thicknesses as small as ~150 μm were achieved. (h,i) 5-point star geometry on customized nozzle. (j) Cross-sectional geometry of 5-point star tube produced using star nozzle.

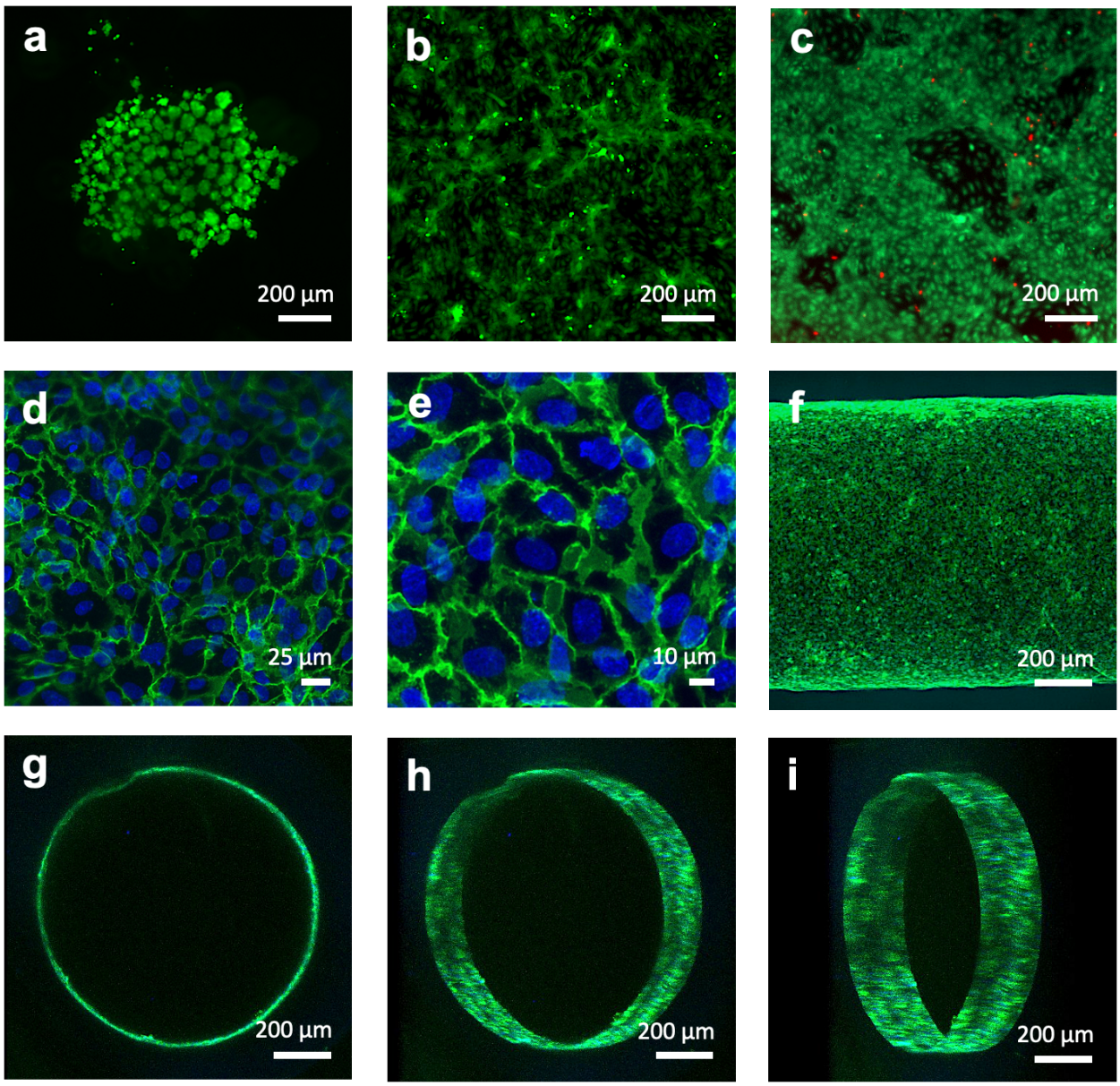

Figure 2.10. Fluorescence and confocal micrographs of endothelial-cell-seeded, cross-linked hydrogel constructs. (a) HUVECs seeded on cross-linked unmodified F127-BUM hydrogel disc after 24 h in culture. Cells stained with calcein AM (green) for visualization show aggregation and rounded morphology, indicating lack of adhesion. Percent coverage was determined to be 20% ± 9% (SD; n = 3). This image is representative of three replicates. (b) HUVECs seeded on cross-linked, collagen I-treated F127-BUM hydrogel disc with collagen I additive after 24 h in culture. Cells stained with calcein AM for visualization show spreading, indicating adhesion. Percent coverage was determined to be 52% ± 8% (SD; n = 3). This image is representative of three replicates. (c) Viability assay (calcein AM, green/ethidium homodimer-1, red) of HUVECs

seeded on cross-linked, collagen-I-treated F127-BUM hydrogel disc with collagen I additive after 72 h in culture. Green indicates live cells, red indicates dead cells; cell viability is high. This image is representative of three replicates. (d,e) Confocal micrographs of HUVECs seeded on the luminal surfaces of tubes composed of cross-linked, collagen-I-treated F127-BUM hydrogel with collagen I additive. Cells stained with DAPI (blue: nuclei) and labeled via indirect immunofluorescence (green: CD31, inter-endothelial junction marker) exhibit characteristic cobblestone morphology. These images are representative of six replicates. (f) Identical treatment to samples in Figure 2.10d,e. Entire width of tube section is visualized, showing good cell coverage. This image is representative of six replicates. (g–i) Identical treatment to samples in Figure 2.10d–f. Luminal surface of tube is visualized via confocal microscopy showing good cell coverage. These images are representative of six replicates.

References

(1) Monahan-Earley, R.; Dvorak, A. M.; Aird, W. C. Evolutionary Origins of the Blood Vascular System and Endothelium. *J. Thromb. Haemost.* **2013**, *11* (s1), 46–66. https://doi.org/10.1111/jth.12253.

(2) Lucas, W. J.; Groover, A.; Lichtenberger, R.; Furuta, K.; Yadav, S.-R.; Helariutta, Y.; He, X.-Q.; Fukuda, H.; Kang, J.; Brady, S. M.; Patrick, J. W.; Sperry, J.; Yoshida, A.; López-Millán, A.-F.; Grusak, M. A.; Kachroo, P. The Plant Vascular System: Evolution, Development and Functions. *J. Integr. Plant Biol.* **2013**, *55* (4), 294–388. https://doi.org/10.1111/jipb.12041.

(3) Kolesky, D. B.; Homan, K. A.; Skylar-Scott, M. A.; Lewis, J. A. Three-Dimensional Bioprinting of Thick Vascularized Tissues. *P. Natl. Acad. Sci.* **2016**, *113* (12), 3179–3184. https://doi.org/10.1073/pnas.1521342113.

(4) Homan, K. A.; Kolesky, D. B.; Skylar-Scott, M. A.; Herrmann, J.; Obuobi, H.; Moisan, A.; Lewis, J. A. Bioprinting of 3D Convoluted Renal Proximal Tubules on Perfusable Chips. *Sci. Rep.* **2016**, *6* (1), 34845. https://doi.org/10.1038/srep34845.

(5) Kolesky, D. B.; Truby, R. L.; Gladman, A. S.; Busbee, T. A.; Homan, K. A.; Lewis, J. A. 3D Bioprinting of Vascularized, Heterogeneous Cell-Laden Tissue Constructs. *Adv. Mater.* **2014**, *26* (19), 3124–3130. https://doi.org/10.1002/adma.201305506.

(6) Wu, W.; DeConinck, A.; Lewis, J. A. Omnidirectional Printing of 3D Microvascular Networks. *Adv. Mater.* **2011**, *23* (24). https://doi.org/10.1002/adma.201004625.

(7) O'Bryan, C. S.; Bhattacharjee, T.; Hart, S.; Kabb, C. P.; Schulze, K. D.; Chilakala, I.; Sumerlin, B. S.; Sawyer, W. G.; Angelini, T. E. Self-Assembled Micro-Organogels for 3D Printing Silicone Structures. *Sci. Adv.* **2017**, *3* (5), e1602800. https://doi.org/10.1126/sciadv.1602800.

(8) Pi, Q.; Maharjan, S.; Yan, X.; Liu, X.; Singh, B.; van Genderen, A. M.; Robledo-Padilla, F.; Parra-Saldivar, R.; Hu, N.; Jia, W.; Xu, C.; Kang, J.; Hassan, S.; Cheng, H.; Hou, X.; Khademhosseini, A.; Zhang, Y. S. Digitally Tunable Microfluidic Bioprinting of Multilayered Cannular Tissues. *Adv. Mater.* **2018**, *30* (43), 1706913. https://doi.org/10.1002/adma.201706913.

(9) Jia, W.; Gungor-Ozkerim, P. S.; Zhang, Y. S.; Yue, K.; Zhu, K.; Liu, W.; Pi, Q.; Byambaa, B.; Dokmeci, M. R.; Shin, S. R.; Khademhosseini, A. Direct 3D Bioprinting of Perfusable Vascular Constructs Using a Blend Bioink. *Biomaterials* **2016**, *106*, 58–68. https://doi.org/10.1016/j.biomaterials.2016.07.038.

(10) Ouyang, L.; Highley, C. B.; Sun, W.; Burdick, J. A. A Generalizable Strategy for the 3D Bioprinting of Hydrogels from Nonviscous Photo-crosslinkable Inks. *Adv. Mater.* **2017**, *29* (8), 1604983. https://doi.org/10.1002/adma.201604983.

(11) Song, K. H.; Highley, C. B.; Rouff, A.; Burdick, J. A. Complex 3D-Printed Microchannels within Cell-Degradable Hydrogels. *Adv. Funct. Mater.* **2018**, *28* (31), 1801331. https://doi.org/10.1002/adfm.201801331.

(12) Gao, Q.; He, Y.; Fu, J.; Liu, A.; Ma, L. Coaxial Nozzle-Assisted 3D Bioprinting with Built-in Microchannels for Nutrients Delivery. *Biomaterials* **2015**, *61*, 203–215. https://doi.org/10.1016/j.biomaterials.2015.05.031.

(13) Zhang, Y.; Yu, Y.; Akkouch, A.; Dababneh, A.; Dolati, F.; T. Ozbolat, I. In Vitro Study of Directly Bioprinted Perfusable Vasculature Conduits. *Biomater. Sci.* **2015**, *3* (1), 134–143. https://doi.org/10.1039/C4BM00234B.

(14) Weinberg, C. B.; Bell, E. A Blood Vessel Model Constructed from Collagen and Cultured Vascular Cells. *Science* **1986**, *231* (4736), 397–400. https://doi.org/10.1126/science.2934816.

(15) Melchiorri, A. J.; Bracaglia, L. G.; Kimerer, L. K.; Hibino, N.; Fisher, J. P. In Vitro Endothelialization of Biodegradable Vascular Grafts Via Endothelial Progenitor Cell Seeding and Maturation in a Tubular Perfusion System Bioreactor. *Tissue Eng. Part C–Me.* **2016**, *22* (7), 663–670. https://doi.org/10.1089/ten.tec.2015.0562.

(16) Li, X.; Xu, J.; Nicolescu, C. T.; Marinelli, J. T.; Tien, J. Generation, Endothelialization, and Microsurgical Suture Anastomosis of Strong 1-Mm-Diameter Collagen Tubes. *Tissue Eng. Pt. A* **2017**, *23* (7–8), 335–344. https://doi.org/10.1089/ten.tea.2016.0339.

(17) Atlan, M.; Lellouch, A. G.; Legagneux, J.; Chaouat, M.; Masquelet, A.-C.; Letourneur, D. A New Synthetic Model for Microvascular Anastomosis Training? A Randomized Comparative Study Between Silicone and Polyvinyl Alcohol Gelatin Tubes. *J. Surg. Educ.* **2018**, *75* (1), 182–187. https://doi.org/10.1016/j.jsurg.2017.06.008.

(18) Carvalho, C. R.; Costa, J. B.; da Silva Morais, A.; López-Cebral, R.; Silva-Correia, J.; Reis, R. L.; Oliveira, J. M. Tunable Enzymatically Cross-Linked Silk Fibroin Tubular Conduits for Guided Tissue Regeneration. *Adv. Healthc. Mater.* **2018**, *7* (17), 1800186. https://doi.org/10.1002/adhm.201800186.

(19) Syedain, Z. H.; Graham, M. L.; Dunn, T. B.; O'Brien, T.; Johnson, S. L.; Schumacher, R. J.; Tranquillo, R. T. A Completely Biological "off-the-Shelf" Arteriovenous Graft That Recellularizes in Baboons. *Sci. Transl. Med.* **2017**, *9* (414), eaan4209. https://doi.org/10.1126/scitranslmed.aan4209.

(20) Chaouat, M.; Le Visage, C.; Baille, W. E.; Escoubet, B.; Chaubet, F.; Mateescu, M. A.; Letourneur, D. A Novel Cross-Linked Poly(Vinyl Alcohol) (PVA) for Vascular Grafts. *Adv. Funct. Mater.* **2008**, *18* (19), 2855–2861. https://doi.org/10.1002/adfm.200701261.

(21) Gao, G.; Lee, J. H.; Jang, J.; Lee, D. H.; Kong, J.-S.; Kim, B. S.; Choi, Y.-J.; Jang, W. B.; Hong, Y. J.; Kwon, S.-M.; Cho, D.-W. Tissue Engineered Bio-Blood-Vessels Constructed Using a Tissue-Specific Bioink and 3D Coaxial Cell Printing Technique: A Novel Therapy for Ischemic Disease. *Adv. Funct. Mater.* **2017**, *27* (33), 1700798. https://doi.org/10.1002/adfm.201700798.

(22) Duchi, S.; Onofrillo, C.; O'Connell, C. D.; Blanchard, R.; Augustine, C.; Quigley, A. F.; Kapsa, R. M. I.; Pivonka, P.; Wallace, G.; Di Bella, C.; Choong, P. F. M. Handheld Co-Axial Bioprinting: Application to in Situ Surgical Cartilage Repair. *Sci. Rep.* **2017**, *7* (1), 5837. https://doi.org/10.1038/s41598-017-05699-x.

(23) Oberg, E.; Jones, F. D.; Horton, H. L.; Ryffel, H. H. *Machinerys Handbook: A Reference Book For The Mechanical Engineer, Designer, Manufacturing Engineer, Draftsman, Toolmaker and Machinist*, 30th ed.; Industrial Press, 2016.

(24) Ratcliffe, A. Tissue Engineering of Vascular Grafts. *Matrix Biol.* **2000**, *19* (4), 353–357. https://doi.org/10.1016/S0945-053X(00)00080-9.

(25) Battiston, B.; Geuna, S.; Ferrero, M.; Tos, P. Nerve Repair by Means of Tubulization: Literature Review and Personal Clinical Experience Comparing Biological and Synthetic Conduits for Sensory Nerve Repair. *Microsurg.* **2005**, *25* (4), 258–267. https://doi.org/10.1002/micr.20127.

(26) Johnson, B. N.; Lancaster, K. Z.; Zhen, G.; He, J.; Gupta, M. K.; Kong, Y. L.; Engel, E. A.; Krick, K. D.; Ju, A.; Meng, F.; Enquist, L. W.; Jia, X.; McAlpine, M. C. 3D Printed Anatomical Nerve Regeneration Pathways. *Adv. Funct. Mater.* **2015**, *25* (39), 6205–6217. https://doi.org/10.1002/adfm.201501760.

(27) Atala, A.; Danilevskiy, M.; Lyundup, A.; Glybochko, P.; Butnaru, D.; Vinarov, A.; Yoo, J. J. The Potential Role of Tissue-Engineered Urethral Substitution: Clinical and Preclinical Studies. *J. Tissue Eng. Regen. M.* **2017**, *11* (1), 3–19. https://doi.org/10.1002/term.2112.

(28) Raya-Rivera, A.; Esquiliano, D. R.; Yoo, J. J.; Lopez-Bayghen, E.; Soker, S.; Atala, A. Tissue-Engineered Autologous Urethras for Patients Who Need Reconstruction: An Observational Study. *Lancet* **2011**, *377* (9772), 1175–1182. https://doi.org/10.1016/S0140-6736(10)62354-9.

(29) Filippo, R. E. D.; Yoo, J. J.; Atala, A. Urethral Replacement Using Cell Seeded Tubularized Collagen Matrices. *J. Urology* **2002**. https://doi.org/10.1016/S0022-5347(05)64414-X.

(30) Yu, Y.; Zhang, Y.; Ozbolat, I. T. A Hybrid Bioprinting Approach for Scale-Up Tissue Fabrication. *J. Manuf. Sci. Eng.* **2014**, *136* (061013). https://doi.org/10.1115/1.4028511.

(31) Mistry, P.; Aied, A.; Alexander, M.; Shakesheff, K.; Bennett, A.; Yang, J. Bioprinting Using Mechanically Robust Core–Shell Cell-Laden Hydrogel Strands. *Macromol. Biosci.* **2017**, *17* (6), 1600472. https://doi.org/10.1002/mabi.201600472.

(32) Colosi, C.; Shin, S. R.; Manoharan, V.; Massa, S.; Costantini, M.; Barbetta, A.; Dokmeci, M. R.; Dentini, M.; Khademhosseini, A. Microfluidic Bioprinting of Heterogeneous 3D Tissue Constructs Using Low-Viscosity Bioink. *Adv. Mater.* **2016**, *28* (4), 677–684. https://doi.org/10.1002/adma.201503310.

(33) Caliari, S. R.; Burdick, J. A. A Practical Guide to Hydrogels for Cell Culture. *Nat. Methods* **2016**, *13* (5), 405–414. https://doi.org/10.1038/nmeth.3839.

(34) Hoffman, A. S. Hydrogels for Biomedical Applications. *Adv. Drug Deliver. Rev.* **2012**, *64*, 18–23. https://doi.org/10.1016/j.addr.2012.09.010.

(35) Malda, J.; Visser, J.; Melchels, F. P.; Jüngst, T.; Hennink, W. E.; Dhert, W. J. A.; Groll, J.; Hutmacher, D. W. 25th Anniversary Article: Engineering Hydrogels for Biofabrication. *Adv. Mater.* **2013**, *25* (36), 5011–5028. https://doi.org/10.1002/adma.201302042.

(36) Place, E. S.; Evans, N. D.; Stevens, M. M. Complexity in Biomaterials for Tissue Engineering. *Nat. Mater.* **2009**, *8* (6), 457–470. https://doi.org/10.1038/nmat2441.

(37) O'Brien, F. J. Biomaterials & Scaffolds for Tissue Engineering. *Mater. Today* **2011**, *14* (3), 88–95. https://doi.org/10.1016/S1369-7021(11)70058-X.

(38) Murphy, S. V.; Atala, A. 3D Bioprinting of Tissues and Organs. *Nat. Biotechnol.* **2014**, *32* (8), 773–785. https://doi.org/10.1038/nbt.2958.

(39) Millik, S. C.; Dostie, A. M.; Karis, D. G.; Smith, P. T.; McKenna, M.; Chan, N.; Curtis, C. D.; Nance, E.; Theberge, A. B.; Nelson, A. 3D Printed Coaxial Nozzles for the Extrusion of Hydrogel Tubes toward Modeling Vascular Endothelium. *Biofabrication* **2019**, *11* (4), 045009. https://doi.org/10.1088/1758-5090/ab2b4d.

(40) Liu, X.; Yuk, H.; Lin, S.; Parada, G. A.; Tang, T.-C.; Tham, E.; de la Fuente-Nunez, C.; Lu, T. K.; Zhao, X. 3D Printing of Living Responsive Materials and Devices. *Adv. Mater.* **2018**, *30* (4), 1704821. https://doi.org/10.1002/adma.201704821.

(41) Gioffredi, E.; Boffito, M.; Calzone, S.; Giannitelli, S. M.; Rainer, A.; Trombetta, M.; Mozetic, P.; Chiono, V. Pluronic F127 Hydrogel Characterization and Biofabrication in Cellularized Constructs for Tissue Engineering Applications. *Procedia CIRP* **2016**, *49*, 125–132. https://doi.org/10.1016/j.procir.2015.11.001.

(42) Suntornnond, R.; Tan, E. Y. S.; An, J.; Chua, C. K. A Highly Printable and Biocompatible Hydrogel Composite for Direct Printing of Soft and Perfusable Vasculature-like Structures. *Sci. Rep.* **2017**, *7* (1), 16902. https://doi.org/10.1038/s41598-017-17198-0.

(43) Müller, M.; Becher, J.; Schnabelrauch, M.; Zenobi-Wong, M. Nanostructured Pluronic Hydrogels as Bioinks for 3D Bioprinting. *Biofabrication* **2015**, *7* (3), 035006. https://doi.org/10.1088/1758-5090/7/3/035006.

(44) Paxton, N.; Smolan, W.; Böck, T.; Melchels, F.; Groll, J.; Jungst, T. Proposal to Assess Printability of Bioinks for Extrusion-Based Bioprinting and Evaluation of Rheological Properties Governing Bioprintability. *Biofabrication* **2017**, *9* (4), 044107. https://doi.org/10.1088/1758-5090/aa8dd8.

(45) Smith, P. T.; Basu, A.; Saha, A.; Nelson, A. Chemical Modification and Printability of Shear-Thinning Hydrogel Inks for Direct-Write 3D Printing. *Polymer* **2018**, *152*, 42–50. https://doi.org/10.1016/j.polymer.2018.01.070.

(46) Prud'homme, R. K.; Wu, G.; Schneider, D. K. Structure and Rheology Studies of Poly(Oxyethylene−oxypropylene−oxyethylene) Aqueous Solution. *Langmuir* **1996**, *12* (20), 4651–4659. https://doi.org/10.1021/la951506b.

(47) Jalaal, M.; Cottrell, G.; Balmforth, N.; Stoeber, B. On the Rheology of Pluronic F127 Aqueous Solutions. *J. Rheol.* **2017**, *61* (1), 139–146. https://doi.org/10.1122/1.4971992.

(48) Basu, A.; Saha, A.; Goodman, C.; Shafranek, R. T.; Nelson, A. Catalytically Initiated Gel-in-Gel Printing of Composite Hydrogels. *ACS Appl. Mater. Inter.* **2017**, *9* (46), 40898–40904. https://doi.org/10.1021/acsami.7b14177.

(49) Baker, B. M.; Chen, C. S. Deconstructing the Third Dimension – How 3D Culture Microenvironments Alter Cellular Cues. *J. Cell Sci.* **2012**, *125* (13), 3015–3024. https://doi.org/10.1242/jcs.079509.

(50) Zheng, Y.; Chen, J.; Craven, M.; Choi, N. W.; Totorica, S.; Diaz-Santana, A.; Kermani, P.; Hempstead, B.; Fischbach-Teschl, C.; López, J. A.; Stroock, A. D. In Vitro Microvessels

for the Study of Angiogenesis and Thrombosis. *P. Natl. Acad. Sci.* **2012**, *109* (24), 9342–9347. https://doi.org/10.1073/pnas.1201240109.

(51) Bischel, L. L.; Sung, K. E.; Jiménez-Torres, J. A.; Mader, B.; Keely, P. J.; Beebe, D. J. The Importance of Being a Lumen. *FASEB J.* **2014**, *28* (11), 4583. https://doi.org/10.1096/fj.13-243733.

(52) Fussell, G. W.; Cooper, S. L. Endothelial Cell Adhesion on RGD-Containing Methacrylate Terpolymers. *J. Biomed. Mater. Res. A* **2004**, *70A* (2), 265–273. https://doi.org/10.1002/jbm.a.30074.

(53) Gombotz, W. R.; Guanghui, W.; Horbett, T. A.; Hoffman, A. S. Protein Adsorption to Poly(Ethylene Oxide) Surfaces. *J. Biomed. Mater. Res.* **1991**, *25* (12), 1547–1562. https://doi.org/10.1002/jbm.820251211.

(54) Harris, J. M. *Poly(Ethylene Glycol) Chemistry: Biotechnical and Biomedical Applications*; Springer Science & Business Media, 1992.

(55) Prime, K. L.; Whitesides, G. M. Adsorption of Proteins onto Surfaces Containing End-Attached Oligo(Ethylene Oxide): A Model System Using Self-Assembled Monolayers. *J. Am. Chem. Soc.* **1993**, *115* (23), 10714–10721. https://doi.org/10.1021/ja00076a032.

(56) Amiji, M.; Park, K. Prevention of Protein Adsorption and Platelet Adhesion on Surfaces by PEO/PPO/PEO Triblock Copolymers. *Biomaterials* **1992**, *13* (10), 682–692. https://doi.org/10.1016/0142-9612(92)90128-B.

(57) Wang, Y.; Wang, T.; Su, Y.; Peng, F.; Wu, H.; Jiang, Z. Remarkable Reduction of Irreversible Fouling and Improvement of the Permeation Properties of Poly(Ether Sulfone) Ultrafiltration Membranes by Blending with Pluronic F127. *Langmuir* **2005**, *21* (25), 11856–11862. https://doi.org/10.1021/la052052d.

(58) Khattak, S. F.; Bhatia, S. R.; Roberts, S. C. Pluronic F127 as a Cell Encapsulation Material: Utilization of Membrane-Stabilizing Agents. *Tissue Eng.* **2005**, *11* (5–6), 974–983. https://doi.org/10.1089/ten.2005.11.974.

(59) Privratsky, J. R.; Newman, P. J. PECAM-1: Regulator of Endothelial Junctional Integrity. *Cell Tissue Res.* **2014**, *355* (3), 607–619. https://doi.org/10.1007/s00441-013-1779-3.

Chapter 3

3D-Printed Protein-Based Bioplastics with Tunable Mechanical Properties Using Glycerol or Hyperbranched Poly(glycerol)s as Plasticizers

This chapter was adapted from the following manuscript:

> Millik, S. C.; Sadaba, N.; Hilburg, S. L.; Sanchez-Rexach, E.; Zhang, M.; Yu, S.; Vass, A. F.; Pozzo, L. D.; Nelson, A. 3D-Printed Protein-Based Bioplastics with Tunable Mechanical Properties Using Glycerol or Hyperbranched Poly(glycerol)s as Plasticizers. *Submitted*, **2024**.

3.1. Abstract

Protein-based materials can be engineered to derive utility from the structures and functions of the incorporated proteins. Modern methods of protein engineering bring promise of unprecedented control over molecular and network design, which will enable new and improved functionalities in materials which incorporate proteins as functional building blocks. For these advantages to be fully realized, there is a need for robust methods for producing protein-based networks, as well as methods for tuning their mechanical properties. Light-based 3D printing techniques afford high-resolution fabrication capability with unparalleled design freedom in an inexpensive and decentralized capacity. This work features 3D printed serum albumin-based bioplastics with mechanical properties modulated through incorporation of glycerol or hyperbranched poly(glycerol)s (HPGs) as plasticizers. These materials capitalize upon important features of serum albumin, including its low intrinsic viscosity, high aqueous solubility, and relatively low cost. The incorporation of glycerol or HPGs of different sizes resulted in softer

and more ductile bioplastics than those obtained natively without additives. These bioplastics showed shape-memory behavior and could be used to fabricate functional objects. These materials are accessible, possess minimal chemical hazards, and can be used for fabricating rigid and strong as well as soft and ductile parts using inexpensive commercial 3D printers.

3.2. Introduction

Protein-based thermosets are an interesting class of material wherein natural or recombinant proteins are covalently incorporated into a polymeric network.[1,2] Such materials include water-filled networks (i.e., hydrogels)[3–5] and bulk polymer networks (e.g., plastics).[6,7] Protein-based materials may derive specific biological functionality[8–12] from the incorporated proteins as well as practical properties such as aqueous processability, chemical degradability, and recyclability.[13–18] Many protein-based materials are also generally biocompatible and have thus seen use in a myriad of bio-interfacing applications.[19–21] Additionally, modern protein engineering methods make it possible to design and synthesize protein-based materials with a level of control yet unattainable with methods of synthetic polymer chemistry.[22–25] This exquisite control over molecular and network design brings promise of future generations of materials with new and improved functionalities.

Additive manufacturing (3D printing) offers numerous advantages over traditional manufacturing techniques, including unparalleled design freedom,[26,27] rapid and low-cost prototyping, personalized manufacturing, and decentralized production capabilities.[28,29] Specifically, light-based 3D printing (i.e., stereolithography, digital light processing, and other vat photopolymerization techniques) uses projected light to selectively cure liquid resins into

solid objects. Light-based 3D printing offers superior resolution over material-deposition-based methods, as well as a high degree of flexibility in patternable materials.[30,31] Over the last decade, commercially available light-based 3D printers have become more capable and affordable. Today, a typical commercial light-based 3D printer can offer ≤ 100 μm resolution at a printing speed of up to ~ 6 cm of vertical build height per hour, in a small (e.g., 20 cm × 20 cm × 40 cm), light (e.g., 4 kg), and inexpensive (e.g., ≤ 300 USD) package.[32]

Despite advances in commercial 3D printing hardware and software, commercial materials for light-based 3D printing remain limited in both functionality and accessibility. Most resins available today are formulations of acrylate monomers fundamentally derived from petroleum feedstocks. Printing with these resins typically requires the use of organic wash solvents and chemical hazard controls, which may be inappropriate or inconvenient for non-expert or casual users. The printed materials derived from these resins are often rigid and brittle thermosets which are neither chemically degradable nor recyclable.[33–38] Thus, there is currently a need for more sustainable, user-friendly, and mechanically diverse materials for 3D printing. Protein-based materials could meet this need.

Protein-based materials that have been explored for 3D printing include those based on gelatin,[39–42] collagen,[43–46] fibrin,[47–49] keratin,[50–52] silk fibroin,[53–56] whey proteins,[57,58] soy proteins,[59,60] and serum albumin.[61–63] Fibrous proteins (e.g., gelatin, collagen, fibrin, keratin, and silk fibroin) typically possess elongated structures, associative chemical functionalities, and low aqueous solubilities.[64] In material applications, these characteristics manifest as high viscosities and high viscoelastic moduli at relatively low protein concentrations. Fibrous proteins thus lend themselves well to applications in extrusion-based 3D printing, where patterning is accomplished by deposition of viscoelastic liquids or gels.[65] Conversely, globular proteins (e.g., whey proteins,

soy proteins, ovalbumin, and serum albumin) typically possess higher aqueous solubilities and lower intrinsic viscosities; these properties enable high protein loading in aqueous solutions while maintaining low-viscosity liquid character.[61] Light-based 3D printing often requires the use of liquid resins with relatively low viscosities for reliable and high-quality fabrication.[66–68] High protein loading in resins is desirable in cases where solvent is to be removed post-printing to afford a finished part consisting of bulk polymer (i.e., "bioplastic") as opposed to a gel. Globular proteins, such as serum albumin, are thus particularly suitable for light-based 3D printing of bioplastics.

Sanchez-Rexach et al. have recently demonstrated light-based 3D printing with aqueous resins comprising bovine serum albumin (BSA) and poly(ethylene glycol) diacrylate (PEGDA).[62] The printed materials were semi-rigid bioplastics which showed moderate ductility. We propose that expanding the range of accessible 3D printed protein-based bioplastics to include stronger and more rigid, as well as softer and more ductile materials, would significantly expand the applicability of such materials.

Here, we report an accessible and mechanically tunable material platform for light-based 3D printing of protein-based bioplastics. We show that rigid and relatively strong bioplastics could be obtained natively, and increasing softness and ductility could be obtained with the inclusion of glycerol or hyperbranched poly(glycerol)s (HPGs) as plasticizing additives (Figure 3.1). We selected BSA as the protein component of our materials and PEGDA as a cross-linker (Figure 3.2a–e). BSA is advantageous as a component in aqueous resins for light-based 3D printing due to its availability, high aqueous solubility, and low intrinsic viscosity.[69,70] We chose to investigate HPGs and glycerol (Figure 3.3a) as additives to the BSA-PEGDA network due to their accessibility, miscibility with BSA and PEGDA, and their ability to afford resins with low

viscosities. Using inexpensive commercial 3D printers, we were able to produce mechanically diverse parts from our materials, including a clip with an integral (also known as “living”) hinge and catch. Finally, to showcase the versatility of this material platform, we demonstrate thermal shape-memory behavior of these bioplastics.

3.3. Materials and Methods

3.3.1. Materials

Bovine serum albumin (BSA; BSAS 1.0) was purchased from Bovogen Biologicals. Glycidol (G5809), calcium hydride (CaH_2; 21170), 1,4-dioxane (296309; anhydrous), N,N-dimethylformamide (DMF; 227056; anhydrous), 1,1,1-tris(hydroxymethyl)propane (TMP; 148083; 99.8%), potassium methoxide solution (CH_3OK; 60402; 25.1% in MeOH), Dowex 50WX8 hydrogen-form resin (44509), potassium hydride (KH; 215813; 32.1 wt% suspension in mineral oil), acetone (179124), lithium bromide (LiBr; 213225), methanol-d_4 (CD_3OD; 441384), deuterium oxide (D_2O; 435767), poly(ethylene glycol) diacrylate (PEGDA; M_n 700; 455008), Antifoam A concentrate (A5633), and tartrazine (T0388) were purchased from MilliporeSigma. Molecular sieves (MK449004; grade 564) were purchased from VWR International. Methanol (MeOH; A452-1), glycerol (G33-1), dimethyl phenylphosphonite (AAA1400614), ethyl acetate (EtOAc; E145-4), and phosphate-buffered saline 10X solution (PBS; BP399-1) were purchased from Fisher Scientific. Spectra/Por 6 dialysis tubing (132633, 132554; 2 kDa, 25 kDa MWCO) was purchased from Repligen. 2,4,6-trimethylbenzoyl chloride (T2470) was purchased from TCI America.

3.3.2. Instrumentation

Proton nuclear magnetic resonance (^{1}H NMR) spectra were obtained using a Bruker AVANCE series instrument with 500 MHz frequency. Dynamic light scattering (DLS) data were obtained with a Zetasizer Nano ZS using a quartz cuvette. Rheometry was performed using a TA Instruments Discovery Hybrid Rheometer-2. Steady-shear experiments were performed using a TA Instruments Advanced Peltier Plate system; aluminum 40 mm, 1° cone geometry; and solvent trap. Oscillatory photo-curing experiments were performed using a TA Instruments UV Light Guide Accessory with disposable acrylic plates, a Mightex 405 nm (5 mW cm^{-2}) light source, and stainless steel 20 mm parallel plate geometry. Circular dichroism (CD) spectra were obtained with a Jasco J-1500 CD spectrophotometer, using a quartz cuvette with 0.5 mm path length. For uniaxial tensile testing, a TestResources 100 Series Universal Test Machine with 1.1 kN and 44 N load cells and tensile grips was used. Thermogravimetric analysis (TGA) was performed using a TA Instruments Q5000 IR thermogravimetric analyzer, using aluminum cups. Differential scanning calorimetry (DSC) was performed using a TA Instruments Discovery DSC 2500, using Tzero hermetically sealed pans and lids. Small-angle X-ray scattering (SAXS) was measured on a Xenocs Xeuss 3.0 instrument with a copper radiation source. A PerkinElmer Frontier FTIR spectrometer equipped with a Universal ATR accessory was used to perform attenuated total reflectance Fourier-transform infrared (ATR-FTIR) spectroscopy. A QUANS 395–400 nm (15 mW cm^{-2}) LED light was used for photo-curing resins during casting. An Anycubic Photon Mono SE was used for 3D printing of all tensile specimens and the structures in Figure 3.4a,b. An Anycubic Photon Ultra was used for 3D printing of structures in Figure 3.4c–g.

3.3.3. Synthesis of Hyperbranched Poly(glycerol)s (HPGs)

3.3.3.1. Purification and Handling of Reagents

For all HPG syntheses, glycidol was dried over CaH_2 for 18 h, vacuum-distilled, and degassed by the freeze-pump-thaw method. Purified glycidol was stored at 5 °C until use. Anhydrous dioxane and DMF, once opened (i.e., stored with perforated seals), were dried over molecular sieves for 24 h and sparged with N_2 before use. Hygroscopic materials (i.e., TMP and HPG macroinitiator) were dried under vacuum prior to weighing. All other reagents were used as received and stored according to manufacturer recommendations, unless otherwise specified.

3.3.3.2. Synthesis of Small-Sized HPG (HPG-S)

The following procedure adapted from Kainthan et al. was used.[71] A 100 mL 2-neck round-bottom Schlenk flask was flame-dried under vacuum. TMP (0.610 g; 4.54 mmol) was added to the flask. MeOH (540 μL) was then added to the TMP in the flask, followed by CH_3OK solution (350 μL; 1.19 mmol; 25.1% in MeOH). All additions were performed under positive pressure of N_2. After the TMP had dissolved, the flask was briefly swirled to homogenize the mixture. Bulk MeOH in the mixture was evaporated with N_2 flow through a bleed needle (16 gauge). After the TMP mixture appeared solid, residual MeOH was removed under vacuum (~ 3 Pa) over 18 h at 21 °C. Note: the TMP was not heated under vacuum to avoid sublimation. Following removal of the MeOH, an oven-dried overhead stirrer assembly was attached to the

flask under positive pressure of N_2. The flask was pre-heated using an aluminum flask carrier at a nominal temperature of 105 °C. PTFE tubing (20 gauge) was then connected to flask through a septum under positive pressure of N_2, and using a syringe pump, glycidol (12 mL; 180 mmol) was added over 24 h, at 105 °C, under N_2, while stirring at ~ 200 rpm. Following completion of glycidol addition, the reaction was allowed to proceed for an additional 18 h under the same conditions. Monomer consumption was confirmed by ^{1}H NMR spectroscopy. The reaction mixture was then cooled, and MeOH (20 mL) was added to dissolve the product. Dowex 50WX8 hydrogen-form resin (~ 1 cc) was finally added to protonate the product. After 15 min, the Dowex resin was removed by centrifugation, and the product was precipitated in acetone. Precipitation in acetone was repeated once. The product was then dissolved in deionized H_2O to ~ 10–15 wt% and dialyzed (2 kDa MWCO) against deionized H_2O for 3 d at 21 °C. Following dialysis, the purified HPG in aqueous solution was filtered with a 0.45 μm polyethersulfone filter and stored at 5 °C until use. Purity was confirmed by ^{1}H NMR spectroscopy in CD_3OD, and appropriate size was confirmed by DLS, using deionized H_2O as the dispersant. Percent yield was ~ 70%. ^{1}H NMR (500 MHz, CD_3OD): δ = 3.90–3.50 (br; 1H, 2H; HPG-S), 1.40 (br, 2H, TMP core), 0.90 (br, 3H, TMP core).

3.3.3.3. Synthesis of Medium-Sized HPG (HPG-M)

The following procedure adapted from Kainthan et al. was used.[71] A 250 mL 2-neck round-bottom Schlenk flask was flame-dried under vacuum. TMP (0.450 g; 3.35 mmol) was added to the flask. MeOH (400 μL) was then added to the TMP in the flask, followed by CH_3OK solution (260 μL; 0.885 mmol; 25.1% in MeOH). All additions were performed under positive

pressure of N_2. After the TMP had dissolved, the flask was briefly swirled to homogenize the mixture. Bulk MeOH in the mixture was evaporated with N_2 flow through a bleed needle (16 gauge). After the TMP mixture appeared solid, residual MeOH was removed under vacuum (~ 3 Pa) over 18 h at 21 °C. Note: the TMP was not heated under vacuum to avoid sublimation. Following removal of the MeOH, an oven-dried overhead stirrer assembly was attached to the flask under positive pressure of N_2. Anhydrous dioxane (45 mL) was then charged to the flask. The flask was pre-heated using an aluminum flask carrier at a nominal temperature of 115 °C. PTFE tubing (20 gauge) was then connected to flask through a septum under positive pressure of N_2, and using a syringe pump, glycidol (45 mL; 674 mmol) was added over 24 h, at 115 °C, under N_2, while stirring at ~ 200 rpm. Following completion of glycidol addition, the reaction was allowed to proceed for an additional 24 h under the same conditions. Monomer consumption was confirmed by ^{1}H NMR spectroscopy. The reaction mixture was then cooled, bulk dioxane was aspirated, and MeOH (100 mL) was added to dissolve the product. Dowex 50WX8 hydrogen-form resin (~ 1 cc) was finally added to protonate the product. After 15 min, the Dowex resin was removed by centrifugation, and the product was precipitated in acetone. Precipitation in acetone was repeated once. The product was then dissolved in deionized H_2O to ~ 10–15 wt% and dialyzed (25 kDa MWCO) against deionized H_2O for 3 d at 21 °C. Following dialysis, the purified HPG in aqueous solution was filtered with a 0.45 μm polyethersulfone filter and stored at 5 °C until use. Purity was confirmed by ^{1}H NMR spectroscopy in CD_3OD, and appropriate size was confirmed by DLS, using deionized H_2O as the dispersant. Percent yield was ~ 80%. ^{1}H NMR (500 MHz, CD_3OD): δ = 3.94–3.53 (br; 1H, 2H; HPG-M).

3.3.3.4. Synthesis of Large-Sized HPG (HPG-L)

The following procedure adapted from Anilkumar et al. was used.[72] HPG-M, to be used as the macroinitiator, was first synthesized using a procedure similar to the one described above, albeit at a smaller scale. Briefly, the reaction was performed in 100 mL flask with an identical setup. A smaller quantity of TMP (0.121 g; 0.900 mmol) was used, with proportional quantities of CH_3OK solution (70 μL; 0.238 mmol; 25.1% in MeOH) and glycidol (12 mL; 180 mmol). Proportionally double the volume of anhydrous dioxane (24 mL) was used. Glycidol was added over 24 h at 95 °C. Following an additional 18 h under the same conditions, the reaction was worked up as described above with isolation of the product by precipitation and dialysis.

For the HPG-L reaction, a 100 mL 2-neck round-bottom Schlenk flask was flame-dried under vacuum. Lyophilized macroinitiator (0.6 g) was dissolved in MeOH (2 mL) and coated onto the bottom of the flask. A diaphragm pump was used to remove the bulk MeOH in the mixture while occasionally rotating the flask to facilitate coating of the bottom. After the mixture appeared solid, residual MeOH was removed under vacuum (~ 3 Pa) over 24 h at 120 °C nominal. Following removal of the MeOH, an oven-dried overhead stirrer assembly was attached to the flask under positive pressure of N_2. The flask was pre-heated using an aluminum flask carrier at a nominal temperature of 108 °C. Anhydrous DMF (8.2 mL) was then charged to the flask. KH suspension (~ 0.04 g; ~ 0.3 mmol; 32.1 wt% in mineral oil) was added under positive pressure of N_2. Note: care was taken to quickly homogenize the KH suspension by vigorous swirling and dispense immediately to avoid settling. The mixture was stirred at 108 °C for 30 min, then PTFE tubing (20 gauge) was connected to flask through a septum under positive pressure of N_2. Using a syringe pump, glycidol (12 mL; 180 mmol) was added over 24 h at 108 °C, under N_2, while stirring at ~ 200 rpm. Following completion of glycidol addition, the reaction was allowed to

proceed for an additional 12 h under the same conditions. Monomer consumption was confirmed by ^{1}H NMR spectroscopy. The reaction mixture was then cooled, and MeOH (20 mL) was added. Dowex 50WX8 hydrogen-form resin (~ 1 cc) was finally added to protonate the product. After 15 min, the Dowex resin was removed by centrifugation, and the product was precipitated in acetone. Precipitation in acetone was repeated once. The product was then dissolved in deionized H_2O to ~ 10–15 wt% and dialyzed (25 kDa MWCO) against deionized H_2O for 3 d at 21 °C. Following dialysis, the purified HPG in aqueous solution was filtered with a 0.45 μm polyethersulfone filter and stored at 5 °C until use. Purity was confirmed by ^{1}H NMR spectroscopy in CD_3OD, and appropriate size was confirmed by DLS, using deionized H_2O as the dispersant. Percent yield was ~ 40%. ^{1}H NMR (500 MHz, CD_3OD): δ = 3.94–3.52 (br; 1H, 2H; HPG-L).

3.3.4. Synthesis of Lithium Phenyl-2,4,6-Trimethylbenzoylphosphinate (LAP)

For all resins, lithium phenyl-2,4,6-trimethylbenzoylphosphinate (LAP) was used as the photoinitiator. LAP was synthesized as previously described by Fairbanks et al.[73] A 250 mL 2-neck round-bottom Schlenk flask containing a 25 mm PTFE-coated elliptical stir bar was flame-dried under vacuum. Dimethyl phenylphosphonite (3.0 mL; 19 mmol) was added to the flask, followed by 2,4,6-trimethylbenzoyl chloride (3.0 mL; 18 mmol), dropwise, under N_2. The mixture was shielded from ambient light and stirred at 120 rpm for 20 h, at 21 °C, under N_2. LiBr (6.2 g; 71 mmol) was then dissolved in EtOAc (100 mL), and the solution added to the reaction mixture. The reaction mixture was then stirred at 50 °C for ~ 15 min, then cooled to 21 °C. After 4 h at 21 °C, the crude product was filtered and washed with excess EtOAc. Bulk

EtOAc was evaporated in the filter by airflow, and residual EtOAc was removed under vacuum. LAP was stored in the dark at 5 °C until use. Purity was confirmed by ^{1}H NMR spectroscopy in D_2O. Percent yield was ~ 90%. ^{1}H NMR (500 MHz, D_2O): δ = 7.73 (m, 2H), 7.57 (m, 1H), 7.48 (m, 2H), 6.89 (s, 2H), 2.24 (s, 3H), 2.04 (s, 6H).

3.3.5. Formulation of Resins

Resins were formulated on a mass fraction basis. Total solute content was kept constant at 42 wt%, including constant 2 wt% LAP. Mass ratio of BSA to PEGDA was kept constant at 3:1. Resins were generally prepared as follows. Deionized water was first added to a vial or centrifuge tube, followed by glycerol or HPG solution, if applicable. Next, BSA was added as a lyophilized powder and dissolved by gentle shaking on an orbital shaker. PEGDA was then added and dissolved with shaking and gentle vortex-mixing, if necessary. The solution was then incubated at 21 °C with gentle shaking for 24 h. LAP was finally added as a fine powder and dissolved within ~ 1 h before use of the resin. The resin was shielded from light following the addition of LAP. Immediately before use, bubbles were removed from the resin by centrifuging at 3000 *g*. For example, to prepare 7 g of a resin with 5% glycerol, deionized water (4.06 g; 58 wt%) was first added, followed by glycerol (0.35 g; 5 wt%). BSA (1.84 g; 26.3 wt%) was then added and dissolved, followed by PEGDA (0.61 g; 8.7 wt%). After 24 h, LAP (0.14 g; 2 wt%) was finally added and dissolved to afford the ready-to-use resin.

3.3.6. Dynamic Light Scattering (DLS) Experiments

Resins for DLS experiments were prepared as described above. After incubation at 21 °C for 24 h, resins were diluted to a total solute content of 10 mg mL^{-1} using 1X phosphate-buffed saline. HPG samples were prepared at a concentration of 10 mg mL^{-1}, using deionized water as the dispersant. Samples were filtered with a 0.22 μm cellulose acetate syringe filter. DLS experiments were run at 25 °C, using a quartz cuvette. Experiments were conducted using 173° non-invasive back scatter configuration. Three measurements, consisting of 10 (10 s) runs each, were performed per sample and averaged.

3.3.7. Circular Dichroism (CD) Spectroscopy of Resins

Resins were prepared as described above. Each resin was diluted with deionized water to a theoretical BSA concentration of 0.25 mg mL^{-1}. A sample containing only BSA at a nominal concentration of 0.25 mg mL^{-1} in 1X PBS was included as a control. Samples were filtered with a 0.22 μm cellulose acetate syringe filter. CD experiments were run at 25 °C, using a quartz cuvette with 0.5 mm path length. Spectra were obtained using a digital integration time of 4 s, a scanning speed of 20 nm min^{-1}, an accumulation of 4 scans, and a bandwidth of 1 nm. The sample chamber was purged with N_2 gas for 15 minutes after loading each sample, prior to running each experiment. Background spectra for deionized water and 1X PBS were recorded and subtracted from the corresponding spectra for each material. Spectra were normalized using the area bounded by each curve.

3.3.8. Rheometry of Resins

Resins for rheometry were prepared as described above. Logarithmic shear rate sweeps in the range of 0.1–100 s^{-1} were performed at 25 °C to determine apparent viscosities of the resins. A 40 mm, 1° cone geometry was used for exact viscosity determination. The truncation gap was 26 μm. A solvent trap was used to prevent water evaporation form the resins. Three runs were performed per sample and averaged.

Oscillatory photo-curing experiments were performed using a 405 nm light source (5 mW cm^{-2}); the light was activated after 30 s from the start of data collection; fast data sampling was used. A 20 mm stainless steel parallel plate geometry with a disposable acrylic lower plate was used for photo-curing experiments; the shear gap was set to 600 μm. Photo-curing experiments were performed at ambient temperature. Three runs were performed per sample and averaged.

3.3.9. Uniaxial Tensile Testing of Bioplastics

For casting of tensile specimens, molds were fabricated by CNC machining the dimensions of the specimen into 25 mm × 75 mm × 5 mm sections of poly(ethylene) bar stock. Machined dimensions were scaled up by 36% from the ISO 527-2 Type 5B specimen values to account for isotropic shrinkage of the specimen during drying. Resins were pipetted into the molds using a positive displacement pipette. Microscope slides (25 mm × 75 mm) were slid onto the molds, and small binder clips were used to secure the slides. The covered molds were centrifuged at 500 *g* to clear potential small bubbles or debris from the gauge region. The resins were then cured for 30 min at ambient temperature under an LED light (395–400 nm; 15 mW cm^{-2}). Specimens were carefully removed from the molds and placed between two sheets of

stainless-steel wire mesh in a custom drying rack. The drying rack was placed in a vacuum oven, and specimens were dried under vacuum (~ 1.5 kPa) for 48 h at 21 °C. Dried specimens were stored in airtight containers until testing.

Uniaxial tensile testing was performed according to ISO 527, under ambient conditions (21 °C, ~ 30% relative humidity). A test speed of 5 mm min^{-1} was used. No extensometer was used; therefore, data are reported with respect to nominal strain. Eight specimens were fabricated for each material to be tested. Specimens exhibiting defects due to errors in casting or drying, such as bubbles, cracks, or substantial warping, were rejected. At least five specimens were tested for each material.

3.3.10. Thermal Analysis of Bioplastics

Thermogravimetric Analysis (TGA) was performed under N_2 atmosphere on 1 mm thick rectangular samples weighing ~ 8 mg. These samples were cast and dried as described above. A 10 °C min^{-1} ramp to 100 °C was performed, followed by a 30 min isothermal interval at 100 °C to remove moisture. Then, a 10 °C min^{-1} ramp to 500 °C was performed.

Differential scanning calorimetry (DSC) was performed on 1 mm thick rectangular samples weighing ~ 6 mg. These samples were cast and dried as described above. Modulated DSC was performed under N_2 atmosphere over a temperature range of −90 °C to 200 °C, at a heating rate of 3 °C min^{-1}, with a modulation temperature amplitude of 0.48 °C, and a modulation period of 60 s.

3.3.11. X-ray Scattering and Shape Recovery Experiments on Bioplastics

Samples for X-ray scattering experiments were fabricated by casting. To do so, resins were pipetted into 1.3 mm deep rectangular poly(styrene) molds. Microscope slides were slid onto the molds, and binder clips were used to secure the slides. The resins were then cured for 30 min at ambient temperature under an LED light (395–400 nm; 15 mW cm^{-2}). Cured samples were carefully removed from the molds and dried and processed as described above for fabrication of tensile specimens.

Strain was applied to rectangular bioplastics samples (8 mm × 24 mm × 1 mm) using a load frame, under ambient conditions, at a speed of 5 mm min^{-1}. Samples with no additive and HPG-M were strained to the approximate nominal strain at break values previously determined for each material during tensile testing; however, the samples did not visibly fracture in this case. The sample with glycerol could not be strained to its previously determined nominal strain at break value without failure at the grips. For the sample with glycerol, the maximum nominal strain that could be achieved without failure at the grips (250%) was used. Thermal recovery was performed using a heat gun with adjustable temperature set to a nominal temperature of 100 °C.

Three spots were tested and averaged for each sample. For each spot, scattering at sample-to-detector distances of 50, 370, 900, and 1800 mm were collected for counting times of 90, 180, 270, and 450 seconds, respectively, in line eraser mode for full 2-D data collection. 2-D data was reduced to 1-D with full azimuthal averaging and merged, subtracting background signal of the empty beam. Data processing was completed with the Xenocs XSACT software.

3.3.12. Fourier-Transform Infrared (FTIR) Spectroscopy of Bioplastics

Samples for ATR-FTIR experiments were fabricated as described above for X-ray scattering experiments. A spectral resolution of 4 cm^{-1} was used, and 32 scans were averaged over a range of 4000–1000 cm^{-1}. A background spectrum for deionized water was recorded and subtracted from spectra for each material. Spectra were normalized by setting ordinate value at 1650 cm^{-1} to 0.9 with zero at 1750 cm^{-1}.

3.3.13. 3D Printing

Resins were prepared as described above but with two additional components. Namely, 600 ppm tartrazine and 300 ppm Antifoam A were added to the resins ~ 1 h before printing. For example, to prepare 30 g of a resin with 15% glycerol, deionized water (17.19 g; 58 wt%) was first added, followed by glycerol (4.50 g; 15 wt%). BSA (5.63 g; 18.8 wt%) was then added and dissolved, followed by PEGDA (1.88 g; 6.27 wt%). After 24 h at 4 °C, LAP (0.60 g; 2 wt%), tartrazine (200 µL; 600 ppm; 10% in H_2O), and Antifoam A (20 µL; 300 ppm) were finally added and dissolved to afford the ready-to-use resin.

The following modifications were made to an Anycubic Photon Mono SE 3D printer before 3D printing with these materials. The factory aluminum build surface was sandblasted to improve print adhesion, and the fume-control fans were disabled by unplugging them from the controller board. The latter measure was taken to reduce evaporation from the aqueous resins during long prints. The following print settings for the Mono SE were used for all resins: layer thickness of 50 µm, normal exposure time of 13 s, bottom exposure time of 13 s, and off time of 1 s. All other settings were kept at their default values. The following modifications were made to an Anycubic Photon Ultra 3D printer before 3D printing with these materials. The factory

build plate was replaced with a smaller (55 mm × 55 mm) build plate machined from aluminum and sandblasted, and the volume of the factory resin tray was reduced to approximately 10 mL to accommodate the smaller build plate by casting silicone elastomer (SYLGARD 184) around a 3D printed mold of the desired volume. The following print settings for the Photon Ultra were used for all resins: layer thickness of 100 μm, normal exposure time of 8 s, bottom exposure time of 8 s, and off time of 1 s. All other settings were kept at their default values. A post-print photo-cure was not used in order to prevent warping (i.e., due to uneven drying during curing) of tensile specimens and other structures. Tensile specimens were dried and tested as described above. Other structures were dried in a similar manner.

3.3.14. Statistical Analysis

No statistical method was used to determine sample sizes. Data were reported as mean ± standard deviation. One-way ANOVA in conjunction with Tukey's HSD test was used to assess statistical significance in tensile testing.

3.4. Results and Discussion

3.4.1. Synthesis of Hyperbranched Poly(glycerol)s (HPGs)

HPGs are typically synthesized via ring-opening multibranching polymerization (ROMBP) of glycidol (Figure 3.3b).[74] It has been previously demonstrated that substoichiometric deprotonation of the initiator, trimethylolpropane (TMP), coupled with slow

addition of monomer (i.e., glycidol), improves control over molecular weights and dispersities of HPGs.[71,75] Further developments, namely, the use of a diluent and use of an HPG macroinitiator for a second ROMBP step, have made it possible to synthesize HPGs in molecular weights of a few kilodaltons to several megadaltons, which correspond to hydrodynamic diameters ranging from a few nanometers to nearly 50 nm.[71,72]

In order to explore the effects of HPG additives on mechanical properties of BSA- and PEGDA-based materials, we synthesized three HPGs of increasing size. Kainthan et al. reported that HPGs ranging from ~ 3 kDa to ~ 700 kDa could be synthesized via either neat reaction or via use of diglyme or dioxane as a diluent.[71] HPGs in the few-kilodalton range can reportedly be synthesized neat with good yields and good dispersities using substoichiometric deprotonation of TMP and slow addition of glycidol. We chose to use this approach for our small-sized HPG (HPG-S). For the medium-sized HPG (HPG-M), we chose to adapt a dioxane-mediated approach. Notably, neither TMP nor HPG are soluble in dioxane. However, dioxane is miscible with glycidol; dioxane thus acts a diluent for the monomer. Remarkably, the use of dioxane in this capacity affords HPGs of high molecular weights and with exceptionally low dispersities. It remains to be determined whether dilution or solvation of glycidol, or another interaction involving dioxane is the principal reason for the improved dispersities. Finally, for synthesis of a large-sized HPG (HPG-L), we used a method recently reported by Anilkumar et al. wherein an HPG synthesized by the dioxane-mediated approach is used as a macroinitiator, and ROMBP is repeated to further grow the HPG.[72]

3.4.2. Formulation of Resins with Glycerol or HPGs

The use of glycerol as a plasticizer has been explored previously for a number of bioplastics and aqueous-processable materials.[76–81] Glycerol has a high capacity for hydrogen bonding with water as well as with polar functional groups of biomacromolecules. These hydrogen-bonding interactions serve to retain water in the bulk material and otherwise increase chain mobility in networks via interactions with polymer chains.[77,82–84] HPGs are globular polymers with glycerol-derivative repeat units, a highly branched architecture, a polyether backbone, and numerous hydroxyl side chains and end groups (Figure 3.3b). Like BSA, HPGs are biocompatible, highly aqueous soluble, and possess low intrinsic viscosities.[72,74] Thus, to soften and plasticize these materials, glycerol, or a small-, medium-, or large-sized HPG—which we refer to as HPG-S, HPG-M, or HPG-L, respectively (Figure 3.3a)—was included in the resins as an additive in quantities up to 15 wt%. Throughout this article, the provided mass fractions for additives refer to the quantities in the resins as formulated.

The resins in this study were formulated for printing on low-cost, commercially available liquid crystal display (LCD) and digital light processing (DLP) 3D printers that use visible light. For this work, we modified the resins from the composition previously reported by Sanchez-Rexach et al.[62] to include lithium phenyl-2,4,6-trimethylbenzoylphosphinate (LAP) as the photo-initiator.[73] In this case, LAP was chosen over other visible-light photo-initiators primarily due to its stability in formulation, low-toxicity, and availability. In contrast to methacrylamide-modified BSA-based compositions previously reported by Smith et al.,[61,63] separate steps for chemical derivatization and isolation of the BSA species are not required for these BSA-PEGDA materials. To produce a usable resin, commercially available BSA was mixed with low-molecular-weight (700 g mol^{-1}) PEGDA in aqueous solution at a 3:1 mass ratio. The total solute content of the

resins was kept constant at 42 wt%, which included 2 wt% LAP. Upon mixing of BSA and PEGDA, the derivatization of BSA with PEGDA occurred via an *aza*-Michael addition of lysine ε-amino groups to acrylate chain ends of PEGDA (Figure 3.2b). Generally, 30–35 surface lysine residues on BSA are available for functionalization,[85] so a 3:1 BSA:PEGDA mass ratio affords approximately one PEGDA chain per available lysine residue. The consumption of the primary amino groups was previously confirmed by a trinitrobenzenesulfonic acid (TNBS) assay, and the generation of secondary amino groups was detected by Fourier-transform infrared (FTIR) spectroscopy.[62] We additionally performed dynamic light scattering (DLS) experiments on a 3:1 mixture of BSA and PEGDA after 24 h, and we observed an increase in Z-average hydrodynamic diameter from 8.4 nm (corresponding to BSA) to 16.2 nm (corresponding to BSA and PEGDA conjugates). In contrast, when hydroxyl-terminated PEG was substituted for PEGDA, the *aza*-Michael reaction was not possible, and a Z-average hydrodynamic diameter of 8.8 nm was observed (Figure 3.2f; Table 3.1). Incubation of these resins at 21 °C for 24 h before use produced resins that exhibited prompt curing under 405 nm irradiation (Figure 3.2g), which was suitable for 3D printing with our selected 3D printers. Far-ultraviolet circular dichroism (CD) spectroscopy of resins after incubation at 21 °C for 24 h showed retention of the characteristic α-helical secondary structure of BSA, albeit with modest changes relative to the buffered pure-BSA spectrum (Figure 3.5). These changes could be due to incubation in unbuffered solution, at high concentration, in the presence of additives, and/or due to some cross-linking of BSA via the Michael addition.

The HPGs we used for this work were synthesized via anionic ring-opening polymerization of glycidol using previously reported procedures.[71,72] We confirmed successful synthesis of all three HPGs by ^{1}H NMR spectroscopy (Figure 3.3c; Figure B1–B3). We used

DLS to confirm appropriate size of the HPGs, and for comparison to the size of BSA. For the HPG-S, HPG-M, and HPG-L, Z-average hydrodynamic diameters were measured to be 4.1 nm, 14.4 nm, and 44.9 nm, respectively. Dispersities by DLS were 0.23, 0.06, and 0.56, respectively (Figure 3.3d; Figure B4–B6). These hydrodynamic diameters showed good agreement with those in the literature.[71,72] Measured Z-average hydrodynamic diameters for commercially available lyophilized BSA preparations are often 8–9 nm, with dispersities of 0.10–0.15 (Table 3.1).

3.4.3. Rheometry of Resins

Glycerol, HPG-S, HPG-M, or HPG-L was included in the resins in quantities up to 15 wt%. Steady-shear rheometry was used to examine the effects of HPG incorporation on resin viscosity. Logarithmic shear rate sweeps in the range of 0.1–100 s^{-1} revealed apparent viscosities < 5 Pa s for all resin formulations tested (Figure 3.3e). These values are below the value (10 Pa s) often correlated with high quality and reliable light-based 3D printing.[61,66,67] Some of the resins showing low viscosities showed low-torque effects at low shear rates and could not be accurately analyzed at those shear rates. Over the tested shear rate ranges, nearly constant apparent viscosity (i.e., apparently Newtonian behavior) was observed for all resins, except the resin with 15 wt% HPG-L. For the resin with 15 wt% HPG-L, an apparent shear thinning was observed with an onset shear rate of 2.7 s^{-1}. As expected, the resin with 15 wt% glycerol showed the lowest viscosity among the resins with 42 wt% solute content, with an average apparent viscosity of 0.022 Pa s over the shear rate range of 1–100 s^{-1}. HPG-S at 15 wt% showed an average apparent viscosity of 0.073 Pa s. HPG-M at 15 wt% showed an average apparent viscosity of 0.38 Pa s. The resin with no additive (i.e., with 30 wt% BSA and 10 wt% PEGDA)

showed an average apparent viscosity of 0.62 Pa s. Finally, the resin with 15 wt% HPG-L showed an apparent zero-shear viscosity of 4.9 Pa s, which decreased to 2.8 Pa s at 100 s^{-1}. For comparison, a control resin with no additive, where the additive mass was replaced with water (i.e., 27 wt% solute, including 2% LAP) showed an average apparent viscosity of 0.011 Pa s.

Apparent viscosities of the resins increased with increasing hydrodynamic size of the additive. The apparent non-Newtonian behavior of the resin with 15 wt% HPG-L could be explained by intermolecular interactions or entanglements that dissociate under shear, which might occur between the large HPG-L molecules but may not occur to the same extent between the smaller and more uniform HPG-S and HPG-M.[72,86,87] Interestingly, the inclusion of 15 wt% HPG-M afforded a resin with lower viscosity than when the same mass was replaced with BSA and PEGDA (i.e., in the case of the resin with 30 wt% BSA and 10 wt% PEGDA). We hypothesize that derivatization with PEGDA and likely oligomerization of the BSA, via the Michael addition, results in increased chain entanglement and thus higher viscosities in resins with higher BSA and PEGDA content. Notably, in the resin without additive, an aliquot diluted to 1 wt% solute content showed Z-average hydrodynamic diameter of 16.2 nm (Figure 3.2f; Table 3.1). This is only slightly larger than the Z-average hydrodynamic diameter at 1 wt% for the HPG-M, i.e., 14.4 nm (Figure 3.3d; Figure B5). However, a dispersity of 0.06 for the HPG-M versus 0.21 for the BSA species indicates that this population of derivatized and oligomerized BSA is less uniform (Figure B5; Table 3.1). Additionally, morphologies of these BSA species would not necessarily be expected to be compact like those of HPGs,[87] and thus greater propensity for entanglements might be expected.

3.4.4. Mechanical Characterization of Bioplastics

We performed uniaxial tensile tests on specimens cast from BSA-PEGDA resins with 0 wt%, 5 wt%, 10 wt%, and 15 wt% glycerol or HPG-M (Figure 3.6a,b). Bioplastics cast from resins with 15 wt% HPG-S and 15 wt% HPG-L were also tested (Figure 3.6c). For the sets of samples with increasing mass fraction (i.e., 0–15 wt%) of glycerol or HPG-M, we observed approximately linear decreases in elastic modulus and yield stress (Figure 3.7a,b). The resin with no additive (i.e., with 30 wt% BSA and 10 wt% PEGDA) produced a bioplastic with a tensile elastic modulus of 1.02 GPa. Inclusion of 15 wt% HPG-M resulted in decrease of the elastic modulus to 296 MPa. Inclusion of 15 wt% glycerol, in comparison, resulted in a further decrease to 29.1 MPa (Figure 3.8a, Table B3). For all materials, except the 15 wt% glycerol material, stress-strain curves showed a characteristic signature of necking, with a local maximum at the yield transition (Figure 3.6).[88] For these materials, this local maximum value of stress was taken as the yield stress. For the 15 wt% glycerol material, yield stress was determined as the plateau stress value immediately following the apparent yield transition. Tensile yield stress for the resin with no additive was 50.0 MPa. The yield stress decreased to 15.1 MPa and 1.8 MPa for the 15 wt% HPG-M and 15 wt% glycerol materials, respectively (Figure 3.8b; Table B3). Overall, when 15 wt% HPG-M was included, both elastic modulus and yield stress showed a 70% decrease relative to the material with no additive. When 15 wt% glycerol was included in the resin, both elastic modulus and yield stress showed a 97% decrease relative to the material with no additive. Indeed, these results indicate that, on a mass basis, glycerol was more potent in reducing elastic modulus and yield stress than HPG-M.

Substitution of some proportion of the covalent network with glycerol or HPG (i.e., relative to the bioplastic with no additive) expectedly had the effects of softening the materials

and reducing the stresses at which permanent deformation occurs. Cross-link densities in these networks are expected to be reduced when glycerol or HPGs are included, as these species do not participate in covalent cross-linking between the polymerizable constituents of the networks (i.e., BSA and PEGDA). Furthermore, force required for displacement of the macromolecular species within these materials is likely to be reduced due to interactions involving glycerol or HPGs. The greater potency of glycerol in plasticizing and softening these bioplastics could be attributed to the smaller size of these molecules and thus a greater extent of possible intermolecular interactions (per unit mass) with the network components, relative to HPG. Analysis by differential scanning calorimetry (DSC) revealed that the 15 wt% glycerol material maintained a single glass transition temperature (T_g) at 45.9 °C (Figure 3.9; Table 3.2), which is indicative of miscibility of glycerol with the network components. In contrast, DSC analysis of the 15 wt% HPG-M material showed two distinct transitions: one at −31.4 °C, corresponding to the T_g for PEGDA and HPG-M, and the other at 60.9 °C, corresponding to the denaturation temperature of BSA (Figure 3.9; Table 3.2). This result suggests that there are two phases present within the 15 wt% HPG-M material: a polymer-rich phase and a BSA-rich phase. Taken together, these results suggest that the glycerol molecules co-locate with PEG chains as well as BSA, whereas the larger HPG molecules do not.

Small-angle X-ray scattering (SAXS) performed on the bioplastics further suggests that glycerol more uniformly permeates the network. A feature at approximately Q = 0.11 $Å^{-1}$ for the material with no additive is attributed to BSA ordering within the bioplastic. While this feature was also observed for the 15 wt% HPG-M material, it was absent for the 15 wt% glycerol material (Figure 3.10). The absence of this feature suggests that BSA-BSA correlations are disrupted as a result of glycerol integration. At low-Q range, approximately Q = 0.003 $Å^{-1}$

through 0.01 $Å^{-1}$, data for each of the materials has a steep upturn consistent with large-scale domains and/or aggregation (Figure 3.10). Though each material exhibits this feature, the higher relative change in intensity for the material with HPG-M, compared to the material with glycerol, further supports that the glycerol-containing material is likely a more homogeneous system.

For the sets of specimens with increasing mass fraction of glycerol or HPG-M, we additionally found that strain at break increased with an approximately linear trend with increasing additive content (Figure 3.7c). Values of strain at break between specimens varied substantially more than those of elastic modulus and yield stress (Figure 3.8a–c). Glycerol was again more potent in increasing strain at break than the HPG, likely due to the increased potential for interactions between glycerol and the network components. The resin with no additive produced a bioplastic with a tensile strain at break of 49.5%. With the inclusion of 15 wt% HPG-M, the strain at break increased to 113%. With inclusion of 15 wt% glycerol, strain at break increased to 358% (Figure 3.8c; Table B3). Tensile toughness (i.e., the energy of tensile deformation until break) was determined as the area under the stress-strain curve until break. The toughness value for the bioplastic with no additive was 19.0 MJ m^{-3}. With glycerol incorporation, toughness initially increased to 29.7 MJ m^{-3} at 5 wt% and then decreased, with increasing glycerol content, to 9.0 MJ m^{-3} at 15 wt% (Figure 3.7d; Table B1). When HPG-M was included, differences in mean toughness values for increasing mass fraction were not statistically significant. The toughness value for the 15 wt% HPG-M material was 14.0 MJ cm^{-3} (Table S4).

The inclusion of 15 wt% HPG-L produced similar results to those of HPG-M, with values of elastic modulus and yield stress virtually identical to those of the bioplastic with HPG-M (Figure 3.6c; Figure 3.8a,b). Relative to the values for the 15 wt% HPG-M material, the 15 wt% HPG-L material showed slightly reduced mean strain at break and mean toughness, at 92% and

13.1 MJ cm^{-3}, respectively (Figure 3.8c,d); however, these differences were not statistically significant. The 15 wt% HPG-L material also showed a smaller reduction in tensile stress post-yield relative to the material with HPG-M (Figure 3.6c). This might be explained by more persistent intermolecular interactions or entanglements between the larger and less uniform HPG-L molecules, post-yield, when compared to HPG-M. Finally, the 15 wt% HPG-S material showed an intermediate mean strain at break between those of the other HPG-containing materials and that of the material containing glycerol, at 233% (Figure 3.6c; Figure 3.8c). Elastic modulus and yield stress values for the 15 wt% HPG-S material tended closer to those of the materials containing the other HPGs, at 248 MPa and 11.6 MPa, respectively, affording a material with higher mean toughness at 19.8 MJ m^{-3} (Fig 3.8a,b,d; Table B3).

3.4.5. 3D Printing

An inexpensive and commercially available LCD 3D printer (Anycubic Photon Mono SE) or DLP 3D printer (Anycubic Photon Ultra) was used for 3D printing. For practical purposes, print settings were not varied between resins. In order to prevent over-curing and improve resolution, 600 ppm tartrazine was added to the resins as a photoabsorber. To demonstrate 3D printability of these plasticized resins, a block "W" and a gecko model[89] were 3D printed with 15 wt% HPG-M and 15 wt% glycerol resins, respectively (Figure 3.4a,b). Generally, resins with lower viscosities appeared to produce prints of higher quality, particularly when printing with the LCD printer. Accordingly, the resin with 15 wt% glycerol showed slightly better structural fidelity than the resin with 15 wt% HPG-M (Figure 3.4a,b).

Determination of tensile properties and their comparison between formulations were performed initially with cast specimens because when casting, it was possible to test all specimens after equal radiant exposure sufficient to cure all formulations without deviation from the specified tensile specimen dimensions. Specimens that were 3D printed using 0 wt% and 15 wt% glycerol or HPG-M were tested for comparison to the cast specimens (Figure 3.6d). Tensile specimens that were 3D printed were dried, stored, and tested identically to their cast counterparts. The 3D printed bioplastic with no additive showed an elastic modulus of 852 MPa, a yield stress of 40.1 MPa, a strain at break of 51.8%, and a toughness of 15.4 MJ cm^{-3} (Figure 3.11; Table B4). Relative to the cast counterparts, these values account for 16.4%, 19.8%, and 18.9% decreases in elastic modulus, yield stress, and toughness, respectively, and a 4.8% increase in strain at break. When 15 wt% glycerol was included in the resin, the 3D printed bioplastic showed an elastic modulus of 17.4 MPa, a yield stress of 1.4 MPa, a strain at break of 427%, and a toughness of 6.8 MJ cm^{-3} (Figure 3.11; Table B4). Relative to the cast counterparts, these values account for 40.3%, 19.8%, and 24.4% decreases in elastic modulus, yield stress, and toughness, respectively, and a 19.1% increase in strain at break. When 15 wt% HPG-M was included, the 3D printed bioplastic showed an elastic modulus of 200 MPa, a yield stress of 10.1 MPa, a strain at break of 163%, and a toughness of 12.1 MJ cm^{-3} (Figure 3.11; Table B4). Relative to the cast counterparts, these values account for 32.6%, 35.9%, and 13.6% decreases in elastic modulus, yield stress, and toughness, respectively, and a 44.0% increase in strain at break. In summary, 3D printed samples showed decreased mean values of elastic modulus and yield stress and increased mean values of strain at break relative to cast samples. These differences are likely due to differences in the extent of curing between the different fabrication methods. These differences resulted in lower mean values of toughness for specimens 3D printed on this printer

with these settings, relative to cast specimens; however, differences in toughness between the specimens fabricated by the different methods were not statistically significant.

The moisture content of the bioplastics was important in determining tensile properties. We observed that otherwise identical material compositions would exhibit different mechanical properties if the materials were not dried to the same extent. To address this source of potential variability, special attention was paid to how tensile specimens were dried and stored, and internal control specimens were used to ensure batches of tensile specimens were prepared consistently. We performed thermogravimetric analysis (TGA) to determine the moisture content of a subset of formulations. The bioplastic with no additive showed a moisture content of 2.4 wt%. When 15 wt% glycerol was included in the resin, the moisture content of the resulting bioplastic increased to 4.1 wt%. When 15 wt% HPG-M was included, the moisture content increased only to 2.8 wt% (Figure 3.12). This data suggests that inclusion of glycerol produces a more hygroscopic or hydrophilic material, and this difference in water content likely plays a role in determining mechanical properties of these bioplastics.[77] Notably, the material with the HPG showed greater thermal stability on a mass-loss basis than the material with glycerol.

3.4.6. Functional Bioplastic Parts and Shape Memory

To demonstrate the practical functionality of these plasticized BSA-PEGDA-based bioplastics, we 3D printed a dialysis clip featuring two important structural features: (1) an integral hinge, and (2) an integral catch (Figure 3.4c,d). An integral hinge is made from the same material as the components it connects; it should be capable of deforming without rupture during multiple cycles of opening and closing.[90] The integral catch needs to be rigid to keep the clip securely

closed, but it should also be capable of elastic deformation. Thus, we hypothesized that the clip would require a rigid yet durable material and opted for the resin with 10 wt% glycerol, which provided a suitable balance of rigidity and durability. We were able to clip and unclip 1000 times without mechanical failure.

Finally, these materials exhibited shape-memory behavior in a manner similar to that previously reported for BSA-PEGDA bioplastics.[62,91] These materials can be shape-programmed when heated, and they maintain their programmed shapes under ambient conditions. After programming, the original shape can be recovered upon heating again. This shape-memory behavior is attributed in part to the unfolding of the BSA within the network during the shape-programming step.[91] The PEGDA cross-links facilitate the shape recovery, and we hypothesize that the unfolded BSA in the network could also regain a non-native globular form during shape recovery. To demonstrate the shape-memory behavior of these materials, we 3D printed a strip of material in a "W" shape using the resin with 15 wt% glycerol (Fig. 3.4e). For the shape-programming of the printed structure, we sandwiched the strip between glass slides to straighten it and heated it to 50 °C, we then allowed it to cool in this position to 21 °C (Figure 3.4f). The straight shape could be retained under ambient conditions (21 °C) indefinitely. However, upon heating the programmed construct at 100 °C, we observed virtually complete recovery of the original "W" shape within two minutes (Figure 3.4g).

In general, the networks with glycerol or HPGs recovered their original shapes faster when heated at the same temperature. For example, the samples with no additive recovered their shapes after 5 min of heating at 100 °C. When 15 wt% HPG-M was included, shape recovery was achieved ~ 60 s at 100 °C, and recovery was even faster (~ 10 s) when 15 wt% glycerol was used. We have previously reported that prolonged periods of heating for shape recovery alter the

mechanical properties of BSA-PEGDA networks (i.e., including stiffening of these materials).[91] These changes were attributed to denaturation of the BSA during extended thermal treatment above its T_g.[91] Our SAXS data in the present work confirm changes to the network microstructure after heating. This is evidenced by the increase in intensity at approximately Q = 0.05 $Å^{-1}$ (corresponding to on the order of 10 nm in real space) attributed to the presence of denatured and/or aggregated BSA (Figure 3.13). Likewise, we observed that extended heating (5 min) of bioplastics with glycerol or HPG-M resulted in a significant shift in this mid-Q regime. In contrast, shorter recovery times of 60 s with HPG-M or 10 s with glycerol showed considerably reduced changes to the scattering signals (Figure 3.13).

3.5. Conclusion

As macromolecules with precisely defined structures and exquisite functionality, proteins are advantageous building blocks for functional polymeric materials. With this work, we have described a platform where BSA was incorporated into thermoset networks via an accessible visible-light-based 3D printing method. The mechanical properties of these bioplastics could be tuned by adding glycerol or HPGs of varying sizes as plasticizers. Inclusion of these additives in aqueous resins allowed modulation of the tensile properties of the bioplastics over a wide range. In fact, this platform includes the strongest and stiffest (50 MPa yield stress; 1.0 GPa elastic modulus), as well as the softest and most ductile (29 MPa elastic modulus; 360% strain at break), bioplastics we have reported to date. These materials depart from the rigid and often brittle thermoset profile that predominates the current market (Figure 3.14; Table B5). In addition to their mechanical versatility, these materials are easily accessible in that they require little

synthetic effort to produce, especially if glycerol is used as the plasticizer. These aqueous resins are 3D printable on inexpensive commercial light-based 3D printers, are expected to present minimal chemical hazards, and are water washable. Finally, an interesting feature of these bioplastics is that they show thermal shape-memory behavior, with plasticized materials showing more rapid shape recovery. Having shown in this work that HPGs are physically well-suited for incorporation into resins for light-based 3D printing (i.e., due to their facile syntheses, high solubilities, and low intrinsic viscosities), future work will be aimed at further exploration of HPG-based materials for light-based 3D printing.

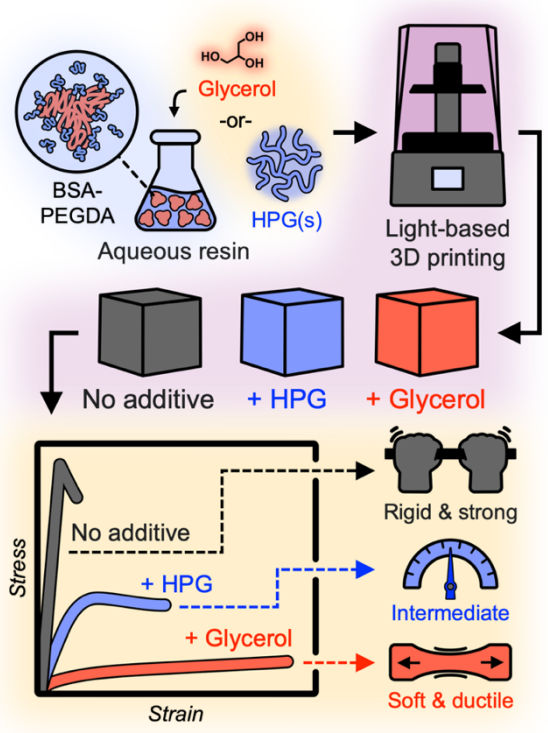

Figure 3.1. Incorporation of glycerol or HPGs as plasticizing additives into BSA-PEGDA-based aqueous resins for light-based 3D printing affords bioplastics with mechanical properties which vary from rigid and strong (obtained natively) to soft and ductile (obtained with plasticizers).

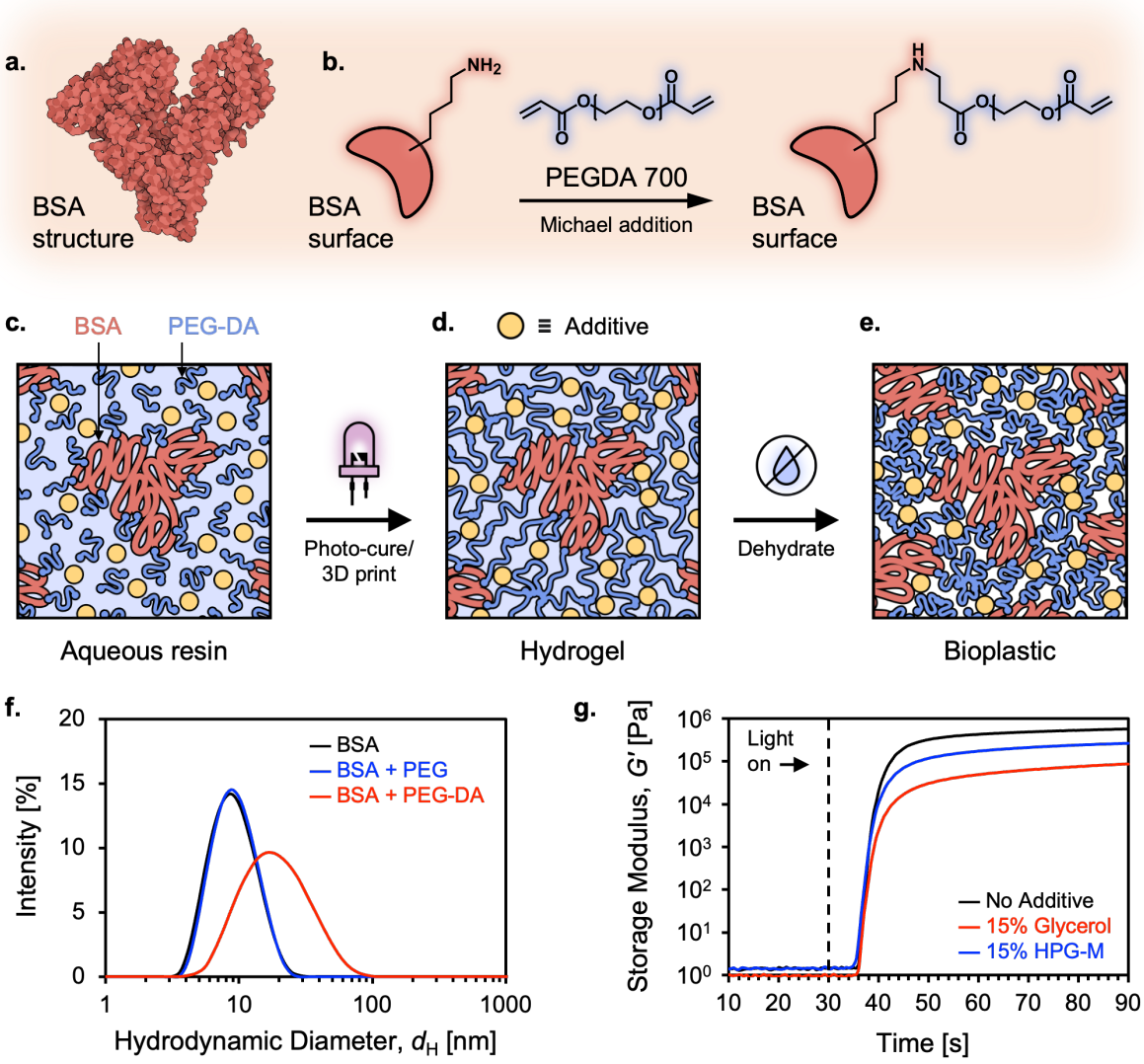

Figure 3.2. (a) BSA cartoon from crystal structure (PDB ID: 3V03).[92–94] (b) Scheme for derivatization of BSA with PEGDA via *aza*-Michael addition. (c) Hypothetical depiction of the aqueous resin state with soluble BSA (red) derivatized with PEGDA (blue), excess soluble PEGDA (blue), and a generic soluble additive (yellow). (d) Depiction of the hydrogel state with copolymerized BSA and PEG-DA following photo-curing of the resin. (e) Depiction of the bioplastic state following dehydration of the hydrogel. (f) Dynamic light scattering traces showing that Michael addition over 24 h incubation of the resin produces BSA-PEGDA conjugate species of increased size. (g) Photo-rheometry showing prompt curing of resins with and without additives at 405 nm (5 mW cm^{-2}) following 24 h incubation.

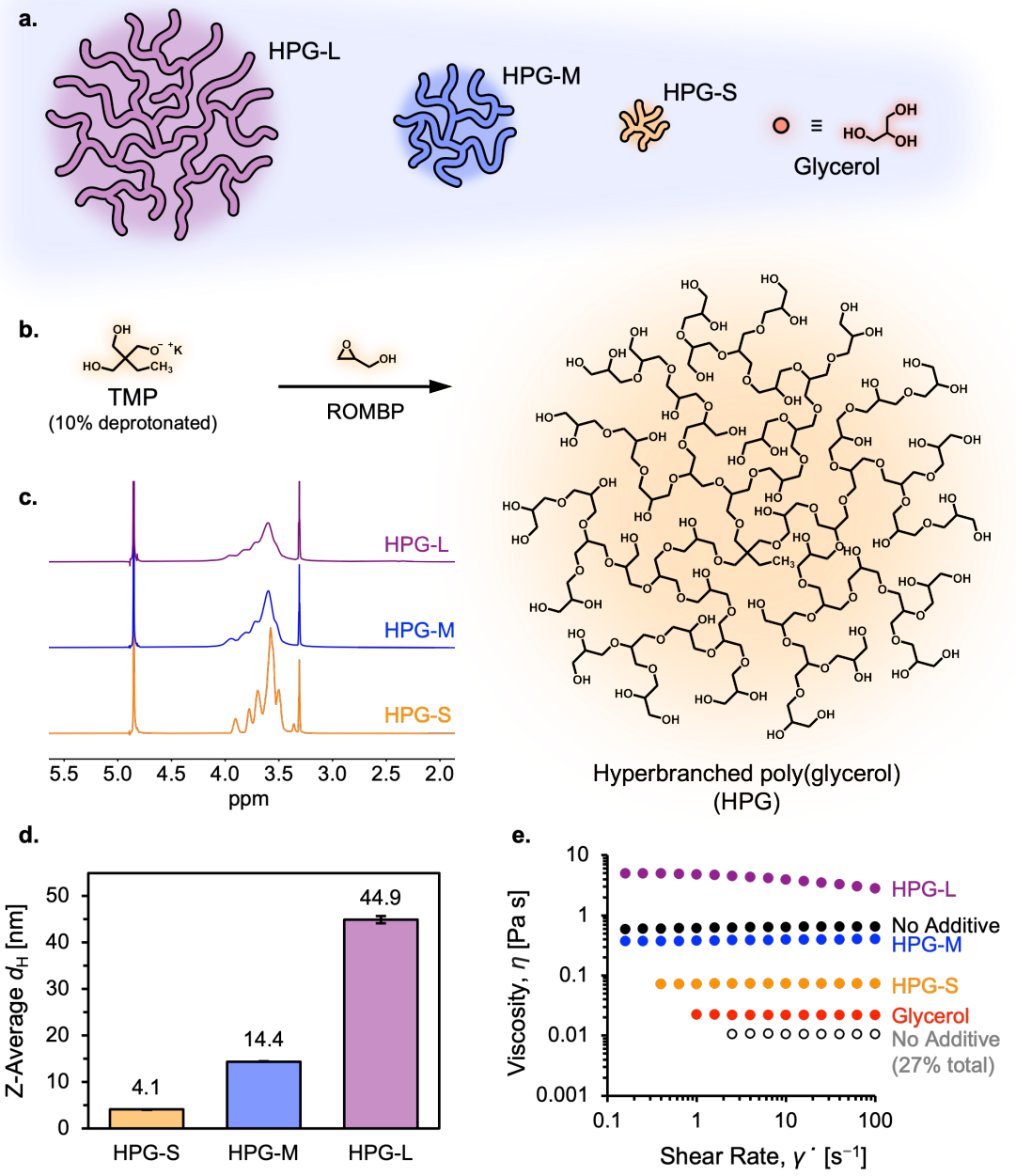

Figure 3.3. (a) Additives explored include large-, medium-, and small-sized HPGs (HPG-L, HPG-M, and HPG-S, respectively), and glycerol. (b) Scheme of HPG synthesis via ring-opening multibranching polymerization. (c) ^{1}H NMR spectra of HPG-S, HPG-M, and HPG-L in methanol-d_4. (d) Hydrodynamic diameters of HPG-S, HPG-M, and HPG-L, determined by dynamic light scattering. (e) Apparent steady-shear viscosities of aqueous resins with different additives included at 15 wt%.

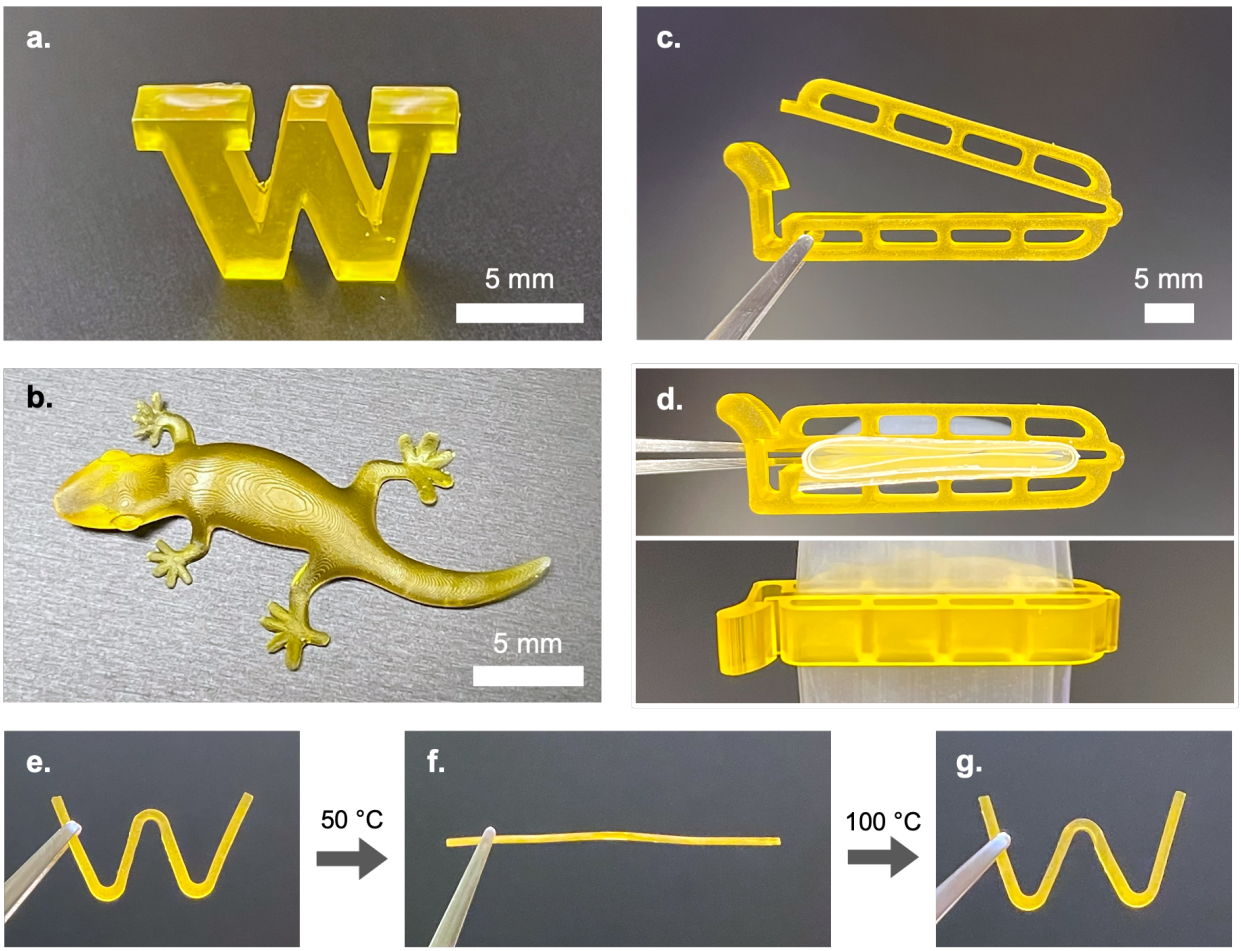

Figure 3.4. 3D printed objects, demonstrating 3D printability and functionality of BSA- and PEG-DA-based bioplastics with additives. (a) Block "W" printed using the resin with 15 wt% HPG-M. (b) Gecko model[89] printed using the resin with 15 wt% glycerol. (c) Dialysis clip, with integral catch and hinge, printed using a resin with 10 wt% glycerol. (d) Dialysis clip clipped onto a folded poly(ethylene) bag. (e) 3D printed "W" as printed with the 15 wt% glycerol resin and dehydrated. (f) "W" after heating at 50 °C, flattening between glass slides, and cooling to 21 °C. (g) "W" after recovery at 100 °C in < 2 min.

Table 3.1. Size and dispersity data for BSA (incubated at 30 wt%), BSA + PEG (incubated at 30 wt% +10 wt%, respectively), and BSA + PEG-DA (incubated at 30 wt% + 10 wt%, respectively).

Sample	Z-Average d_H [nm]	PDI
BSA	8.37 ± 0.07	0.135 ± 0.012
BSA + PEG	8.78 ± 0.04	0.158 ± 0.006
BSA + PEG-DA	16.24 ± 0.04	0.213 ± 0.003

Values reported as mean ± SD

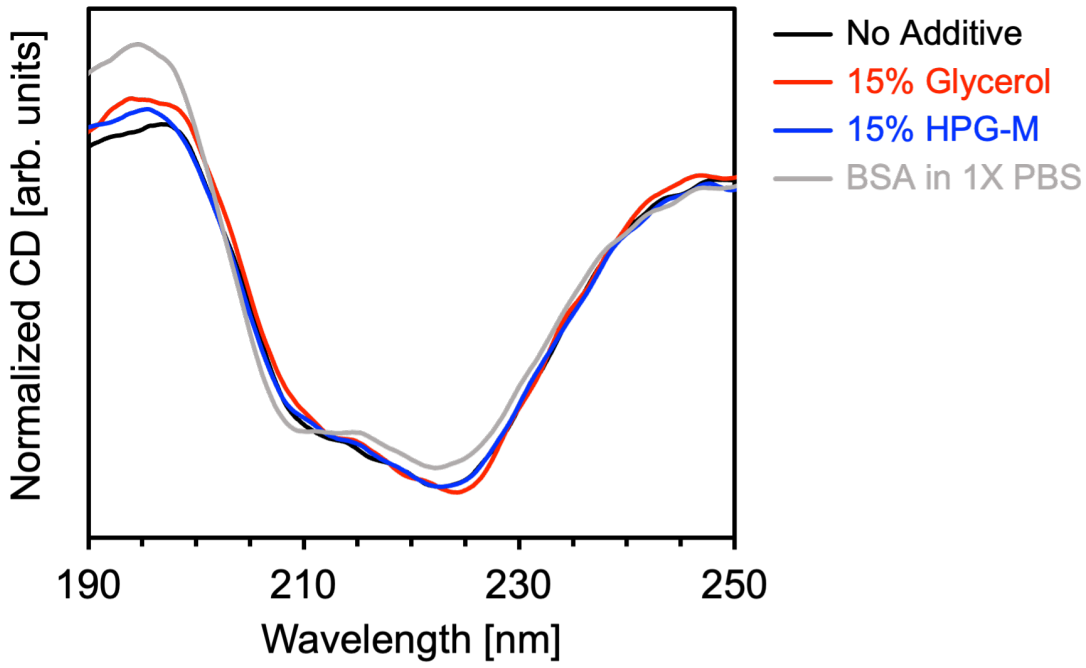

Figure 3.5. CD spectra of resins diluted to 0.25 mg mL^{-1} protein concentration with deionized water.

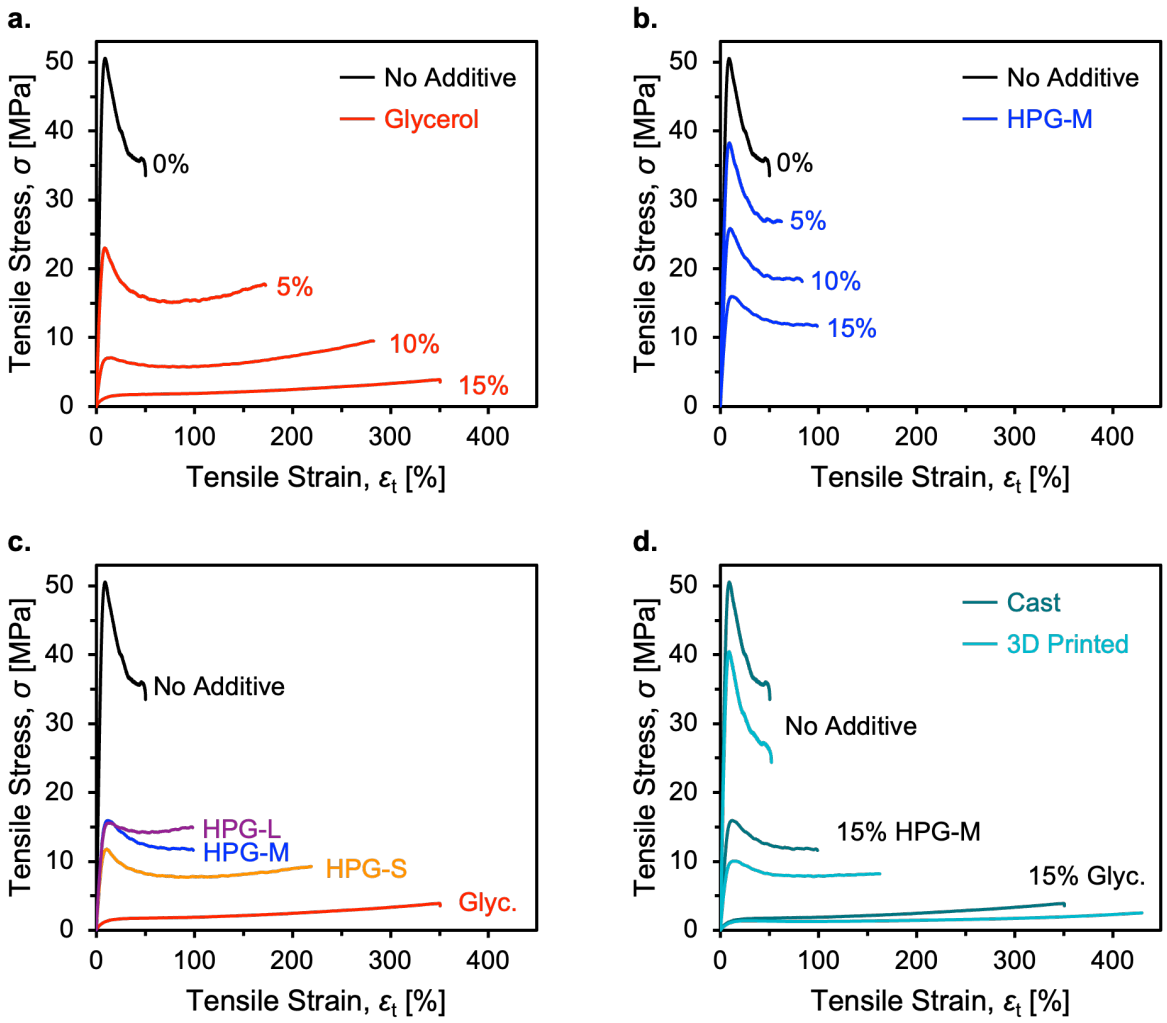

Figure 3.6. Representative tensile stress-strain curves of bioplastics with no additive and bioplastics with glycerol, HPG-S, HPG-M, and HPG-L included as additives. (a) Tensile stress-strain curves of cast bioplastics with increasing glycerol content (0–15 wt% in the resins). (b) Tensile stress-strain curves of cast bioplastics with increasing HPG-M content (0–15 wt% in the resins). (c) Tensile stress-strain curves of cast bioplastics with no additive and bioplastics with glycerol, HPG-S, HPG-M, and HPG-L included at 15 wt% in the resins. (d) Tensile stress-strain curves comparing cast and 3D printed bioplastics with no additive, and bioplastics with HPG-M and glycerol included at 15 wt%.

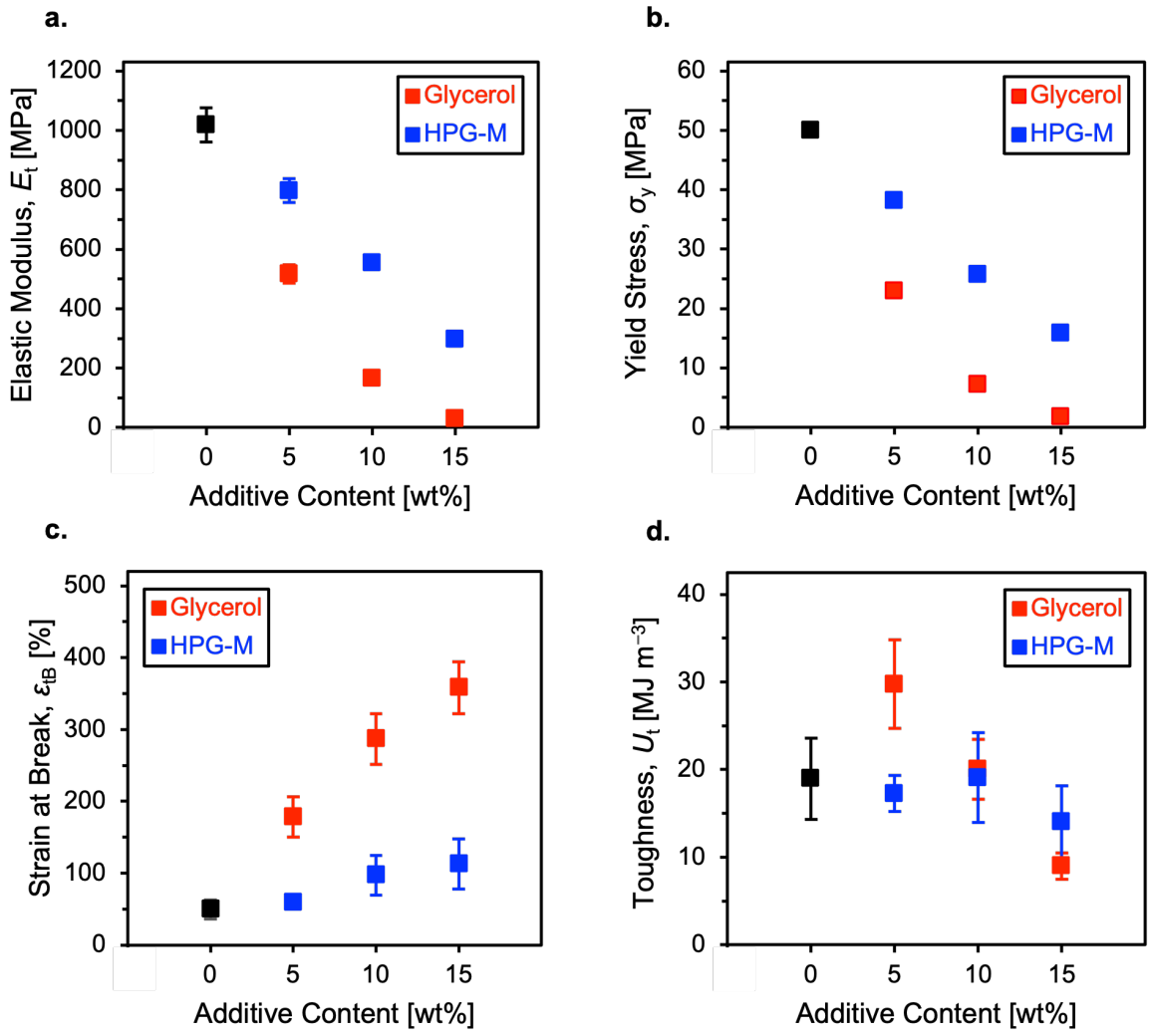

Figure 3.7. Tensile properties of cast bioplastics with increasing glycerol and HPG-M content. (a) Elastic modulus values with respect to additive content. (b) Yield stress values with respect to additive content. (c) Strain at break values with respect to additive content. (d) Toughness values with respect to additive content.

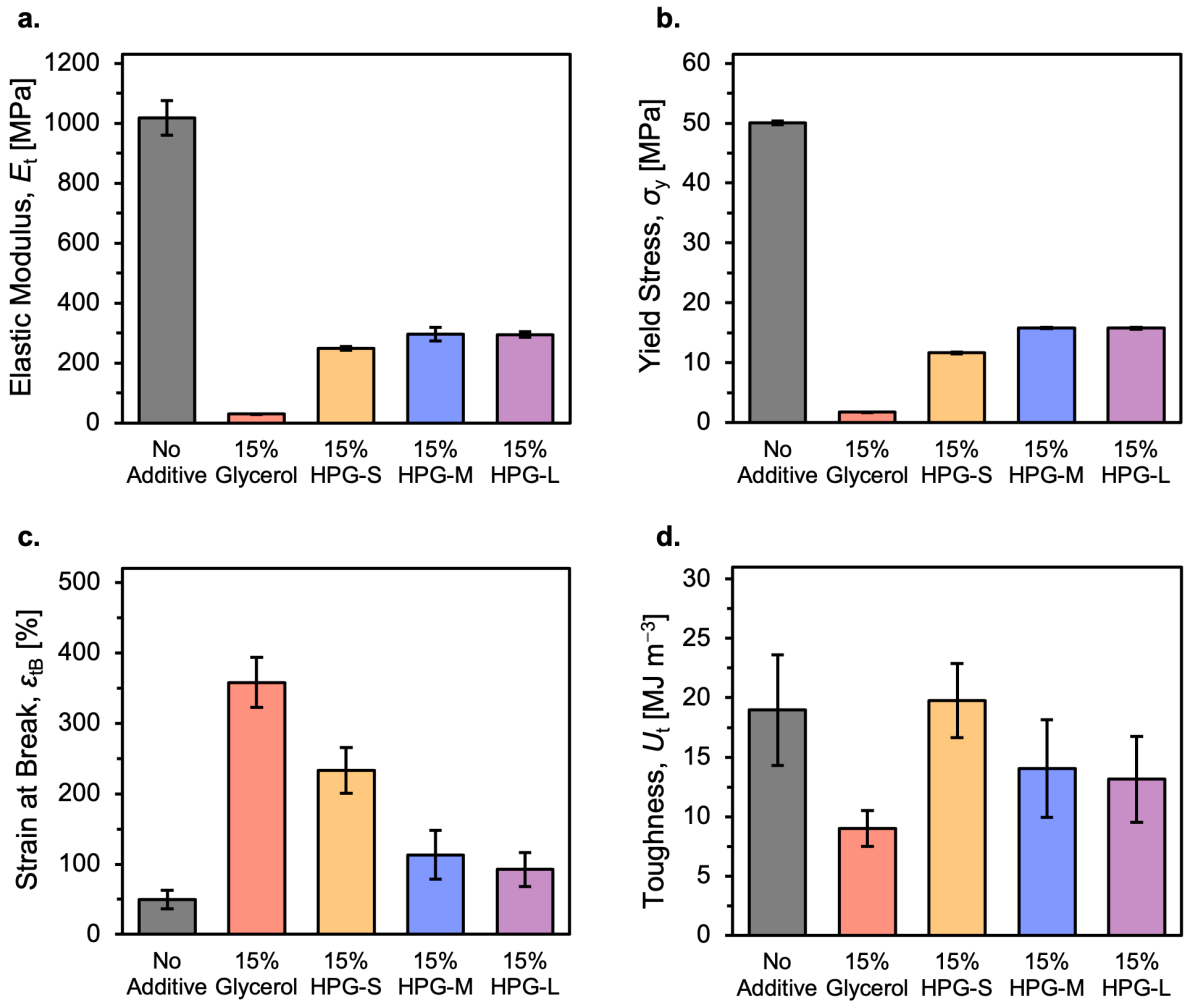

Figure 3.8. Tensile properties of cast bioplastics with no additive and bioplastics with glycerol, HPG-S, HPG-M, and HPG-L included at 15 wt% in the resins. (a) Elastic modulus values with respect to additive at 15 wt%. (b) Yield stress values with respect to additive at 15 wt%. (c) Strain at break values with respect to additive at 15 wt%. (d) Toughness values with respect to additive at 15 wt%.

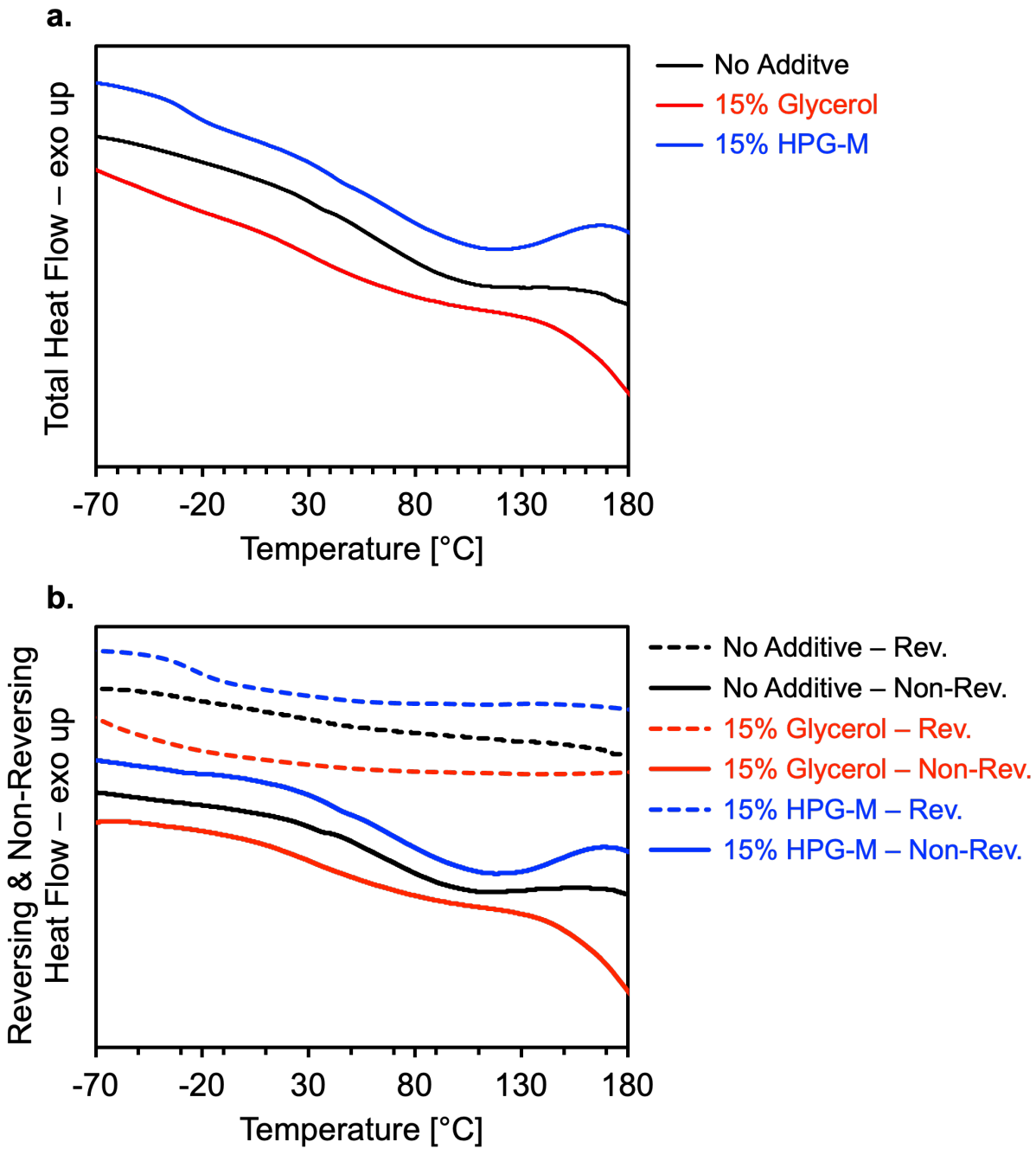

Figure 3.9. Modulated DSC of bioplastics (a) Total heat flow curves. (b) Reversing and non-reversing heat flow curves.

Table 3.2. T_g values from DSC analysis of bioplastics.

Material	$T_{g,1}$ [°C]	$T_{g,2}$ [°C]
No Additive	50.1	–
15% Glycerol	45.9	–
15% HPG-M	−31.4	60.9

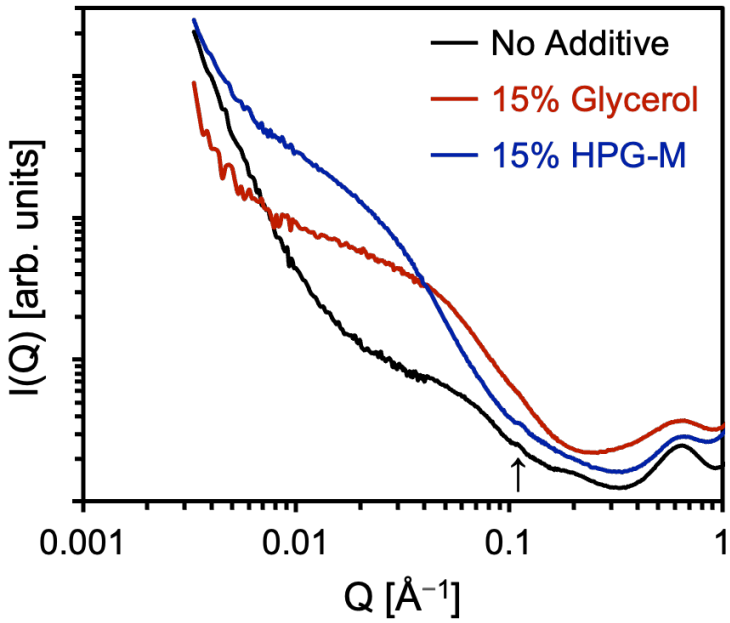

Figure 3.10. X-ray scattering analysis of as-fabricated bioplastics with different additives. Arrow indicates features likely related to BSA ordering.

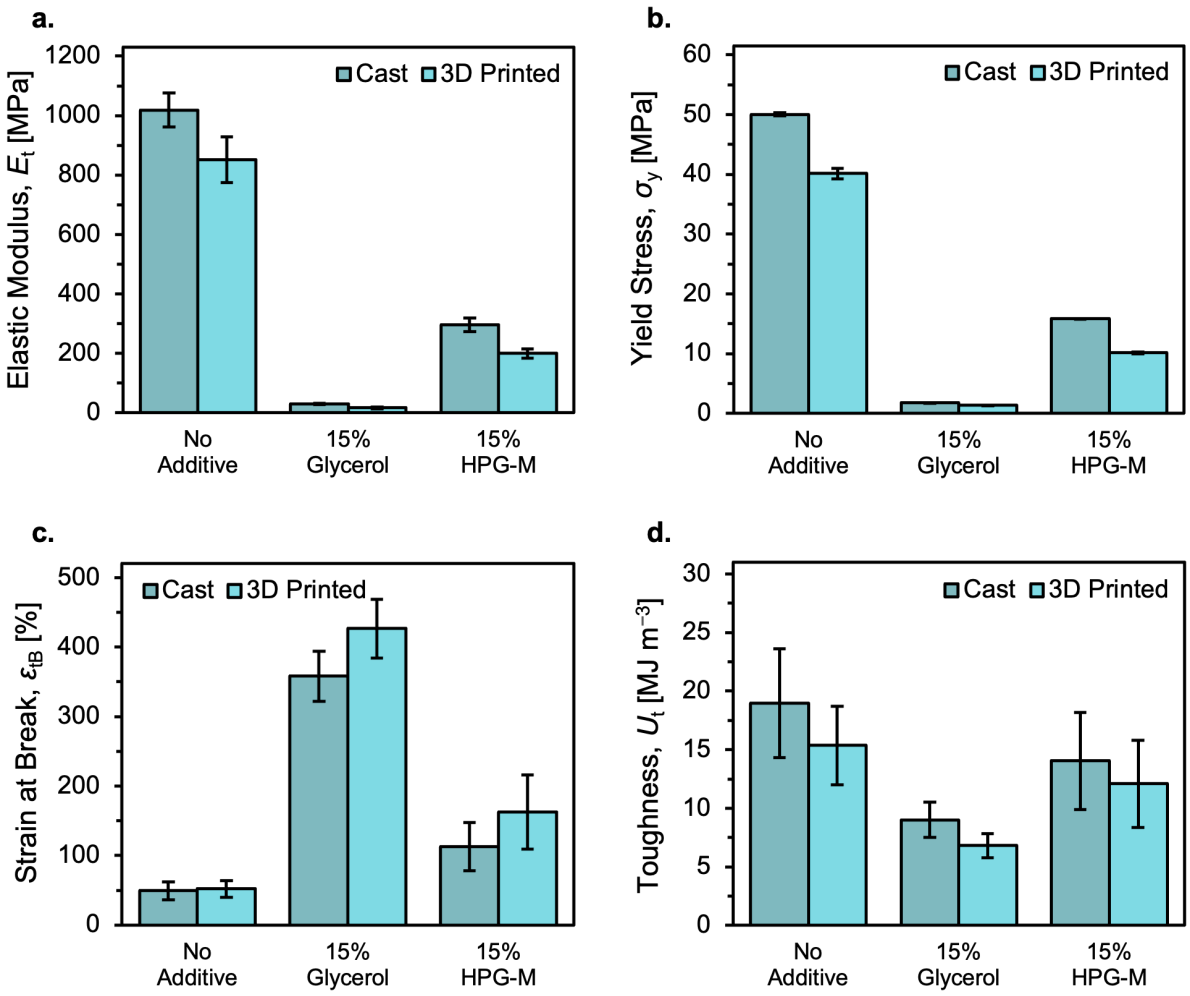

Figure 3.11. Tensile properties of cast bioplastics versus 3D printed bioplastics. (a) Elastic modulus comparison. (b) Yield stress comparison. (c) Strain at break comparison. (d) Toughness comparison.

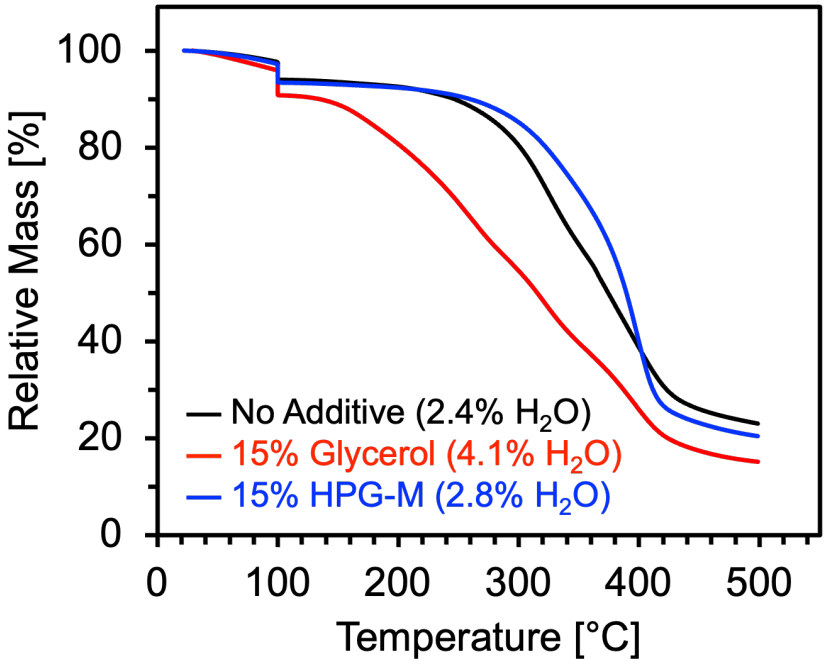

Figure 3.12. TGA curves for bioplastics.

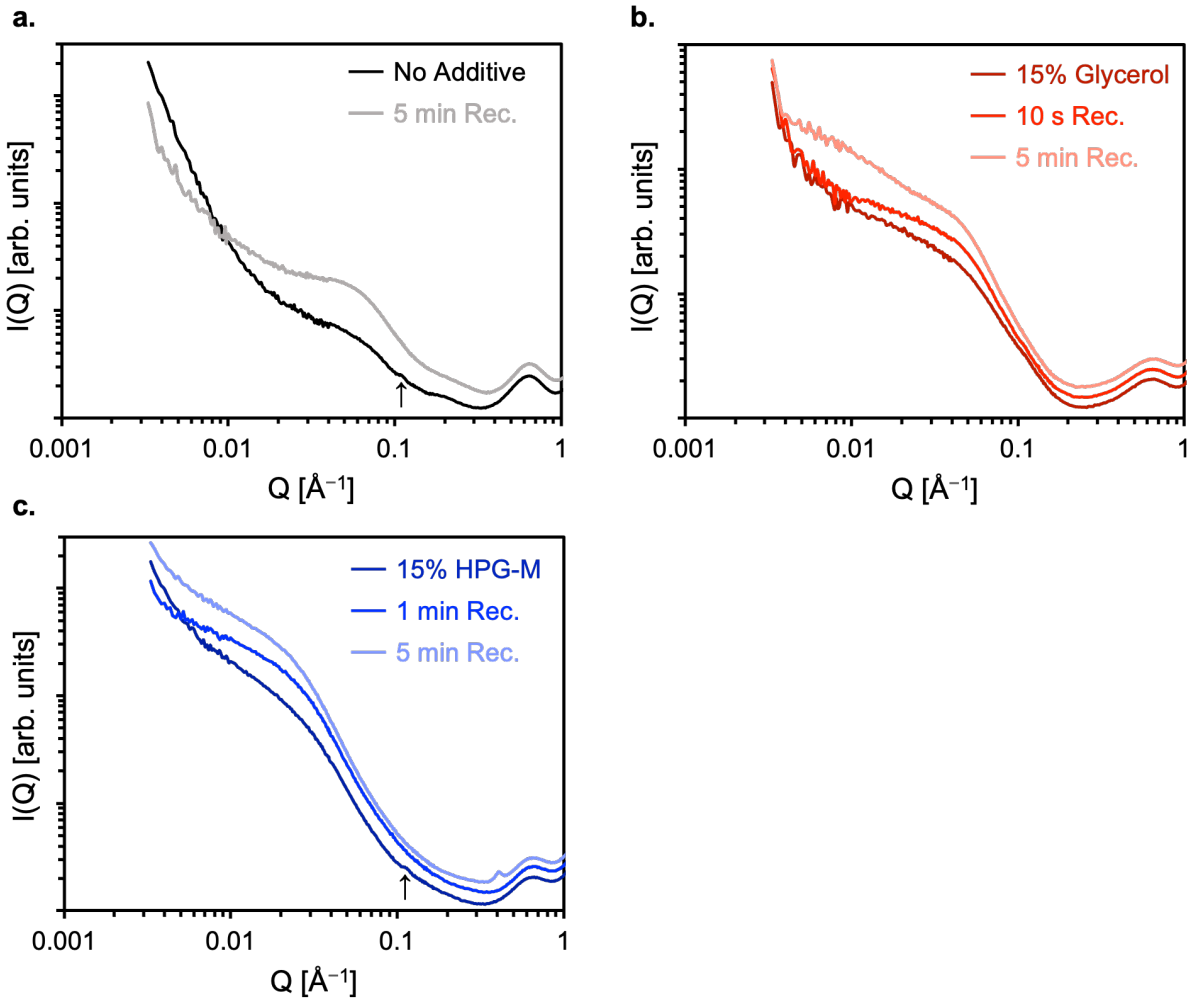

Figure 3.13. X-ray scattering analysis of bioplastics before and after thermal shape-recovery. Arrows indicate features likely related to BSA ordering. (a) Bioplastic with no additive as fabricated versus after strain and thermal recovery for 5 min. (b) Bioplastic fabricated from resin with 15 wt% glycerol as fabricated versus after strain and thermal recovery for 10 s, and thermal recovery for 5 min. (c) Bioplastic fabricated from resin with 15 wt% HPG-M as fabricated versus after strain and thermal recovery for 1 min, and thermal recovery for 5 min.

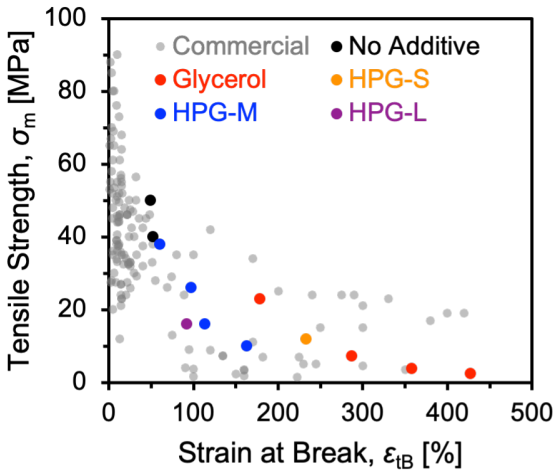

Figure 3.14. Ashby plot of tensile strength versus strain at break, comparing commercial materials for light-based 3D printing to the BSA-PEGDA materials with and without plasticizing additives (this work). Numerical data available in Appendix B (Table B1).

References

(1) Raquez, J.-M.; Deléglise, M.; Lacrampe, M.-F.; Krawczak, P. Thermosetting (Bio)Materials Derived from Renewable Resources: A Critical Review. *Prog. Polym. Sci.* **2010**, *35* (4), 487–509. https://doi.org/10.1016/j.progpolymsci.2010.01.001.

(2) Cao, Y.; Olsen, B. D. Strengthening and Toughening of Protein-Based Thermosets via Intermolecular Self-Assembly. *Biomacromolecules* **2022**, *23* (8), 3286–3295. https://doi.org/10.1021/acs.biomac.2c00372.

(3) Li, Y.; Xue, B.; Cao, Y. 100th Anniversary of Macromolecular Science Viewpoint: Synthetic Protein Hydrogels. *ACS Macro Lett.* **2020**, *9* (4), 512–524. https://doi.org/10.1021/acsmacrolett.0c00109.

(4) Lei, H.; Dong, L.; Li, Y.; Zhang, J.; Chen, H.; Wu, J.; Zhang, Y.; Fan, Q.; Xue, B.; Qin, M.; Chen, B.; Cao, Y.; Wang, W. Stretchable Hydrogels with Low Hysteresis and Anti-Fatigue Fracture Based on Polyprotein Cross-Linkers. *Nat Commun.* **2020**, *11* (1), 4032. https://doi.org/10.1038/s41467-020-17877-z.

(5) Huerta-López, C.; Alegre-Cebollada, J. Protein Hydrogels: The Swiss Army Knife for Enhanced Mechanical and Bioactive Properties of Biomaterials. *Nanomaterials* **2021**, *11* (7), 1656. https://doi.org/10.3390/nano11071656.

(6) Su, J.; Zhao, K.; Ren, Y.; Zhao, L.; Wei, B.; Liu, B.; Zhang, Y.; Wang, F.; Li, J.; Liu, Y.; Liu, K.; Zhang, H. Biosynthetic Structural Proteins with Super Plasticity, Extraordinary Mechanical Performance, Biodegradability, Biocompatibility and Information Storage Ability. *Angew. Chem. Int. Edit.* **2022**, *61* (12), e202117538. https://doi.org/10.1002/anie.202117538.

(7) Perez-Puyana, V. M.; Jiménez-Rosado, M.; Martínez, I.; Romero, A. Tuning the Mechanical and Functional Properties of Pea Protein-Based Bioplastics via Different Physical and Chemical Cross-Linking Methods. *ACS Appl. Polym. Mater.* **2024**, *6* (3), 1891–1899. https://doi.org/10.1021/acsapm.3c02737.

(8) Baler, K.; Michael, R.; Szleifer, I.; Ameer, G. A. Albumin Hydrogels Formed by Electrostatically Triggered Self-Assembly and Their Drug Delivery Capability. *Biomacromolecules* **2014**, *15* (10), 3625–3633. https://doi.org/10.1021/bm500883h.

(9) Miserez, A.; Yu, J.; Mohammadi, P. Protein-Based Biological Materials: Molecular Design and Artificial Production. *Chem. Rev.* **2023**, *123* (5), 2049–2111. https://doi.org/10.1021/acs.chemrev.2c00621.

(10) Doolan, J. A.; Alesbrook, L. S.; Baker, K.; Brown, I. R.; Williams, G. T.; Hilton, K. L. F.; Tabata, M.; Wozniakiewicz, P. J.; Hiscock, J. R.; Goult, B. T. Next-Generation Protein-Based Materials Capture and Preserve Projectiles from Supersonic Impacts. *Nat. Nanotechnol.* **2023**, *18* (9), 1060–1066. https://doi.org/10.1038/s41565-023-01431-1.

(11) Zhang, K.; Zhou, Y.; Zhang, J.; Liu, Q.; Hanenberg, C.; Mourran, A.; Wang, X.; Gao, X.; Cao, Y.; Herrmann, A.; Zheng, L. Shape Morphing of Hydrogels by Harnessing Enzyme

Enabled Mechanoresponse. *Nat. Commun.* **2024**, *15* (1), 249. https://doi.org/10.1038/s41467-023-44607-y.

(12) Guicherd, M.; Ben Khaled, M.; Guéroult, M.; Nomme, J.; Dalibey, M.; Grimaud, F.; Alvarez, P.; Kamionka, E.; Gavalda, S.; Noël, M.; Vuillemin, M.; Amillastre, E.; Labourdette, D.; Cioci, G.; Tournier, V.; Kitpreechavanich, V.; Dubois, P.; André, I.; Duquesne, S.; Marty, A. An Engineered Enzyme Embedded into PLA to Make Self-Biodegradable Plastic. *Nature* **2024**, *631* (8022), 884–890. https://doi.org/10.1038/s41586-024-07709-1.

(13) Hu, X.; Cebe, P.; Weiss, A. S.; Omenetto, F.; Kaplan, D. L. Protein-Based Composite Materials. *Mater. Today* **2012**, *15* (5), 208–215. https://doi.org/10.1016/S1369-7021(12)70091-3.

(14) Abascal, N. C.; Regan, L. The Past, Present and Future of Protein-Based Materials. *Open Biol.* **2018**, *8* (10), 180113. https://doi.org/10.1098/rsob.180113.

(15) Giaveri, S.; Schmitt, A. M.; Roset Julià, L.; Scamarcio, V.; Murello, A.; Cheng, S.; Menin, L.; Ortiz, D.; Patiny, L.; Bolisetty, S.; Mezzenga, R.; Maerkl, S. J.; Stellacci, F. Nature-Inspired Circular-Economy Recycling for Proteins: Proof of Concept. *Adv. Mater.* **2021**, *33* (44), 2104581. https://doi.org/10.1002/adma.202104581.

(16) Yuan, Y.; Solin, N. Water Processable Bioplastic Films from Functionalized Protein Fibrils. *Adv. Mater. Interfaces* **2022**, *9* (27), 2200926. https://doi.org/10.1002/admi.202200926.

(17) Lin, S.; Liu, W.; Fu, X.; Luo, M.; Zhong, W.-H. Protein-Based Materials for Sustainable, Multifunctional Air Filtration. *Sep. Purif. Technol.* **2024**, *335*, 126252. https://doi.org/10.1016/j.seppur.2023.126252.

(18) Capezza, A. J.; Mezzenga, R. Proteins for Applied and Functional Materials. *Biomacromolecules* **2024**, *25* (8), 4615–4618. https://doi.org/10.1021/acs.biomac.4c00884.

(19) Gagner, J. E.; Kim, W.; Chaikof, E. L. Designing Protein-Based Biomaterials for Medical Applications. *Acta Biomater.* **2014**, *10* (4), 1542–1557. https://doi.org/10.1016/j.actbio.2013.10.001.

(20) Varanko, A.; Saha, S.; Chilkoti, A. Recent Trends in Protein and Peptide-Based Biomaterials for Advanced Drug Delivery. *Adv. Drug Deliver. Rev.* **2020**, *156*, 133–187. https://doi.org/10.1016/j.addr.2020.08.008.

(21) Chu, S.; Wang, A. L.; Bhattacharya, A.; Montclare, J. K. Protein Based Biomaterials for Therapeutic and Diagnostic Applications. *Prog. Biomed. Eng.* **2021**, *4* (1), 012003. https://doi.org/10.1088/2516-1091/ac2841.

(22) Fang, J.; Mehlich, A.; Koga, N.; Huang, J.; Koga, R.; Gao, X.; Hu, C.; Jin, C.; Rief, M.; Kast, J.; Baker, D.; Li, H. Forced Protein Unfolding Leads to Highly Elastic and Tough Protein Hydrogels. *Nat. Commun.* **2013**, *4* (1), 2974. https://doi.org/10.1038/ncomms3974.

(23) Dooling, L. J.; Buck, M. E.; Zhang, W.-B.; Tirrell, D. A. Programming Molecular Association and Viscoelastic Behavior in Protein Networks. *Adv. Mater.* **2016**, *28* (23), 4651–4657. https://doi.org/10.1002/adma.201506216.

(24) Huang, P.-S.; Boyken, S. E.; Baker, D. The Coming of Age of de Novo Protein Design. *Nature* **2016**, *537* (7620), 320–327. https://doi.org/10.1038/nature19946.

(25) Mout, R.; Bretherton, R. C.; Decarreau, J.; Lee, S.; Gregorio, N.; Edman, N. I.; Ahlrichs, M.; Hsia, Y.; Sahtoe, D. D.; Ueda, G.; Sharma, A.; Schulman, R.; DeForest, C. A.; Baker, D. De Novo Design of Modular Protein Hydrogels with Programmable Intra- and Extracellular Viscoelasticity. *P. Natl. Acad. Sci.* **2024**, *121* (6), e2309457121. https://doi.org/10.1073/pnas.2309457121.

(26) Thompson, M. K.; Moroni, G.; Vaneker, T.; Fadel, G.; Campbell, R. I.; Gibson, I.; Bernard, A.; Schulz, J.; Graf, P.; Ahuja, B.; Martina, F. Design for Additive Manufacturing: Trends, Opportunities, Considerations, and Constraints. *CIRP Ann.* **2016**, *65* (2), 737–760. https://doi.org/10.1016/j.cirp.2016.05.004.

(27) Rosen, D.; Kim, S. Design and Manufacturing Implications of Additive Manufacturing. *J. Mater. Eng. Perform.* **2021**, *30* (9), 6426–6438. https://doi.org/10.1007/s11665-021-06030-6.

(28) Tofail, S. A. M.; Koumoulos, E. P.; Bandyopadhyay, A.; Bose, S.; O'Donoghue, L.; Charitidis, C. Additive Manufacturing: Scientific and Technological Challenges, Market Uptake and Opportunities. *Mater. Today* **2018**, *21* (1), 22–37. https://doi.org/10.1016/j.mattod.2017.07.001.

(29) Kanishka, K.; Acherjee, B. Revolutionizing Manufacturing: A Comprehensive Overview of Additive Manufacturing Processes, Materials, Developments, and Challenges. *J. Manuf. Process.* **2023**, *107*, 574–619. https://doi.org/10.1016/j.jmapro.2023.10.024.

(30) Gross, B. C.; Erkal, J. L.; Lockwood, S. Y.; Chen, C.; Spence, D. M. Evaluation of 3D Printing and Its Potential Impact on Biotechnology and the Chemical Sciences. *Anal. Chem.* **2014**, *86* (7), 3240–3253. https://doi.org/10.1021/ac403397r.

(31) Zhang, F.; Zhu, L.; Li, Z.; Wang, S.; Shi, J.; Tang, W.; Li, N.; Yang, J. The Recent Development of Vat Photopolymerization: A Review. *Addit. Manuf.* **2021**, *48*, 102423. https://doi.org/10.1016/j.addma.2021.102423.

(32) *Anycubic 3D Printer | For Freedom to Make*. https://www.anycubic.com/ (accessed 2024-10-07).

(33) Sanchez-Rexach, E.; Johnston, T. G.; Jehanno, C.; Sardon, H.; Nelson, A. Sustainable Materials and Chemical Processes for Additive Manufacturing. *Chem. Mater.* **2020**, *32* (17), 7105–7119. https://doi.org/10.1021/acs.chemmater.0c02008.

(34) Voet, V. S. D.; Guit, J.; Loos, K. Sustainable Photopolymers in 3D Printing: A Review on Biobased, Biodegradable, and Recyclable Alternatives. *Macromol. Rapid Commun.* **2021**, *42* (3), 2000475. https://doi.org/10.1002/marc.202000475.

(35) Maines, E. M.; Porwal, M. K.; Ellison, C. J.; Reineke, T. M. Sustainable Advances in SLA/DLP 3D Printing Materials and Processes. *Green Chem.* **2021**, *23* (18), 6863–6897. https://doi.org/10.1039/D1GC01489G.

(36) Sardon, H.; Long, T.; Le Ferrand, H. Sustainable Additive Manufacturing of Plastics. *ACS Sustainable Chem. Eng.* **2022**, *10* (6), 1983–1985. https://doi.org/10.1021/acssuschemeng.2c00475.

(37) Lopez de Pariza, X.; Varela, O.; Catt, S. O.; Long, T. E.; Blasco, E.; Sardon, H. Recyclable Photoresins for Light-Mediated Additive Manufacturing towards Loop 3D Printing. *Nat. Commun.* **2023**, *14* (1), 5504. https://doi.org/10.1038/s41467-023-41267-w.

(38) Machado, T. O.; Stubbs, C. J.; Chiaradia, V.; Alraddadi, M. A.; Brandolese, A.; Worch, J. C.; Dove, A. P. A Renewably Sourced, Circular Photopolymer Resin for Additive Manufacturing. *Nature* **2024**, *629* (8014), 1069–1074. https://doi.org/10.1038/s41586-024-07399-9.

(39) Billiet, T.; Gevaert, E.; De Schryver, T.; Cornelissen, M.; Dubruel, P. The 3D Printing of Gelatin Methacrylamide Cell-Laden Tissue-Engineered Constructs with High Cell Viability. *Biomaterials* **2014**, *35* (1), 49–62. https://doi.org/10.1016/j.biomaterials.2013.09.078.

(40) You, F.; Wu, X.; Chen, X. 3D Printing of Porous Alginate/Gelatin Hydrogel Scaffolds and Their Mechanical Property Characterization. *Int. J. Polym. Mater. Polym. Biomater.* **2017**, *66* (6), 299–306. https://doi.org/10.1080/00914037.2016.1201830.

(41) Xu, W.; Molino, B. Z.; Cheng, F.; Molino, P. J.; Yue, Z.; Su, D.; Wang, X.; Willför, S.; Xu, C.; Wallace, G. G. On Low-Concentration Inks Formulated by Nanocellulose Assisted with Gelatin Methacrylate (GelMA) for 3D Printing toward Wound Healing Application. *ACS Appl. Mater. Inter.* **2019**, *11* (9), 8838–8848. https://doi.org/10.1021/acsami.8b21268.

(42) Du, J.; Dai, H.; Wang, H.; Yu, Y.; Zhu, H.; Fu, Y.; Ma, L.; Peng, L.; Li, L.; Wang, Q.; Zhang, Y. Preparation of High Thermal Stability Gelatin Emulsion and Its Application in 3D Printing. *Food Hydrocolloid.* **2021**, *113*, 106536. https://doi.org/10.1016/j.foodhyd.2020.106536.

(43) Inzana, J. A.; Olvera, D.; Fuller, S. M.; Kelly, J. P.; Graeve, O. A.; Schwarz, E. M.; Kates, S. L.; Awad, H. A. 3D Printing of Composite Calcium Phosphate and Collagen Scaffolds for Bone Regeneration. *Biomaterials* **2014**, *35* (13), 4026–4034. https://doi.org/10.1016/j.biomaterials.2014.01.064.

(44) Nocera, A. D.; Comín, R.; Salvatierra, N. A.; Cid, M. P. Development of 3D Printed Fibrillar Collagen Scaffold for Tissue Engineering. *Biomed. Microdevices* **2018**, *20* (2), 26. https://doi.org/10.1007/s10544-018-0270-z.

(45) Marques, C. F.; Diogo, G. S.; Pina, S.; Oliveira, J. M.; Silva, T. H.; Reis, R. L. Collagen-Based Bioinks for Hard Tissue Engineering Applications: A Comprehensive Review. *J Mater. Sci.–Mater. Med.* **2019**, *30* (3), 32. https://doi.org/10.1007/s10856-019-6234-x.

(46) Suo, H.; Zhang, J.; Xu, M.; Wang, L. Low-Temperature 3D Printing of Collagen and Chitosan Composite for Tissue Engineering. *Mater. Sci. Eng. C* **2021**, *123*, 111963. https://doi.org/10.1016/j.msec.2021.111963.

(47) Abelseth, E.; Abelseth, L.; De la Vega, L.; Beyer, S. T.; Wadsworth, S. J.; Willerth, S. M. 3D Printing of Neural Tissues Derived from Human Induced Pluripotent Stem Cells

Using a Fibrin-Based Bioink. *ACS Biomater. Sci. Eng.* **2019**, *5* (1), 234–243. https://doi.org/10.1021/acsbiomaterials.8b01235.

(48) Lee, C.; Abelseth, E.; de la Vega, L.; Willerth, S. M. Bioprinting a Novel Glioblastoma Tumor Model Using a Fibrin-Based Bioink for Drug Screening. *Mater. Today Chemistry* **2019**, *12*, 78–84. https://doi.org/10.1016/j.mtchem.2018.12.005.

(49) de Melo, B. A. G.; Jodat, Y. A.; Cruz, E. M.; Benincasa, J. C.; Shin, S. R.; Porcionatto, M. A. Strategies to Use Fibrinogen as Bioink for 3D Bioprinting Fibrin-Based Soft and Hard Tissues. *Acta Biomater.* **2020**, *117*, 60–76. https://doi.org/10.1016/j.actbio.2020.09.024.

(50) Placone, J. K.; Navarro, J.; Laslo, G. W.; Lerman, M. J.; Gabard, A. R.; Herendeen, G. J.; Falco, E. E.; Tomblyn, S.; Burnett, L.; Fisher, J. P. Development and Characterization of a 3D Printed, Keratin-Based Hydrogel. *Ann. Biomed. Eng.* **2017**, *45* (1), 237–248. https://doi.org/10.1007/s10439-016-1621-7.

(51) Rojas-Martínez, L. E.; Flores-Hernandez, C. G.; López-Marín, L. M.; Martinez-Hernandez, A. L.; Thorat, S. B.; Reyes Vasquez, C. D.; Del Rio-Castillo, A. E.; Velasco-Santos, C. 3D Printing of PLA Composites Scaffolds Reinforced with Keratin and Chitosan: Effect of Geometry and Structure. *Eur. Polym. J.* **2020**, *141*, 110088. https://doi.org/10.1016/j.eurpolymj.2020.110088.

(52) Brodin, E.; Boehmer, M.; Prentice, A.; Neff, E.; McCoy, K.; Mueller, J.; Saul, J.; Sparks, J. L. Extrusion 3D Printing of Keratin Protein Hydrogels Free of Exogenous Chemical Agents. *Biomed. Mater.* **2022**, *17* (5), 055006. https://doi.org/10.1088/1748-605X/ac7f15.

(53) Sommer, M. R.; Schaffner, M.; Carnelli, D.; Studart, A. R. 3D Printing of Hierarchical Silk Fibroin Structures. *ACS Appl. Mater. Inter.* **2016**, *8* (50), 34677–34685. https://doi.org/10.1021/acsami.6b11440.

(54) Shi, W.; Sun, M.; Hu, X.; Ren, B.; Cheng, J.; Li, C.; Duan, X.; Fu, X.; Zhang, J.; Chen, H.; Ao, Y. Structurally and Functionally Optimized Silk-Fibroin–Gelatin Scaffold Using 3D Printing to Repair Cartilage Injury In Vitro and In Vivo. *Adv. Mater.* **2017**, *29* (29), 1701089. https://doi.org/10.1002/adma.201701089.

(55) Kim, S. H.; Yeon, Y. K.; Lee, J. M.; Chao, J. R.; Lee, Y. J.; Seo, Y. B.; Sultan, M. T.; Lee, O. J.; Lee, J. S.; Yoon, S.; Hong, I.-S.; Khang, G.; Lee, S. J.; Yoo, J. J.; Park, C. H. Precisely Printable and Biocompatible Silk Fibroin Bioink for Digital Light Processing 3D Printing. *Nat. Commun.* **2018**, *9* (1), 1620. https://doi.org/10.1038/s41467-018-03759-y.

(56) Wang, Q.; Han, G.; Yan, S.; Zhang, Q. 3D Printing of Silk Fibroin for Biomedical Applications. *Materials* **2019**, *12* (3), 504. https://doi.org/10.3390/ma12030504.

(57) Liu, Y.; Liu, D.; Wei, G.; Ma, Y.; Bhandari, B.; Zhou, P. 3D Printed Milk Protein Food Simulant: Improving the Printing Performance of Milk Protein Concentration by Incorporating Whey Protein Isolate. *Innov. Food Sci. Emerg. Technol.* **2018**, *49*, 116–126. https://doi.org/10.1016/j.ifset.2018.07.018.

(58) Liu, Y.; Zhang, W.; Wang, K.; Bao, Y.; Regenstein, J. M.; Zhou, P. Fabrication of Gel-Like Emulsions with Whey Protein Isolate Using Microfluidization: Rheological Properties and 3D Printing Performance. *Food Bioprocess Technol.* **2019**, *12* (12), 1967–1979. https://doi.org/10.1007/s11947-019-02344-5.

(59) Chen, J.; Mu, T.; Goffin, D.; Blecker, C.; Richard, G.; Richel, A.; Haubruge, E. Application of Soy Protein Isolate and Hydrocolloids Based Mixtures as Promising Food Material in 3D Food Printing. *J. Food Eng.* **2019**, *261*, 76–86. https://doi.org/10.1016/j.jfoodeng.2019.03.016.

(60) Ainis, W. N.; Feng, R.; van den Berg, F. W. J.; Ahrné, L. Comparing the Rheological and 3D Printing Behavior of Pea and Soy Protein Isolate Pastes. *Innov. Food Sci. Emerg. Technol.* **2023**, *84*, 103307. https://doi.org/10.1016/j.ifset.2023.103307.

(61) Smith, P. T.; Narupai, B.; Tsui, J. H.; Millik, S. C.; Shafranek, R. T.; Kim, D.-H.; Nelson, A. Additive Manufacturing of Bovine Serum Albumin-Based Hydrogels and Bioplastics. *Biomacromolecules* **2020**, *21* (2), 484–492. https://doi.org/10.1021/acs.biomac.9b01236.

(62) Sanchez-Rexach, E.; Smith, P. T.; Gomez-Lopez, A.; Fernandez, M.; Cortajarena, A. L.; Sardon, H.; Nelson, A. 3D-Printed Bioplastics with Shape-Memory Behavior Based on Native Bovine Serum Albumin. *ACS Appl. Mater. Inter.* **2021**, *13* (16), 19193–19199. https://doi.org/10.1021/acsami.0c22377.

(63) Smith, P. T.; Altin, G.; Millik, S. C.; Narupai, B.; Sietz, C.; Park, J. O.; Nelson, A. Methacrylated Bovine Serum Albumin and Tannic Acid Composite Materials for Three-Dimensional Printing Tough and Mechanically Functional Parts. *ACS Appl. Mater. Inter.* **2022**, *14* (18), 21418–21425. https://doi.org/10.1021/acsami.2c01446.

(64) Mason, T. O.; Shimanovich, U. Fibrous Protein Self-Assembly in Biomimetic Materials. *Adv. Mater.* **2018**, *30* (41), 1706462. https://doi.org/10.1002/adma.201706462.

(65) Mu, X.; Agostinacchio, F.; Xiang, N.; Pei, Y.; Khan, Y.; Guo, C.; Cebe, P.; Motta, A.; Kaplan, D. L. Recent Advances in 3D Printing with Protein-Based Inks. *Prog. Polym. Sci.* **2021**, *115*, 101375. https://doi.org/10.1016/j.progpolymsci.2021.101375.

(66) Melchels, F. P. W.; Bertoldi, K.; Gabbrielli, R.; Velders, A. H.; Feijen, J.; Grijpma, D. W. Mathematically Defined Tissue Engineering Scaffold Architectures Prepared by Stereolithography. *Biomaterials* **2010**, *31* (27), 6909–6916. https://doi.org/10.1016/j.biomaterials.2010.05.068.

(67) Schüller-Ravoo, S.; Teixeira, S. M.; Feijen, J.; Grijpma, D. W.; Poot, A. A. Flexible and Elastic Scaffolds for Cartilage Tissue Engineering Prepared by Stereolithography Using Poly(Trimethylene Carbonate)-Based Resins. *Macromol. Biosci.* **2013**, *13* (12), 1711–1719. https://doi.org/10.1002/mabi.201300399.

(68) Mondschein, R. J.; Kanitkar, A.; Williams, C. B.; Verbridge, S. S.; Long, T. E. Polymer Structure-Property Requirements for Stereolithographic 3D Printing of Soft Tissue Engineering Scaffolds. *Biomaterials* **2017**, *140*, 170–188. https://doi.org/10.1016/j.biomaterials.2017.06.005.

(69) Peters, T., Jr. *All About Albumin: Biochemistry, Genetics, and Medical Applications*; Academic Press, Inc., 1996.

(70) Masuelli, M. A. Study of Bovine Serum Albumin Solubility in Aqueous Solutions by Intrinsic Viscosity Measurements. *Adv. Phys. Chem.* **2013**, *2013* (1), 360239. https://doi.org/10.1155/2013/360239.

(71) Kainthan, R. K.; Muliawan, E. B.; Hatzikiriakos, S. G.; Brooks, D. E. Synthesis, Characterization, and Viscoelastic Properties of High Molecular Weight Hyperbranched Polyglycerols. *Macromolecules* **2006**, *39* (22), 7708–7717. https://doi.org/10.1021/ma0613483.

(72) Anilkumar, P.; Lawson, T. B.; Abbina, S.; Mäkelä, J. T. A.; Sabatelle, R. C.; Takeuchi, L. E.; Snyder, B. D.; Grinstaff, M. W.; Kizhakkedathu, J. N. Mega Macromolecules as Single Molecule Lubricants for Hard and Soft Surfaces. *Nat. Commun.* **2020**, *11* (1), 2139. https://doi.org/10.1038/s41467-020-15975-6.

(73) Fairbanks, B. D.; Schwartz, M. P.; Bowman, C. N.; Anseth, K. S. Photoinitiated Polymerization of PEG-Diacrylate with Lithium Phenyl-2,4,6-Trimethylbenzoylphosphinate: Polymerization Rate and Cytocompatibility. *Biomaterials* **2009**, *30* (35), 6702–6707. https://doi.org/10.1016/j.biomaterials.2009.08.055.

(74) Wilms, D.; Stiriba, S.-E.; Frey, H. Hyperbranched Polyglycerols: From the Controlled Synthesis of Biocompatible Polyether Polyols to Multipurpose Applications. *Acc. Chem. Res.* **2010**, *43* (1), 129–141. https://doi.org/10.1021/ar900158p.

(75) Sunder, A.; Hanselmann, R.; Frey, H.; Mülhaupt, R. Controlled Synthesis of Hyperbranched Polyglycerols by Ring-Opening Multibranching Polymerization. *Macromolecules* **1999**, *32* (13), 4240–4246. https://doi.org/10.1021/ma990090w.

(76) McHugh, T. H.; Krochta, J. M. Sorbitol- vs Glycerol-Plasticized Whey Protein Edible Films: Integrated Oxygen Permeability and Tensile Property Evaluation. *J. Agric. Food Chem.* **1994**, *42* (4), 841–845. https://doi.org/10.1021/jf00040a001.

(77) Godbillot, L.; Dole, P.; Joly, C.; Rogé, B.; Mathlouthi, M. Analysis of Water Binding in Starch Plasticized Films. *Food Chem.* **2006**, *96* (3), 380–386. https://doi.org/10.1016/j.foodchem.2005.02.054.

(78) Lavorgna, M.; Piscitelli, F.; Mangiacapra, P.; Buonocore, G. G. Study of the Combined Effect of Both Clay and Glycerol Plasticizer on the Properties of Chitosan Films. *Carbohydr. Polym.* **2010**, *82* (2), 291–298. https://doi.org/10.1016/j.carbpol.2010.04.054.

(79) Mohsin, M.; Hossin, A.; Haik, Y. Thermal and Mechanical Properties of Poly(Vinyl Alcohol) Plasticized with Glycerol. *J. Appl. Polym. Sci.* **2011**, *122* (5), 3102–3109. https://doi.org/10.1002/app.34229.

(80) Gao, C.; Pollet, E.; Avérous, L. Properties of Glycerol-Plasticized Alginate Films Obtained by Thermo-Mechanical Mixing. *Food Hydrocolloid.* **2017**, *63*, 414–420. https://doi.org/10.1016/j.foodhyd.2016.09.023.

(81) Tarique, J.; Sapuan, S. M.; Khalina, A. Effect of Glycerol Plasticizer Loading on the Physical, Mechanical, Thermal, and Barrier Properties of Arrowroot (Maranta Arundinacea) Starch Biopolymers. *Sci. Rep.* **2021**, *11* (1), 13900. https://doi.org/10.1038/s41598-021-93094-y.

(82) Domján, A.; Bajdik, J.; Pintye-Hódi, K. Understanding of the Plasticizing Effects of Glycerol and PEG 400 on Chitosan Films Using Solid-State NMR Spectroscopy. *Macromolecules* **2009**, *42* (13), 4667–4673. https://doi.org/10.1021/ma8021234.

(83) Özeren, H. D.; Wei, X.-F.; Nilsson, F.; Olsson, R. T.; Hedenqvist, M. S. Role of Hydrogen Bonding in Wheat Gluten Protein Systems Plasticized with Glycerol and Water. *Polymer* **2021**, *232*, 124149. https://doi.org/10.1016/j.polymer.2021.124149.

(84) Ben, Z. Y.; Samsudin, H.; Yhaya, M. F. Glycerol: Its Properties, Polymer Synthesis, and Applications in Starch Based Films. *Eur. Polym. J.* **2022**, *175*, 111377. https://doi.org/10.1016/j.eurpolymj.2022.111377.

(85) Hermanson, G. T. *Bioconjugate Techniques*, 3rd ed.; Elsevier, 2013.

(86) Schubert, C.; Osterwinter, C.; Tonhauser, C.; Schömer, M.; Wilms, D.; Frey, H.; Friedrich, C. Can Hyperbranched Polymers Entangle? Effect of Hydrogen Bonding on Entanglement Transition and Thermorheological Properties of Hyperbranched Polyglycerol Melts. *Macromolecules* **2016**, *49* (22), 8722–8737. https://doi.org/10.1021/acs.macromol.6b00674.

(87) Lezov, A.; Gubarev, A.; Kaiser, T.; Tobaschus, W.; Tsvetkov, N.; Nischang, I.; Schubert, U. S.; Frey, H.; Perevyazko, I. "Hard" Sphere Behavior of "Soft", Globular-like, Hyperbranched Polyglycerols – Extensive Molecular Hydrodynamic and Light Scattering Studies. *Macromolecules* **2020**, *53* (21), 9220–9233. https://doi.org/10.1021/acs.macromol.0c01340.

(88) Kinloch, A. J.; Young, R. J. *Fracture Behavior of Polymers*, 1st ed.; Springer Dordrecht, 2013.

(89) Thingiverse.com. *Gecko by WebmasterZero*. Thingiverse. https://www.thingiverse.com/thing:1363148 (accessed 2024-10-07).

(90) Balderrama-Armendariz, C. O.; MacDonald, E.; Roberson, D. A.; Ruiz-Huerta, L.; Maldonado-Macias, A.; Valadez-Gutierrez, E.; Caballero-Ruiz, A.; Espalin, D. Folding Behavior of Thermoplastic Hinges Fabricated with Polymer Extrusion Additive Manufacturing. *Int. J. Adv. Manuf. Technol.* **2019**, *105* (1), 233–245. https://doi.org/10.1007/s00170-019-04196-x.

(91) Yu, S.; Sadaba, N.; Sanchez-Rexach, E.; Hilburg, S. L.; Pozzo, L. D.; Altin-Yavuzarslan, G.; Liz-Marzán, L. M.; Jimenez de Aberasturi, D.; Sardon, H.; Nelson, A. 4D Printed Protein-AuNR Nanocomposites with Photothermal Shape Recovery. *Adv. Funct. Mater.* **2024**, *34* (14), 2311209. https://doi.org/10.1002/adfm.202311209.

(92) Majorek, K. A.; Porebski, P. J.; Chruszcz, M.; Almo, S.; Minor, W.; New York Structural Genomics Research Consortium (NYSGRC). Crystal Structure of Bovine Serum Albumin, 2011. https://doi.org/10.2210/pdb3v03/pdb.

(93) Majorek, K. A.; Porebski, P. J.; Dayal, A.; Zimmerman, M. D.; Jablonska, K.; Stewart, A. J.; Chruszcz, M.; Minor, W. Structural and Immunologic Characterization of Bovine, Horse, and Rabbit Serum Albumins. *Mol. Immunol.* **2012**, *52* (3), 174–182. https://doi.org/10.1016/j.molimm.2012.05.011.

(94) Goodsell, D. S.; Autin, L.; Olson, A. J. *Illustrate*: Software for Biomolecular Illustration. *Structure* **2019**, *27* (11), 1716-1720.e1. https://doi.org/10.1016/j.str.2019.08.011.

Chapter 4

Protein-Based Dynamic Hydrogels Utilizing Native Ligand Binding Toward Applications in Therapeutic Delivery and 3D Bioprinting

This chapter was adapted from the following manuscript:

> Millik, S. C.; Le, L.; Nelson, A. Protein-Based Dynamic Hydrogels Utilizing Native Ligand Binding Toward Applications in Therapeutic Delivery and 3D Bioprinting. *In preparation*, **2024**.

4.1. Abstract

Hydrogels comprising networks formed from reversible interactions have shown utility in minimally invasive delivery of encapsulated therapeutics. Additionally, such dynamic hydrogels are well suited for patterning cells and other biologics via direct ink writing (DIW)—for example, in 3D bioprinting of functional tissue- and organ-like structures. Here, we report dynamic hydrogels formed from two distinct nanoparticle-like structures, a globular hyperbranched poly(glycerol) (HPG) and a soluble albumin nanostructure (SAN). Functionalization of the HPG with palmitate moieties enables its self-association, as well as interaction with native serum albumin or SANs toward the formation of viscoelastic networks. The extent of these interactions can be tuned by modifying the SAN size in addition to other formulation parameters. These interactions can also be competitively inhibited by free palmitate for further modification of rheological properties. Notably, these non-covalent HPG- and SAN-based hydrogels also resist dissolution in aqueous media over multiple weeks. Finally, we

demonstrate proof of concept of in vitro release of a model protein therapeutic from these materials, and we show a preliminary example of DIW.

4.2. Introduction

Dynamic hydrogels have been studied over the past few decades for injection or extrusion-based processes in applications such as 3D bioprinting, therapeutic cell delivery, and drug delivery.[1–9] Dynamic network structure gives these hydrogels complex viscoelastic properties.[7–10] These materials can exhibit solid-like behavior with dominant elastic character or liquid-like behavior with dominant viscous character depending on the magnitude of applied stress. Transitions between these states is reversible via self-healing, due to the reversible nature of the bonds that form the network. Under low-stress conditions prior to extrusion (i.e., "at rest"), solid-like behavior can mechanically support cells or particles dispersed within the gel, ensuring homogeneous incorporation of these species.[8,9] Under increased stress during extrusion, mechanical disruption of network structure (i.e., yielding) causes a transition to a liquid-like state to allow flow from a syringe. During flow, viscosity decreases under shear (i.e., shear thinning and thixotropy) to facilitate extrusion through a nozzle or needle. During extrusion, retention of network structure in the bulk, despite interfacial yielding and flow (i.e., plug flow), can additionally protect cells and other biologics from mechanical stress.[3,9] Upon deposition onto a surface or upon injection, bulk solid-like behavior facilitates retention of cells or therapeutic agents locally or affords stable form factor of fabricated constructs, in the case of 3D printing.[7,8]

Dynamic hydrogels reported for injection/extrusion-based processes include those based on collagen, gelatin, fibrin, hyaluronic acid, alginate, cellulose derivatives, recombinant

polypeptides, and poly(ethylene glycol), with many systems comprising multiple components.[11–20] These materials generally rely on ionic bonds, host-guest interactions, dynamic covalent bonds, specific biomolecular interactions, topological entanglements, or jamming for formation of dynamic network structure.[1,2] Limitations of dynamic hydrogels for injection/extrusion reported to date are typically related to either their rheological properties or their biocompatibility.[4–7,9,21] To our knowledge, there is currently no gold standard for a dynamic hydrogel for injection/extrusion-based applications in the biomedical space. This is perhaps reflective of the difficulty of designing a material which simultaneously exhibits the complex rheology required for extrusion-based fabrication and possesses the specific biological functionality required for the biomedical application in question.[5,7–9,21,22]

The rheological properties required for direct ink writing (DIW) are more stringent than those required for injection.[7–9,23] For DIW, sufficient viscous character at moderate shear rates is necessary for smooth extrusion; however, prompt recovery of high elastic character post-deposition is necessary to prevent distortion of the printed structure due to material flow over time.[7,9] Hydrogels prepared from high concentrations (e.g., 30 wt%) of the commercially available nonionic surfactant, Pluronic F-127, show exemplary rheological properties for DIW.[24–26] These gels exhibit excellent stability at rest, without apparent flow over time. Yet, under shear load, F-127 gels exhibit suitable yielding, strong shear thinning, and smooth extrusion. Once the shear load is removed, F-127 gels promptly self-heal with high mechanical stability indefinitely thereafter. We and others have previously demonstrated DIW with F-127 gels, as well as fabrication of core-shell filaments and tubes where the rheological properties of these gels proved essential for effective fabrication.[24–27] Nevertheless, drawbacks of F-127 gels include their limited biocompatibility[28,29] and the high injection/extrusion forces necessary for their

deposition from syringes—both disadvantages are largely the result of the high concentration of F-127 necessary for gelation.[23,30,31] These disadvantages generally preclude the use of F-127 gels in effective delivery of therapeutics or as a bioinks.

Dynamic hydrogels that have shown promise for injection/extrusion-based applications in the biomedical space include the host-guest systems reported by Burdick and coworkers.[4,12,14,32–35] These gels feature a hyaluronic acid network reversibly held together by supramolecular association of cyclodextrin (host) and adamantane (guest) moieties. These gels have shown utility in 3D bioprinting as well as in the delivery of therapeutics.[4,33–36] As another notable example, the polymer-nanoparticle hydrogels reported by Appel and coworkers have shown promise for delivery of diverse therapeutic agents, including small molecules, proteins, and cells.[16,37–40] These gels feature a network largely comprising polymeric core-shell nanoparticles cross-linked by physical association of hydrophobically modified cellulose derivatives.

Protein-based hydrogels can offer unique advantages derived from the structures and functions of their protein constituents. These advantages can include specific biological functionality for the end use (e.g., derived from biomolecular recognition involving the protein) as well as useful material properties related to material synthesis or processing.[22,41,42] Protein-based hydrogels are generally biocompatible and thus lend themselves well to use in a variety of bio-interfacing applications.[5,22,43–45] Additionally, modern methods of protein engineering enable unparalleled control over material composition and architecture, bringing promise of new and improved functionality in the next generation of protein-based materials.[46–48] For these reasons, greater understanding of methods for synthesizing hydrogel networks from functional protein building blocks is valuable.

Serum albumin is often considered a commodity protein; it is ubiquitous in research labs and as a component of many biomedical products. Albumin has numerous applications in fundamental research as well as in clinical medicine.[49–54] As the most abundant soluble protein in vertebrates, albumin is easily purified in high yields and is thus available at relatively low cost.[49] In contrast with the notion that albumin is a simple commodity is the fact that it possesses sophisticated functionality. Perhaps most notably, serum albumins exhibit diverse binding affinity to a myriad of endogenous and exogenous substances.[49,55–57] Among these substances are long-chain fatty acids, to which albumin binds multivalently (≤ 6 M M^{-1}) with high affinity ($K_A \sim 1–69 \times 10^7$ M^{-1}).[49,58] Indeed, serum albumins are also biocompatible, enzymatically degradable, and highly aqueous-soluble. Many solvent-accessible lysine residues can also serve as handles for covalent modification or cross-linking.[59] Overall, serum albumin is an abundant and relatively inexpensive protein with numerous attributes which make it a promising candidate for use as a biomaterial building block. We hypothesized that long-chain fatty acid binding of serum albumin could be utilized for synthesis of non-covalent networks to afford dynamic hydrogels suitable for injection/extrusion.

Here, we report dynamic hydrogels comprising serum albumin-based nanostructures and a high-molecular-weight hyperbranched poly(glycerol) (HPG) functionalized with palmitate moieties. These gels utilize palmitate binding of bovine serum albumin (BSA) within soluble albumin nanostructures (SANs) as well as self-association of palmitate moieties for non-covalent network formation. These gels exhibit reversible gel-sol transitions in response to shear load, with prompt self-healing and recovery of solid-like character once the shear load is removed. We report rheological evaluation of these materials as well as tuning of their rheological properties toward effective application. Notably, despite being formed from non-covalent interactions, these

materials show impressive stability in aqueous media. Finally, as proof of concept, we show in vitro release of a model protein therapeutic from these materials, and we demonstrate their 3D printability via DIW.

4.3. Materials and Methods

4.3.1. Materials

Bovine serum albumin (BSA; BSAS 1.0) was purchased from Bovogen Biologicals. IgG from bovine serum (IgG; I5506), glycidol (G5809), glutaraldehyde solution (G7526; 8.7% w/w), calcium hydride (CaH_2; 21170), 1,4-dioxane (296309; anhydrous), *N*,*N*-dimethylformamide (DMF; 227056; anhydrous), *N*-methyl-2-pyrrolidone (NMP; 328634; anhydrous), 1,1,1-tris(hydroxymethyl)propane (TMP; 148083; 99.8%), potassium methoxide solution (CH_3OK; 60402; 25.1% in MeOH), palmitoyl chloride (P78; 98.6%), palmitic acid *N*-hydroxysuccinimide ester (NHS-palmitate; P1162; 99%), *N*,*N*-diisopropylethylamine (DIPEA; D125806; 99.8%), sodium phosphate monobasic monohydrate (71507), sodium phosphate dibasic dihydrate (71643), ethanolamine (398136), hydrochloric acid (HX0603), sodium borohydride ($NaBH_4$; 213462), sodium azide (NaN_3; S2002), Dowex 50WX8 hydrogen-form resin (44509), acetone (179124), diethyl ether (Et_2O; 673811), methanol-d_4 (CD_3OD; 441384), Antifoam A concentrate (A5633), 3-[(3-cholamidopropyl)dimethylammonio]-1-propanesulfonate (CHAPS; 220201), and Amicon Ultra-15 Centrifugal Filter Units (UFC905008; 50 kDa MWCO) were purchased from MilliporeSigma. Molecular sieves (MK449004; grade 564) were purchased from VWR International. Methanol (MeOH; A452-1), sodium chloride (S271), propylene glycol

(ICN15195790), phosphate-buffered saline 10X solution (PBS; BP399-1), DMEM (31053028), and FluoroBrite DMEM (A1896701) were purchased from Fisher Scientific. Sulfo-Cyanine5 NHS ester (NHS-sulfo-Cy5; 23320) was purchased from Lumiprobe. Spectra/Por 6 dialysis tubing (132554; 25 kDa MWCO) was purchased from Repligen.

4.3.2. Instrumentation

Proton nuclear magnetic resonance (^{1}H NMR) spectra were obtained using a Bruker AVANCE series instrument operating at 500 MHz frequency. Dynamic light scattering (DLS) data were obtained with a Zetasizer Nano ZS using a quartz cuvette. Rheometry was performed using a TA Instruments Discovery Hybrid Rheometer-2 with Advanced Peltier Plate system. Circular dichroism (CD) spectra were obtained with a Jasco J-1500 CD spectrophotometer, using a quartz cuvette with 0.5 mm path length. Spectrophotometry (UV-vis) was performed using a Thermo Scientific NanoDrop One spectrophotometer and BioTek Cytation 5 cell imaging multimode reader. Fluorometry was also performed using the BioTek Cytation 5. Injection force testing was performed using a TestResources 100 Series Universal Test Machine with 1.1 kN and 44 N load cells and compression fixtures.

4.3.3. Synthesis of HPG:

Prior to the HPG synthesis, glycidol was dried over CaH_2 for 18 h, vacuum-distilled, and degassed by the freeze-pump-thaw method. The purified glycidol was stored at 5 °C until use. Anhydrous dioxane and NMP, once opened (i.e., stored with perforated seals), were dried over

molecular sieves for 24 h and sparged with N_2 before use. TMP was dried under vacuum prior to weighing. All other reagents were used as received and stored according to manufacturer recommendations, unless otherwise specified.

A 250 mL 2-neck round-bottom Schlenk flask was flame-dried under vacuum. TMP (0.450 g; 3.35 mmol) was added to the flask. MeOH (400 μL) was then added to the TMP in the flask, followed by CH_3OK solution (260 μL; 0.885 mmol; 25.1% in MeOH). All additions were performed under positive pressure of N_2. After the TMP had dissolved, the flask was briefly swirled to homogenize the mixture. Bulk MeOH in the mixture was evaporated with N_2 flow through a bleed needle (16 gauge). After the TMP mixture appeared solid, residual MeOH was removed under vacuum (~ 3 Pa) over 18 h at 21 °C. Note: the TMP was not heated under vacuum to avoid sublimation. Following removal of the MeOH, an oven-dried overhead stirrer assembly was attached to the flask under positive pressure of N_2. Anhydrous dioxane (45 mL) was then charged to the flask. The flask was pre-heated using an aluminum flask carrier at a nominal temperature of 115 °C. PTFE tubing (20 gauge) was then connected to flask through a septum under positive pressure of N_2, and using a syringe pump, glycidol (45 mL; 674 mmol) was added over 24 h, at 115 °C, under N_2, while stirring at ~ 200 rpm. Following completion of glycidol addition, the reaction was allowed to proceed for an additional 24 h under the same conditions. Monomer consumption was confirmed by ^1H NMR spectroscopy. The reaction mixture was then cooled, bulk dioxane was aspirated, and MeOH (100 mL) was added to dissolve the product. Dowex 50WX8 hydrogen-form resin (~ 1 cc) was finally added to protonate the product. After 15 min, the Dowex resin was removed by centrifugation, and the product was precipitated in acetone. Precipitation in acetone was repeated once. The product was then dissolved in deionized H_2O to ~ 10–15 wt% and dialyzed (25 kDa MWCO) against

deionized H_2O for 3 d at 21 °C. Following dialysis, the purified HPG in aqueous solution was filtered with a 0.45 μm polyethersulfone filter and stored at ~ 25 wt% at 5 °C until use. Purity was confirmed by ^1H NMR spectroscopy in CD_3OD, and appropriate size was confirmed by DLS. Percent yield was ~ 80%. ^1H NMR (500 MHz, CD_3OD): δ = 3.94–3.53 (br; 1H, 2H; HPG).

4.3.4. Synthesis of HPG-C16

An aqueous solution of HPG (~ 60 mL; ~ 25 wt%) was transferred to a 250 mL round-bottom Schlenk flask. The HPG solution was frozen using liquid N_2 and lyophilized over 48 h. The flask containing the HPG was then heated under vacuum (95 °C; ~ 3 Pa) for 18 h to remove trace water. The mass of this dry HPG was determined to be 14.8 g (222 mmol hydroxyl). Data from prior experiments using size-exclusion chromatography with multi-angle light scattering and inverse-gated ^{13}C NMR spectroscopy were used to determine a hydroxyl content for high-molecular-weight HPGs of 15 mmol g^{-1}; this value was used to calculate equivalents of hydroxyl groups of the HPG. Anhydrous NMP (100 mL) was added to the flask containing the dry HPG, and the HPG was dissolved at 50 °C. Following dissolution of the HPG, the reaction mixture was allowed to cool to 21 °C, and DIPEA (510 μL; 2.93 mmol) was added. Next, PTFE tubing (20 gauge) was connected to flask through a septum under positive pressure of N_2, and using a syringe pump, palmitoyl chloride solution (20.6 mL; 2.27 mmol; 3.33% v/v in anhydrous NMP) was added over 1 h, at 21 °C, under N_2, while stirring at 400 rpm. Following complete addition of the palmitoyl chloride, the reaction mixture was heated to 40 °C and was allowed to proceed for ~ 20 h. The reaction mixture was then transferred to dialysis tubing (25 kDa MWCO) and was dialyzed against MeOH for ~ 24 h at 21 °C. During dialysis, some material precipitated from

solution and largely redissolved after four changes of the dialysate. Following dialysis, a small amount of remaining insoluble material was separated via centrifugation for 10 min at 3000 *g* and discarded. Following centrifugation, the solution of crude product was concentrated using a rotary evaporator and precipitated in acetone. Three additional precipitations were performed: once more in acetone, and twice in Et_2O. After each precipitation, the product was redissolved in MeOH. Following the final precipitation, the product was isolated as solid grains and dried under vacuum (~ 3 Pa) over several days. Purity and functionalization were confirmed by ^{1}H NMR spectroscopy in CD_3OD. Functionalization was determined relative to the HPG repeat unit using ^{1}H NMR spectroscopy. A factor of 1.1, corresponding to the average number of hydroxyl groups per repeat unit, previously determined from experiments with inverse-gated ^{13}C NMR spectroscopy and size-exclusion chromatography with multi-angle light scattering, was used to estimate the degree of functionalization relative to hydroxyl groups, $f_n = 0.70$. Appropriate size was confirmed by DLS. Percent yield was ~ 95%. ^{1}H NMR (500 MHz, CD_3OD): δ = 3.94–3.53 (br; HPG), 2.37 (br, –CH_2–), 1.63 (br, –CH_2–), 1.30 (br, –CH_2–), 0.91 (t, –CH_3).

4.3.5. Synthesis of SANs

Lyophilized BSA powder (2.00 g) was dissolved in 0.35 M phosphate buffer (58.69 mL; pH ~ 7.4 at 37 °C; I = 1.00 M, adjusted with NaCl) to afford a 0.5 mM solution of BSA. This solution was filtered with a 0.22 μm syringe filter (25 mm, cellulose acetate). The filtered solution (50 mL; 0.025 mmol) was then added to a 250 mL round-bottom flask equipped with an egg-shaped PTFE stir bar (1 in × 0.5 in). The flask was lowered into a water bath at 37 °C, Antifoam A solution (20 μL; 25% w/w in propylene glycol) was added to the BSA solution, and

the solution was stirred for 20 min at 250 rpm. Using a syringe pump, glutaraldehyde solution (8.7% w/w in H_2O) was added over 3 h, at 37 °C, 250 rpm. Depending on the target size of the SAN, different addition rates were used to add different amounts of glutaraldehyde. For SAN-30, an addition rate of 0.377 mL h^{-1} was used (1.13 mL solution; 1.00 mmol glutaraldehyde). For SAN-45, an addition rate of 0.425 mL h^{-1} was used (1.27 mL solution; 1.13 mmol glutaraldehyde). For SAN-60, an addition rate of 0.471 mL h^{-1} was used (1.41 mL solution; 1.25 mmol glutaraldehyde). Note: the source, age, and storage conditions for glutaraldehyde were found to be important for synthesizing SANs reproducibly in the nominal sizes. Some calibration of reaction conditions, especially between lots of glutaraldehyde could be necessary. Additionally, careful adjustment of the syringe pump and verification of accurate dispensing is essential, since relatively small differences in quantity of glutaraldehyde added can result in significant differences in sizes of the SANs. Immediately following complete addition of glutaraldehyde, ethanolamine hydrochloride solution (2.5 M) was added (4.00 mL, 10 mmol for SAN-30; 4.50 mL, 11.3 mmol for SAN-45; 5.00 mL, 12.5 mmol for SAN-60). The reaction was allowed to proceed under the same conditions (37 °C, 250 rpm) for 1 h. Next, $NaBH_4$ solution (1.0 M) was added (2.5 mL, 2.5 mmol for SAN-30; 2.8 mL, 2.8 mmol for SAN-45; 3.1 mL, 3.1 mL for SAN-60). After 30 min, an equivalent portion of $NaBH_4$ was added, and the reaction was allowed to proceed under the same conditions (37 °C, 250 rpm) for another 30 min. Note: $NaBH_4$ was pre-weighed and was dissolved in deionized H_2O immediately before addition to the reaction mixture. A bleed needle was used to vent the reaction vessel following addition of $NaBH_4$. The reaction mixture was incubated at 5 °C, stirring at 80 rpm for ~ 20 h. For purification, the reaction mixture was dialyzed (25 kDa MWCO) against deionized H_2O for 3 d at 5 °C. Following dialysis, the SAN solution was filtered using 1 μm syringe filter (25 mm,

glass fiber), frozen using liquid N_2, and lyophilized over 3 d. Appropriate size was confirmed by DLS. Typical percent yield was ~ 90%. SANs were stored at −20 °C or −80 °C until use.

4.3.6. Dynamic Light Scattering (DLS)

For DLS of HPG, deionized H_2O or MeOH was used as the dispersant. For DLS of HPG-C16, MeOH was used as the dispersant. Samples were filtered with 0.22 μm cellulose acetate syringe filters. DLS experiments were run at 25 °C, using a quartz cuvette. Experiments were conducted using 173° non-invasive back scatter configuration. Three measurements, consisting of 10 (10 s) runs each, were performed per sample and averaged.

4.3.7. Circular Dichroism (CD) Spectroscopy of SANs

SANs and BSA (for comparison) were dissolved in 25 mM phosphate buffer (pH ~ 7.4) at a concentration of 0.25 mg mL^{-1}. Samples were filtered with a 0.22 μm syringe filter (25 mm, cellulose acetate). CD experiments were run at 25 °C, using a quartz cuvette with 0.5 mm path length. Spectra were obtained using a digital integration time of 4 s, a scanning speed of 20 nm min^{-1}, an accumulation of 4 scans, and a bandwidth of 1 nm. The sample chamber was purged with N_2 gas for 15 minutes after loading each sample, prior to running each experiment. A background spectrum for 25 mM phosphate buffer was recorded and subtracted from the spectrum for each material. Spectra were normalized using the area bounded by each curve.

4.3.8. Preparation of Hydrogels

Hydrogels were prepared by adding solid components to one syringe and liquid components (1X PBS unless specified otherwise) to another, connecting both syringes with 90° elbow connector, and mixing the components by pushing the contents of the syringes back and forth between the two syringes. Contents of the syringes were dissolved and homogenized over 3 d. The connected syringes were stored at 5 °C during this time, and their contents were mixed occasionally, every few hours, over the course of the 3 d. Finally, when the contents of the syringes appeared homogeneous, the contents were transferred to a single syringe, the syringe was capped, and it was centrifuged for 30 s at 1000 *g* with the tip of the syringe oriented upward, to aid in removal of excess air from the syringes. Note: care was taken to use minimal centrifugal force to avoid leakage from syringes. Capped syringes with excess air removed were additionally centrifuged tip-down in 10 min intervals at 3000 *g* to remove small bubbles, when necessary. Hydrogels were stored in capped syringes at 5 °C until use.

For example, to prepare 2.0 g of a 15 wt% hydrogel with 1:1 HPG-C16 and SAN-45, HPG-C16 (0.12 g) was first added to a syringe with the plunger removed, followed by SAN-45 (0.18 g). The plunger was removed from the second syringe, an elbow connector was attached, and the elbow connector was capped. 1X PBS (1.7 mL) was carefully added to the capped syringe without spillage into the elbow connector. The plunger was reattached, and the syringe was inverted and quickly shaken in a single motion to remove PBS from the tip of the syringe. The cap could then be removed from the elbow connector without risk of expelling PBS from the slightly pressurized system. The two syringes were then connected, their contents were dissolved and homogenized, and excess air and small bubbles were removed, as described above.

For preparing pre-saturated SAN hydrogels, pre-saturation of SANs with palmitate was accomplished by preparing stock solutions of the SANs, mixing them with an excess of powdered palmitate (50 mg palmitate for ~ 2.8 mL SAN solution), incubating with orbital shaking (21 °C, 25 h, 150 rpm), and filtration with 0.22 μm syringe filter (25 mm, cellulose acetate). The pre-saturated SAN stock solutions were used to prepare the pre-saturated SAN hydrogels. Standard SAN hydrogels were prepared analogously for direct rheologic comparison.

4.3.9. Rheometry of Hydrogels

Hydrogels for rheometry were prepared as described above. Particular care was taken to remove bubbles prior to testing, via centrifugation. For all experiments, a cross-hatched 20 mm stainless steel geometry was used, with a cross-hatched lower plate, and a solvent trap to minimize evaporation. The shear gap was set to 750 μm, with a trim gap of 25 μm. Samples were conditioned at 25 °C, using a 5 min pre-shear at a shear rate of 0.1 s^{-1}, followed by equilibration for 5 min. For all experiments, at least three runs were performed per sample and averaged. Logarithmic shear rate sweeps in the range of 0.1–100 s^{-1} were performed at 25 °C to determine apparent viscosities of the hydrogels, as well as probe apparent shear thinning behavior. Oscillatory strain amplitude sweeps in the range of 0.1– 100% were performed at a constant angular frequency of 10 rad s^{-1}, at 25 °C, to determine the limit of the linear viscoelastic regime. The limit of the linear viscoelastic regime in terms of stress amplitude was taken as the yield stress. Oscillatory frequency sweeps in the range of 0.1–100 rad s^{-1} were performed at a constant strain amplitude within the linear regime (1%), at 25 °C, to probe time-dependent viscoelastic behavior of the hydrogels. Multi-step oscillatory tests, with alternating small-amplitude and

large-amplitude steps, were used to investigate thixotropy and self-healing behavior of the hydrogels. For these tests, seven steps (60 s each), with alternating high (200%) and low (1%) strain amplitude, at constant angular frequency of 10 rad s^{-1}, at 25 °C, were used. Tests with longer (600 s) steps were also performed. Finally, temperature ramps from 5–50 °C at a rate of 2 °C min^{-1} were performed at a constant strain amplitude of 1% and a constant angular frequency of 10 rad s^{-1}.

4.3.10. Injection Force Measurements

A custom syringe holder (Figure C3) was design and 3D printed using fused filament fabrication, with poly(lactide) filament. The syringe holder was designed to interface with the compression fixtures of a TestResources 100 Series Universal Test Machine and hold a 1 mL syringe (BD, 309628) with the tip of the syringe oriented downward. Tests were performed with 23 G and 27 G needles of 0.5 in length. Hydrogels were prepared as described above. A slight excess of hydrogel was loaded into the syringe prior to each test. A pre-load of 0.1 N was used for each test. An injection rates of 1.2 mL min^{-1} (68 mm min^{-1}) was used over a test period of 10 s. For all experiments, three runs were performed and averaged.

4.3.11. Hydrogel Dissolution Experiments

Hydrogels for dissolution experiments were prepared as described above. Each gel was prepared using the corresponding dissolution medium. Dissolution media were 1X PBS and DMEM with 10% FBS and 1% penicillin-streptomycin. NaN_3 (50 mM) was included in

dissolution media to prevent microbial contamination. Hydrogels (300 mg) were loaded into 1.5 mL microcentrifuge tubes (VWR, 89000-028) and centrifuged for 1 min at 3000 *g* to uniformly localize the gel samples to the bottoms of the tubes. Dissolution medium (1000 μL) was placed over each sample. Tubes were incubated at 37 °C without agitation. Time points for sampling were 0.5 d, 1.5 d, 3.5 d, 7.5 d, 15.5 d, and 31.5 d. At each time point, the supernatant was carefully collected from each tube and replaced with 1000 μL of fresh dissolution medium. Collected supernatants were frozen with liquid N_2 and lyophilized. Mass loss from gels due to dissolution was estimated from dry mass remaining after lyophilization, assuming concentrations of the components of the dissolution media remained constant.

4.3.12. In Vitro IgG Release Experiments

Lyophilized bovine IgG powder was reconstituted in 1X PBS to a concentration of 5 mg mL^{-1}. Aliquots (1.0 mL) of the IgG stock solution were stored at −20 °C until use. NHS-sulfo-Cy5 (5 mg) was dissolved in anhydrous DMF to prepare a stock solution (10 mM) and stored air-free at −20 °C until use. NHS-palmitate (11.6 g) was dissolved in anhydrous DMF to prepare a stock solution (15 mM) and stored air-free at −20 °C until use.

IgG solution (4.7 mL; 0.14 μmol) was transferred to a glass vial. The IgG solution was diluted twofold with 0.1 M phosphate buffer (pH ~ 7.4) with 20% v/v DMSO, and 4% w/v CHAPS. NHS-sulfo-Cy5 solution (80 μL; 0.80 μmol) was added to IgG solution and promptly mixed in. The reaction was allowed to proceed for 2 h, at 21 °C, with orbital shaking at 150 rpm. Half of the reaction mixture (4.7 mL; 0.07 μmol IgG) was then transferred to a second glass vial, and NHS-palmitate solution (80 μL; 1.2 μmol) was added to the second vial and promptly mixed

in. The rection was allowed to proceed for 4 h, at 21 °C, with orbital shaking at 150 rpm. Both reaction mixtures were refrigerated for 12 h. Each crude IgG product was purified by diafiltration (Amicon Ultra-15; 50 kDa MWCO) against 75 mL of 1X PBS with 10% v/v DMSO followed by 75 mL of 1X PBS. A significant amount of protein adhering to the filter as well as a small amount of insoluble product appearing during filtration against pure PBS were taken as evidence of successful palmitate labeling. These phenomena were not observed with Cy5 labeling alone. The small amount of insoluble material was separated by centrifugation and discarded. The pure modified IgG species were concentrated to ~ 5 mg mL^{-1} in 1X PBS and stored at 5 °C until use within 3 d. Cy5-containing mixtures were shielded from light whenever possible. Degree of labeling with the Cy5 dye was determined by spectrophotometry (i.e., using absorbance at 280 nm and 646 nm) to be 2.2 M M^{-1} and 2.0 M M^{-1} for IgG-Cy5 and IgG-Cy5-C16, respectively. Percent yield was ~ 93% and ~ 62% for IgG-Cy5 and IgG-Cy5-C16, respectively.

Hydrogels for dissolution experiments were prepared as described above, using 1X PBS with NaN_3 (50 mM) to prevent microbial contamination. The release medium was FluoroBrite DMEM with 10% FBS, 1% penicillin-streptomycin, and 50 mM NaN_3. Hydrogels (300 mg) were loaded into 1.5 mL microcentrifuge tubes (VWR, 89000-028) and centrifuged for 1 min at 3000 *g* to uniformly localize the gel samples to the bottoms of the tubes. Dissolution medium (1000 µL) was placed over each sample. Tubes were incubated at 37 °C without agitation. Time points for sampling were 0.5 d, 1.5 d, 3.5 d, 7.5 d, 15.5 d, and 31.5 d. At each time point, the supernatant was carefully collected from each tube and replaced with 1000 µL of fresh release medium. Quantities of IgG-Cy5 and IgG-Cy5-C16 were determined by measuring fluorescence intensity of the supernatants using a standard curve.

4.3.13. Direct Ink Writing (DIW)

Direct ink writing was performed on a HyRel Engine SR extrusion-based 3D printer equipped with an SDS-5 syringe dispenser. Standard 5 mL syringes (BD) were used with 27 G needles with 0.5 in length. An extrusion rate of 70 pulse μL^{-1}, a print speed of 200 mm min^{-1}, and a layer height of 0.21 mm were used for all prints.

4.4. Results and Discussion

Our aim was to utilize protein-ligand interactions to obtain hydrogels that could (1) be conveniently mixed, (2) be dispensed from a syringe using modest force, yet (3) would exhibit mechanical stability once injected or deposited on a surface. Initial experiments with palmitate-functionalized branched poly(ethylene glycol)s suggested a potential need for higher valency branched architectures in order to obtain self-supporting hydrogels. We hypothesized that hyperbranched poly(glycerol)s (HPGs) could fill this need. HPGs are hyperbranched polyethers with a globular structure and glycerol-derivative repeat units.[60] They thus possess an abundance of hydroxyl side chains and end groups. Their globular structure and hydrophilic surface functionality afford high aqueous solubilities and low intrinsic viscosities.[60–62] HPGs have additionally been shown to possess good biocompatibility in cell culture and in vivo.[60,63,64] HPGs are typically synthesized by ring-opening multi-branching polymerization (ROMBP) of glycidol. Sunder at al. first demonstrated that substoichiometric deprotonation of the triol initiator, trimethylolpropane, in conjunction with slow addition of glycidol, improves control over size

and uniformity of HPGs.[61] Kainthan et al. later reported that use of 1,4-dioxane as a diluent during ROMBP yields high-molecular-weight HPGs with excellent size uniformity.[62] Here, we adopted the approach of Kainthan et al. to synthesize HPGs with Z-average hydrodynamic diameters, $d_H \approx 14$ nm with dispersities by DLS of ~ 0.04 (Figure 4.1a,b).

We hypothesized that HPGs derivatized with palmitate moieties could exhibit supramolecular assembly with serum albumin via the native long-chain fatty acid binding of serum albumins. HPGs derivatized with hydrophobic aliphatic moieties have been previously reported as synthetic analogs of serum albumin and have been explored for therapeutic delivery.[60,63,64] Upon synthesizing HPGs functionalized with palmitoyl moieties at ~ 0.7% (relative to hydroxyl groups) (Figure 4.1c,d), we observed self-association of these hydrophobically derivatized HPGs in aqueous solution to afford robust physical hydrogels at ≥ 15 wt% polymer content (Figure 4.2a,b). Small-amplitude oscillatory shear experiments were performed to determine the strength and stiffness of a 15 wt% HPG-C16 gel, as well as the extent of its elastic character. This gel showed a storage modulus, $G' \approx 6800$ Pa, $\tan \delta \approx 0.13$, and an apparent yield stress, $\sigma_y \approx 130$ Pa at angular frequency, $\omega = 10$ rad s^{-1} (Figure 4.2c–g). Notably, HPG-C16 gels were opaque upon mixing but became nearly transparent after being allowed to rest. This change in opacity was reversible (Figure 4.2b). In order to test whether assembly between HPG-C16 and serum albumin would occur, 1:1 mixtures of HPG-C16 and BSA were prepared on a mass basis. This ratio of components nominally affords ~ 1.2 palmitate moieties per primary binding site of BSA. Interestingly, mixtures of HPG-C16 and BSA were nearly transparent, showing viscous liquid character (Figure 4.3a,d,e). Increasing transparency was observed at higher total BSA and HPG-C16 concentrations at constant mass ratio, as well as at higher BSA concentrations relative to that of HPG-C16. Increasing the amount of BSA in the

mixture relative to that of HPG-C16 also failed to afford a gel, and in fact yielded mixtures that flowed more readily. A 1:1 mixture with a total BSA and HPG-C16 content of 15 wt% showed tan $\delta > 1$ over the frequency range, 0.1 rad $s^{-1} \leq \omega \leq 100$ rad s^{-1} (Figure 4.3d). Steady-shear rheometry was used to measure apparent viscosity of this material with respect to shear rate. Logarithmic shear-rate sweeps showed apparent shear thinning behavior over the range of shear rates, 0.1 $s^{-1} \leq \dot{\gamma} \leq 100$ s^{-1}, with an apparent viscosity, $\eta \approx 31$ Pa s at $\dot{\gamma} = 1.0$ s^{-1} (Figure 4.3b,g). Increasing the total concentration to 30 wt% afforded markedly increased viscosity, $\eta \approx 1200$ Pa s at $\dot{\gamma} = 1.0$ s^{-1} (Figure 4.3c,g). When the viscosity curves for the 15 wt% and 30 wt% materials were fit to a power law model, power law indices of $n = 0.50$ and $n = 0.38$, respectively, were determined, indicating more pronounced shear thinning behavior for the more concentrated mixture (Figure 4.3g). In order to further probe the effect of the albumin-palmitate interactions on rheology of these materials, we performed a series of tests on gels where the BSA was pre-saturated with free palmitate. The maximum palmitate loading achievable for BSA in vitro is 6 M M^{-1}.[49] Pre-saturated BSA and HPG-C16 mixtures were obtained simply by incubating a solution of BSA in the presence of excess powdered palmitate for 24 h,[49] removing excess palmitate by filtration, and mixing the filtrate with HPG-C16. These mixtures containing free palmitate competitively bound to BSA showed markedly different rheologic behavior. For pre-saturated 1:1 mixtures at 15 wt% and 30 wt% total concentrations, frequency sweeps showed tan $\delta < 1$ over the entire frequency range investigated, indicating gel-like behavior (Figure 4.3d,e). Remarkably, for the pre-saturated mixtures, curves for viscoelastic moduli, G' and G'', showed similar profiles to those of the pure HPG-C16 gel. Steady-shear curves also showed altered profiles when the BSA was pre-saturated, bearing resemblance to those of the pure HPG-C16 gel. Notably, these mixtures containing free palmitate also appeared more opaque, with the 15

wt% mixture showing similar appearance to that of the pure HPG-C16 gel (Figure 4.2b; Figure 4.3a). Again, increased transparency was observed at 30 wt%. Taken together, these rheologic findings supported the hypothesis that BSA was interacting with HPG-C16 via its palmitate moieties. However, these interactions, which could apparently be competitively inhibited, were not conducive to the formation of a physical network required for a self-supporting hydrogel.

We hypothesized that substituting larger-scale species with higher valency for palmitate binding, for the native, predominantly monomeric BSA could afford productive self-assembly toward network formation. Palmer and coworkers have previously reported a simple and scalable approach for synthesizing nano-sized covalently cross-linked serum albumin species.[65–67] These species were obtained by cross-linking albumin in dilute solution using glutaraldehyde. We adapted this approach to produce soluble albumin nanostructures (SANs) in Z-average hydrodynamic diameters, $d_H \approx 30$ nm (SAN-30), $d_H \approx 45$ nm (SAN-45), $d_H \approx 60$ nm (SAN-60), with dispersities by DLS ~ 0.24–0.27 (Figure 4.4a–c). These SANs retained high aqueous solubilities and relatively low intrinsic viscosities reminiscent of native BSA. Circular dichroism (CD) spectroscopy of the SANs additionally showed retention of the characteristic α-helical secondary structure of serum albumins (Figure 4.4d), suggesting that intact BSA units of the SANs could retain capacity for ligand binding. Upon mixing SAN-45 with HPG-C16 in a 3:2 mass ratio, at 15 wt% total concentration, we observed gel formation (Figure 4.5a,b,d). Initially, excesses of the SANs over HPG-C16 were included in formulations, to attempt to account for expected obstruction of some proportion of fatty acid binding site due to cross-linking of the albumin. The 15 wt% 3:2 gel was transparent (Figure 4.5b) like the HPG-C16 and BSA mixtures, possibly suggesting disruption of HPG-C16 self-association. Yet, the mixtures with the SAN showed tan $\delta < 1$ over the entire frequency range investigated (Figure 4.5d), indicating dominant

elastic character afforded by continuous network structure. This gel exhibited $G' \approx 2200$ Pa, tan $\delta \approx 0.42$, and $\sigma_y \approx 270$ Pa at $\omega = 10$ rad s^{-1} (Figure 4.5d,e,g,h). This gel also exhibited $\eta \approx 630$ Pa s at $\dot{\gamma} = 1.0$ s^{-1} and $n = 0.27$ (Figure 4.5c,f). Finally, when the SAN-45 was pre-saturated with free palmitate in a manner analogous to that with BSA, the palmitate-saturated gel looked optically similar the unsaturated gel; however, the saturated gel showed significantly different rheological behavior (Figure 4.5c–h). This suggested that the SAN-45 exhibited palmitate-binding, and this interaction could be competitively inhibited—*vide infra*. We chose this 15 wt% 3:2 gel made with SAN-45 (unsaturated) as our "intermediate" formulation and proceeded to investigation of the rheological effects of individually increasing or decreasing (1) the total concentration, (2) the mass ratio of the SAN to HPG-C16, and (3) the size of the SAN.

For the investigation of the effects of varying total concentration, the mass ratio of the two components was kept constant at 3:2, and SAN-45 was used in all formulations. We observed that a 10 wt% mixture appeared opaque and exhibited a weak gel character (Figure 4.6a,g). Increasing total concentration to 20 wt% afforded a strong, transparent gel (Figure 4.6a,g,j). The overall trends observed were that viscosity, storage modulus, and yield stress increased steadily with total concentration; however, n and tan δ did not change significantly between 10 wt% and 15 wt%, and only showed statistically significant but slight reductions at 20 wt% (Figure 4.7a,d,g). This indicated that a slightly more elastic and more strongly shear thinning gel could be produced by increasing total concentration; however, these changes would be accompanied by a more prominent increase in the material's resistance to being sheared or dispensed from a syringe. While we desired stability of the gel at rest, as well as strong shear thinning behavior, we found that the 20 wt% gel offered excessive resistance to mixing, removal of bubbles via centrifugation, and injection/extrusion.

Next, we investigated the effects of varying the mass of ratio of the SAN and HPG-C16. Total concentration was kept constant at 15 wt%, and SAN-45 was used in all formulations. The three formulations tested, 7:3, 3:2, and 1:1, SAN to HPG-C16, were largely transparent, but showed slightly increasing opacity with increasing HPG-C16 content (Figure 4.6b). Increasing elastic character, quantified by tan δ, and increasing extent of shear thinning, quantified by n, were also apparent with increasing HPG-C16 content (Figure 4.7b,e). Changes in viscosity, storage modulus, and yield stress were not substantial, especially when increasing HPG-C16 content from 40% of the macromolecule content (in the 3:2 formulation) to 50% (in the 1:1 formulation) (Figure 4.7b,e,h). Ultimately, the 7:3 and 3:2 formulations showed dominant viscous character (tan $\delta > 1$) at low angular frequencies (Figure 4.6h), and thus were not very stable (i.e., flowed noticeably) at rest.

Finally, we investigated the effects of varying the SAN size. Total concentration was kept constant at 15 wt%, and the mass ratio of the two components was kept constant at 3:2. Again, the three formulations, made with SAN-30, SAN-45, or SAN-60, were largely transparent (Figure 4.6c). The formulation with SAN-30 showed viscoelastic liquid (as opposed to gel) character (Figure 4.6i). Between the SAN-45 and SAN-60 formulations, increasing size of the SAN did not result in substantial changes in viscosity, storage modulus, and yield stress; however, moderate decreases in tan δ and n indicated increased elastic character and shear thinning behavior (Figure 4.7c,f,i). To obtain a hydrogel that could (1) be conveniently mixed, (2) be dispensed from a syringe using modest force, yet (3) would exhibit mechanical stability once injected or deposited on a surface, we decided to proceed with 15 wt% total concentration and 1:1 mass ratio of SAN-60 to HPG-C16. We refer to this formulation as the “combined” formulation, as it involved combing the approaches of increasing HPG-C16 content and SAN

size relative to the intermediate formulation (Figure 4.8a). This gel exhibited $G' \approx 3400$ Pa, tan $\delta \approx 0.33$, and $\sigma_y \approx 170$ Pa at $\omega = 10$ rad s^{-1} (Figure 4.8c,d,f,g). This gel also showed $\eta \approx 510$ Pa s at $\dot{\gamma} = 1.0$ s^{-1} and a power law index, $n \approx 0.04$ (Figure 4.8b,e). This gel was noticeably more stable at rest than the intermediate formulation but still exhibited good flowability under shear load.

To investigate the thixotropy and self-healing behaviors of the intermediate and combined gels, we performed multi-step oscillatory tests with alternating small-amplitude (γ_0 = 1%) and large-amplitude (γ_0 = 200%) steps. Both intermediate and combined gels exhibited time-dependent disruption of their physical network structures at high strain amplitude, with prompt recovery of moduli during the subsequent low-amplitude interval (Figure 4.8h). The combined gel exhibited slightly more pronounced thixotropic behavior, as evidenced by the more pronounced gradients of the modulus curves in both the high-strain and low-stain intervals (Figure 4.8h). Finally, to investigate thermo-rheological behaviors of these gels, temperature ramps were performed on both intermediate and combined gels. Tan $\delta < 1$ was observed for both gels between 5 °C and 50 °C. Both gels exhibited increasing tan δ with increasing temperature. Both gels showed dominant albeit reduced elastic character, as well as reduced G', at 37 °C (Figure 4.8i,j).

Next, to investigate in greater detail the effects of competitive inhibition of HPG-C16 binding of the SANs, we prepared intermediate and combined gels containing SANs pre-saturated with palmitate. In general, during steady-shear rheometry, gels comprising non-saturated SANs and HPG-C16 exhibited edge fracture and occasionally sample displacement from the shear gap at high shear rates, due to viscoelastic instability. This is a signature of high elastic character at high shear rates or over short timescales.[68] In the steady-shear curves of the intermediate and combined gels, viscoelastic instability is evidenced by minima in steady-shear

stress at moderate to high shear rates (Figure 4.5c; Figure 4.9a). Interestingly, when SANs were pre-saturated with free palmitate, both intermediate and combined gels could be sheared noticeably more smoothly, and signs of viscoelastic instability were absent from steady-shear curves (Figure 4.5c; Figure 4.9a). In addition, tan δ was greater for both pre-saturated intermediate and combined gels at moderate to high frequencies. However, interestingly, in these pre-saturated gels, tan δ was lower at low frequencies (Figure 4.5d,g; Figure 4.9b,e). This was a serendipitous finding, as it indicated that pre-saturation of SANs with free palmitate contributed simultaneously to smoother extrusion of the gels in addition to improving mechanical stability at rest. In addition, for the intermediate gel, pre-saturation resulted in decreased viscosity, storage modulus, and yield stress (Figure 4.5c–h). For the combined gel, changes in viscosity, storage modulus, and yield stress were not substantial (Figure 4.9a–f).

Injection force measurements are a direct means of assessing clinically relevant rheology of injectable materials under high shear load (Figure 4.10a). Forces < 20 N are preferred for clinical application of injectable formulations.[8,69,70] Additionally, quantification of injection/extrusion force can be valuable for assessing printability of a material via direct ink writing.[7] To investigate injectability/extrudability of these hydrogels, we performed force measurements using 1 mL syringes equipped with 23 gauge and 27 gauge needles of 0.5 in length (Figure 4.10b). All tests were performed at an injection rate of 1.2 mL min^{-1}. Using 23 gauge needles, the 15 wt% HPG-C16 gel, the intermediate gel, and the combined gel all showed injection forces < 10 N (Figure 4.10c). Using 27 gauge needles, the 15 wt% HPG-C16 gel and intermediate gel showed injection force < 20 N. The combined gel showed slightly higher injection force at 22 N (Figure 4.10d). For comparison, a 30wt% Pluronic F-127 gel was tested. The F-127 gel showed an injection force of ~ 15 N through the 23 G needle (Figure 4.10c);

however, the injection force increased beyond clinically relevant levels to ~ 67 N when the 27 G needle was used (Figure 4.10d).

Interestingly, all investigated mixtures containing some portion of HPG-C16 showed limited solubility in excess aqueous media. Despite the fact that homogeneous, nearly transparent hydrogels can be prepared from HPG-C16 at ≥ 15 wt% polymer content, when HPG-C16 containing gels are incubated in excess aqueous solution, they appear to exhibit further phase separation (Figure 4.11a). The same phenomenon was observed at 21 °C and 37 °C. Thus, to explore dissolution of these materials in relevant aqueous media, we performed dissolution experiments over a period of one month (Figure 4.11b–d). Each gel (0.3 g) was incubated in a 1.5 mL microcentrifuge tube containing an additional 1.0 mL of dissolution medium. Tests were performed under static conditions at 37 °C. When 1X phosphate buffered saline (PBS) was used as the dissolution medium, the materials showed dissolution profiles characteristic of a first-order process (Figure 4.11c). In this case, the 15 wt% HPG-C16 gel exhibited the least mass loss, at 6.4% over 31.5 d. The 15 wt% 1:1 mixture of BSA and HPG-C16 exhibited the greatest mass loss, at 53% over 31.5 d. The intermediate and combined gels exhibited moderate degrees of mass loss, at 24% and 15%, respectively, over 31.5 d (Figure 4.11c). We hypothesized that serum components present in cell culture applications or in vivo could accelerate dissolution of these materials by potentially competing with binding interactions and/or solubilizing the network components. Therefore, we conducted an analogous test with Dulbecco's Modified Eagle's Medium (DMEM) supplemented with 10% fetal bovine serum (FBS) as the dissolution medium. Relative to results with 1X PBS, we observed similar degrees of mass loss in the serum-containing DMEM until the 15.5 d time point. Interestingly, at the 31.5 d time point, mass loss was markedly increased (Figure 4.11d). The 15 wt% 1:1 mixture of BSA and HPG-C16 exhibited

virtually complete dissolution over this period. Surprisingly, the 15 wt% HPG-C16 gel exhibited 87% mass loss over 31.5 d. The intermediate and combined gels exhibited 71% and 40% mass loss over 31.5 d (Figure 4.11d).

Next, to demonstrate in vitro release of a model protein therapeutic from these gels, we prepared gels containing 1 mg mL^{-1} IgG labeled with either a sulfo-Cyanine5 dye or both a sulfo-Cyanine5 dye and palmitate. Derivatization of protein and peptides therapeutics with fatty acids is a proven strategy to extend the half-lives of these species in vivo.[71] Toward such application, we sought to investigate whether fatty acid derivatization of IgG would slow its release from our materials in vitro (Figure 4.12a) The extent of labeling of the IgG with palmitate was kept low to retain solubility of the labeled IgG in pure aqueous buffer free of albumin or solubilizing detergents. As with the dissolution experiments, 0.3 g of each gel was incubated in a 1.5 mL microcentrifuge tube containing an additional 1.0 mL of release medium. Tests were performed under static conditions at 37 °C. The release medium was DMEM with 10% FBS. Release of IgG was tracked over approximately two weeks by measuring fluorescence of the Cynanine5 dye relative to a standard curve. The three gels (15 wt% HPG-C16, intermediate, and combined) all showed ~ 50–60% IgG release over 15.5 d (Figure 4.12b,c,e,f) On average, IgG labeled with palmitate released more slowly (Figure 4.12b); however, the differences were not substantial with the degree of palmitate labeling employed. The 15 wt% 1:1 mixture of BSA and HPG-C16 showed full release over the two-week period (Figure 4.12d).

Finally, as an initial proof of concept, we used DIW to pattern a single-layer serpentine structure using the intermediate formulation (Figure 4.13a,b). This material exhibited smooth and consistent extrusion but was not ideal for patterning multiple layers without the use of a support material or secondary cross-linking. The combined formulation was better suited for printing

multi-layered constructs. Using the combined formulation, we were able to print a cuboidal structure; however, some distortion of the structure after several minutes was observed (Figure 4.13c).

4.5. Conclusion

Dynamic hydrogels, which exhibit solid-like behavior at rest but can be injected or 3D printed via stress-induced flow from a syringe, are valuable in therapeutic delivery and biofabrication applications. Relatively few examples of dynamic hydrogels that utilize biomolecular recognition in network design currently exist in the literature. To our knowledge, all previous reports of dynamic hydrogels which incorporate specific protein or peptide interactions toward network formation feature engineered peptides or recombinant proteins, which may limit their scalability or accessibility. Here, we have exploited the long-chain fatty acid binding functionality of one of the most readily available proteins, bovine serum albumin, for the synthesis and rheological tuning of novel injectable/extrudable hydrogels. We have also highlighted the utility of a globular, high-molecular-weight hyperbranched poly(glycerol) in presenting palmitate moieties to the albumin species, as well as in formation of pure hyperbranched poly(glycerol) networks. Finally, we have preliminarily characterized the injectability of these hydrogels, their dissolution behavior, their ability to gradually release a model protein therapeutic, and their promise for direct ink writing. Future work will be aimed at further tuning these materials for specific applications in therapeutic delivery and biofabrication.

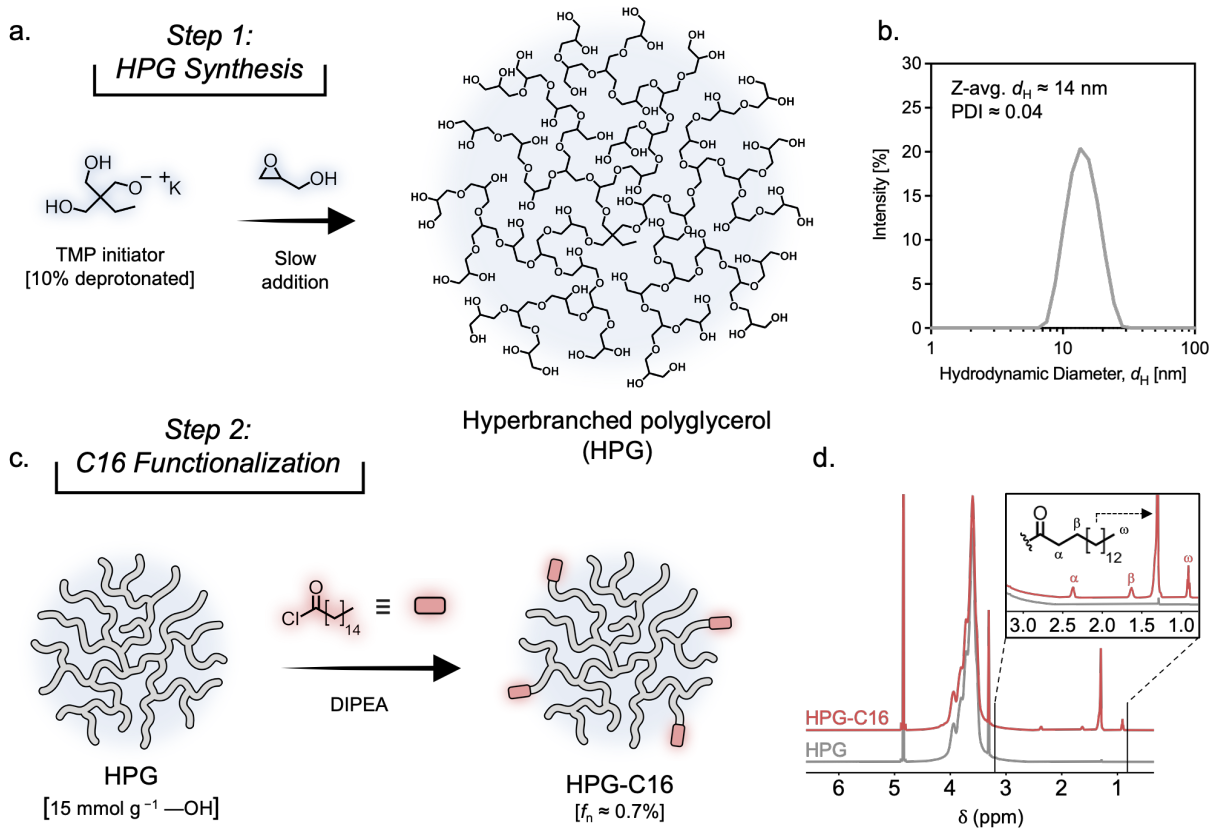

Figure 4.1. (a) Abbreviated synthetic scheme for hyperbranched poly(glycerol) (HPG). (b) Dynamic light scattering trace for HPG. A Z-average hydrodynamic diameter, $d_H \approx 14$ nm was obtained, with a dispersity by DLS of ~ 0.04. (c) Abbreviated synthetic scheme for HPG functionalized with palmitate moieties (HPG-C16). Palmitate functionalization relative to hydroxyl groups, $f_n = 0.7\%$ was obtained. (d) ^{1}H NMR spectra (500 MHz, CD_3OD) of HPG and HPG-C16.

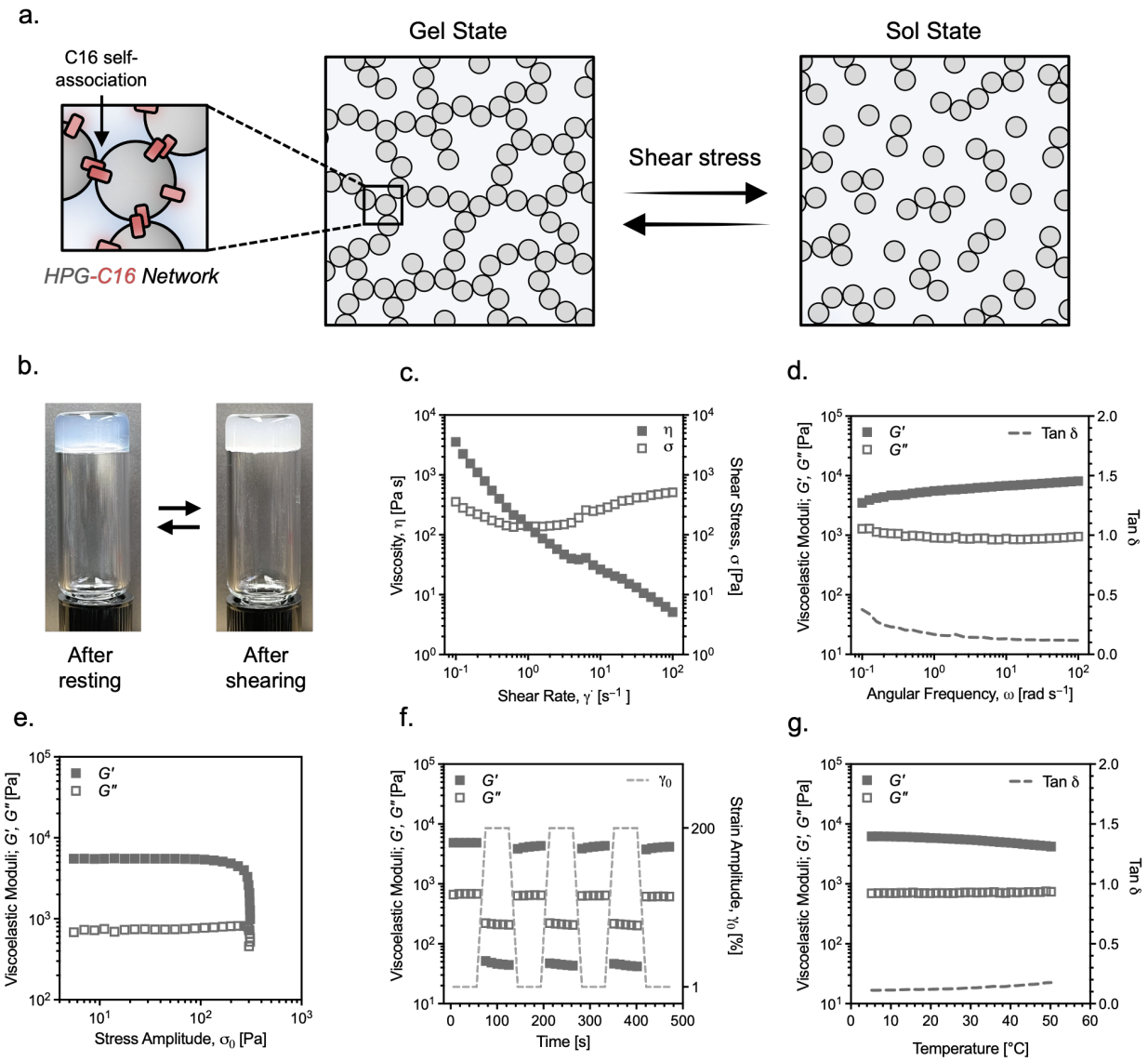

Figure 4.2. (a) Hypothetical depiction of HPG-C16 self-association in formation of dynamic networks. (b) 15 wt% HPG-C16 hydrogel vial inversion, showing the reversible transition between a nearly transparent gel state and an opaque gel state. (c) Steady-shear viscosity and stress curves for the 15 wt% HPG-C16 hydrogel. (d) Frequency sweep data for the 15 wt% HPG-C16 hydrogel. (e) Stress amplitude sweep data for the 15 wt% HPG-C16 hydrogel. (f) Multi-step high- and low-amplitude oscillatory tests showing self-healing and thixotropy of 15 wt% HPG-C16 hydrogel. (g) Temperature ramp data for the 15 wt% HPG-C16 hydrogel.

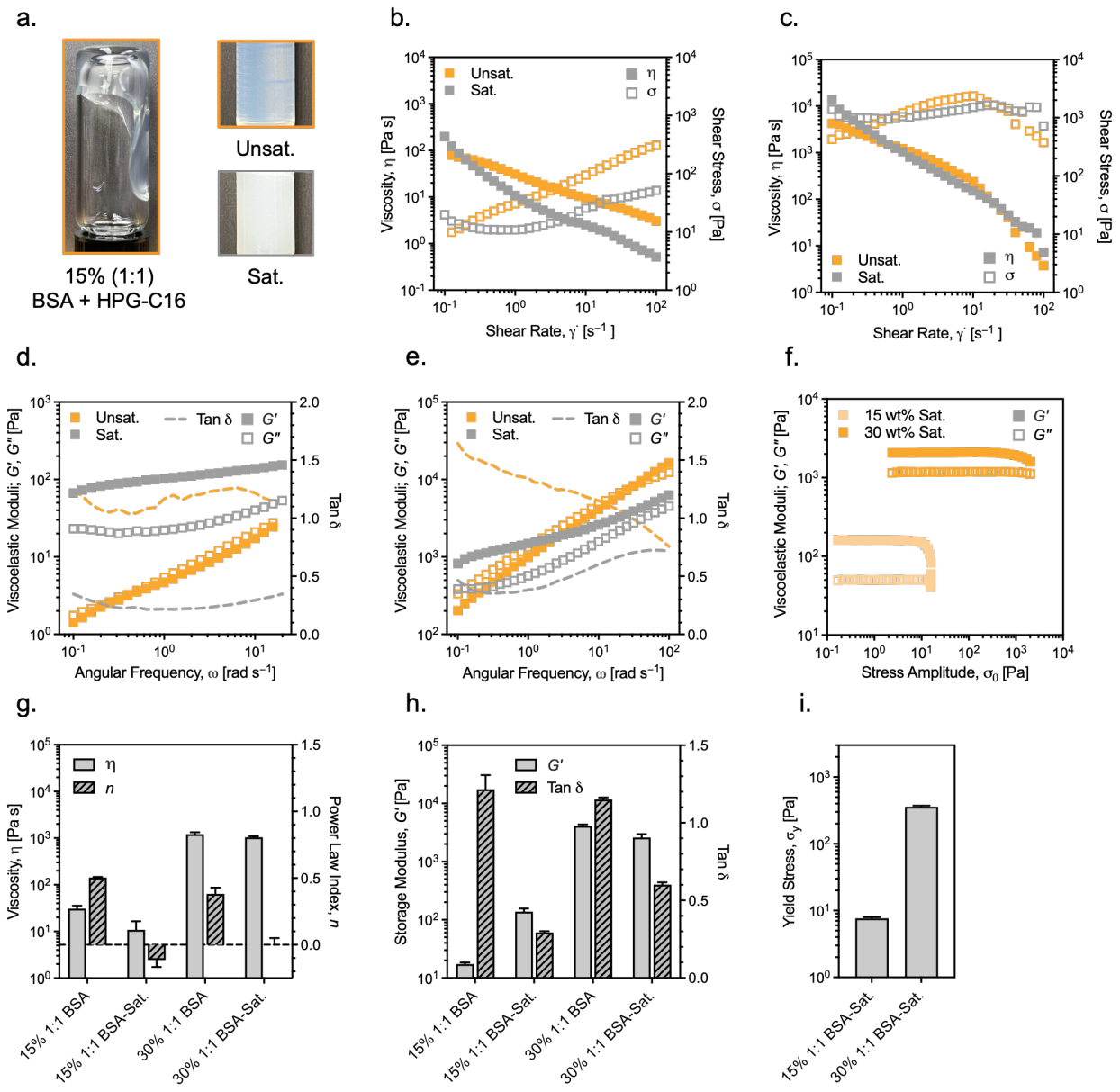

Figure 4.3. (a) Photograph of the 15 wt% 1:1 BSA and HPG-C16 mixture after vial inversion, showing viscous liquid character (left); and photographs showing the appearance of unsaturated and saturated 15 wt% 1:1 BSA and HPG-C16 mixtures (right). "Unsaturated" (unsat.) refers to mixtures comprising fatty-acid-free BSA. "Saturated" (sat.) refers to mixtures comprising BSA pre-saturated with free palmitate. (b) Steady-shear viscosity and stress curves for the 15 wt% 1:1 BSA and HPG-C16 mixtures (unsaturated and saturated). (c) Steady-shear viscosity and stress curves for the 30 wt% 1:1 BSA and HPG-C16 mixtures (unsaturated and saturated). (d) Frequency sweep data for the 15 wt% 1:1 BSA and HPG-C16 mixtures (unsaturated and

saturated). (e) Frequency sweep data for the 30 wt% 1:1 BSA and HPG-C16 mixtures (unsaturated and saturated). (f) Stress amplitude sweep data for the 15 wt% and 30 wt% saturated 1:1 BSA and HPG-C16 mixtures. Unsaturated mixtures did not show yield stresses. (g) Comparison of apparent viscosity at shear rate, $\dot{\gamma} = 1.0\ s^{-1}$ and power law index, n, for all 1:1 BSA and HPG-C16 mixtures. (h) Comparison of G' and tan δ at angular frequency, $\omega = 10$ rad s^{-1} for all 1:1 BSA and HPG-C16 mixtures. (i) Comparison of apparent yield stress for 15 wt% and 30 wt% saturated 1:1 BSA and HPG-C16 mixtures.

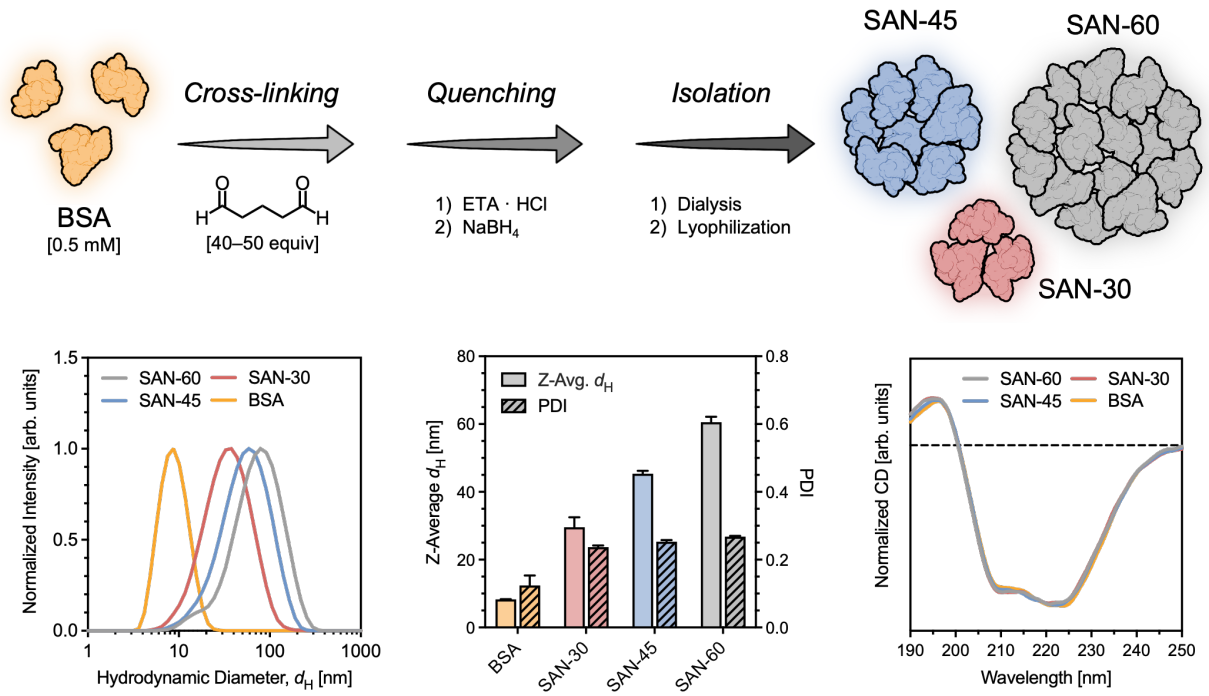

Figure 4.4. (a) Abbreviated synthetic scheme for SAN-30, SAN-45, and SAN-60. (b) Dynamic light scattering traces for SANs and native BSA. (c) Comparison of Z-average hydrodynamic diameters, d_H and dispersities by DLS for SANs and native BSA. (d) Circular dichroism (CD) spectra for SANs and native BSA showing that SANs retained the characteristic α-helical secondary structure of serum albumin.

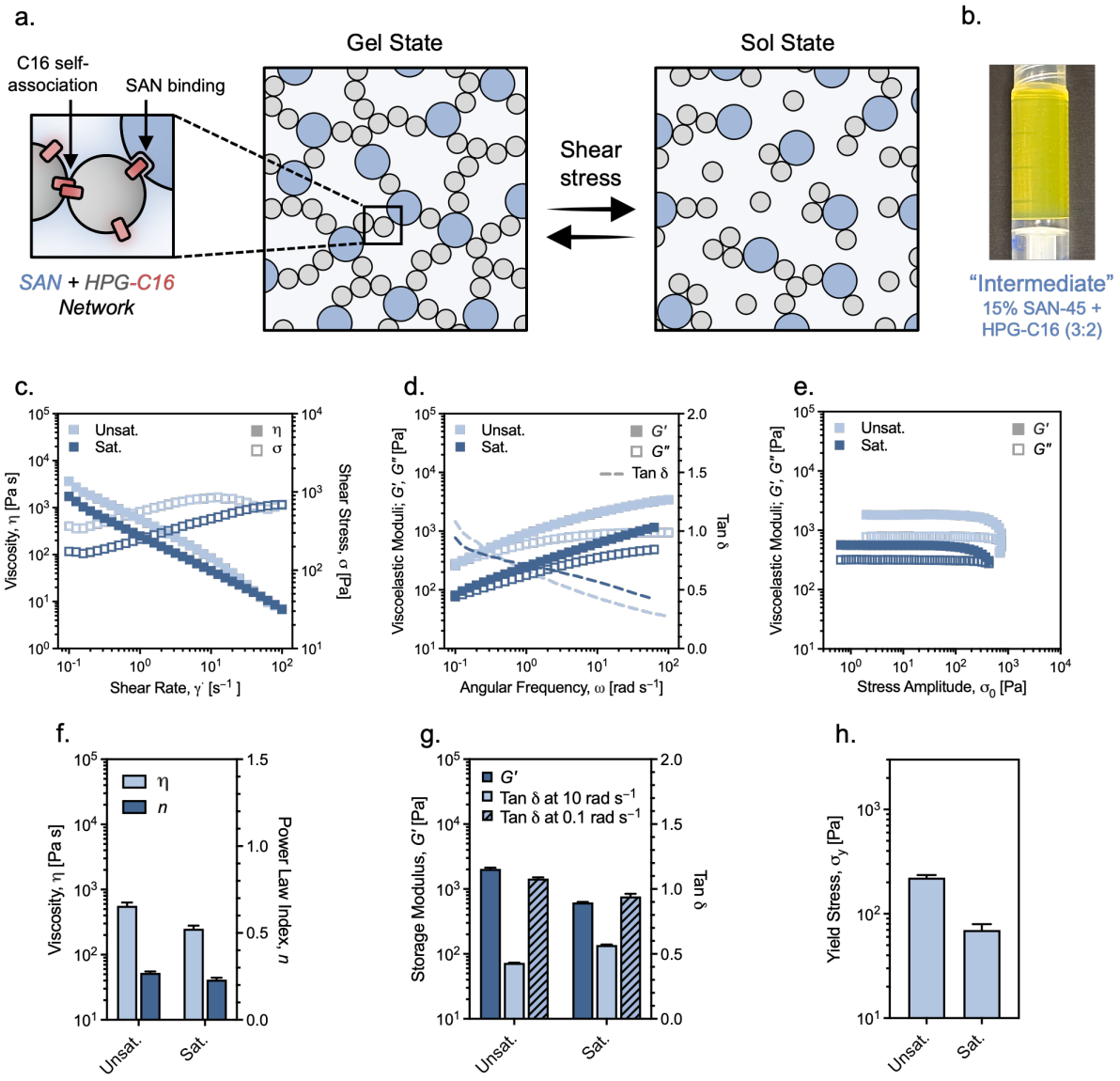

Figure 4.5. (a) Hypothetical depiction of SAN + HPG-C16 dynamic network formation. (b) The 15 wt% (3:2) SAN-45 and HPG-C16 hydrogel (termed "intermediate") inverted, inside of a syringe. (c) Steady-shear viscosity and stress curves for the intermediate gel (unsaturated and saturated). "Unsaturated" (unsat.) refers to mixtures comprising fatty-acid-free SAN. "Saturated" (sat.) refers to mixtures comprising SAN pre-saturated with free palmitate. (d) Frequency sweep data for the intermediate gel (unsaturated and saturated). (e) Stress amplitude sweep data for the intermediate gel (unsaturated and saturated). (f) Comparison of apparent viscosity at shear rate, $\dot{\gamma} = 1.0\ s^{-1}$ and power law index, n, for the intermediate gel (unsaturated and saturated). (g) Comparison of G' at angular frequency, $\omega = 10$ rad s^{-1}, and tan δ at two angular frequencies, for

the intermediate gel (unsaturated and saturated). (h) Comparison of apparent yield stress for the intermediate gel (unsaturated and saturated).

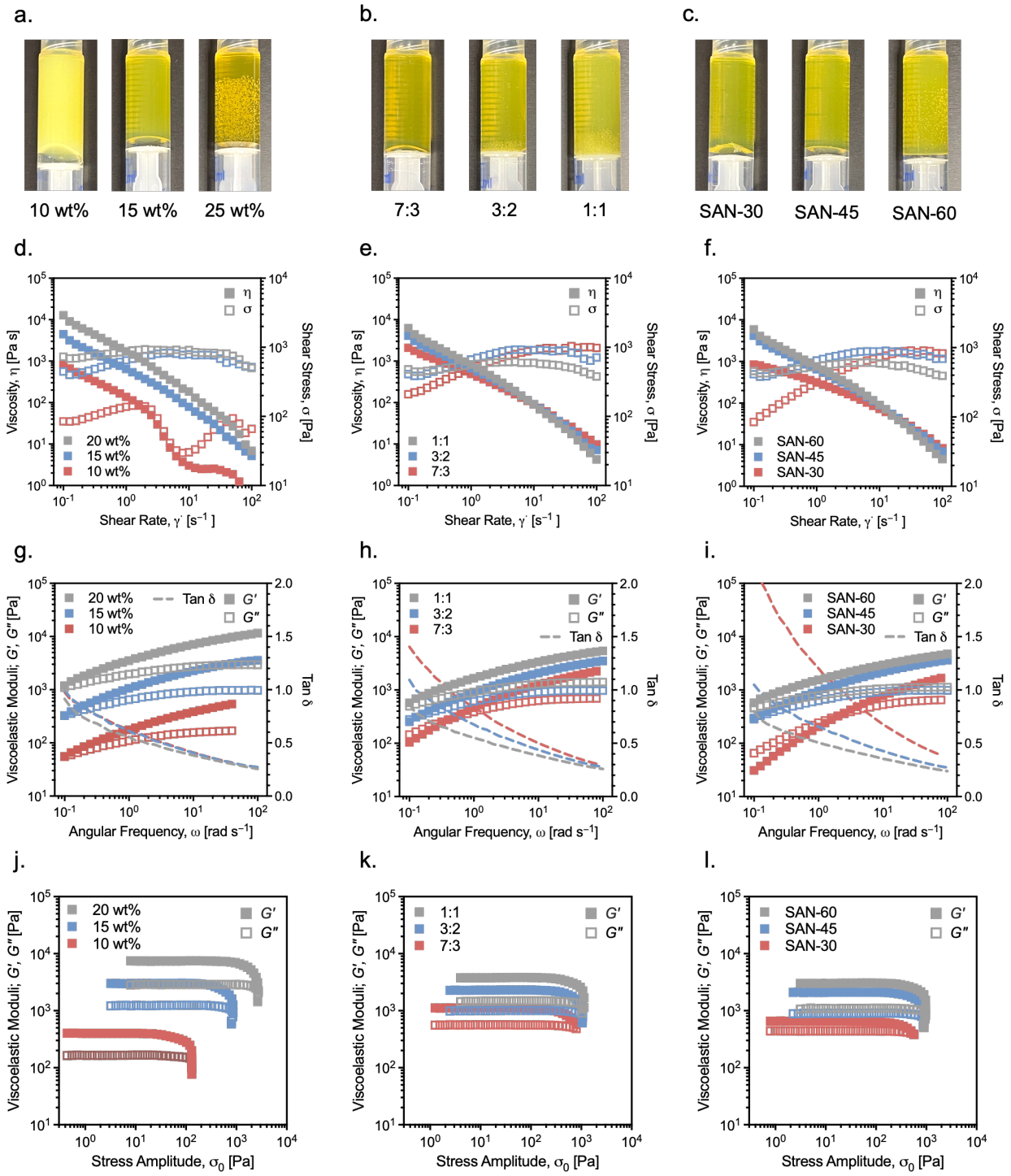

Figure 4.6. (a) Photographs of hydrogels with 3:2 mass fraction of SAN-45 and HPG-C16, with variable total concentration. (b) Photographs of hydrogels with 15 wt% SAN-45 and HPG-C16, with variable mass fraction of the components. (c) Photograph of hydrogels with 15 wt% (3:2) SAN and HPG-C16, with variable SAN size. (d–f) Steady-shear viscosity and stress curves for the three variable sets. (g–i) Frequency sweep data for the three variable sets. (j–l) Stress amplitude sweep data for the three variable sets.

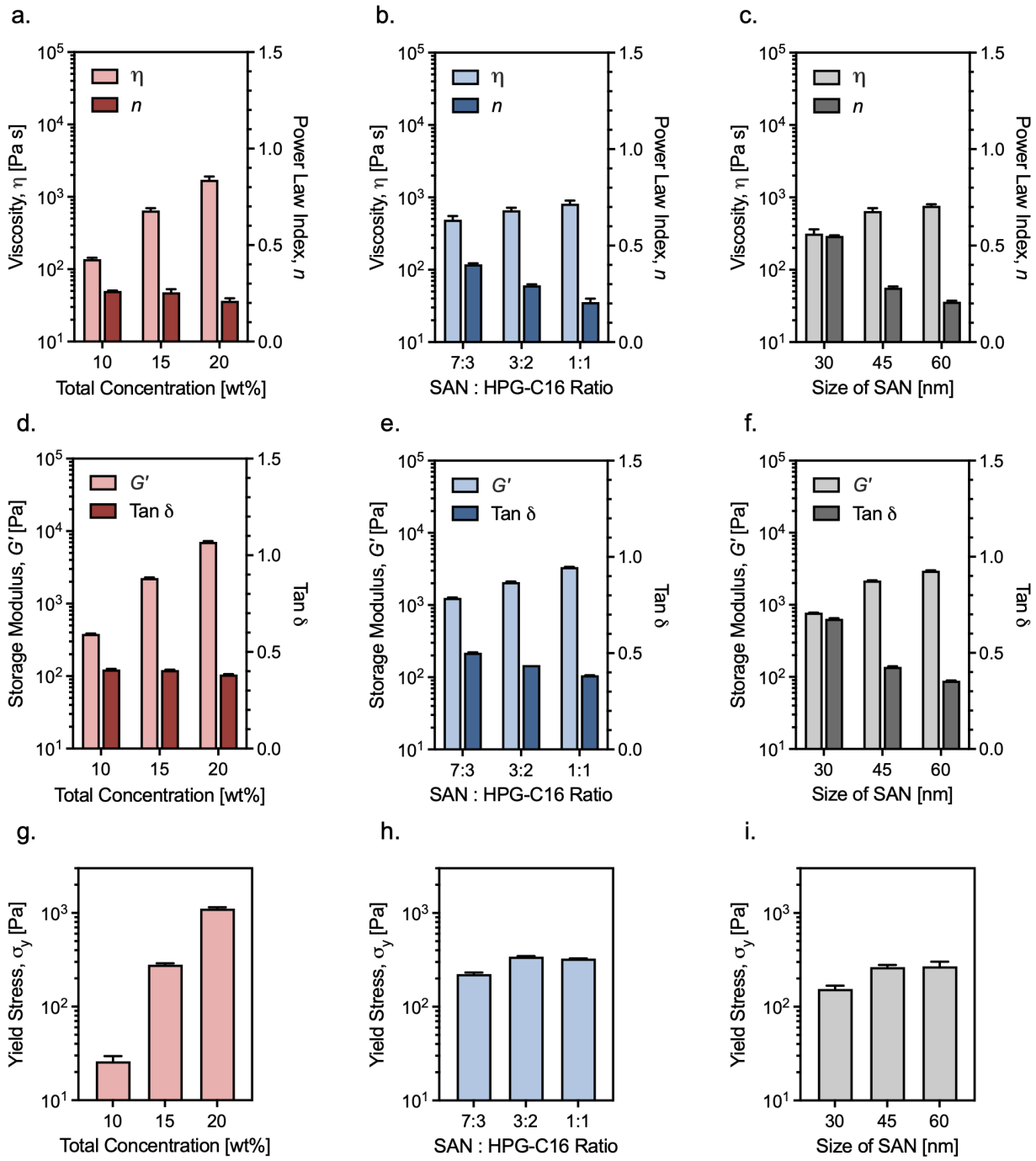

Figure 4.7. (a–c) Comparisons of apparent viscosity at shear rate, $\dot{\gamma} = 1.0\ s^{-1}$ and power law index, n, for the three variable sets (varied total concentration, varied ratio of components, and varied SAN size). (d–f) Comparisons of G' and tan δ at angular frequency, $\omega = 10$ rad s^{-1} for the three variable sets. (g–i) Comparison of apparent yield stress for the three variable sets.

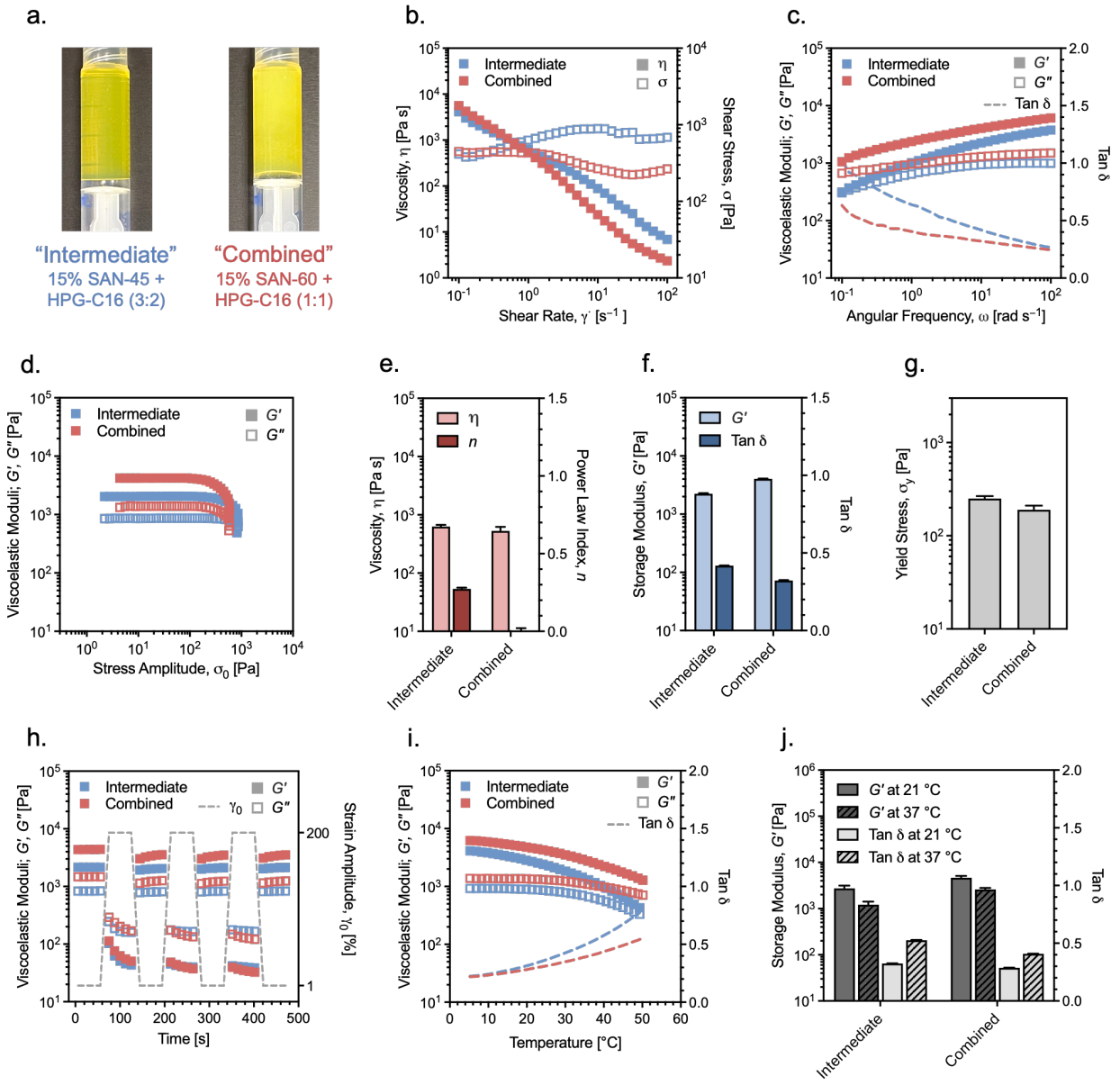

Figure 4.8. (a) The 15 wt% (1:1) SAN-60 and HPG-C16 hydrogel (termed "combined") inverted, inside of a syringe (right), compared to the intermediate gel (left). (b) Steady-shear viscosity and stress curves for the intermediate and combined gels. (c) Frequency sweep data for the intermediate and combined gels. (d) Stress amplitude sweep data for the intermediate and combined gels. (e) Comparison of apparent viscosity at shear rate, $\dot{\gamma} = 1.0$ s^{-1} and power law index, n, for the intermediate and combined gels. (f) Comparison of G' and tan δ at angular frequency, $\omega = 10$ rad s^{-1} for the intermediate and combined gels. (g). Comparison of apparent yield stress for the intermediate and combined gels. (h) Multi-step high- and low-amplitude oscillatory tests showing self-healing and thixotropy of intermediate and combined gels. (i)

Temperature ramp data for the intermediate and combined gels. (j) Comparison of G' and tan δ at 21 °C and 37 °C for the intermediate and combined gels.

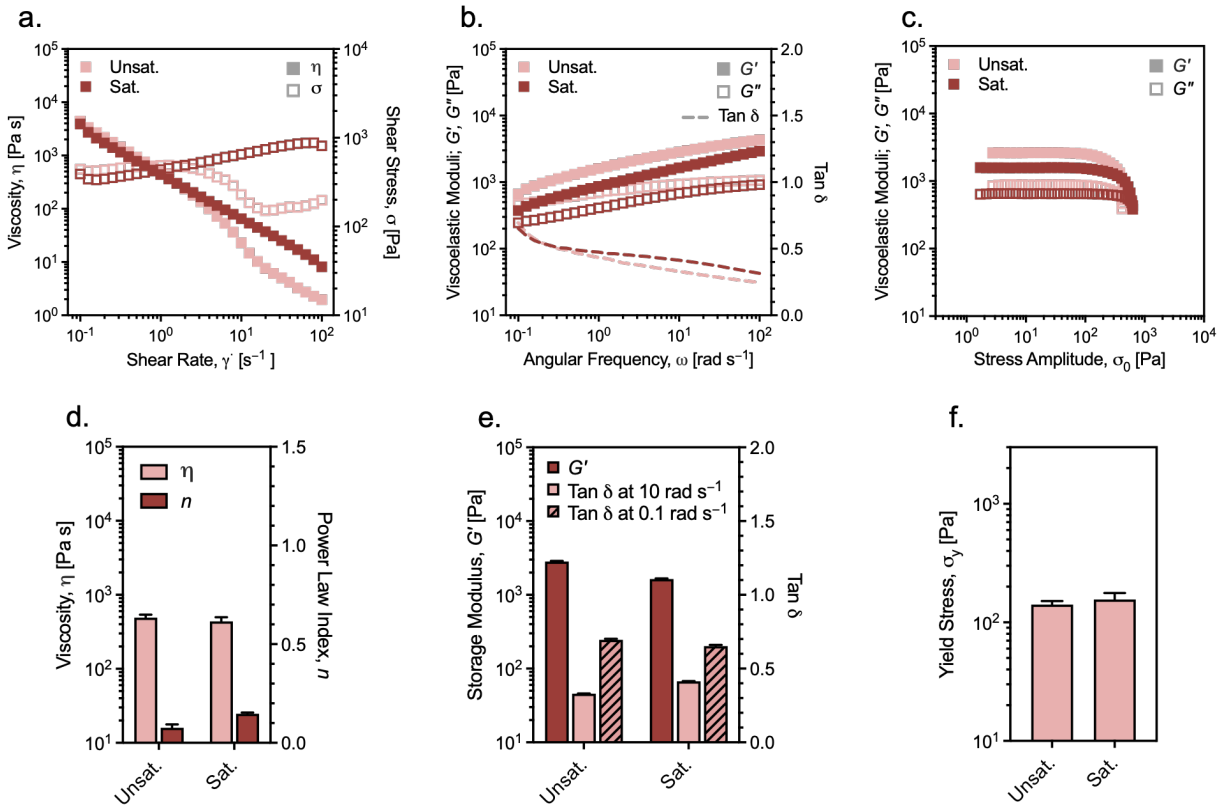

Figure 4.9. (a) Steady-shear viscosity and stress curves for the 15 wt% (1:1) SAN-60 and HPG-C16 hydrogel (termed "combined")—saturated and unsaturated. (b) Frequency sweep data for the combined gel (saturated and unsaturated). (c) Stress amplitude sweep data for the combined gel (saturated and unsaturated). (d) Comparison of apparent viscosity at shear rate, $\dot{\gamma} = 1.0\ s^{-1}$ and power law index, n, for the combined gel (saturated and unsaturated). (e) Comparison of G' at angular frequency, $\omega = 10$ rad s^{-1}, and tan δ at two angular frequencies, for the combined gel (saturated and unsaturated). (f) Comparison of apparent yield stress for the combined gel (saturated and unsaturated).

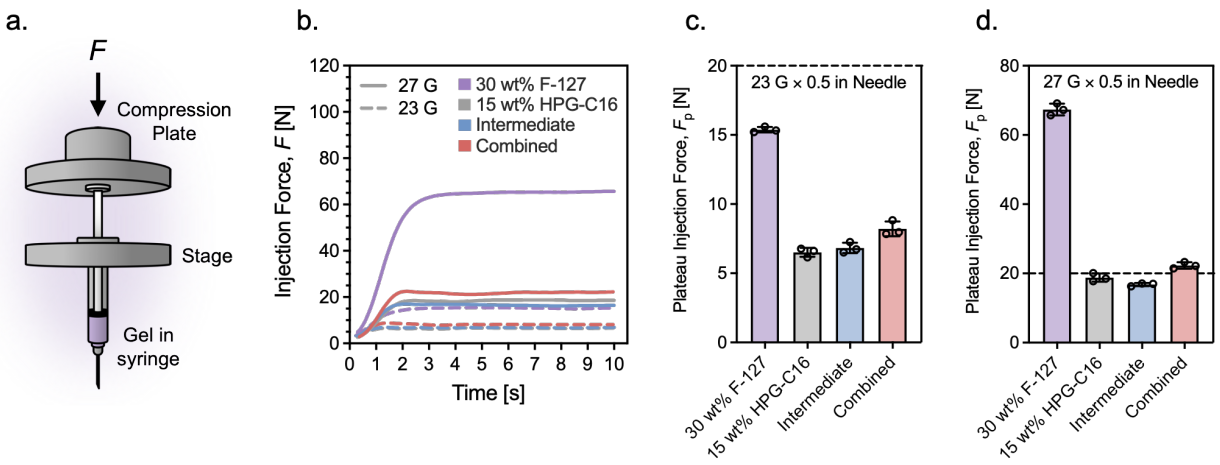

Figure 4.10. (a) Schematic representation of injection force measurement using a load frame. (b) Injection force curves obtained using 1 mL syringes with 0.5 in needles (23 G and 27 G), using a 1.2 mL min^{-1} injection rate. (c) Comparison of plateau force using 23 G needle. (d) Comparison of plateau force using 27 G needle. Data for 30 wt% F-127 gel included for comparison.

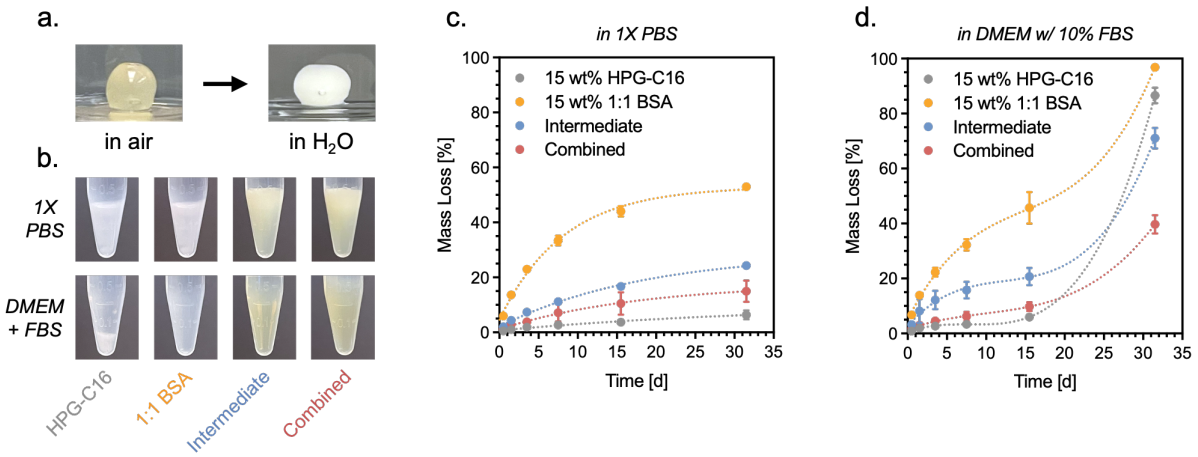

Figure 4.11. (a) SAN + HPG-C16 gel before and after immersing in water. The increased opacity suggests phase separation is occurring in the presence of excess aqueous medium. (b) Materials after 31.5 d in dissolution medium (1X PBS or DMEM with 10% FBS) at 37 °C, static conditions. (c) Cumulative mass loss of materials in 1X PBS at 37 °C, static conditions. (d) Cumulative mass loss of materials in DMEM with 10% FBS at 37 °C, static conditions.

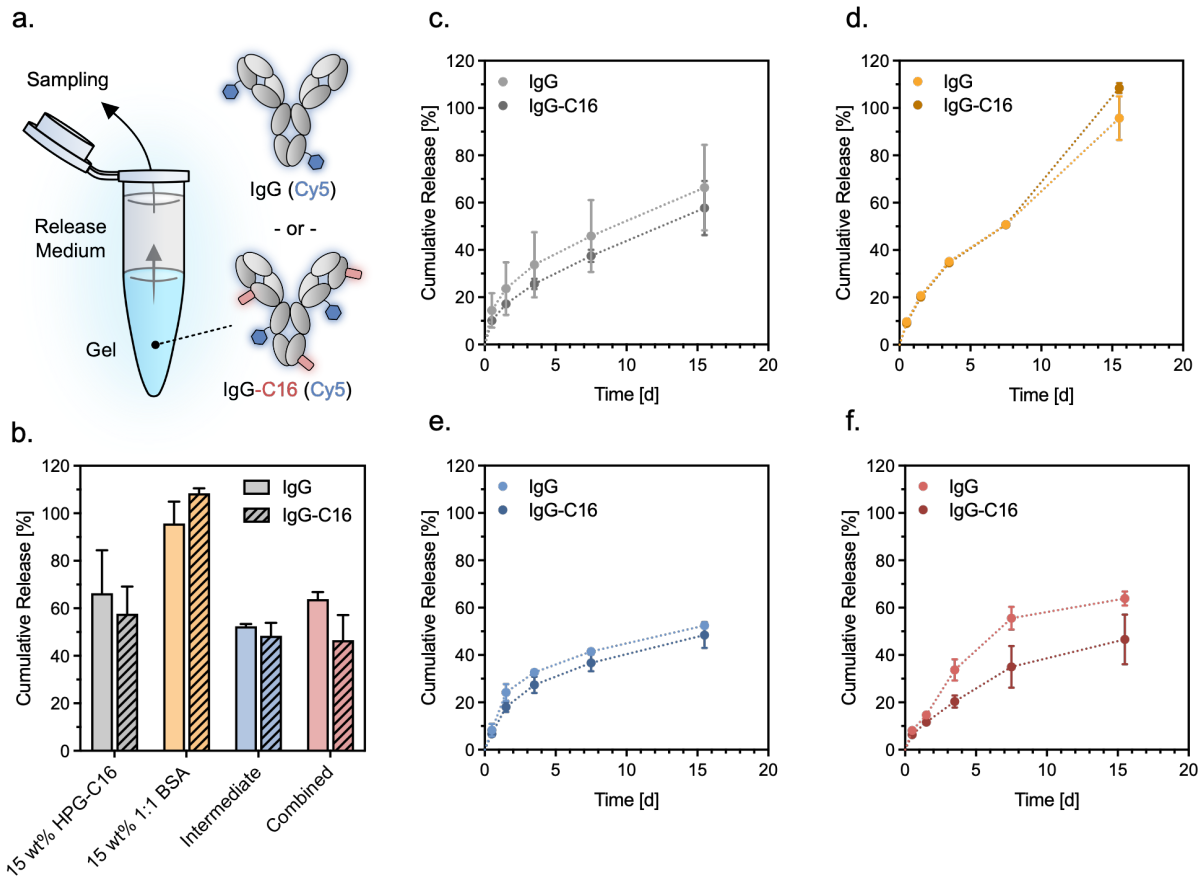

Figure 4.12. (a) Schematic representation of in vitro release experiments. (b) Comparison of cumulative release of Cy5-labeled IgG or Cy-5 labeled IgG-C16 from materials after 15.5 d in DMEM with 10% FBS at 37 °C, static conditions. (c–f) Cumulative release of Cy5-labeled IgG or Cy5-labeled IgG-C16 from materials over 15.5 d.

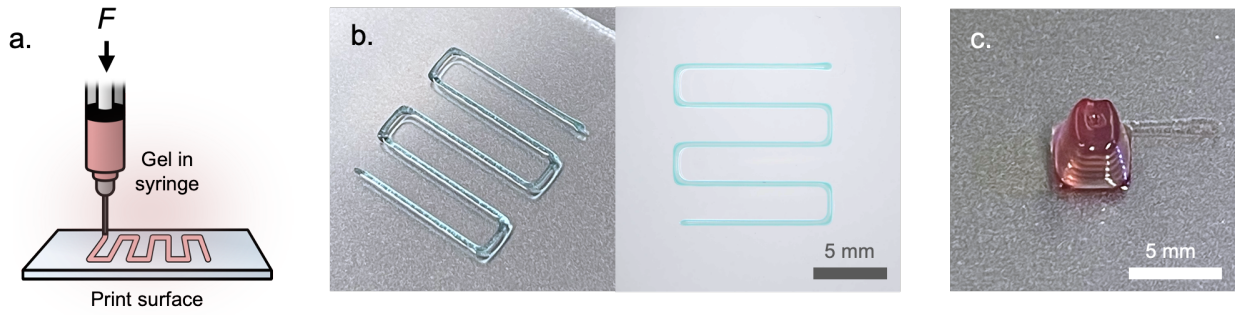

Figure 4.13. (a) Schematic representation of direct ink writing. (b) Single-layer print with intermediate gel (dyed blue). (c) Multi-layered print with combined gel (dyed maroon).

References

(1) Guvendiren, M.; Lu, H. D.; Burdick, J. A. Shear-Thinning Hydrogels for Biomedical Applications. *Soft Matter* **2011**, *8* (2), 260–272. https://doi.org/10.1039/C1SM06513K.

(2) Appel, E. A.; Barrio, J. del; Loh, X. J.; Scherman, O. A. Supramolecular Polymeric Hydrogels. *Chem. Soc. Rev.* **2012**, *41* (18), 6195–6214. https://doi.org/10.1039/C2CS35264H.

(3) Marquardt, L. M.; Heilshorn, S. C. Design of Injectable Materials to Improve Stem Cell Transplantation. *Curr. Stem Cell Rep.* **2016**, *2* (3), 207–220. https://doi.org/10.1007/s40778-016-0058-0.

(4) Loebel, C.; Rodell, C. B.; Chen, M. H.; Burdick, J. A. Shear-Thinning and Self-Healing Hydrogels as Injectable Therapeutics and for 3D-Printing. *Nat. Protoc.* **2017**, *12* (8), 1521–1541. https://doi.org/10.1038/nprot.2017.053.

(5) Hospodiuk, M.; Dey, M.; Sosnoski, D.; Ozbolat, I. T. The Bioink: A Comprehensive Review on Bioprintable Materials. *Biotechnol. Adv.* **2017**, *35* (2), 217–239. https://doi.org/10.1016/j.biotechadv.2016.12.006.

(6) Uman, S.; Dhand, A.; Burdick, J. A. Recent Advances in Shear-Thinning and Self-Healing Hydrogels for Biomedical Applications. *J. Appl. Polym. Sci.* **2020**, *137* (25), 48668. https://doi.org/10.1002/app.48668.

(7) Schwab, A.; Levato, R.; D'Este, M.; Piluso, S.; Eglin, D.; Malda, J. Printability and Shape Fidelity of Bioinks in 3D Bioprinting. *Chem. Rev.* **2020**, *120* (19), 11028–11055. https://doi.org/10.1021/acs.chemrev.0c00084.

(8) Lopez Hernandez, H.; Souza, J. W.; Appel, E. A. A Quantitative Description for Designing the Extrudability of Shear-Thinning Physical Hydrogels. *Macromol. Biosci.* **2021**, *21* (2), 2000295. https://doi.org/10.1002/mabi.202000295.

(9) Hull, S. M.; Brunel, L. G.; Heilshorn, S. C. 3D Bioprinting of Cell-Laden Hydrogels for Improved Biological Functionality. *Adv. Mater.* **2022**, *34* (2), e2103691. https://doi.org/10.1002/adma.202103691.

(10) Sathaye, S.; Mbi, A.; Sonmez, C.; Chen, Y.; Blair, D. L.; Schneider, J. P.; Pochan, D. J. Rheology of Peptide- and Protein-Based Physical Hydrogels: Are Everyday Measurements Just Scratching the Surface? *Wiley Interdiscip. Rev. Nanomed. Nanobiotechnol.* **2015**, *7* (1), 34–68. https://doi.org/10.1002/wnan.1299.

(11) Lu, H. D.; Soranno, D. E.; Rodell, C. B.; Kim, I. L.; Burdick, J. A. Secondary Photocrosslinking of Injectable Shear-Thinning Dock-and-Lock Hydrogels. *Adv. Healthc. Mater.* **2013**, *2* (7), 1028–1036. https://doi.org/10.1002/adhm.201200343.

(12) Rodell, C. B.; Kaminski, A. L.; Burdick, J. A. Rational Design of Network Properties in Guest-Host Assembled and Shear-Thinning Hyaluronic Acid Hydrogels. *Biomacromolecules* **2013**, *14* (11), 4125–4134. https://doi.org/10.1021/bm401280z.

(13) Rutz, A. L.; Hyland, K. E.; Jakus, A. E.; Burghardt, W. R.; Shah, R. N. A Multimaterial Bioink Method for 3D Printing Tunable, Cell-Compatible Hydrogels. *Adv. Mater.* **2015**, *27* (9), 1607–1614. https://doi.org/10.1002/adma.201405076.

(14) Highley, C. B.; Rodell, C. B.; Burdick, J. A. Direct 3D Printing of Shear-Thinning Hydrogels into Self-Healing Hydrogels. *Adv. Mater.* **2015**, *27* (34), 5075–5079. https://doi.org/10.1002/adma.201501234.

(15) Skardal, A.; Devarasetty, M.; Kang, H.-W.; Mead, I.; Bishop, C.; Shupe, T.; Lee, S. J.; Jackson, J.; Yoo, J.; Soker, S.; Atala, A. A Hydrogel Bioink Toolkit for Mimicking Native Tissue Biochemical and Mechanical Properties in Bioprinted Tissue Constructs. *Acta Biomater.* **2015**, *25*, 24–34. https://doi.org/10.1016/j.actbio.2015.07.030.

(16) Appel, E. A.; Tibbitt, M. W.; Webber, M. J.; Mattix, B. A.; Veiseh, O.; Langer, R. Self-Assembled Hydrogels Utilising Polymer-Nanoparticle Interactions. *Nat. Commun.* **2015**, *6*, 6295. https://doi.org/10.1038/ncomms7295.

(17) Zhu, K.; Chen, N.; Liu, X.; Mu, X.; Zhang, W.; Wang, C.; Zhang, Y. S. A General Strategy for Extrusion Bioprinting of Bio-Macromolecular Bioinks through Alginate-Templated Dual-Stage Crosslinking. *Macromol. Biosci.* **2018**, *18* (9), e1800127. https://doi.org/10.1002/mabi.201800127.

(18) Lindsay, C. D.; Roth, J. G.; LeSavage, B. L.; Heilshorn, S. C. Bioprinting of Stem Cell Expansion Lattices. *Acta Biomater.* **2019**, *95*, 225–235. https://doi.org/10.1016/j.actbio.2019.05.014.

(19) Hu, T.; Cui, X.; Zhu, M.; Wu, M.; Tian, Y.; Yao, B.; Song, W.; Niu, Z.; Huang, S.; Fu, X. 3D-Printable Supramolecular Hydrogels with Shear-Thinning Property: Fabricating Strength Tunable Bioink via Dual Crosslinking. *Bioact. Mater.* **2020**, *5* (4), 808–818. https://doi.org/10.1016/j.bioactmat.2020.06.001.

(20) Shin, J. Y.; Yeo, Y. H.; Jeong, J. E.; Park, S. A.; Park, W. H. Dual-Crosslinked Methylcellulose Hydrogels for 3D Bioprinting Applications. *Carbohydr. Polym.* **2020**, *238*, 116192. https://doi.org/10.1016/j.carbpol.2020.116192.

(21) Dubbin, K.; Tabet, A.; Heilshorn, S. C. Quantitative Criteria to Benchmark New and Existing Bio-Inks for Cell Compatibility. *Biofabrication* **2017**, *9* (4), 044102. https://doi.org/10.1088/1758-5090/aa869f.

(22) Caliari, S. R.; Burdick, J. A. A Practical Guide to Hydrogels for Cell Culture. *Nat. Methods* **2016**, *13* (5), 405–414. https://doi.org/10.1038/nmeth.3839.

(23) Malda, J.; Visser, J.; Melchels, F. P.; Jüngst, T.; Hennink, W. E.; Dhert, W. J. A.; Groll, J.; Hutmacher, D. W. 25th Anniversary Article: Engineering Hydrogels for Biofabrication. *Adv. Mater.* **2013**, *25* (36), 5011–5028. https://doi.org/10.1002/adma.201302042.

(24) Kolesky, D. B.; Truby, R. L.; Gladman, A. S.; Busbee, T. A.; Homan, K. A.; Lewis, J. A. 3D Bioprinting of Vascularized, Heterogeneous Cell-Laden Tissue Constructs. *Adv. Mater.* **2014**, *26* (19), 3124–3130. https://doi.org/10.1002/adma.201305506.

(25) Müller, M.; Becher, J.; Schnabelrauch, M.; Zenobi-Wong, M. Nanostructured Pluronic Hydrogels as Bioinks for 3D Bioprinting. *Biofabrication* **2015**, *7* (3), 035006. https://doi.org/10.1088/1758-5090/7/3/035006.

(26) Kang, H.-W.; Lee, S. J.; Ko, I. K.; Kengla, C.; Yoo, J. J.; Atala, A. A 3D Bioprinting System to Produce Human-Scale Tissue Constructs with Structural Integrity. *Nat. Biotechnol.* **2016**, *34* (3), 312–319. https://doi.org/10.1038/nbt.3413.

(27) Millik, S. C.; Dostie, A. M.; Karis, D. G.; Smith, P. T.; McKenna, M.; Chan, N.; Curtis, C. D.; Nance, E.; Theberge, A. B.; Nelson, A. 3D Printed Coaxial Nozzles for the Extrusion of Hydrogel Tubes toward Modeling Vascular Endothelium. *Biofabrication* **2019**, *11* (4), 045009. https://doi.org/10.1088/1758-5090/ab2b4d.

(28) Khattak, S. F.; Bhatia, S. R.; Roberts, S. C. Pluronic F127 as a Cell Encapsulation Material: Utilization of Membrane-Stabilizing Agents. *Tissue Eng.* **2005**, *11* (5–6), 974–983. https://doi.org/10.1089/ten.2005.11.974.

(29) Arranja, A.; Schroder, A. P.; Schmutz, M.; Waton, G.; Schosseler, F.; Mendes, E. Cytotoxicity and Internalization of Pluronic Micelles Stabilized by Core Cross-Linking. *J. Control. Release* **2014**, *196*, 87–95. https://doi.org/10.1016/j.jconrel.2014.10.001.

(30) Prud'homme, R. K.; Wu, G.; Schneider, D. K. Structure and Rheology Studies of Poly(Oxyethylene−oxypropylene−oxyethylene) Aqueous Solution. *Langmuir* **1996**, *12* (20), 4651–4659. https://doi.org/10.1021/la951506b.

(31) Jalaal, M.; Cottrell, G.; Balmforth, N.; Stoeber, B. On the Rheology of Pluronic F127 Aqueous Solutions. *J. Rheol.* **2017**, *61* (1), 139–146. https://doi.org/10.1122/1.4971992.

(32) Rodell, C. B.; Mealy, J. E.; Burdick, J. A. Supramolecular Guest–Host Interactions for the Preparation of Biomedical Materials. *Bioconjugate Chem.* **2015**, *26* (12), 2279–2289. https://doi.org/10.1021/acs.bioconjchem.5b00483.

(33) Mealy, J. E.; Rodell, C. B.; Burdick, J. A. Sustained Small Molecule Delivery from Injectable Hyaluronic Acid Hydrogels through Host–Guest Mediated Retention. *J. Mater. Chem. B* **2015**, *3* (40), 8010–8019. https://doi.org/10.1039/C5TB00981B.

(34) Ouyang, L.; Highley, C. B.; Rodell, C. B.; Sun, W.; Burdick, J. A. 3D Printing of Shear-Thinning Hyaluronic Acid Hydrogels with Secondary Cross-Linking. *ACS Biomater. Sci. Eng.* **2016**, *2* (10), 1743–1751. https://doi.org/10.1021/acsbiomaterials.6b00158.

(35) Ouyang, L.; Highley, C. B.; Sun, W.; Burdick, J. A. A Generalizable Strategy for the 3D Bioprinting of Hydrogels from Nonviscous Photo-crosslinkable Inks. *Adv. Mater.* **2017**, *29* (8), 1604983. https://doi.org/10.1002/adma.201604983.

(36) Wang, L. L.; Sloand, J. N.; Gaffey, A. C.; Venkataraman, C. M.; Wang, Z.; Trubelja, A.; Hammer, D. A.; Atluri, P.; Burdick, J. A. Injectable, Guest–Host Assembled Polyethylenimine Hydrogel for siRNA Delivery. *Biomacromolecules* **2017**, *18* (1), 77–86. https://doi.org/10.1021/acs.biomac.6b01378.

(37) Grosskopf, A. K.; Roth, G. A.; Smith, A. A. A.; Gale, E. C.; Hernandez, H. L.; Appel, E. A. Injectable Supramolecular Polymer–Nanoparticle Hydrogels Enhance Human Mesenchymal Stem Cell Delivery. *Bioeng. Transl. Med.* **2020**, *5* (1), e10147. https://doi.org/10.1002/btm2.10147.

(38) Correa, S.; Meany, E. L.; Gale, E. C.; Klich, J. H.; Saouaf, O. M.; Mayer, A. T.; Xiao, Z.; Liong, C. S.; Brown, R. A.; Maikawa, C. L.; Grosskopf, A. K.; Mann, J. L.; Idoyaga, J.; Appel, E. A. Injectable Nanoparticle-Based Hydrogels Enable the Safe and Effective

Deployment of Immunostimulatory CD40 Agonist Antibodies. *Adv. Sci.* **2022**, *9* (28), 2103677. https://doi.org/10.1002/advs.202103677.

(39) Meany, E. L.; Andaya, R.; Tang, S.; Kasse, C. M.; Fuji, R. N.; Grosskopf, A. K.; d'Aquino, A. L.; Bartoe, J. T.; Ybarra, R.; Shelton, A.; Pederson, Z.; Hu, C.; Leung, D.; Nagapudi, K.; Ubhayakar, S.; Wright, M.; Yen, C.-W.; Appel, E. A. Injectable Polymer-Nanoparticle Hydrogel for the Sustained Intravitreal Delivery of Bimatoprost. *Adv. Ther.* **2023**, *6* (2), 2200207. https://doi.org/10.1002/adtp.202200207.

(40) Yan, J.; Ou, B. S.; Saouaf, O. M.; Meany, E. L.; Eckman, N.; Appel, E. A. A Regimen Compression Strategy for Commercial Vaccines Leveraging an Injectable Hydrogel Depot Technology for Sustained Vaccine Exposure. *Adv. Ther.* **2024**, *7* (1), 2300108. https://doi.org/10.1002/adtp.202300108.

(41) Baler, K.; Michael, R.; Szleifer, I.; Ameer, G. A. Albumin Hydrogels Formed by Electrostatically Triggered Self-Assembly and Their Drug Delivery Capability. *Biomacromolecules* **2014**, *15* (10), 3625–3633. https://doi.org/10.1021/bm500883h.

(42) Zhang, K.; Zhou, Y.; Zhang, J.; Liu, Q.; Hanenberg, C.; Mourran, A.; Wang, X.; Gao, X.; Cao, Y.; Herrmann, A.; Zheng, L. Shape Morphing of Hydrogels by Harnessing Enzyme Enabled Mechanoresponse. *Nat. Commun.* **2024**, *15* (1), 249. https://doi.org/10.1038/s41467-023-44607-y.

(43) Gagner, J. E.; Kim, W.; Chaikof, E. L. Designing Protein-Based Biomaterials for Medical Applications. *Acta Biomater.* **2014**, *10* (4), 1542–1557. https://doi.org/10.1016/j.actbio.2013.10.001.

(44) Varanko, A.; Saha, S.; Chilkoti, A. Recent Trends in Protein and Peptide-Based Biomaterials for Advanced Drug Delivery. *Adv. Drug Deliver. Rev.* **2020**, *156*, 133–187. https://doi.org/10.1016/j.addr.2020.08.008.

(45) Chu, S.; Wang, A. L.; Bhattacharya, A.; Montclare, J. K. Protein Based Biomaterials for Therapeutic and Diagnostic Applications. *Prog. Biomed. Eng.* **2021**, *4* (1), 012003. https://doi.org/10.1088/2516-1091/ac2841.

(46) Fang, J.; Mehlich, A.; Koga, N.; Huang, J.; Koga, R.; Gao, X.; Hu, C.; Jin, C.; Rief, M.; Kast, J.; Baker, D.; Li, H. Forced Protein Unfolding Leads to Highly Elastic and Tough Protein Hydrogels. *Nat. Commun.* **2013**, *4* (1), 2974. https://doi.org/10.1038/ncomms3974.

(47) Dooling, L. J.; Buck, M. E.; Zhang, W.-B.; Tirrell, D. A. Programming Molecular Association and Viscoelastic Behavior in Protein Networks. *Adv. Mater.* **2016**, *28* (23), 4651–4657. https://doi.org/10.1002/adma.201506216.

(48) Huang, P.-S.; Boyken, S. E.; Baker, D. The Coming of Age of de Novo Protein Design. *Nature* **2016**, *537* (7620), 320–327. https://doi.org/10.1038/nature19946.

(49) Peters, T., Jr. *All About Albumin: Biochemistry, Genetics, and Medical Applications*; Academic Press, Inc., 1996.

(50) Miele, E.; Spinelli, G. P.; Miele, E.; Tomao, F.; Tomao, S. Albumin-Bound Formulation of Paclitaxel (Abraxane® ABI-007) in the Treatment of Breast Cancer. *Int. J. Nanomed.* **2009**.

(51) Francis, G. L. Albumin and Mammalian Cell Culture: Implications for Biotechnology Applications. *Cytotechnology* **2010**, *62* (1), 1–16. https://doi.org/10.1007/s10616-010-9263-3.

(52) Caraceni, P.; Tufoni, M.; Bonavita, M. E. Clinical Use of Albumin. *Blood Transfus.* **2013**, *11* (Suppl 4), s18–s25. https://doi.org/10.2450/2013.005s.

(53) Horváthy, D. B.; Simon, M.; Schwarz, C. M.; Masteling, M.; Vácz, G.; Hornyák, I.; Lacza, Z. Serum Albumin as a Local Therapeutic Agent in Cell Therapy and Tissue Engineering. *BioFactors* **2017**, *43* (3), 315–330. https://doi.org/10.1002/biof.1337.

(54) Mishra, V.; Heath, R. J. Structural and Biochemical Features of Human Serum Albumin Essential for Eukaryotic Cell Culture. *Int. J. Mol. Sci.* **2021**, *22* (16), 8411. https://doi.org/10.3390/ijms22168411.

(55) Kragh-Hansen, U. Structure and Ligand Binding Properties of Human Serum Albumin. *Dan. Med. Bull.* **1990**, *37* (1), 57–84.

(56) Kragh-Hansen, U.; Chuang, V. T. G.; Otagiri, M. Practical Aspects of the Ligand-Binding and Enzymatic Properties of Human Serum Albumin. *Biol. Pharm. Bull.* **2002**, *25* (6), 695–704. https://doi.org/10.1248/bpb.25.695.

(57) Fasano, M.; Curry, S.; Terreno, E.; Galliano, M.; Fanali, G.; Narciso, P.; Notari, S.; Ascenzi, P. The Extraordinary Ligand Binding Properties of Human Serum Albumin. *IUBMB Life* **2005**, *57* (12), 787–796. https://doi.org/10.1080/15216540500404093.

(58) Richieri, G. V.; Anel, A.; Kleinfeld, A. M. Interactions of Long-Chain Fatty Acids and Albumin: Determination of Free Fatty Acid Levels Using the Fluorescent Probe ADIFAB. *Biochemistry* **1993**, *32* (29), 7574–7580. https://doi.org/10.1021/bi00080a032.

(59) Hermanson, G. T. *Bioconjugate Techniques*, 3rd ed.; Elsevier, 2013.

(60) Wilms, D.; Stiriba, S.-E.; Frey, H. Hyperbranched Polyglycerols: From the Controlled Synthesis of Biocompatible Polyether Polyols to Multipurpose Applications. *Acc. Chem. Res.* **2010**, *43* (1), 129–141. https://doi.org/10.1021/ar900158p.

(61) Sunder, A.; Hanselmann, R.; Frey, H.; Mülhaupt, R. Controlled Synthesis of Hyperbranched Polyglycerols by Ring-Opening Multibranching Polymerization. *Macromolecules* **1999**, *32* (13), 4240–4246. https://doi.org/10.1021/ma990090w.

(62) Kainthan, R. K.; Muliawan, E. B.; Hatzikiriakos, S. G.; Brooks, D. E. Synthesis, Characterization, and Viscoelastic Properties of High Molecular Weight Hyperbranched Polyglycerols. *Macromolecules* **2006**, *39* (22), 7708–7717. https://doi.org/10.1021/ma0613483.

(63) Kainthan, R. K.; Janzen, J.; Kizhakkedathu, J. N.; Devine, D. V.; Brooks, D. E. Hydrophobically Derivatized Hyperbranched Polyglycerol as a Human Serum Albumin Substitute. *Biomaterials* **2008**, *29* (11), 1693–1704. https://doi.org/10.1016/j.biomaterials.2007.11.030.

(64) Misri, R.; Wong, N. K. Y.; Shenoi, R. A.; Lum, C. M. W.; Chafeeva, I.; Toth, K.; Rustum, Y.; Kizhakkedathu, J. N.; Khan, M. K. Investigation of Hydrophobically Derivatized Hyperbranched Polyglycerol with PEGylated Shell as a Nanocarrier for Systemic

Delivery of Chemotherapeutics. *Nanomed. Nanotechnol. Biol. Med.* **2015**, *11* (7), 1785–1795. https://doi.org/10.1016/j.nano.2015.04.016.

(65) Elmer, J.; Cabrales, P.; Wang, Q.; Zhang, N.; Palmer, A. F. Synthesis and Biophysical Properties of Polymerized Human Serum Albumin. *Biotechnol. Progr.* **2011**, *27* (1), 290–296. https://doi.org/10.1002/btpr.531.

(66) Belcher, D. A.; Williams, A. T.; Palmer, A. F.; Cabrales, P. Polymerized Albumin Restores Impaired Hemodynamics in Endotoxemia and Polymicrobial Sepsis. *Sci. Rep.* **2021**, *11* (1), 10834. https://doi.org/10.1038/s41598-021-90431-z.

(67) Eren, E.; Black, S. M.; Reader, B. F.; Beal, E.; Cuddington, C.; Belcher, D. A.; Palmer, A. F.; Whitson, B. A. Novel Polymerized Human Serum Albumin For Ex Vivo Lung Perfusion. *ASAIO J.* **2023**, *69* (7), 716–723. https://doi.org/10.1097/MAT.0000000000001918.

(68) Chan, S. T.; Varchanis, S.; Haward, S. J.; Shen, A. Q. Perspective on Edge Fracture. *J. Rheol.* **2023**, *67* (4), 949–963. https://doi.org/10.1122/8.0000625.

(69) Chen, M. H.; Wang, L. L.; Chung, J. J.; Kim, Y.-H.; Atluri, P.; Burdick, J. A. Methods To Assess Shear-Thinning Hydrogels for Application As Injectable Biomaterials. *ACS Biomater. Sci. Eng.* **2017**, *3* (12), 3146–3160. https://doi.org/10.1021/acsbiomaterials.7b00734.

(70) Watt, R. P.; Khatri, H.; Dibble, A. R. G. Injectability as a Function of Viscosity and Dosing Materials for Subcutaneous Administration. *Int. J. Pharm.* **2019**, *554*, 376–386. https://doi.org/10.1016/j.ijpharm.2018.11.012.

(71) Kurtzhals, P.; Østergaard, S.; Nishimura, E.; Kjeldsen, T. Derivatization with Fatty Acids in Peptide and Protein Drug Discovery. *Nat. Rev. Drug Discov.* **2023**, *22* (1), 59–80. https://doi.org/10.1038/s41573-022-00529-w.

Appendix A

3D-Printed Coaxial Nozzles for the Extrusion of Hydrogel Tubes Toward Modeling Vascular Endothelium

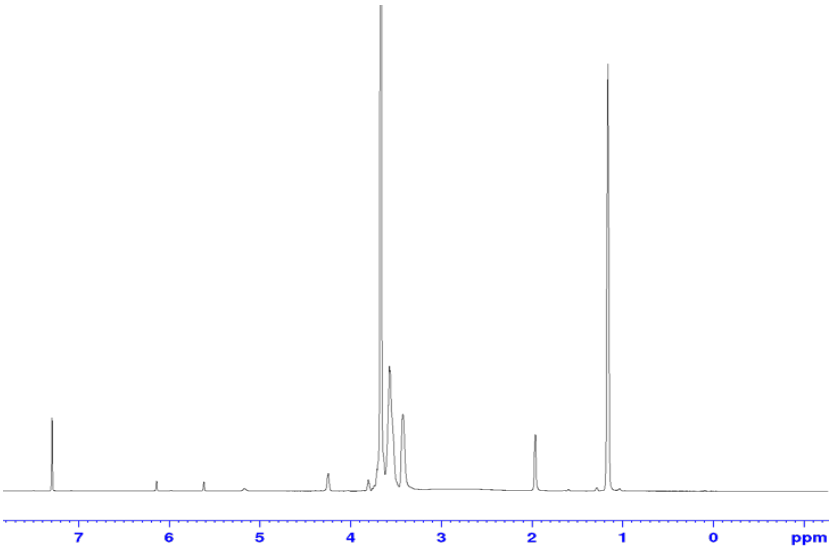

Figure A1. ^{1}H NMR spectrum of F127-BUM (500 MHz, 293 K, $CDCl_3$).

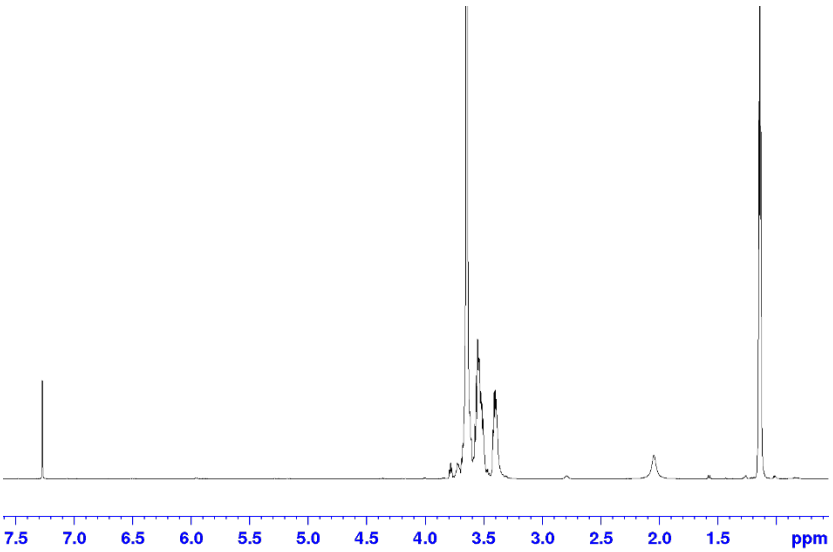

Figure A2. ^{1}H NMR spectrum of F127 (500 MHz, 293 K, $CDCl_3$).

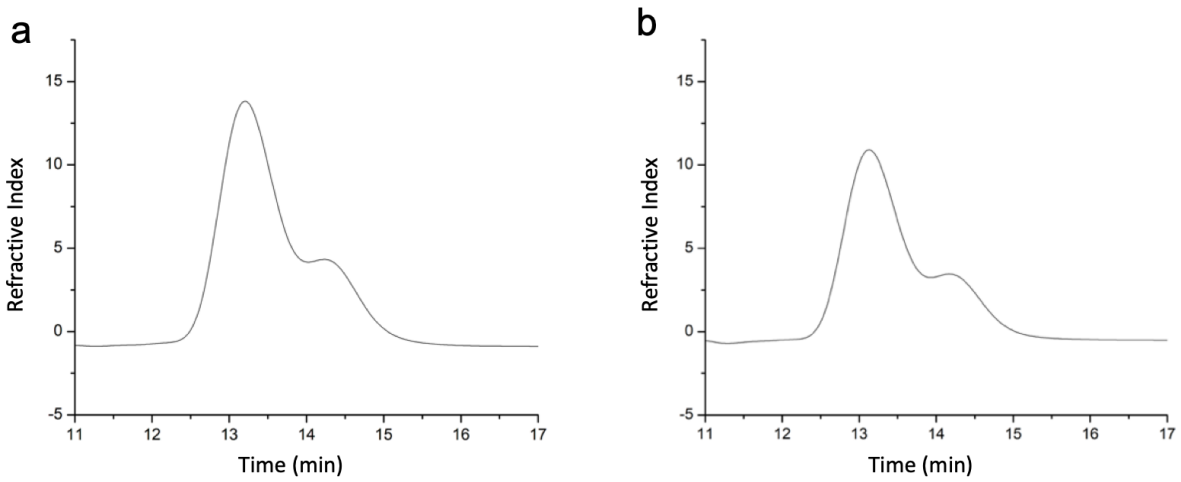

Figure A3. (a) GPC trace of F127; $Đ$ = 1.28. (b) GPC trace of F127-BUM; $Đ$ = 1.28.

Appendix B

3D-Printed Protein-Based Bioplastics with Tunable Mechanical Properties Using Glycerol or Hyperbranched Poly(glycerol)s as Plasticizers

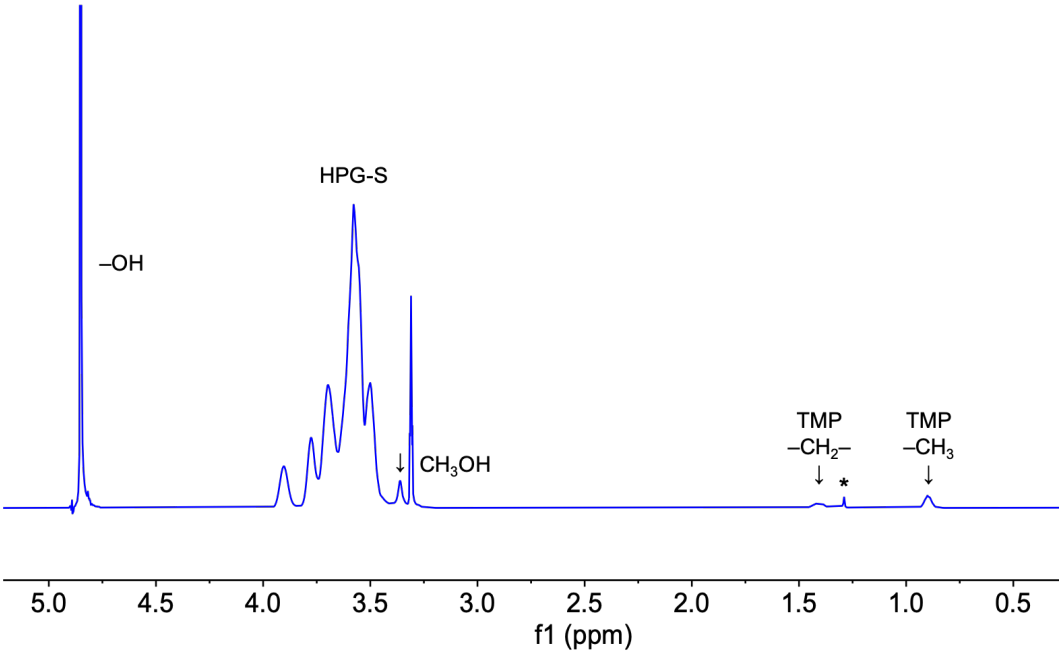

Figure B1. ^{1}H NMR spectrum of HPG-S (500 MHz, CD_3OD). Asterisk denotes signal from vacuum grease. "TMP" refers to TMP core of HPG.

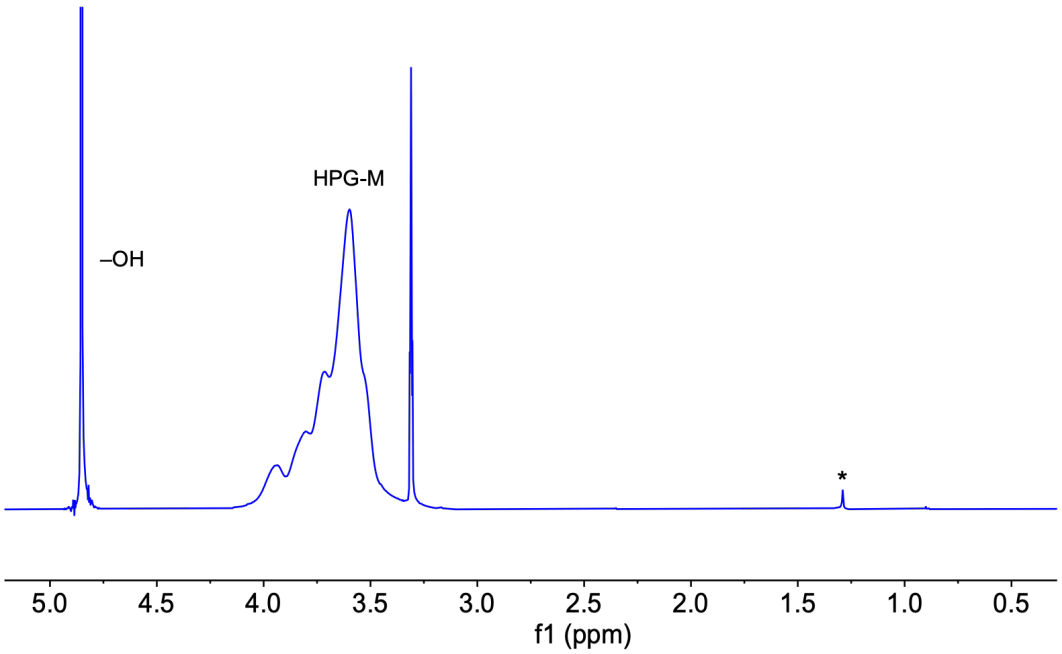

Figure B2. ^{1}H NMR spectrum of HPG-M (500 MHz, CD_3OD). Asterisk denotes signal from vacuum grease.

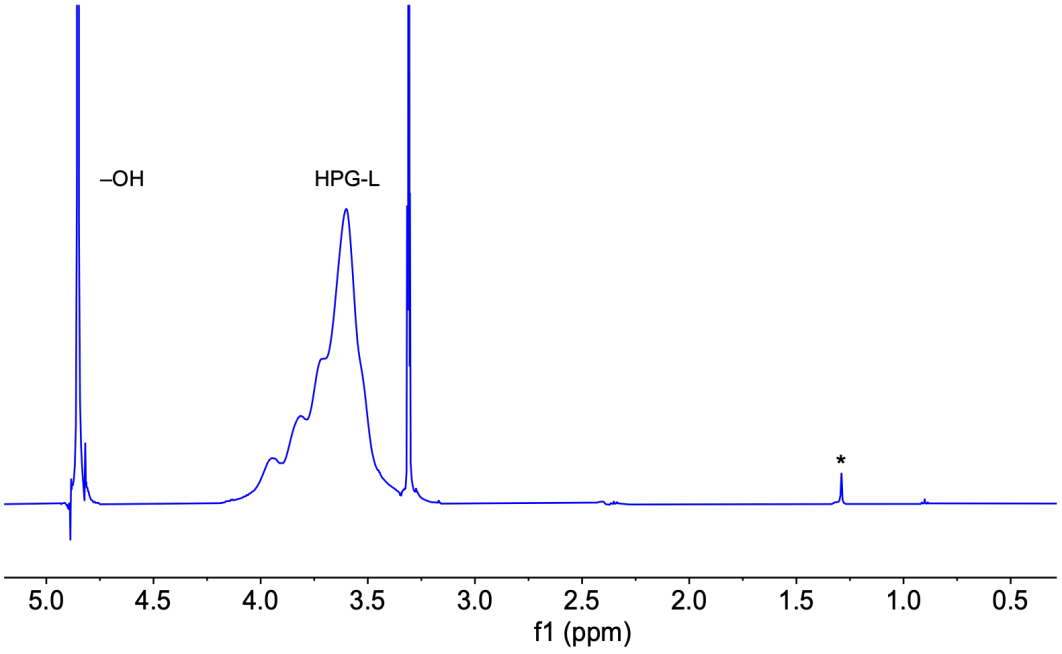

Figure B3. ^{1}H NMR spectrum of HPG-L (500 MHz, CD_3OD). Asterisk denotes signal from vacuum grease.

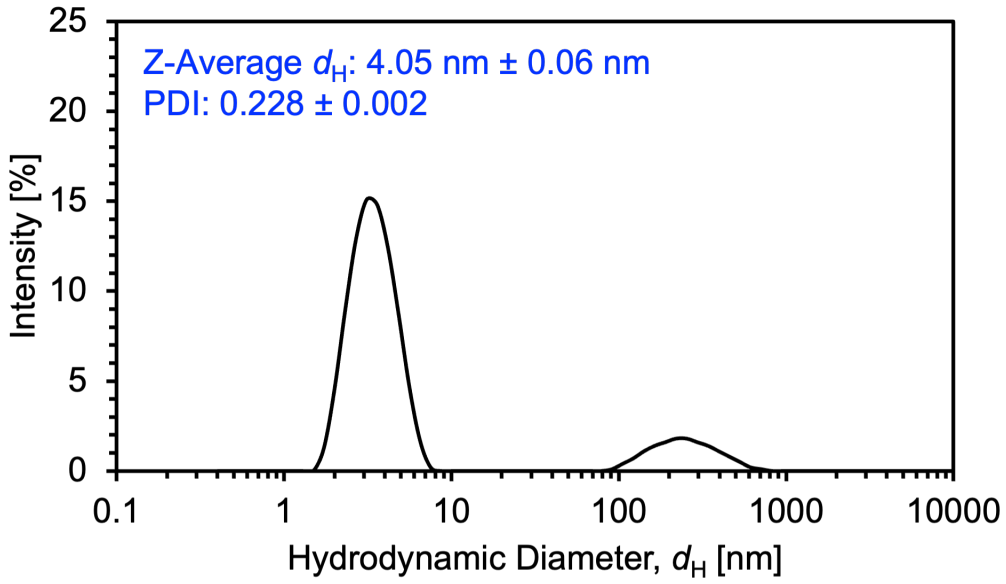

Figure B4. DLS trace for HPG-S in deionized water.

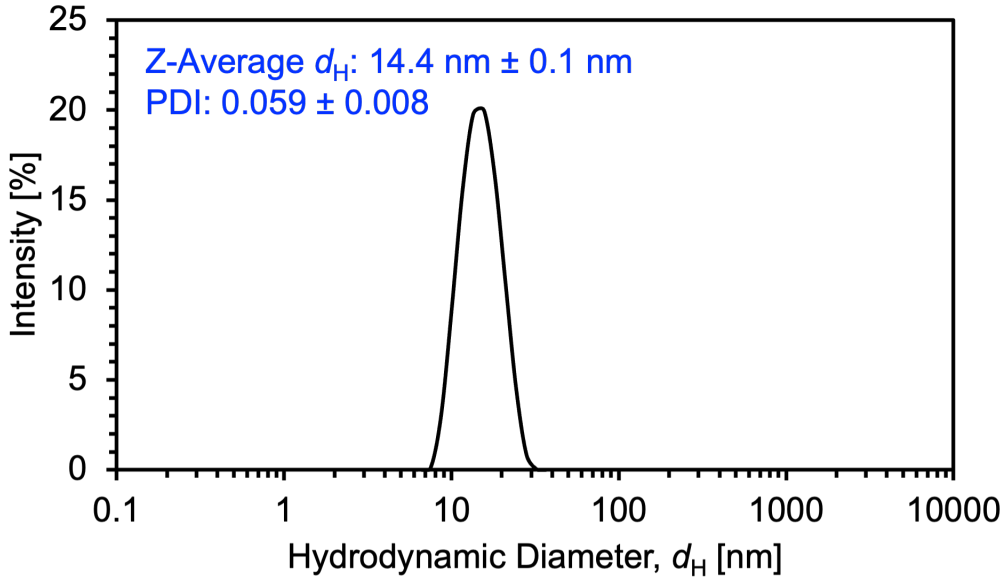

Figure B5. DLS trace for HPG-M in deionized water.

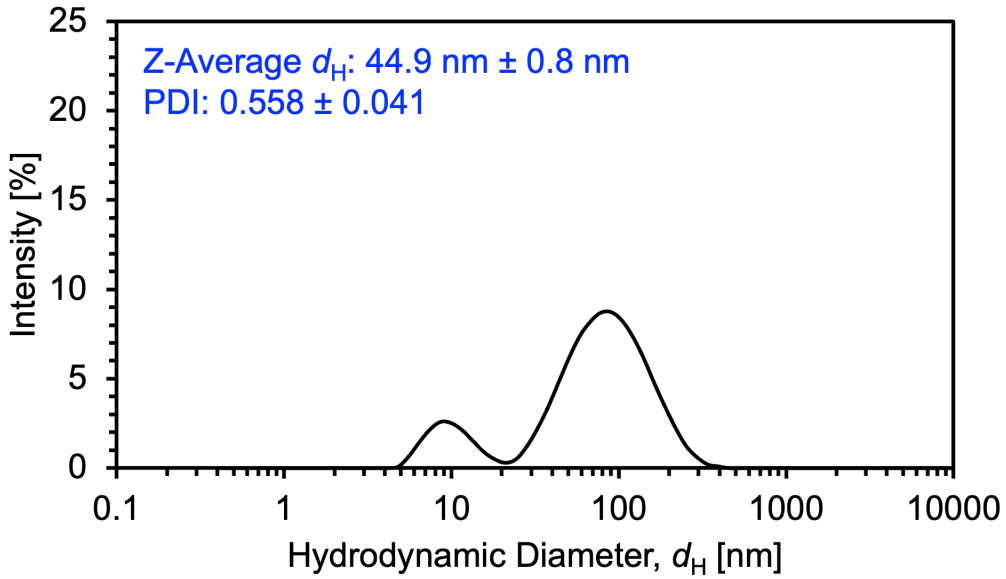

Figure B6. DLS trace for HPG-L in deionized water.

Table B1. Tensile properties of cast bioplastics with increasing glycerol content.

Glycerol Content [wt%]	Elastic Modulus, E_t [MPa]	Yield Stress, σ_y [MPa]	Strain at Break, ε_{tb} [%]	Toughness, U_t [MJ m^{-3}]
0	1018 ± 57	50.04 ± 0.29	49 ± 13	19.0 ± 4.6
5	517 ± 30	22.94 ± 0.27	178 ± 28	29.7 ± 5.1
10	166 ± 17	7.15 ± 0.12	287 ± 35	20.0 ± 3.4
15	29.1 ± 2.0	1.770 ± 0.039	358 ± 36	9.0 ± 1.5

Tensile properties reported as mean ± SD

Table B2. Tensile properties of cast bioplastics with increasing HPG-M content.

HPG Content [wt%]	Elastic Modulus, E_t [MPa]	Yield Stress, σ_y [MPa]	Strain at Break, ε_{tb} [%]	Toughness, U_t [MJ m^{-3}]
0	1018 ± 57	50.04 ± 0.29	49 ± 13	19.0 ± 4.6
5	797 ± 40	38.16 ± 0.19	59.5 ± 7.6	17.3 ± 2.0
10	554 ± 17	25.75 ± 0.11	97 ± 27	19.1 ± 5.1
15	296 ± 22	15.81 ± 0.10	113 ± 35	14.0 ± 4.1

Tensile properties reported as mean ± SD

Table B3. Tensile properties of cast bioplastics with different additives at 15 wt%.

Additive (15 wt%)	Elastic Modulus, E_t [MPa]	Yield Stress, σ_y [MPa]	Strain at Break, ε_{tb} [%]	Toughness, U_t [MJ m^{-3}]
No Additive	1018 ± 57	50.04 ± 0.29	49 ± 13	19.0 ± 4.6
Glycerol	29.1 ± 2.0	1.770 ± 0.039	358 ± 36	9.0 ± 1.5
HPG-S	248.1 ± 6.1	11.62 ± 0.16	233 ± 33	19.8 ± 3.1
HPG-M	296 ± 22	15.81 ± 0.10	113 ± 35	14.0 ± 4.1
HPG-L	295 ± 10	15.75 ± 0.12	92 ± 24	13.1 ± 3.6

Tensile properties reported as mean ± SD

Table B4. Tensile properties of cast bioplastics versus 3D printed bioplastics.

Specimen	Elastic Modulus, E_t [MPa]	Yield Stress, σ_y [MPa]	Strain at Break, ε_{tb} [%]	Toughness, U_t [MJ m^{-3}]
No Additive Cast	1018 ± 57	50.04 ± 0.29	49 ± 13	19.0 ± 4.6
No Additive 3DP	852 ± 78	40.14 ± 0.86	52 ± 12	15.4 ± 3.3
15% Glycerol Cast	29.1 ± 2.0	1.770 ± 0.039	358 ± 36	9.0 ± 1.5
15% Glycerol 3DP	17.4 ± 3.2	1.363 ± 0.052	427 ± 42	6.8 ± 1.0
15% HPG-M Cast	296 ± 22	15.81 ± 0.10	113 ± 35	14.0 ± 4.1
15% HPG-M 3DP	200 ± 15	10.14 ± 0.18	163 ± 53	12.1 ± 3.7

Tensile properties reported as mean ± SD

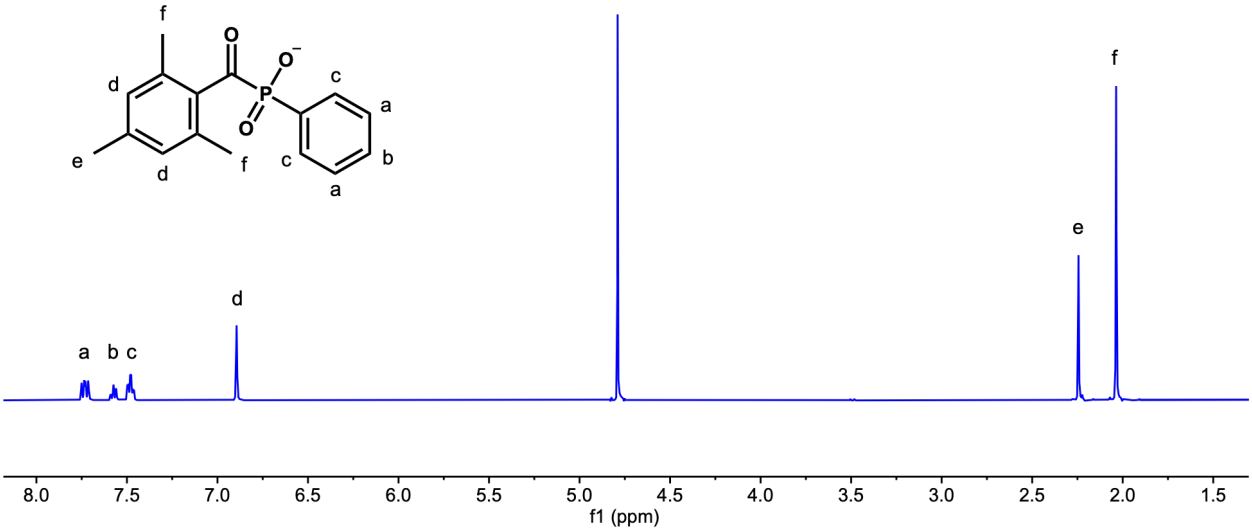

Figure B7. ^{1}H NMR spectrum of LAP (500 MHz, D_2O).

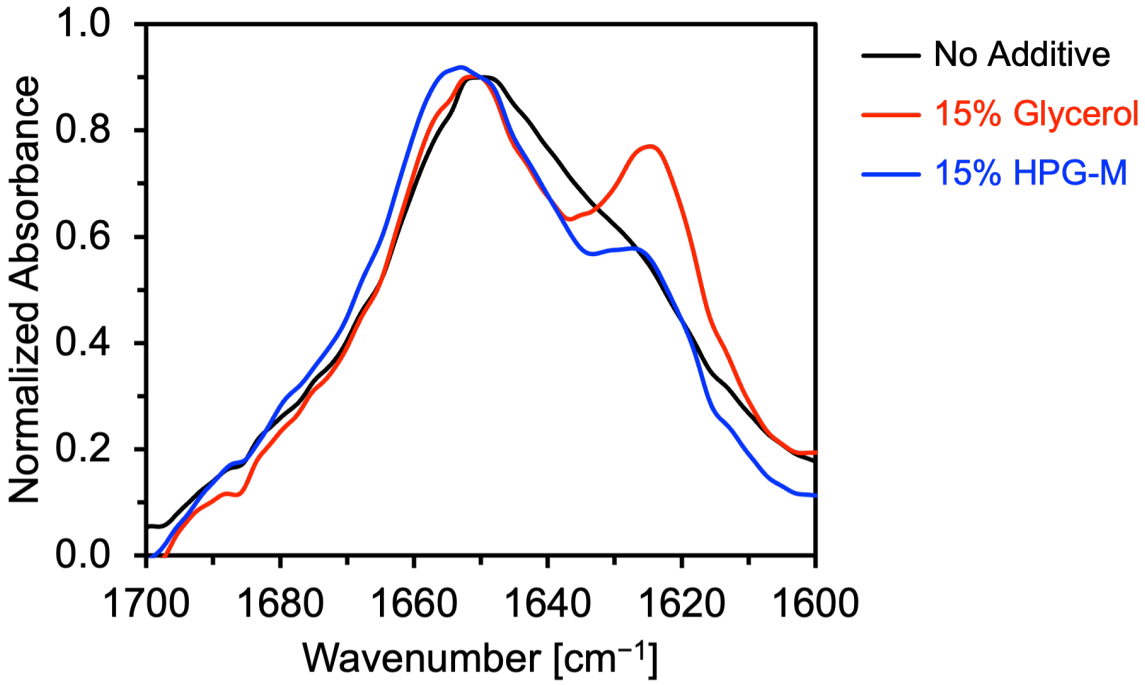

Figure B8. ATR-FTIR spectra for bioplastics (amide I region).

Table B5. Numerical data for Ashby plot (Figure 3.14). Tensile strength and strain at break values for commercial resins for light-based 3D printing.

Manufacturer	Material	Tensile Strength, σ_m [MPa]	Strain at Break, ε_{tb} [%]
Anycubic[a)]	Standard	41	10
Anycubic[a)]	Standard +	35	18
Anycubic[a)]	Water-Wash +	38	11.5
Anycubic[a)]	ABS-Like +	32	25
Anycubic[a)]	DLP Craftsman	43	40
Anycubic[a)]	Plant-Based	44	10
Anycubic[a)]	UV Tough	38	40
Formlabs[b)]	Elastic 50A V1 – Green	1.6	100
Formlabs[b)]	Elastic 50A V1 – Postcured	3.2	160
Formlabs[b)]	Elastic 50A V2 – Green	1.7	160
Formlabs[b)]	Elastic 50A V2 – Postcured	3.4	160
Formlabs[b)]	Flexible 80A – Green	3.7	100
Formlabs[b)]	Flexible 80A – Postcured	8.9	120
Formlabs[b)]	BioMed Clear – Postcured	52	12
Formlabs[b)]	BioMed Flex 80A – Postcured	7.2	135
Formlabs[b)]	BioMed Elastic 50A – Postcured	2.3	150
Formlabs[b)]	IBT Flex – Postcured	7.2	135
Formlabs[b)]	Dental LT Comfort – Postcured	–	33
Formlabs[b)]	Dental LT Clear V2 – Postcured	–	12
Formlabs[b)]	Dental Model – Green	33	25
Formlabs[b)]	Dental Model – Postcured	61	5
Formlabs[b)]	BioMed Durable – Postcured	29	33
Formlabs[b)]	Silicone 40 – Postcured	5	230
Formlabs[b)]	BioMed Black – Postcured	36	14
Formlabs[b)]	BioMed White – Postcured	46	10
Formlabs[b)]	BioMed Amber – Postcured	73	12
Formlabs[b)]	ESD – Postcured	44	12
Formlabs[b)]	Custom Tray – Postcured	70	3
Formlabs[b)]	Surgical Guide – Postcured	–	12
Formlabs[b)]	Castable Wax – Green	12	13
Formlabs[b)]	High Temp – Green	21	14
Formlabs[b)]	High Temp – Postcured	58	3.3
Formlabs[b)]	Tough 1500 – Green	26	69
Formlabs[b)]	Tough 1500 – Postcured	33	51
Formlabs[b)]	Tough 2000 – Green	29	74
Formlabs[b)]	Tough 2000 – Postcured	46	48

Formlabs[b)]	PU Rigid 1000 – Postcured	35	80
Formlabs[b)]	PU Rigid 650 – Postcured	34	170
Formlabs[b)]	Rigid 10K – Green	55	2
Formlabs[b)]	Rigid 10K – UV Cure	65	1
Formlabs[b)]	Rigid 10K – UV+Thermal Cure	53	1
Formlabs[b)]	Rigid 10K – UV+Media Blast	88	1.7
Formlabs[b)]	Rigid 4000 – Green	33	23
Formlabs[b)]	Rigid 4000 – Postcured	69	5.3
Formlabs[b)]	Standard Clear V5	46	13
Formlabs[b)]	Precision Model – Green	44	11
Formlabs[b)]	Precision Model – Postcured	50	8.6
Formlabs[b)]	Model V1	27	14
Formlabs[b)]	Model V2	33	25
Formlabs[b)]	Model V3 – Green	27	14
Formlabs[b)]	Model V3 – Postcured	48	4.8
Formlabs[b)]	Fast Model – Green	46	22
Formlabs[b)]	Fast Model – Postcured	55	15
Formlabs[b)]	Black V5 – Green	48	19
Formlabs[b)]	Black V5 – Postcured	57	14
Formlabs[b)]	White V5 – Green	46	22
Formlabs[b)]	White V5 – Postcured	64	15
Formlabs[b)]	Grey V5 – Green	46	22
Formlabs[b)]	Grey V5 – Postcured	54	15
Formlabs[b)]	Grey Pro – Green	35	32.5
Formlabs[b)]	Grey Pro – Postcured	61	13
Formlabs[b)]	Clear V5 – Green	46	13
Formlabs[b)]	Clear V5 – Postcured	51	10
Formlabs[b)]	Draft – Green	24	14
Formlabs[b)]	Draft – Postcured	36	5
Formlabs[b)]	Draft – Postcured+Thermal	52	4
Formlabs[b)]	Flame Retardant – Green	24	20
Formlabs[b)]	Flame Retardant – Postcured	38	9.4
Formlabs[b)]	Color Base V4 – Green	38	12
Formlabs[b)]	Color Base V4 – Postcured	65	6
Formlabs[b)]	Durable – Green	13	75
Formlabs[b)]	Durable – Postcured	28	55
ELEGOO[c)]	Standard	32	17.5
ELEGOO[c)]	Rapid Standard	38	11.1
ELEGOO[c)]	Standard V2.0	33	10
ELEGOO[c)]	8K Standard	39	9.4

ELEGOO[c)]	Water-Washable	23	14.9
ELEGOO[c)]	8K Water-Washable	24	–
ELEGOO[c)]	ABS-Like V1	39	–
ELEGOO[c)]	ABS-Like V2 Grey	36	–
ELEGOO[c)]	ABS-Like V3	40	24
ELEGOO[c)]	Plant-Based	27	21.8
ELEGOO[c)]	Thermochromic	39	9.4
Siraya Tech[d)]	ABS-Like	32	40
Siraya Tech[d)]	Regular Tough	50	32
Siraya Tech[d)]	Plant-Based	28	3
Siraya Tech[d)]	High Temperature Resistant	35	5
Siraya Tech[d)]	Castable	20	5
eSUN[e)]	Standard	57	32
eSUN[e)]	S200 Standard	50	24
eSUN[e)]	eResin PLA Pro	55	10
eSUN[e)]	Bio-Based PLA	43	26.5
eSUN[e)]	PW100 PLA Water Washable	48	25
eSUN[e)]	Water-Washable	33	23.5
eSUN[e)]	Hard Tough	45	43.5
eSUN[e)]	High Temp – Green	45	11.8
eSUN[e)]	High Temp – Postcured	54	6.4
eSUN[e)]	DM 100 Dental Model	26	25.5
eSUN[e)]	DM100 Dental Restoration	56	14
eSUN[e)]	eResin-Flex	7	225
eSUN[e)]	Water-Washable	33	23.5
eSUN[e)]	PA100 Nylon-Like	68	15
eSUN[e)]	PM200 PMMA-Like	45	36
eSUN[e)]	SG100 Surgical Guide	47	28.4
eSUN[e)]	OM100 Ortho Model	34	8.8
eSUN[e)]	WO100 Water-Washable Ortho	23	14.9
eSUN[e)]	TC100 Temporary C&B	30	6.5
eSUN[e)]	eResn-ABS	52	16
eSUN[e)]	eResin-Elastic	4.5	300
SUNLU[f)]	Standard	36	10
SUNLU[f)]	Water-Washable	50	12
SUNLU[f)]	ABS-Like	34	20
SUNLU[f)]	Plant-Based	28	8.5
Carbon[g)]	CE 221	85	3
Carbon[g)]	MPU 100	35	15
Carbon[g)]	RPU 70	40	30

Carbon[g)]	RPU 130	35	100
Carbon[g)]	Loctite 3843	38	52
Carbon[g)]	UMA 90	30	30
Carbon[g)]	EPX 82	80	5
Carbon[g)]	EPX 86FR	90	10
Carbon[g)]	EPX 150	76	9
Carbon[g)]	Loctite IND405 Black	24	89
Carbon[g)]	FPU 50	25	200
Carbon[g)]	Loctite IND147	67	2.4
Carbon[g)]	Loctite IND405	42	120
Carbon[g)]	Loctite IND3380	28	2.5
Carbon[g)]	EPU 40	19	400
Carbon[g)]	EPU 41 – Green	15	300
Carbon[g)]	EPU 43	17	380
Carbon[g)]	EPU 43 – IPA Wash	19	420
Carbon[g)]	EPU 44	24	275
Carbon[g)]	EPU 45	24	290
Carbon[g)]	EPU 45 – IPA Wash	24	240
Carbon[g)]	EPU 46	23	330
Carbon[g)]	EPU46 Soft	21	300
Carbon[g)]	EPU46 Extra Soft	15	250
Carbon[g)]	SIL 30	3.5	350
Carbon[g)]	Loctite MED414	1.4	223
Carbon[g)]	DPR 10	45	4
Forward AM[h)]	Ulteacur3D FL300	5	245
Forward AM[h)]	Ulteacur3D FL60	4	90
Forward AM[h)]	Ulteacur3D EL60	9	95
Forward AM[h)]	Ulteacur3D EL150	7	182
Forward AM[h)]	Ulteacur3D EL4000	11	170
Forward AM[h)]	Ulteacur3D RD35	80	6
This Work	No Additive	50	49
This Work	No Additive – 3DP	40	52
This Work	5% Glycerol	23	178
This Work	10% Glycerol	7.2	287
This Work	15% Glycerol	3.9	358
This Work	15% Glycerol – 3DP	2.5	427
This Work	5% HPG-M	38	60
This Work	10% HPG-M	26	97
This Work	15% HPG-M	16	113
This Work	15% HPG-M – 3DP	10	163

This Work	15% HPG-S	12	233
This Work	15% HPG-L	16	92

[a)] Data obtained from Anycubic; [b)] Data obtained from Formlabs; [c)] Data obtained from ELEGOO; [d)] Data obtained from Siraya Tech;[9] [e)] Data obtained from eSUN; [f)] Data obtained from SUNLU; [g)] Data obtained from Carbon; [h)] Data obtained from Forward AM.

Appendix C

Dynamic Protein-Based Hydrogels Utilizing Native Ligand Binding Toward Applications in Therapeutic Delivery and 3D Bioprinting

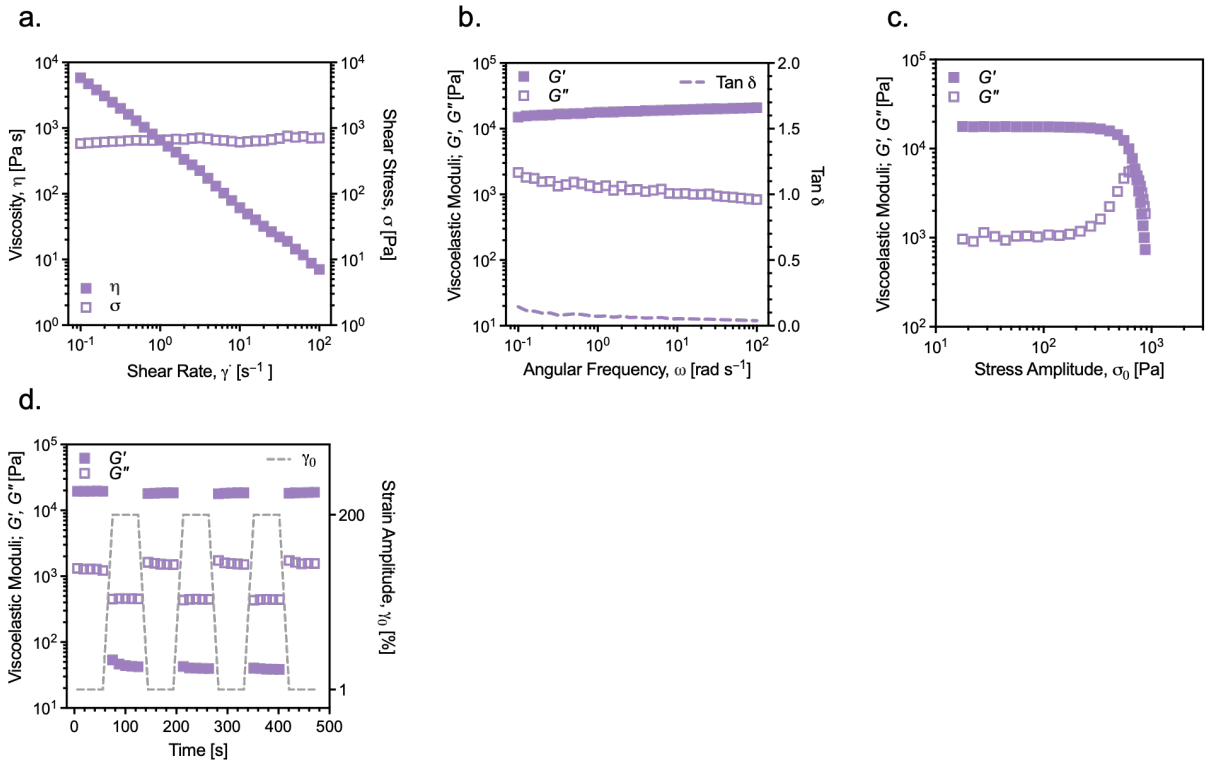

Figure C1. (a) Steady-shear viscosity and stress curves for 30 wt% F-127 hydrogel. (b) Frequency sweep data for 30 wt% F-127 hydrogel. (c) Stress amplitude sweep data for 30 wt% F-127 hydrogel. (d) Multi-step high- and low-amplitude oscillatory tests showing self-healing and thixotropy of 30 wt% F-127 hydrogel.

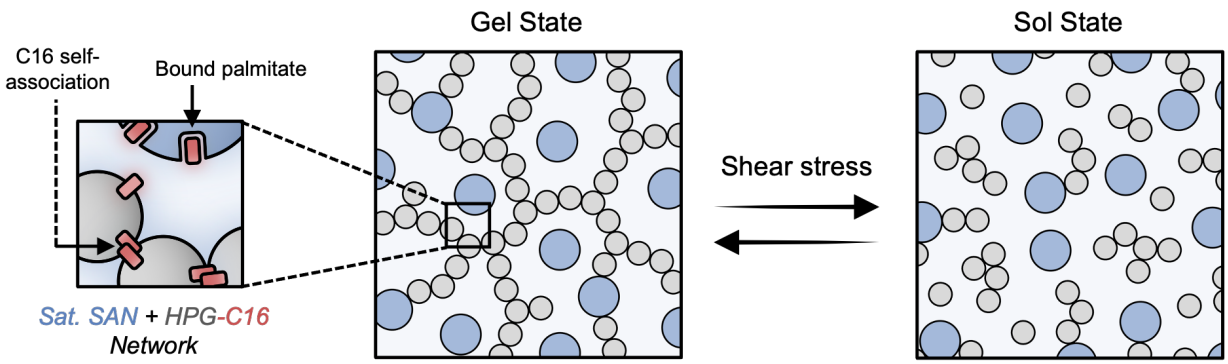

Figure C2. Hypothetical depiction of saturated SAN + HPG-C16 dynamic network formation.

Figure C3. Custom syringe holder used for injection force measurements. It was 3D printed using fused filament fabrication, with poly(lactide) filament.